First-Row Metal Catalysts for
Hydrogenolysis of Carbon–Sulfur and Carbon–Oxygen Bonds.

by

Orain Brown

A thesis submitted in partial fulfillment of the requirements for the degree of

Doctor of Philosophy

Department of Chemistry
University of Alberta

Abstract

A series of phosphoranimide-supported first-row transition metal clusters were prepared, structurally characterized, and investigated for catalytic hydrogenolysis of carbon-heteroatom bonds. Homoleptic heterocubane clusters, as well as two-dimensional bi- and tetranuclear compounds of manganese, nickel and copper were isolated and characterized. Noteworthy among these is the unique low-valent cluster $[Cu_4(NP^tBu_3)_4Li_2]$, which revealed the ion-specific cation-induced redox modulation of tetranuclear $[M(NP^tBu_3)]_4$ clusters (M = Ni, Cu).

Binuclear and tetranuclear nickel clusters, $[Ni(NP^tBu_3)_2]_2$ and $[Ni(NPEt_3)_2]_4$, are effective precatalysts for the hydrodesulfurization of dibenzothiophene, mediated by stoichiometric potassium *tert*-butoxide, under relatively mild conditions (150-200 °C and 1-34 atm hydrogen). Under the reaction conditions, the nickel clusters are transformed to nanoparticles, which function as active catalysts for hydrodesulfurization.

Supported heterogeneous catalysts were rationally prepared by protolytic grafting of nickel phosphoranimide clusters onto alumina and silica. These alumina- and silica-supported - catalysts display improved reactivity and selectivity for hydrodesulfurization, compared to the unsupported analogues. Simple Ni(II) alkoxides, derived *in situ*, and soluble Ni(0) complexes are also effective precatalysts for hydrodesulfurization under these conditions, establishing that the phosphoranimide ligand serves only to control the grafting and initiate hydrogenolysis. For all desulfurization reactions, the promotional effect of potassium ions was determined,

attributable to the formation of cation-π interactions with the aromatic rings of dibenzothiophene and potassium-promoted hydrogenolysis of nickel sulfide.

Finally, a simple copper/molecular sieves system for catalytic hydrodeoxygenation of aryl ketones under very mild conditions (120 °C, 1 atm H_2) is reported. The copper catalysts are conveniently generated *in situ* from the decomposition of CuO^tBu under hydrogen. While a homogeneous catalytic specie is sufficient to hydrogenate the ketone to the corresponding alcohol, full deoxygenation requires the formation of a heterogeneous copper catalyst, in the presence of molecular sieves.

Preface

Sections of Chapters 2 and 3 of this thesis have been submitted for publication in the Journal of the American Chemical Society as: Orain Brown, Robin J. Hamilton, Robert McDonald, and Jeffrey M. Stryker, 'Supported Nickel Nanaocatalysts for Potassium Alkoxide-Promoted Hydrodesulfurization of Dibenzothiophene.' I was responsible for the experiments, data collection and manuscript preparation. Robin J. Hamilton contributed of the development of the concepts and to the manuscript edits. Robert McDonald collected X-ray crystallographic data and performed the structure solutions. Jeffrey M. Stryker was the supervisory author, and was involved in the management of the project and the preparation of the manuscript.

Dr. Kai Ylijoki of Saint Mary's University, has collaborated with us to perform computational analysis on the copper clusters described in Chapter 1. A manuscript describing the synthesis and characterization of these copper clusters, along with the computational analysis, is currently in preparation.

Acknowledgements

I thank Prof. Jeffrey M. Stryker for allowing me the opportunity to work on this research project. His patience and willingness to promote intellectual independence has both inspired and challenged me during the past five years. Our many conversations have deepened my understanding and appreciation of chemistry. I also thank the members of my supervisory and examination committees, for their guidance and advice during my studies

I am also grateful to current and previous members of the Stryker group, particularly Dr. Robin Hamilton, David Scott and Asama Vorapattanapong, whose advice, assistance and friendship have been invaluable.

The support staff in the Department of Chemistry have been crucial in ensuring that this project kept moving forward. In particular, X-ray crystallographers Dr. Mike Ferguson and Dr. Bob McDonald, Wayne Moffat of analytical services and Jason Dibbs in the glass shop have been excellent resources, and even better friends.

Finally, I wish to thank my grandma Shirley, my mother Merline, and most importantly my loving wife Shanyeak; their confidence in my abilities defies logic, yet it has been my greatest source of inspiration during the past five years.

Table of Contents

List of Figures

List of Schemes   Page

List of Equations   **Page**

List of Symbols and Abbreviations

Å	Angstroms
atm	Atmosphere
BBN	Borabicyclononane
Bu	Butyl
BP	Biphenyl
BP-SH	2-phenylthiophenol
^{t}Bu	*tert*-butyl
cm^{-1}	Wavenumbers
COD	Cyclooctadiene
Cp	Cyclopentadienyl
Cp*	Pentamethylcyclopentadienyl
Cy	Cyclohexyl
Cyclooct.	Cyclooctane
d	Days
dippe	1,2-Bis(diisopropylphosphino)ethane
DBT	Dibenzothiophene
e	Electron
equiv.	Equivalents
Et	Ethyl
g	Grams
GC-FID	Gas chromatography with flame ionization detector
GC-MS	Gas chromatography–mass spectrometry
h	Hours
Hz	Hertz
IR	Infrared
KDA	Potassium di-isopropyl amide
LDA	Lithium di-isopropyl amide
L	Ligand
M	Metal
Me	Methyl

mg	Milligrams
mHz	Megahertz
min	Minutes
mL	millilitre
mmol	millimoles
mol	Moles
MS	Molecular sieves
NHC	N-heterocyclic carbene
nm	Nano meters
NMR	Nuclear magnetic resonance
Ph	Phenyl
ppm	Parts per million
^{i}Pr	*iso*-propyl
R	Generic alkyl/aryl substituent
RT	Room temperature
THF	Tetrahydrofuran
TMS	Trimethylsilyl
Tol	Toluene
UV-Vis	Ultra violet/visible
μ	Mu (bridging mode)
°C	Degrees Celsius
η	Eta (hapticity)
XRD	X-ray diffraction

Prologue: Polymetallic clusters of the first-row metals for challenging carbon-heteroatom bond hydrogenolysis

Why first-row metals?

Transition metal catalysis is indispensable to modern economies. Transition metal-catalyzed reactions are present in almost every area of the chemical industry, from petroleum refining and ammonia production to pharmaceutical and other fine chemicals manufacturing. Recent Nobel prizes in asymmetric hydrogenation (2001, Ru),[1-3] olefin metathesis (2005, Ru),[4-6] and cross-coupling (2010, Pd),[7-8] confirm that transition metal catalysis has indeed "conferred the greatest benefit to mankind".[9]

The identity of such 'Nobel' metals (Ru, Pd, etc.) underscores a salient point: that second and third row d-block metals are prevalent among critically-important industrial catalysts.[10] In the long term, this is unsustainable; precious metals are uneconomically costly, terrestrially limited, and often highly toxic. In contrast, the first-row transition metals are widely available, inexpensive, and generally biocompatible. Replacing precious metals in catalysis with inexpensive, earth-abundant first row transition metals is therefore an attractive research target.

The development of first-row transition metal catalysts has lagged behind precious metals because the base metals are generally considered to be inherently less active/selective than their heavier congeners, but this view is evolving rapidly.[11-12] Advancements in ligand design,

1

inter alia, has allowed some base metals to display 'precious metal-like' activity in processes such as reduction/hydrogenation of unsaturated molecules[13-16] and C–C bond formation.[17-20]

Polynuclear molecular architectures can also coax 'precious metal-like' activity from the base metals. Biological systems have long relied on polymetallic arrays of the base metals for challenging transformations under ambient conditions. [21-22] This principle has been extended to organometallic chemistry with increasingly frequent reports of reactive molecular clusters of first row transition metals, activating typically inert bonds, e.g., C–H,[23] C–C,[24-25] and N≡N,[26-27] under very mild conditions. The cooperative reactivity provided by first-row metal atoms in discrete clusters holds promise for the wide-scale use of earth-abundant metals for challenging industrial catalytic transformations, under atypically mild conditions.

Catalytic hydrogenolysis of challenging bonds

The Stryker group is particularly interested in exploiting the unique reactivity of polymetallic first-row metal clusters for the hydrogenolysis of strong carbon–heteroatom bonds in aryl ethers, thioethers, and related heteroaromatic compounds. The hydrogenolysis of C–S bonds by catalytic hydrodesulfurization (HDS) is fundamental to petroleum refining and is carried out on a massive scale in refineries worldwide.[28-29] Driven by environmental concern and strict regulations, HDS is now among the most important chemical processes worldwide.[30] Similarly, the selective hydrogenolysis of C–O bonds in biomass-derived molecules is critical for the renewable production of small aromatic compounds used for bio-fuels and commodity chemicals. [31-34]

While the catalytic activation of C–S or C–O bonds using first row metals (primarily nickel) has been reported, these methods rely on energetic nucleophilic reductants, including Grignard,[35-37] organoboron,[38-39] organozinc,[40] and hydrosilane[41-42] reagents. The use of stoichiometric quantities of these reagents limits potential applications of such desulfurization/deoxygenation reactions to small-scale, fine-chemicals organic synthesis.

R, R' = H, alkyl, aryl
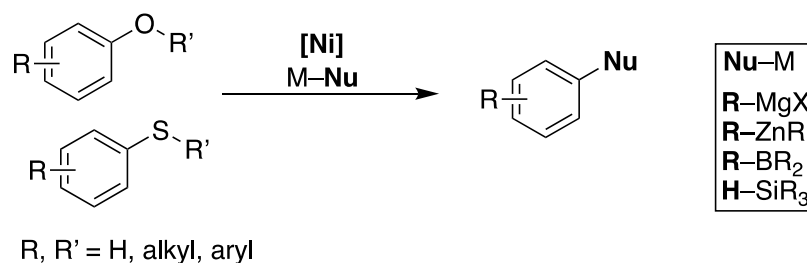
Equation **1.1**

For high-volume reductive processes such as HDS or the hydroprocessing of biomass oxygenates, the use of molecular hydrogen is axiomatic. It is the least expensive, most atom-economical, and "greenest" reductant. Molecular hydrogen, unfortunately, is kinetically unreactive compared to silanes or Grignard reagents. Thus, catalytic hydrogenolysis of inert C–O/S bonds, using first row transition metals under mild conditions remains extremely rare. Hartwig's reports of nickel-catalyzed C_{aryl}–O bond hydrogenolysis (Equation **1.2**),[43-44] along with the Stryker group's recent exploration of metal-catalyzed, *base-promoted* hydrodesulfurization[45-46] are among the few such examples.

[Ni] (20 mol %)
H_2 (1 atm)

NaOtBu (2.5 equiv),
m-xylene, 120 °C,
16-48 h

OH +

99 % yields

SIPr.HCl

[Ni] = Ni(COD)$_2$/ 2 SIPr.HCl 16h
Ni(COD)$_2$ 48h
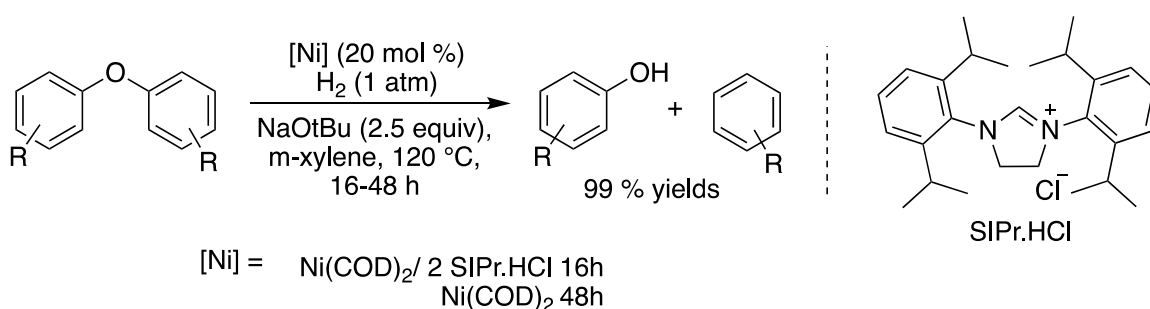
Equation **1.2**

Design strategy: polymetallic molecular clusters and basic "single-atom" bridges

The hydrogenolysis of C–S bonds on an industrial scale is accomplished by heterogeneous cobalt- or nickel-promoted molybdenum catalysts at high temperature and very high pressure of hydrogen.[28] For the strongest C_{aryl}–S bonds, however, the process is unsustainably inefficient and energy-intensive. Despite decades of research, the complexity of the heterogeneous catalysts means that the active site(s) are not completely understood and the scope for further optimization is limited. The current catalysts simply cannot achieve desired levels of reactivity.

Here polymetallic clusters of first-row metals may prove particularly relevant. Soluble molecular clusters provide a convenient tool for modelling the polymetallic active sites present in heterogeneous catalysts.[47] The insights gained from the physical characterization and mechanistic study of these molecular models can be invaluable in understanding of the functioning of the 'true' active sites in current heterogeneous catalysts.[48] More importantly, the enhanced reactivity afforded by discreet molecular cluster composed of first row metals

presents the opportunity *to develop a new class of inexpensive, yet highly efficient catalysts for hydrotreatment*.

Polymetallic clusters have been used as organometallic models for the active sites of hydrodesulfurization catalyst for decades.[29, 48] The activation of C–S bonds by these molecular species is well-documented and is discussed in greater detail in Chapter 2. Among these, nickel clusters **1**[49-50] and **2**[51] are noteworthy because they illustrate the efficacy of multimetallic *cooperative* reactivity for facile hydrogenolysis of exceptionally strong C–S bonds of dibenzothiophene and 4,6-dimethyldibenzothiophene (Scheme **1.1**); commercial catalysts struggle to effect similar transformations, even at high temperatures. The reactivity of nickel complexes **1** and **2** highlights that, given an appropriate polymetallic coordination environment, first-row transition metals are well placed to challenge the activation of highly refractory bonds.

Scheme **1.1**

The structures of clusters **1** and **2** are similar – and instructive: a multimetallic array of metals, supported by strongly donating ligands, held together by *single atom bridges*, so that the metal atoms are in close proximity, if not bonded. The Stryker group has been interested in developing polymetallic precatalysts for the hydrogenolysis of C–X bonds using precisely this molecular architecture. The catalysts envisioned are constructed from first row transition metals exclusively. These metals, constrained by single-atom bridges, allow for cooperative activation of reactants and substrate molecules. The metal atoms must be coordinatively unsaturated but not sterically encumbered, allowing for facile donor bonding and activation. Finally, the metal atoms must be electron rich and, preferably, low valent, in order to mediate the hydrogenolysis of strong C–X bonds under mild conditions.

The chapters that follow will recount our attempts to use polymetallic arrays of first-row transition metals as catalyst for the hydrogenolysis of C–S and C–O bonds. In chapter 1, the use of phosphoranimide ligands to nucleate the desired polymetallic clusters is discussed. Clusters of manganese, copper and nickel are described, of which only the nickel compounds displayed catalytic activity for the hydrogenolysis of carbon–heteroatom bonds. Chapters 2 and 3 explore the application of these active nickel clusters in catalytic C–S bond hydrogenolysis. Chapter 3 in particular presents the discovery of functional heterogeneous HDS catalysts by immobilizing well-defined nickel clusters on prepared inorganic supports. Finally, Chapter 4 highlights the hydrogenolysis of C–O bonds in aryl ketones and aldehydes catalyzed by polymetallic nickel compounds, as well as by simpler, more convenient copper salts.

1. New trialkylphosphoranimide-supported first-row transition metal clusters

1.1 Introduction and background

1.1.1 Trialkylphosphoranimde ligands: A brief historical overview

Anionic trialkylphosphoranimides are ideal ligands for nucleating polymetallic clusters. The phosphoranimide ligand is isoelectronic with more common anionic ligands such as alkoxide [$^-$OCR$_3$], siloxide [$^-$OSiR$_3$] and is capable of donating up to six electrons, from one σ- and two π-molecular orbitals on the nitrogen atom. [52-53]

The phosphoranimide ligand can adopt a range of coordination modes, binding to between one and three transition metal atoms. When bound to a single metal atom, the phosphoranimide can form one σ- and two π-bonds to the metal (**A** Figure **1.1**). This results in short, very strong M–N bonds and nearly linear P–N–M bond angles.[52, 54] In the terminal binding mode, the ligand can also act as a four-electron donor (**B**, Figure **1.1**). In this coordination mode, the M–N bonds are longer and the M–N–P angle deviates from linear. Terminal binding modes are preferred for early transition metals in high oxidation states where the greater electron density stabilizes the electrophilic metal atom.[54-56]

Figure **1.1** Common coordination modes for phosphoranimide ligands to transition metals.

In less electrophilic transition metals, bridging coordination modes (**C** and **D**, Figure **1.1**) are more common and lead to the nucleation of polymetallic clusters.[52] In binding mode **C**, the phosphoranimide is a doubly bridging ligand, donating between four and six electrons to two metal atoms. This typically leads to symmetrical bimetallic complexes, with longer M–N bonds and more acute M–N–P angles than for terminal coordination.[57] The triply-bridging binding mode (**D**, Figure **1.1**), leads to clusters with the highest nuclearity; heterocubane structures are typically formed in the later first-row transition metals.[53] Here the ligand donates two electrons to each of three perpendicularly arranged metal atoms.

Beside the oxidation state of the transition metal, the identity and size of the substituents on phosphorus influences the hapticity of the ligand. Dehnicke showed that phosphoranimides bearing sterically small methyl or ethyl groups form heterocubane clusters exclusively with mid to late first-row metals atoms (**3**, Figure **1.2**).[52, 58-62] The larger *tert*-butylphosphoranimide ligand, used by Stephan and later by Stryker, leads to the formation of mononuclear,[54-56] two-dimensional binuclear, or tetranuclear clusters. (**4**, Figure **1.2**)[57, 63-65,66] This ability to control the

cluster nuclearity though manipulation of the steric properties of the substituent groups on the phosphoranimide is a powerful tool for the rational design and synthesis of polymetallic clusters.
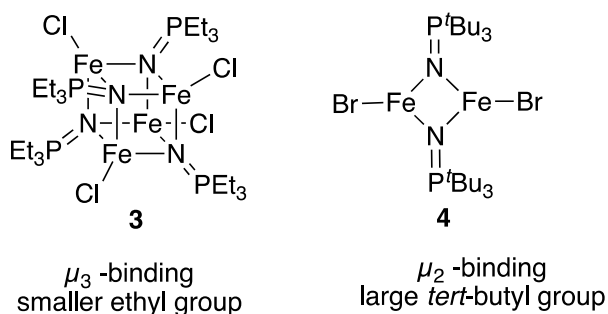
Figure **1.2** Varying the size of the substituents on phosphorous lead to distinct binding modes.

The steric bulk of the alkyl substituents on the phosphoranimide influences the nuclearity of the clusters, but still remains sufficiently displaced from the metal so as not to impede substrate coordination.[67] In phosphoranimides, the nitrogen atom displaces the steric bulk of the R groups away from the metal centres, allowing for greater accessibility without promoting coordinative saturation. Ligand cone angles and "displaced volume" metrics illustrate this point.[67-69] *Tert*-butylphosphine has a hemispherical cone angle of 182°, (42.4 % buried volume) indicating that about half the metal surface is buried beneath the volume of the ligand (Figure **1.3**).[67, 69] In contrast, the phosphoranimide ligand derived from $^tBu_3P$ has a cone angle of just 87°(Figure **1.3**), indicating vastly improved metal accessibility.[70] The isolobal cyclopentadienyl ligand has similar steric demand to the phosphoranimide, but the displaced steric bulk of the

phosphoranimide ensures that the primary coordination sphere remains uncrowded, allowing more facile substrate coordination.[70-71]
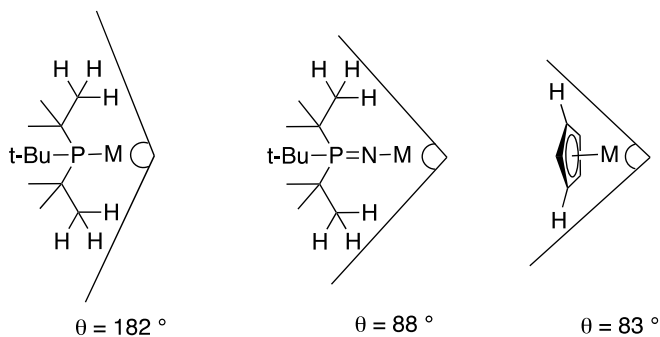
Figure **1.3** Cone angles for various ligands. [67, 70-72]

1.1.2 Synthesis of trialkylphosphoranimide ligands and complexes

 Dehnicke pioneered the synthesis of first-row transition metal phosphoranimide complexes, typically by the high temperature desilylation of molten trimethylsilyl-trialkylphosphoranimide in the presence of a fluoride flux (Scheme **1.2**).[52] Trimethylsilyl-trialkylphosphoranimides, obtained from the interrupted Staudinger reaction of a trialkylphosphine and trimethylsilyl azide,[73] react to form polymetallic clusters, mostly heterocubane in structure (**5** Scheme **1.2**).[52] Dehnicke's work was limited to small substituents (methyl, ethyl) on the trimethylsilyl-trialkylphosphoranimide precursor, which melt at low enough temperatures to function as solvent for the reaction.

$$\text{Me}_3\text{SiN}_3 \ + \ \text{R}_3\text{P} \quad \xrightarrow[- \text{N}_2]{\Delta} \quad \text{Me}_3\text{Si}-\text{NPR}_3$$

$$\text{Me}_3\text{Si}-\text{NPR}_3 \ + \ \text{MX}_2 \quad \xrightarrow[\substack{\Delta \\ -\text{Me}_3\text{SiF} \\ -\text{KX}}]{\text{KF}} \quad$$

5

M = Mn, Fe, Co, Ni
R = Me, Et
X = Cl, Br
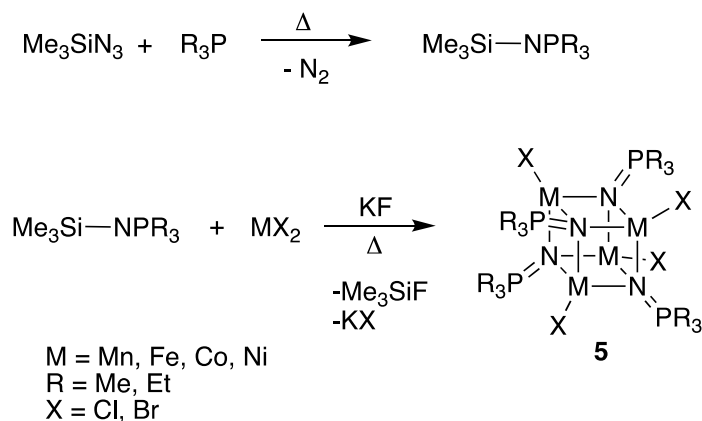
Scheme **1.2**

For higher molecular weight alkyl groups such as *tert*-butyl, alkali metal salts can be isolated by controlled hydrolysis[74] followed by deprotonation with a strong base (Scheme **1.3**).[75] Hamilton and co-workers in the Stryker group have since improved the efficiency and control of the hydrolysis step, by substituting anhydrous potassium hydrogen bifluoride for methanol or water (Scheme **1.3**).[65] The scalability of these methods is severely limited by reliance on toxic and explosive azides in the ligand synthesis.

$$\text{Me}_3\text{Si}-\text{NPR}_3 \quad \xrightarrow[- \text{Me}_3\text{Si}-\text{OMe}]{\text{MeOH}} \quad \text{HNPR}_3 \quad \xrightarrow{\text{MeLi}} \quad \text{LiNPR}_3$$

2 HFKF
- Me₃SiF

$$[\text{H}_2\text{NPR}_3]^+ \ \text{F}^-$$

MeLi
- LiF, CH₄
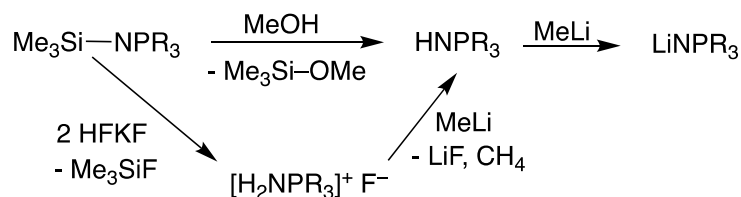
Scheme **1.3**

A safer route updates a classical synthesis,[76] converting a dibromophosphorane to a phosphoraniminium bromide salt, [R₃PNH₂]Br by reaction with lithium amide. Subsequent deprotonations provide the anionic phosphoranimide salt (Scheme **1.4**). Alternatively, the

dibromophosphorane can be converted in one pot to the potassium phosphoranimide salt by reaction with excess potassium amide, formed *in situ*, in liquid ammonia.[77] Unfortunately, this procedure is not yet adapted to the preparation of KNP^{t}Bu$_3$.

$$R_3PBr_2 \xrightarrow[\text{Et}_2\text{O, RT}]{\text{LiNH}_2} [R_3PNH_2]Br \xrightarrow[\text{Et}_2\text{O, RT}]{\text{NaH or KH}} \text{Na/KNPR}_3$$

$$\underrightarrow{\text{KH/KNH}_2 \atop \text{NH}_3}$$

R = Cy, Et, ^{i}Pr, Ph

Scheme **1.4**

1.1.3 Previous synthetic work from the Stryker group.

The Stryker group has constructed a diverse library of mid-to-late first-row transition metal clusters supported by μ_1- , μ_2- and μ_3- phosphoranimide ligands (Scheme **1.5**). The basic building blocks for these compounds are bimetallic and tetrametallic halide-capped phosphoranimide clusters (**5**, **6**, Scheme **1.5**; R = Et, ^{t}Bu, M = Fe, Co, Ni) formed from a 1:1 mixture of the ligand and a metal halide. From here one of two synthetic strategies was used to prepare functional polymetallic precatalysts: 1) The halide is exchanged for a hydrocarbon ligand that readily undergoes hydrogenolysis (alkyl, allyl) or a second equivalent of the anionic phosphoranimide.[45, 64-65, 77-78] 2) The halide complex is reduced to give a lower valent, more reactive metal center.[46, 63-64, 66, 79-80]

Alkylation of **5** or **6** provides alkyl- and allyl-capped clusters **7**-**10**. When exposed to hydrogen, the M–C bonds in these undergo hydrogenolysis to form metal hydrides, which are the putative

catalysts for hydrogenation and hydrotreatment reactions. In practice, the hydrogenolysis reaction was often slow or required high pressure; **8c**, for example, requires single-electron oxidation to mixed-valence cluster **9** before hydrogenolysis occurs under mild conditions (1 atm of H_2, RT–110 °C).[77] Mixed-valence cluster **9**, reported by Dr. Houston Brown, is as an excellent *homogeneous* catalyst for KH promoted HDS.[45, 78]
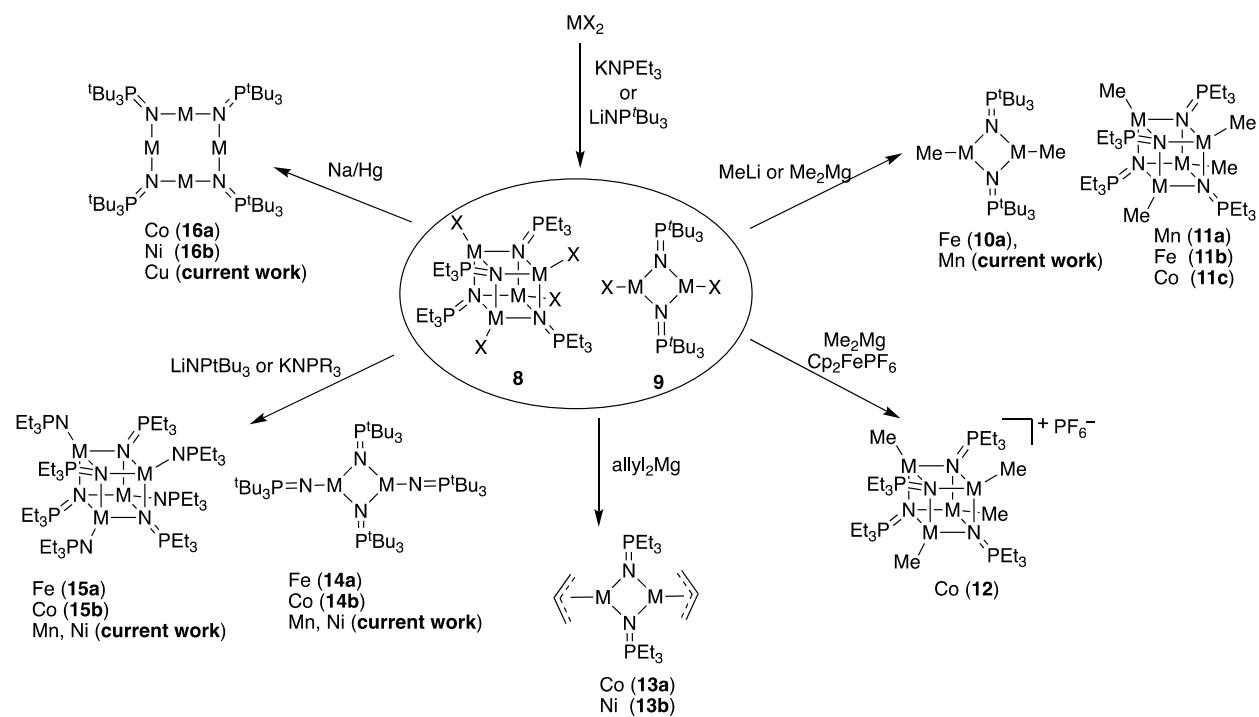
Scheme **1.5**

Replacing the halide atoms in **5** and **6** with a second equivalent of the phosphoranimide ligand gives homoleptic clusters **11** and **12**. The strongly basic lone pair on the terminal phosphoranimide ligand provides an ideal site for heterolytic activation of H_2 to form the desired metal hydrides and an equivalent of the free (protonated) ligand. Brown, Hebert, and Vorapattanapong have used the Fe and Co analogues of **11/12** as catalysts for hydrogenation

and hydrodesulfurization reactions.[63, 65, 81] The homoleptic clusters **11/12** can be conveniently prepared directly from the metal halide and two equivalents of the anionic phosphoranimide.

Finally, Jeffrey Bunquin in the group discovered the low-coordinate tetranuclear clusters **13a** and **13b** by reduction of the cobalt and nickel homologues of **6** using Na(Hg).[63, 66] The linear two-coordinate d^8-Co(I) and d^9-Ni(I) atoms in **13a/b** are electron rich and highly unsaturated, allowing facile binding and activation of hydrogen and substrate molecules. Both complexes find utility as precatalysts for hydrogenation,[66, 79] hydrosilylation,[79] HDS[46] and HDO.[80]

1.2 Results and discussion: New manganese and copper clusters

Our specific objectives include expanding the group library of phosphoranimide-supported first-row transition metal clusters, in order to discover new precatalysts for HDS and other processes involving the activation of strong C-X bonds (X = H, O, N). To accomplish this, the synthetic strategies highlighted in Scheme **1.5** were applied to copper and manganese, hitherto unexplored by the Stryker group. In addition, the rich nickel chemistry described by previous co-workers was extended to the synthesis of unreported nickel(II) (bis)phosphoranimide complexes and an exploration of catalytic C-X bond hydrogenolysis.

1.2.1 Trialkylphosphoranimide clusters of manganese

Manganese catalysis is not as well established as for other late first-row transition metals (Fe, Co, Ni), but interest in this earth abundant, environmentally benign metal is growing.[82] Manganese-catalyzed epoxidation reactions are well-known,[83-84] and catalytic C–H activation,[85]

hydrosilylation,[86-87] hydrogenation[88-90] reactions, among others, have been reported with increasing frequency in recent years. Moreover low-valent manganese has featured in stoichiometric C–S bond activations as discussed in chapter 2.[91-95] This led us to prepare polymetallic manganese clusters and explore their reactivity.

A simple salt metathesis reaction between equimolar $LiNP^tBu_3$ and a manganese dihalide led to the expected dimeric compounds, $[MnBr(NP^tBu_3)]_2$ **14a** and $[MnCl(NP^tBu_3)]_2$ **14b** (Equation **1.3**). Hebert and Bunquin reported that low temperatures (−35 °C) are imperative to form analogous iron, cobalt and nickel complexes,[63, 65] but this proved unnecessary for manganese. The isolation of pure **14a** required rigorous exclusion of LiBr through iterative low-temperature (-35 °C) recrystallizations from toluene. The empirical formulae of the pink solids **14a/b** were determined from elemental analysis and the bimetallic structure for **14a** was confirmed by X-ray crystallography of single crystals obtained from a cold (−35 °C), saturated THF solution.

$$MnX_2 \xrightarrow[\substack{THF,\ RT \\ -\ LiBr\ or\ LiCl}]{LiNP^tBu_3\ (0.9\ equiv)} [MnX(\mu_2\text{-}NP^tBu_3)]_2$$

$$\begin{array}{c} P^tBu_3 \\ \| \\ N \\ X-Mn \quad Mn-X \\ N \\ \| \\ P^tBu_3 \end{array}$$

X = Br (**17a**) 51 % yield
Cl (**17b**) 74 % yield
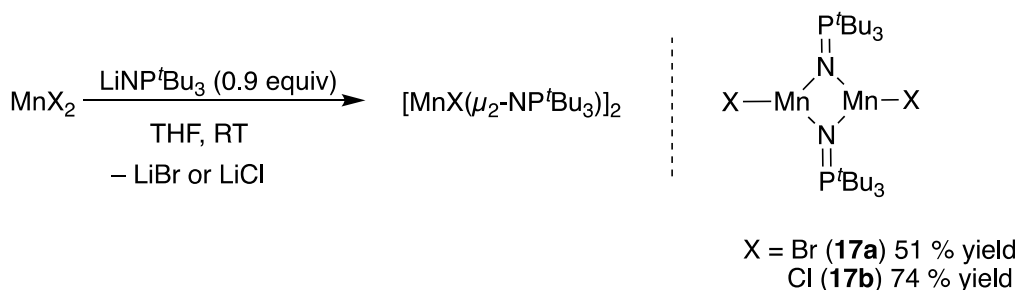
Equation **1.3**

 The solid-state structure of **14a** reveals the bimetallic Mn_2N_2 core (Figure **1.4**), isostructural with the previously described analogous Co complex $[CoCl(NP^tBu_3)]_2$ **6a**.[63] Both Mn atoms are four-coordinate and adopt a distorted tetrahedral geometry, with bond angles ranging from

95.39(4)° to 123.38(4)° The bromide atoms adopt a cis arrangement above the plane of the

manganese atoms. The distance between the metal atoms (2.75 Å) is within the range reported

for Mn–Mn interactions,[96] but the existence or strength of an actual bond has not been

assessed. No X-ray structure has been obtained for **14b**, but the solid-state structure is

anticipated to be similar to **14a**. Magnetic characterization is also pending.
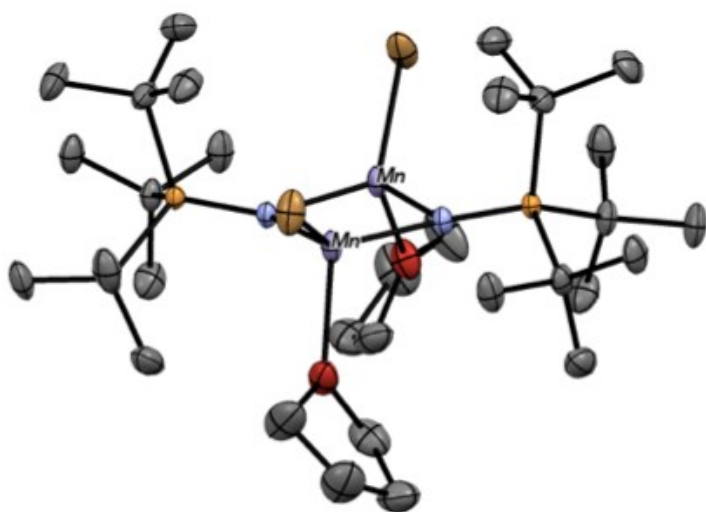
Figure **1.4** ORTEP diagram of compound [MnBr(NP^{t}Bu$_3$)]$_2$ **14a**. The thermal ellipsoids are shown at 30% probability. Hydrogen atoms have been omitted for clarity. R_1 = 0.0286, wR_2 = 0.0737

Table **1.1** Selected bond lengths and angles for [MnBr(NP^{t}Bu$_3$)]$_2$ **14a**

Bond distances (Å)		Angles (°)	
Mn–Mn	2.7527(7)	N–M–N	96.30(5)
Mn–Br	2.5314(4)	Mn–N–M	83.58(5)
Mn–O	2.2063(16)	Mn–N–P	138.69(9)
Mn–N	2.0551(15)		
P–N	1.5824(15)		

Treatment of THF solutions of **14a/b** with MeLi or Me$_2$Mg does not produce the alkylated manganese cluster, [MnMe(NP^{t}Bu$_3$)]$_2$ **17**. Intractable crude product mixtures were obtained even after adding the transmetallating reagent slowly and at low temperatures (Scheme **1.6**). By reversing the order of addition and installing the alkyl group first, followed by the addition of the *tert*-butylphosphoranimide anion, the methyl dimer [MnMe(NP^{t}Bu$_3$)]$_2$ **15** was isolated in 43% yield (Scheme **1.6**). Hebert previously developed this method to prepare the analogous iron compound **7a**.[65] The separation of the product from LiBr again proved problematic and several recrystallizations at −35 °C were required to produce **15** in sufficient purity for elemental analysis.
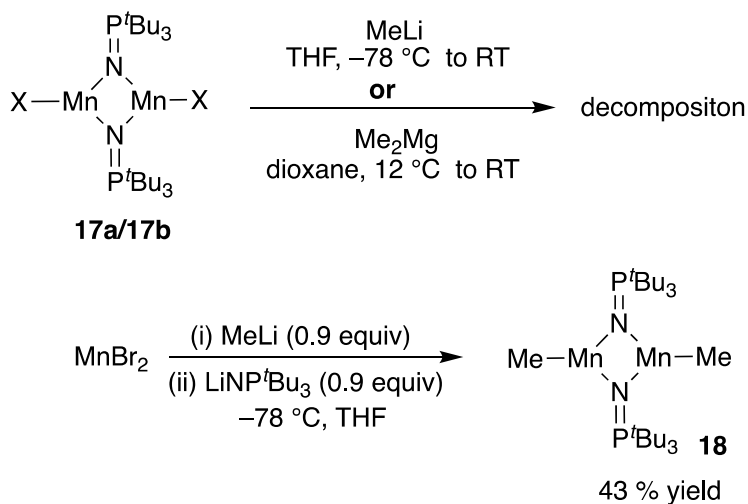
Scheme **1.6**

This cluster is extremely air sensitive and decomposes slowly in solution and in solid state to form an uncharacterized, insoluble black solid, presumably accelerated by with trace oxygen

present in the solvents or the glove box atmosphere. On exposure to hydrogen, a solution of **15** in THF darkened rapidly; on heating to 65 °C, visible decomposition to a black precipitate ensued. Despite the facile reaction with H_2, Mn dimer **15** does not catalyze the hydrogenation of unsaturated molecules.

a   b
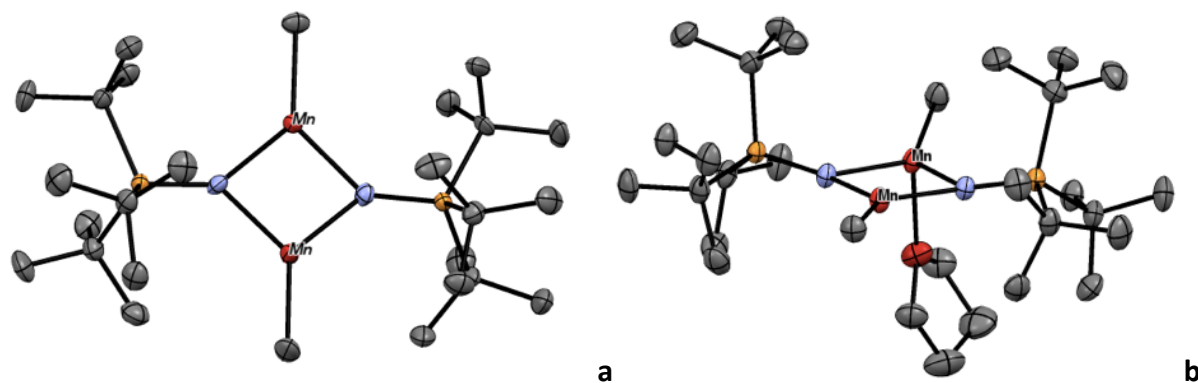
Figure **1.5** ORTEP diagrams of compound [MnMe(NP^{t}Bu$_3$)]$_2$ **15** (a) and [(MnMe(NP^{t}Bu$_3$))$_2$(THF)] **15b** (b). The thermal ellipsoids are shown at 30% probability. Hydrogen atoms have been omitted for clarity. R_1 (**15**) = 0.0446 (18), wR_2 (**15**) = 0.1199. R_1 (**15b**) = 0.0311, wR_2 (**15b**) = 0.0837

Table **1.2** Select bond lengths and bond angles for[MnMe(NP^{t}Bu$_3$)]$_2$ **15**

Bond distances (Å)		Bond angles (°)	
Mn–Mn	2.7706(11)	N–Mn–N	94.02(17)
Mn–N	2.033(4)	N–Mn–CH$_3$	133.0(2)
Mn–CH$_3$	2.118(6)	Mn–N–Mn	85.89(16)
P–N	1.580(4)		

Homoleptic (bis)tri-*tert*-butylphosphoranimide manganese(II) complex **16** was also prepared (Equation **1.4**). The bimetallic cluster forms readily from the reaction of two equivalents of anionic phosphoranimide with MnCl$_2$ or MnBr$_2$. The green, pentane soluble solid, pure by

elemental analysis, reflects the expected empirical composition for two phosphoranimide

ligands per metal atom. X-ray crystallography established the dimeric structure.

$$MnBr_2 \xrightarrow[\substack{THF, RT, 16\ h \\ -\ 2\ LiBr}]{LiNP^tBu_3\ (2\ equiv)}$$

$^tBu_3PN-Mn \quad Mn-NP^tBu_3$ with bridging N–P^{t}Bu$_3$ groups above and below **19**

71 % yield
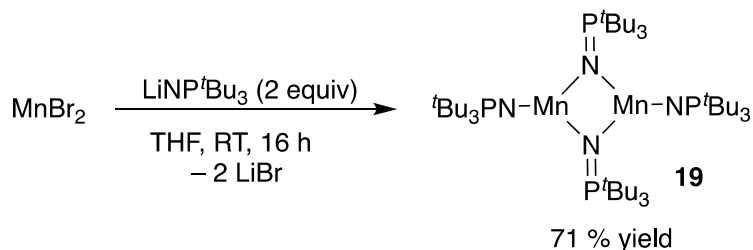
Equation **1.4**

In the solid-state, **16** retains the dimeric Mn_2N_2 core present in **14a** and **15/15b**. The

manganese atoms are three-coordinate, bound to two μ_2-phosphoranimide ligands as well as to

a terminal ligand, in an approximate trigonal planar geometry, with bond angles in the cyclic N–

M–N more acute (90.48(8)°) than the exocyclic angles. To accommodate the large steric bulk of

the ligands, the cluster is arranged so that the alkyl substituents of the terminal

phosphoranimide ligands are above the plane of the metal atoms, while the two bridging

ligands are mutually oriented below the plane.

The M–N bond lengths in the Mn_2N_2 ring are longer (2.084(2) Å) than those for the terminally

coordinated phosphoranimides (1.912(2) Å). The M–N bond in the terminal ligand likely

includes both σ- and π-contributions of electron density from the phosphoranimide nitrogen to

the metal d-orbitals, leading to a stronger and shorter bond. The P–N bond lengths are

marginally shorter for the terminal phosphoranimide compared to the bridging ligand, and it is

tempting to invoke increased π-overlap between the filled p-orbitals on nitrogen and orbitals on phosphorus. However, previous reports warn against over-interpreting P–N bond lengths, which vary only slightly, and may arise mostly from steric and crystal packing forces.[55] The M–N–P bond angle for the terminal ligand is close to linear (167.3(2)°), indicating a partially *sp*-hybridized nitrogen, with both M–N and N–P π interactions.
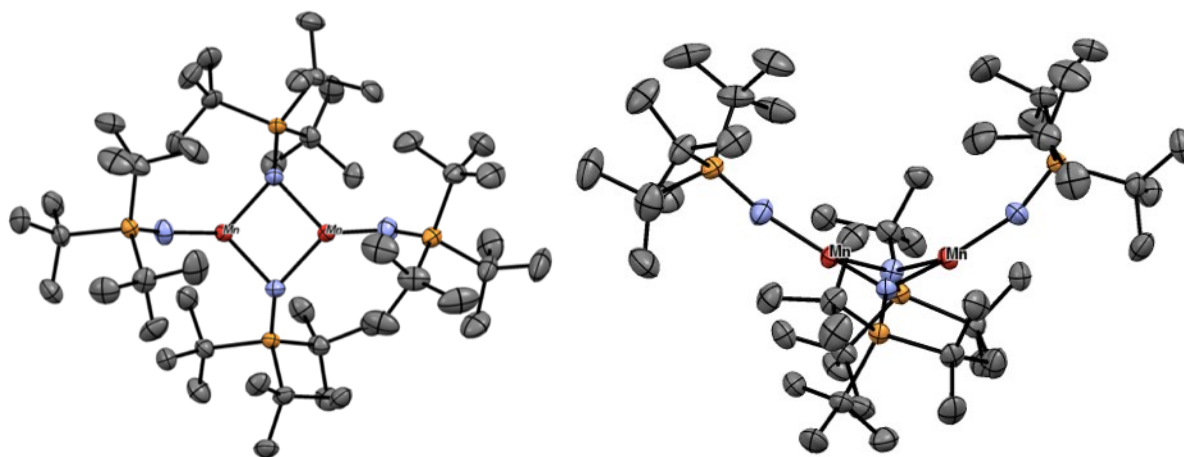
Figure **1.6** ORTEP diagrams of compound [Mn(NP*t*Bu₃)₂]₂ **16**. The thermal ellipsoids are shown at 50% probability. Hydrogen atoms have been omitted for clarity. R_1 = 0.0434, wR_2 = 0.1158

Table **1.3** Select bond lengths and bond angles for [Mn(NP*t*Bu₃)₂]₂ **16**

Bond distances (Å)		Bond angles (°)	
M---M	2.7127(9)	M–N–M cyclic	82.25(8)
M–N cyclic	2.084(2)	N–M–N cyclic	90.48(8)
M–N exocyclic	1.912(2)	M–N–P cyclic	141.2(1)
P–N cyclic	1.563(2)		134.6(1)
P–N exocyclic	1.534(2)	M–N–P exocyclic	167.3(2)
			160.4(2)

The extra π-donation of electron density from the terminal ligand stabilizes the coordinatively unsaturated electron deficient manganese: dimer **16** can be stored in solution or in the solid state for several months without decomposition. Alternatively, the larger steric bulk of the terminal phosphoranimide ligand, compared to methyl, can impede the decomposition of the cluster.

Dehnicke reported the synthesis of the alkyl-capped heterocubane manganese cluster [MnMe(NPEt$_3$)]$_4$ **8a** using the high-temperature desilylation route, followed by alkylation.[52] A metathesis reaction between KNPEt$_3$ and MnCl$_2$, followed by transmetallation using Me$_2$Mg in dioxane afforded the same product but by a convenient, scalable route (left, Scheme **1.7**). The homoleptic cluster [Mn(NPEt$_3$)$_2$]$_4$ **17** (right, Scheme **1.7**) is also isolable, albeit not as single crystals. The structure is assigned tentatively, based on the heterocubane structure determined for the analogous cobalt complex [Co(NPEt$_3$)$_2$]$_4$ **12b** (see Scheme **1.4**).[77]
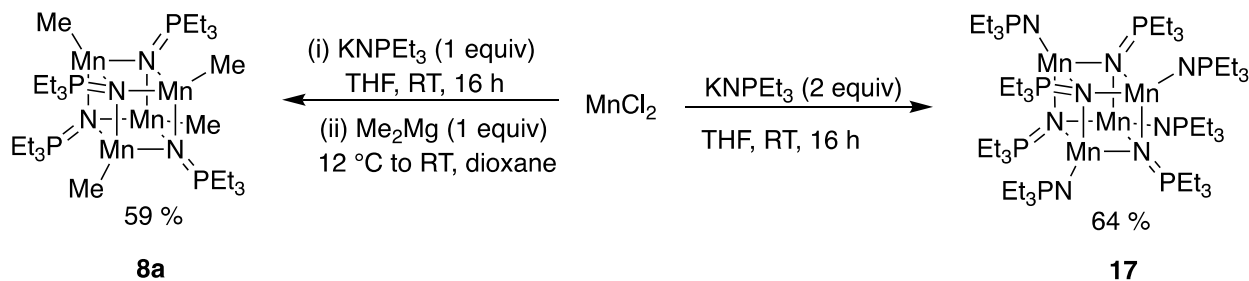
Scheme **1.7**

The heterocubane Mn$_4$N$_4$ core of bis(phosphoranimide) **17** was confirmed indirectly by subsequent transformation. The reaction with excess 9-borabyclononane (9-BBN) provided

pure single crystals of an unusual adduct, which was analyzed by XRD (Equation **1.5**). In this

reaction, borane binds to and abstracts the terminal phosphoranimide ligands, leading to

hydridomanganese intermediates which evolve further to the borabicyclononane adduct **18**.

The tetranuclear heterocubane Mn_4N_4 core of this cluster **18** logically originated from a similar

heterocubane structure, as assigned for **17**. In the crystallized product **18**, however, one

terminal chloride ligand is present among the sea of hydrides (Figure **1.7**). The chloride may be

the result of incomplete phosphoranimide substitution during the initial ligand exchange or,

more likely, the result of adventitious BBN-Cl present in our commerical 9-BBN. The reaction,

however, reveals a useful strategy for the *in situ* formation of metal hydrides from

bisphosphoranimide metal complexes. Activation of bisphosphoranimide complexes by borane

was recently described by Tao Bai[81] (formerly of the Stryker group) and is discussed in greater

detail in Chapter 2.
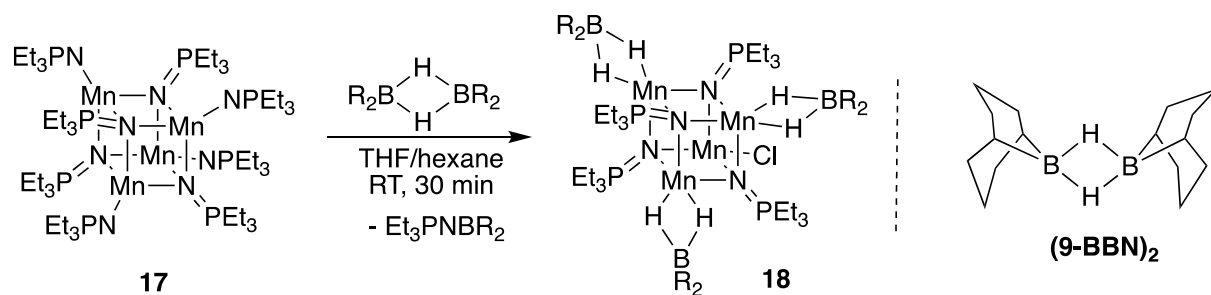
Equation **1.5**
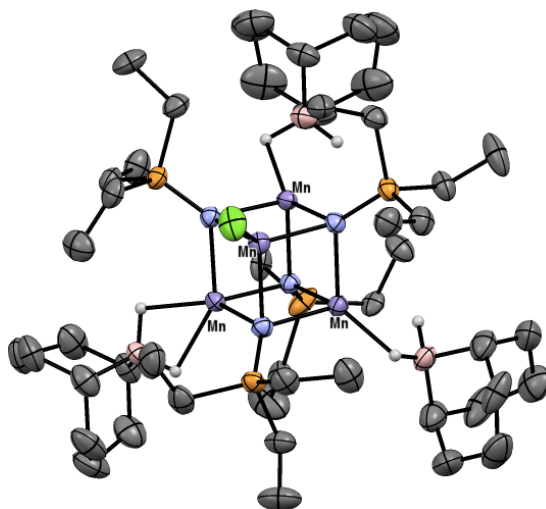
Figure **1.7** ORTEP diagrams of compound **18**. The thermal ellipsoids are shown at 30% probability. Most hydrogen atoms have been omitted for clarity. R1 = 0.0326, R2 = 0.0808

Manganese compounds are known to mediate the activation of C–S bonds,[91-92, 97] which led us to evaluate clusters **8a**, **15**, **16** and **17** as catalysts for the hydrodesulfurization of DBT. All of these precatalysts promote the K–H mediated hydrogenolysis of DBT under hydrogen (Equation **1.6**), but the efficiency is dwarfed by the more active Co and Ni catalysts previously reported by Brown[45, 77-78] and Bunquin.[46, 63] The exploration of new manganese phosphoranimide complexes as hydrotreatment catalysts was, therefore, dropped.
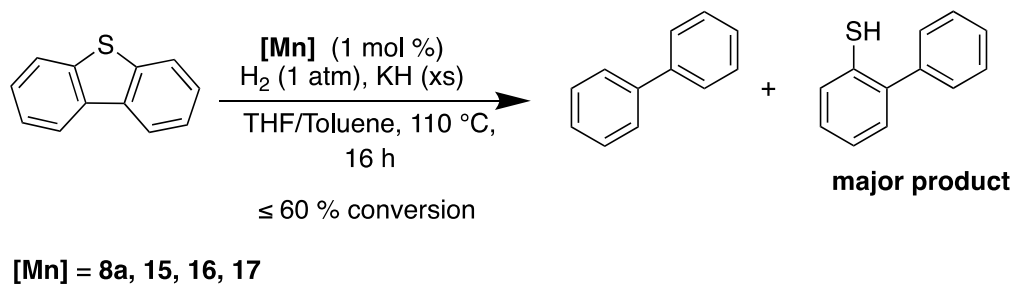
Equation **1.6**

1.2.2 Tri-tert-butylphosphoranimide clusters of copper – redox modulation by alkali metal cations

Copper is instrumental in numerous catalytic transformations but the most relevant to this current work is the hydrogenolysis of C–O bonds in biomass-derived molecules. Carbonyl compounds, and alcohols undergo hydrodeoxygenation in the presence of heterogeneous copper catalysts.[98-100] No discreet molecular copper clusters have been explored for similar reactions however.

The linear two-coordinate geometry observed in Bunquin's tetranuclear Co and Ni complexes (**13a**, **13b**)[63, 66] is not common for these metals, but is ubiquitous in copper complexes.[101] In the few trialkylphopsphoranimide copper clusters described by Dehnicke, [52] and later by Prof Andrew Johnson,[102] this linear two-coordinate geometry persists. Johnson's tetranuclear copper complexes [(R$_3$PNCu)$_4$] (R = Ph **19a**, Me$_2$N **19b** Equation **1.7**)[102] appeared in the literature while the experimental work for this thesis was ongoing, and are structurally similar to Bunquin's Co **13a** and Ni **13b** compounds. The use of less sterically demanding substituents on phosphorous (Ph, NMe$_2$) led to planar Cu$_4$N$_4$ cores in **19a/b** as opposed to the puckered arrangement seen for clusters **13a/b**. However copper complexes with the very large *tert*-butyl phosphoranimide ligand remained unexplored until this current work.

$$(CuMes)_n \xrightarrow[\substack{-78\ °C\ to\ RT \\ Tol \\ -\ mesitylene}]{HNPR_3}$$

R = Ph **19a**
R = NMe$_2$ **19b**
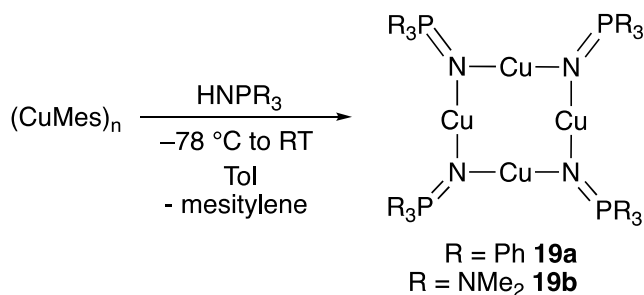
Equation **1.7**

The bimetallic clusters, [MX(NP^{t}Bu$_3$)]$_2$, (e.g. **6**, **11a/b**) which are accessible for divalent Mn, Co, Fe, and Ni, are not isolable for copper(II). Instead, the addition of equimolar LiNP^{t}Bu$_3$ to CuBr$_2$ led to incomplete exchange and reduction, resulting in the pentanuclear Cu(I) cluster, [[Cu$_5$Br$_3$(NP^{t}Bu$_3$)(NHP^{t}Bu$_3$)] **20** (Figure **1.8**). The single phosphoranimine ligand in **20** arises from protonation by adventitious water present in the "anhydrous" copper bromide used.
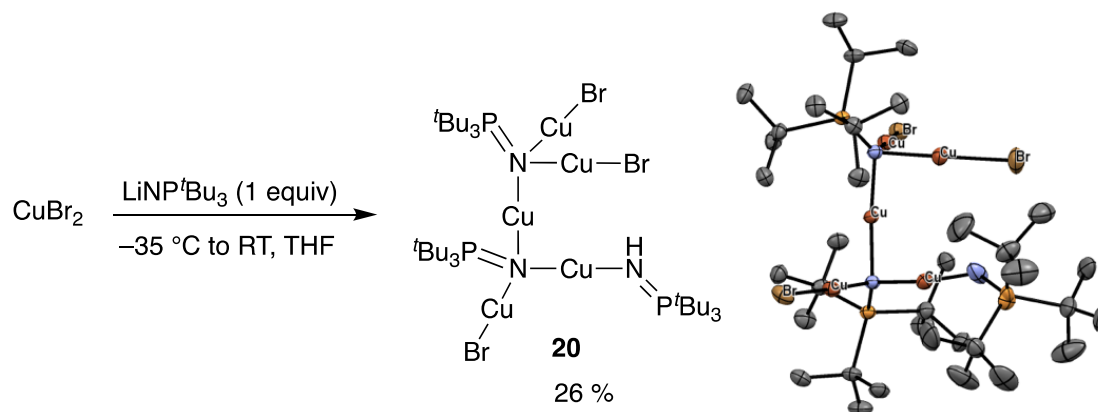
Figure 1.8 Synthesis and ORTEP diagram of [Cu$_5$Br$_3$(NP^{t}Bu$_3$)$_2$(NHP^{t}Bu$_3$)] **20**. The thermal ellipsoids are shown at 30% probability. Hydrogen atoms have been omitted for clarity. R_1 = 0.0253, wR_2 = 0.0728

The solid-state structure of **20** bears a strong resemblance to the co-planar tetranuclear Co(I) **13a** and Ni(I) **13b** complexes (see scheme **1.4**).[66] To prepare the corresponding Cu$_4$N$_4$ structure, equimolar LiNP^{t}Bu$_3$ was added to rigorously dry CuBr$_2$ at low temperature (-35 °C), followed by reduction using excess Na/Hg. The expected product, neutral Cu(I) cluster [Cu(NP^{t}Bu$_3$)]$_4$ **22**, was not obtained from this procedure. Instead, a nearly isostructural heterobimetallic copper-lithium cluster [(Cu(NP^{t}Bu$_3$)$_4$Li$_2$] **21** was isolated and structurally confirmed by X-ray crystallography (Scheme **1.7** and Figure **1.9**).
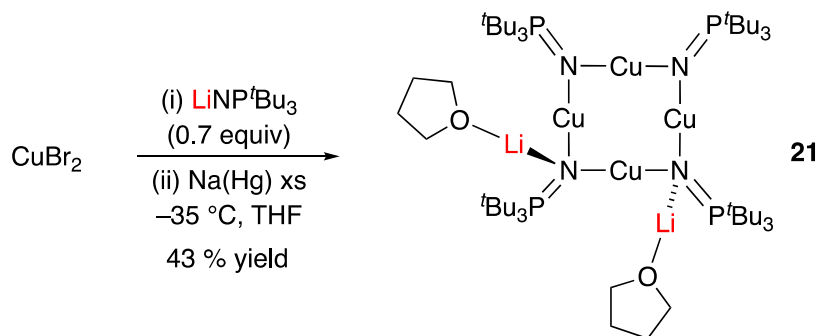
Equation **1.8**
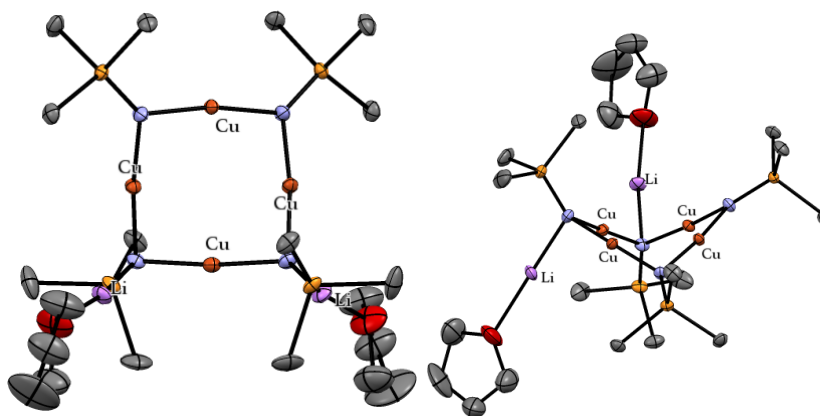
Figure 1.9 ORTEP diagrams of [(Cu(NP^{t}Bu$_3$)$_4$Li$_2$(THF)$_2$] **21**. The thermal ellipsoids are shown at 30% probability. Hydrogen atoms, and some carbon atoms of the *tert*-butyl groups have been omitted for clarity. $R_1 = 0.0281$, $wR_2 = 0.0812$

The dilithium copper cluster **21** is neutral overall, but the lithium centres do not bear anionic counterions in the solid state structure. *This cluster thus formally constitutes an unprecedented example of a soluble molecular cluster bearing Cu or Li atoms in the zero-valent state*. The ^{7}Li NMR spectrum of the reduced cluster **21** reveals a signal at 1.35 ppm in benzene-d$_6$ and shifts to –2.54 ppm in THF. The ^{7}Li signal for compound **21** is distinct from those observed for LiCl and LiBr (–4.71 ppm and –4.62 ppm respectively in THF). This indicates that residual Li$^+$ salts were not responsible for the observed NMR signal for the dilithium copper cluster **21**. The most logical hypothesis for product formation is that Cu(I) cluster, [Cu(NP^{t}Bu$_3$)]$_4$ **22**, is formed *in situ*,

followed by lithium cation binding and further reduction of the Cu_4N_4 cluster. The presence of the coordinated alkali metal cation significantly reduces the reduction potential of the neutral tetramer, triggering the 'over-reduction.'

The cation binding and over-reduction appear to be highly specific for Li^+ ions. When the potassium salt of the anionic phosphoranimide is used in the metathesis reaction with $CuBr_2$, followed by reduction with excess Na/Hg, only the 'neutral' cluster **22** is isolated (Equation **1.9**, Figure **1.9**). Similar results were obtained starting with $NaNP^tBu_3$, suggesting the modulation of reduction potential as a function of cation identity.[103-104]
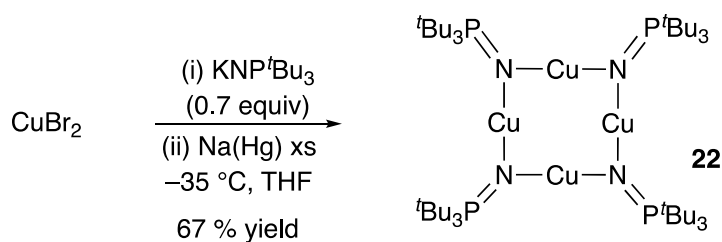
Equation **1.9**
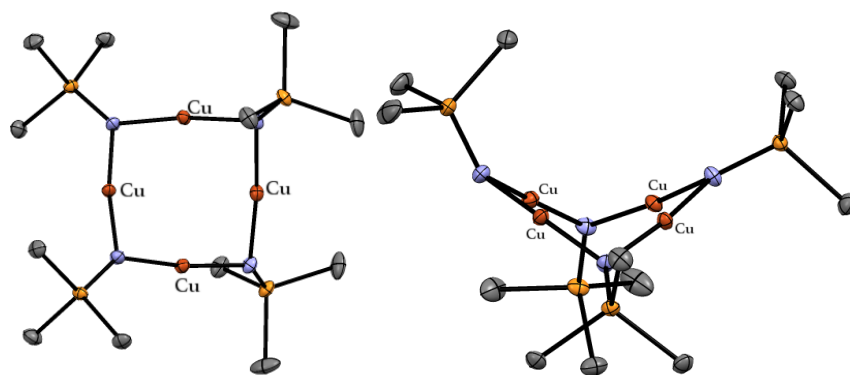
Figure **1.9** ORTEP diagrams of $[(Cu(NP^tBu_3)]_4$ **22**. The thermal ellipsoids are shown at 30% probability. Hydrogen atoms, some carbon atoms of the *tert*-butyl groups and a single THF molecule have been omitted for clarity. $R_1 = 0.0311$, $wR_2 = 0.0827$

27

This intriguing observation warranted independent confirmation. Cyclic voltammetry confirms the importance of lithium binding for the two-electron reduction of **22** (Figure **1.10**). The CV of the tetramer **22** is essentially featureless throughout the potential range (black trace). The voltammogram significantly changes in the presence of excess Li cation (blue trace); two irreversible reduction waves are observed. The effects of Na^+ and K^+ ions have not been assessed by cyclic voltammetry, but the evidence from synthetic experiments (*vide supra*) suggests neither of these cations promote the over reduction to form the Na or K analogues of $[(Cu(NP^tBu_3)_4Li_2(THF)_2]$ **21**. Zhao observed similar behavior for the tetranuclear nickel cluster 16b: while 'over reduction' is apparent in the cyclic voltamograms recorded in the presence of excess Li^+ ions, neither Na^+ nor K^+ facilitate new redox events.[64, 105]
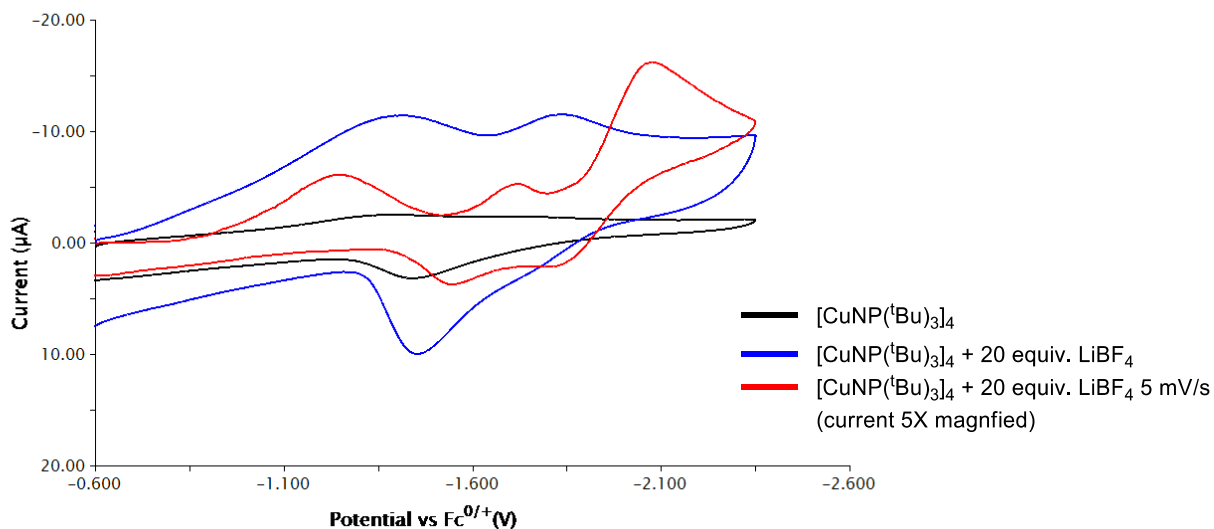
Figure **1.10** The effect on Li^+ coordination on the reduction potential/profile of tetranuclear copper(I) cluster $[Cu(NP^tBu_3)]_4$ **22**. The measurements were recorded in THF with 0.1 mol/L *n*-Bu_4NPF_6 used as the electrolyte.

The efficiency of redox modulation of transition metal centres by alkali and alkali earth metals is usually a function of Lewis acidity.[103-104] This corresponds with the observations that only the lithium cations– the strongest Lewis acid among the alkali metals ions– promotes the 'over-reduction' of the tetrameric copper and nickel clusters. While the small size of the Li^+ ion contributes to its Lewis acidity, it also allows facile coordination to the sterically crowded nitrogen atom of the phosphoranimide ligand, without requiring significant structural reorganization.

Despite the difference in composition, clusters **21** and **22** are nearly isostructural in the solid state (Figure **1.11** *cf* Figures **1.8** and **1.9**). Both molecules crystallize in the same space group with close to identical unit cell parameters. The length of the Cu–N bonds and the bond angles within the Cu_4N_4 ring are largely unchanged between the two systems. The only obvious difference between the structures is the inclusion of Li atoms and coordinated THF in **21**. The absence of any perturbations in the Cu_4N_4 core suggests that the four copper atoms are electronically nearly equivalent.

21   **22**
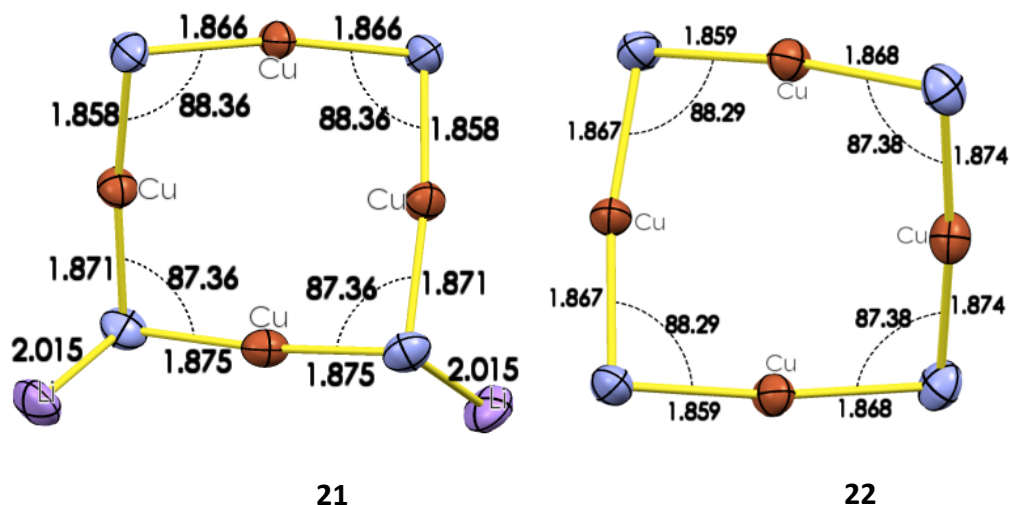
Figure **1.11** ORTEP diagrams of [(Cu(NP^{t}Bu$_3$)$_4$Li$_2$] **21** and [Cu(NP^{t}Bu$_3$)]$_4$ **22**. The thermal ellipsoids are shown at 30% probability. Carbon and hydrogen atoms have been omitted for clarity. (see Figures **1.8** and **1.9** above for full details)

Unexpectedly, clusters **21** and **22** are completely stable to hydrogenolysis, even under high pressure. This remains under study, primarily by computational collaborators.

1.2.3 (Bis)tri-alkylphosphoranimide clusters of nickel

Nickel is widely used for the catalytic activation of carbon-heteroatom bonds, [41, 106-107] and thus attention was turned to this metal, in the search for active catalysts. In the initial exploration of nickel phosphoranimide clusters, Zhao and Bunquin prepared several precatalysts, most notably [Ni(η^3–allyl)(NPEt$_3$)]$_2$ **10b** and [Ni(NP^{t}Bu$_3$)]$_4$ **13b**.[63-64, 66] Both compounds catalyze hydrogenation and base-promoted HDS with varying levels of success.[45-46, 63-64, 66] The syntheses of **10b** and **13b** are inconvenient, however, requiring multiple, carefully-controlled steps to isolate pure material. In contrast, bisphosphoranimide complexes of Fe, Co, and Mn (*vide supra*) are trivial to prepare in a single step from the metal halide. The nickel analogue, however, was not reported before now.

As for other later first-row metals, complexes with nickel/phosphoranimide ratios of 1:2 can been prepared at room temperature from simple halide salts (Scheme **1.8**). The *tert*-butylphosphoranimide complex [Ni(NP^{t}Bu$_3$)$_2$]$_2$ **23** is isolated as a yellow brown solid, while tetrameric [Ni(NPEt$_3$)$_2$]$_4$ **24** is purple waxy solid. The dimeric cluster **23** crystallizes from saturated pentane to produce dark brown crystals suitable for X-ray diffraction. The solid-state

structure of [Ni(NPEt$_3$)$_2$]$_4$ **24** has not been determined, but a heterocubane core is similar to

that for [Co(NPEt$_3$)$_2$]$_4$ **12b**, is assigned tentatively.
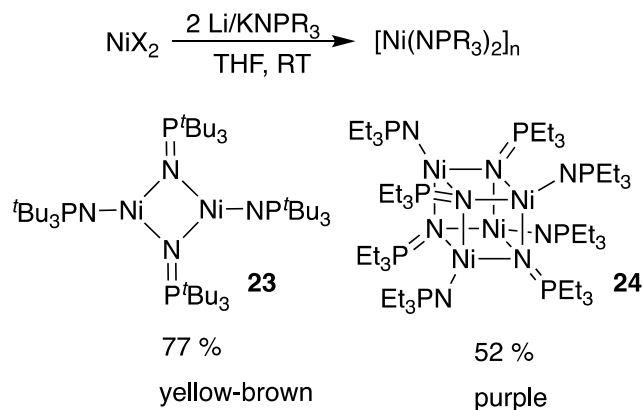
Scheme **1.8**

The solid-state structure of **23** (Figure **1.12**) is not unlike that observed for the analogous

manganese complex **16**, or the iron and cobalt complexes **11a/b** first prepared by Hebert.[65, 81]

The bridging phosphoranimide ligands form shorter Ni–N bonds to the metal in the Ni$_2$N$_2$ core

compared to the terminal Ni–N bonds. Here again the cluster is puckered to minimize steric

interactions between the bulky substituents on the phosphoranimide ligands. In this structure,

the nickel atoms also are approach each closely 2.6248(8) Å allowing for possible intermetallic

bonding interactions.
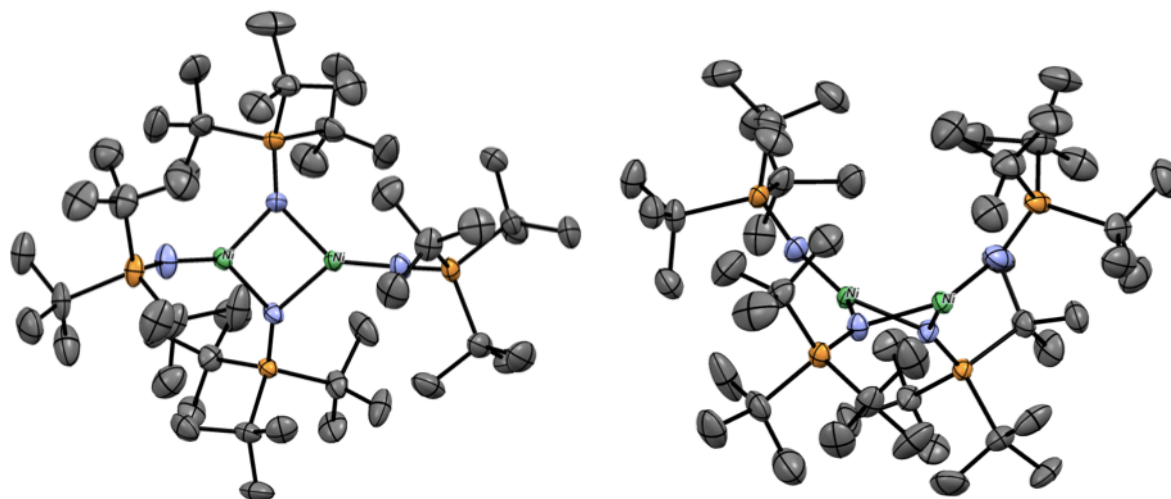
Figure **1.12** ORTEP diagrams of compound [Ni(NP^{t}Bu$_3$)$_2$]$_2$ **23**. The thermal ellipsoids shown at 50% probability. Hydrogen atoms have been omitted for clarity. R_1 = 0.0407, wR_2 = 0. 0.1157

Both of these d^8-Ni(II) compounds are precatalysts for hydrodesulfurization in the presence of

basic potassium salts, as discussed in Chapter 2. The terminal phosphoranimide ligands in **23**

and **24** are sufficiently basic to deprotonate hydroxyl residues on the surface of silica and

alumina; this reaction has been used to immobilize the clusters on inorganic supports.

Functional heterogeneous catalysts for base-promoted HDS are discussed in Chapters 3.

The synthesis bisphsophoranimide dimer **23** completed the series of bisphosphoranimide

complexes of the late first-row metals (Mn, Fe, Co, Ni). Structural and electronic variations

within this series of bimetallic clusters were therefore considered. The four complexes are

nearly isostructural, showing only subtle variations in the solid-state. The ORTEP diagrams

(Figure **1.13**) reveal that the geometry of the M$_2$N$_2$ core remains fairly constant across the

series. This suggests that the bonding in the clusters is primarily influenced by the minimization

of steric interactions among the *tert*-butyl substituents on the phosphoranimide ligands. From manganese through nickel, the minor decreases in the M–N bond lengths for both cyclic and exocyclic ligands is easily attributed to the progressive contraction of the ionic radius. The geometry of the M_2N_2 core is comprised of two approximately 90° N–M–N angles and two more acute M–N–M angles for the bridging ligands. For the Ni cluster **23**, the angle subtended at the metal atoms decreases sharply, so that both N–M–N and M–N–M bond angles are *ca* 83°, but the reason for this is not obvious.
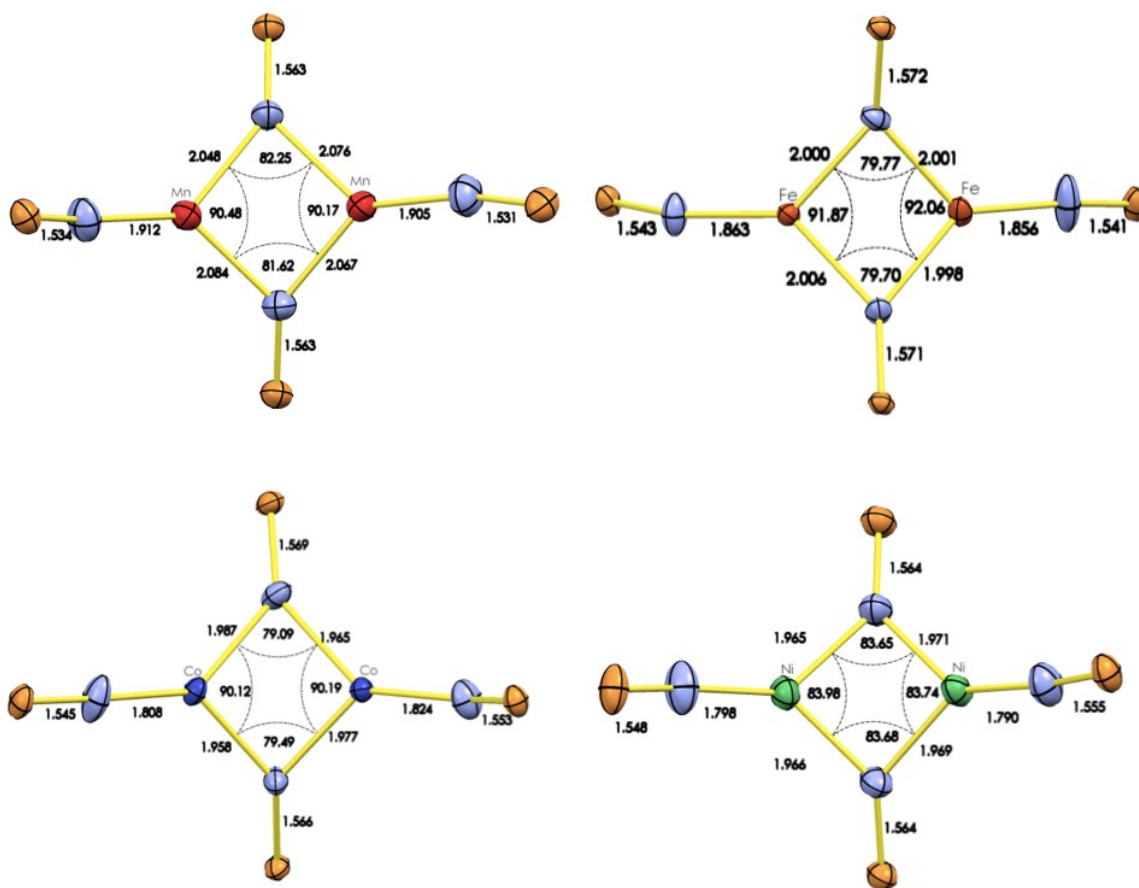
Figure 1.13 ORTEP diagrams of late first-row metal (bis)phosphoranimide complexes [M(NP^{t}Bu$_3$)$_2$]$_2$ (M = Mn, Fe, Co, Ni). The thermal ellipsoids are shown at 30% probability. Carbon and hydrogen atoms have been omitted for clarity.

Trends in the electronic properties of the (bis)phosphoranimide series are less clear. Multiple absorptions in the visible region (630 – 650 nm) of the UV-Vis spectra of the $[M(NP^tBu_3)_2]_2$ (M = Mn, Fe, Co, Ni) complexes (Figure **1.14**) reveal multiple charge transfer absorptions, presumably metal-to-ligand and/or ligand-to-metal. The general hypsochromic shift in the UV absorbances from manganese to nickel is tentatively assigned to the increasing occupancy of the metal d-orbitals in the late metals, reducing the opportunity for d–d and ligand to metal charge transfer (LMCT) processes.
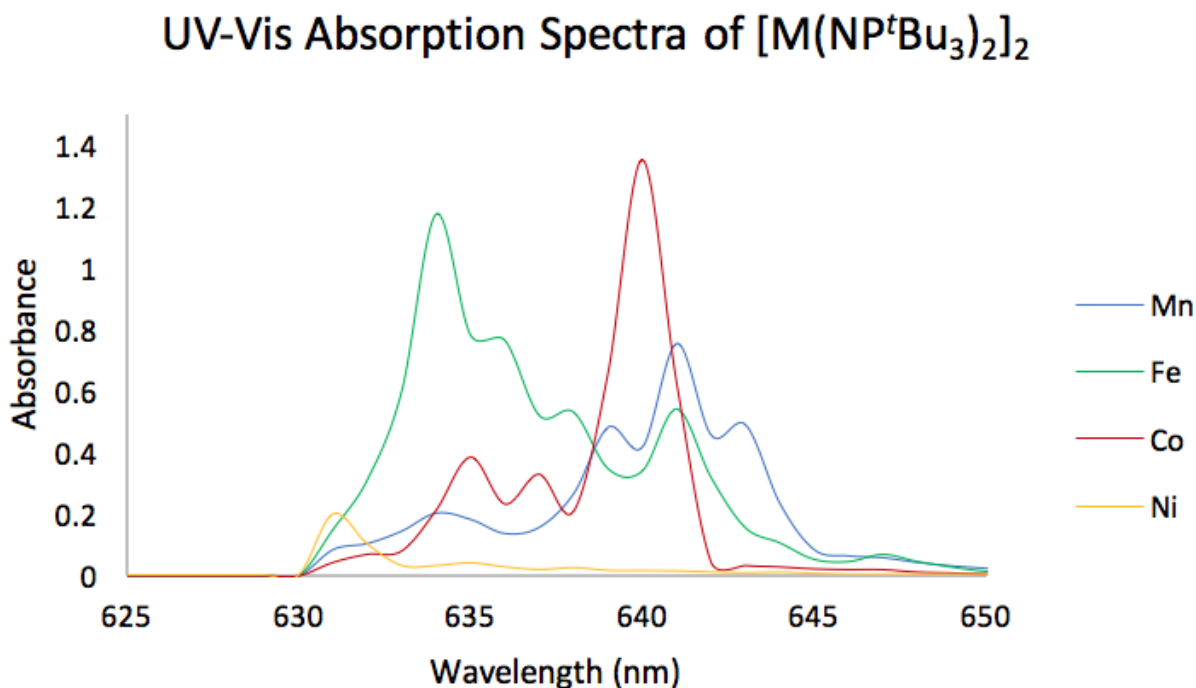
Figure **1.14** UV-Vis absorbance spectra for (bis)phosphoranimide complexes $[M(NP^tBu_3)_2]_2$ (M = Mn, Fe, Co, Ni)

1.3 Conclusion

New first-row transition metal phosphoranimide clusters Mn, Cu and Ni have been prepared, isolated, and characterized. By controlling the oxidation state of the metal and the size of the substituents on the phosphoranimide ligand, common structural motifs are observed. Two-dimensional complexes of manganese (**14a, 15**, **16**), nickel (**23**), and copper (**21**, **22**) were obtained from use of the bulky tri-*tert*-butylphosphoranimide ligand (Figure **1.15**). The tetrametallic copper complexes **21** and **22** displayed unexpected, yet insightful, Li^+ cation-induced redox variability. The use of the small triethylphosphoranimide ligand allows for triply-bridging coordination, giving partially characterized heterocubane clusters of manganese (**17**) and nickel (**24**). The manganese and copper complexes are not particularly active as precatalysts for hydrogenation or hydrotreatment; greater success was realized using the two nickel clusters, as described in Chapters 2 and 3 of this thesis.
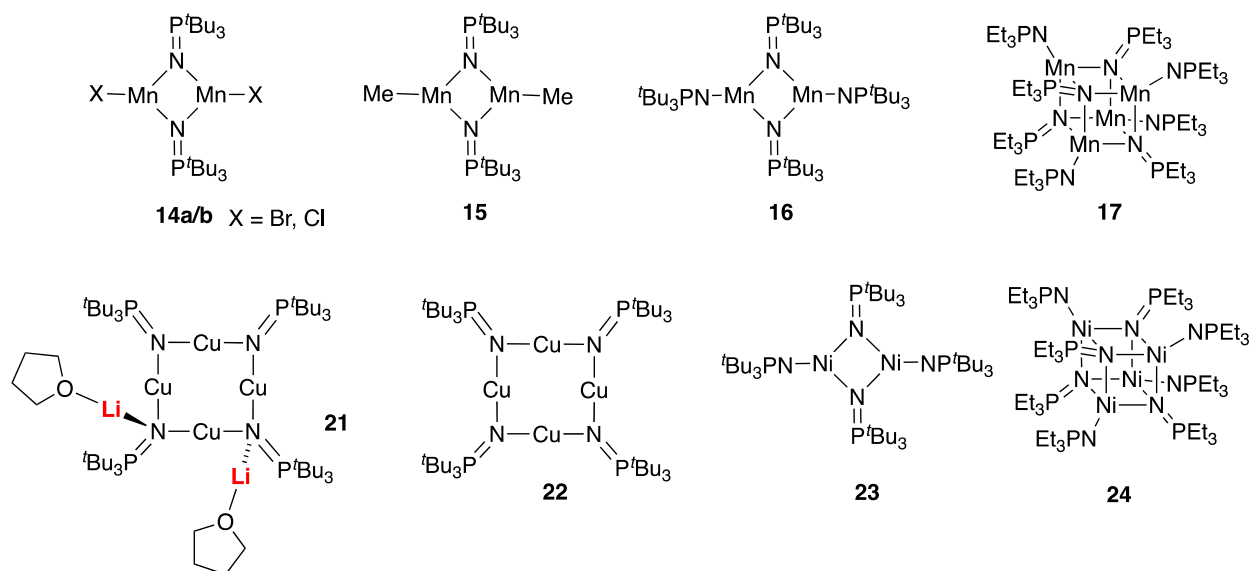
Figure **1.15** Tri-alkylphosphoranimide clusters of Mn, Ni and Cu described chapter 1

2. Potassium promoted HDS in the presence of first-row transition metal clusters

2.1 Introduction and background

2.1.1 Hydrodesulfurization: modern requirements and challenges

Organic molecules containing sulfur and nitrogen atoms occur naturally in most crude petroleum deposits; in heavy crude oils, such as that obtained from the Alberta's Oil sands as much as 4-8 wt % S and 0.5-0.6 wt % N are present.[28] The combustion of organic molecules containing these heteroatoms leads to the formation of nitrogen oxides (NO_x) and sulfur oxides (SO_x) which are potent respiratory irritants as well as corrosive environmental pollutants.[108] Sulfur oxides are particularly concerning because they inhibit the proper functioning of motor vehicle emissions control systems, designed to reduce the volume harmful NOx, volatile hydrocarbons (VOCs), and carbon monoxide entrained in automobile exhaust (Figure **2.1**). The availability of low sulfur fuels has therefore emerged as one of the most impactful interventions for reducing hazardous emissions from the combustion of fossil based fuels.[109]

Sulfur oxides bind strongly to and inhibit the precious metals surfaces in automobile catalytic converter
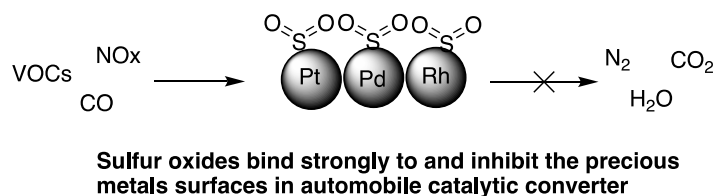
Figure **2.1**. Inhibition of catalytic converters by sulfur oxides

Globally, regulatory bodies have responded with increasingly strict controls on residual sulfur levels in transportation fuels. The United States Environment Protection Agency (US EPA), and

Environment Canada mandate the use of ultra-low sulfur diesel fuel (ULSD, <15 ppm sulfur) for road transportation.[109-110] For scale, crude bitumen from Alberta, contains on average 40,000– 50,000 ppm sulfur. Even marine and locomotive diesel fuels, once loosely regulated, now conform to strict sulfur rules, leading to uniform adaptation of stringent sulfur standards across the entire transportation fuel sector.[109]

Current technology for the hydrodesulfurization (HDS) of fossil fuels involves heating the petroleum feedstock over a cobalt molybdenum sulfide (CoMoS) catalyst dispersed high surface area alumina.[111-112] The process requires temperatures up to 400 °C and hydrogen pressures as high as 2000 psi.[28, 113] Under these conditions, C–S bonds are hydrogenolyzed affording desulfurized hydrocarbons; gaseous H_2S is also liberated. (Figure **2.2**).
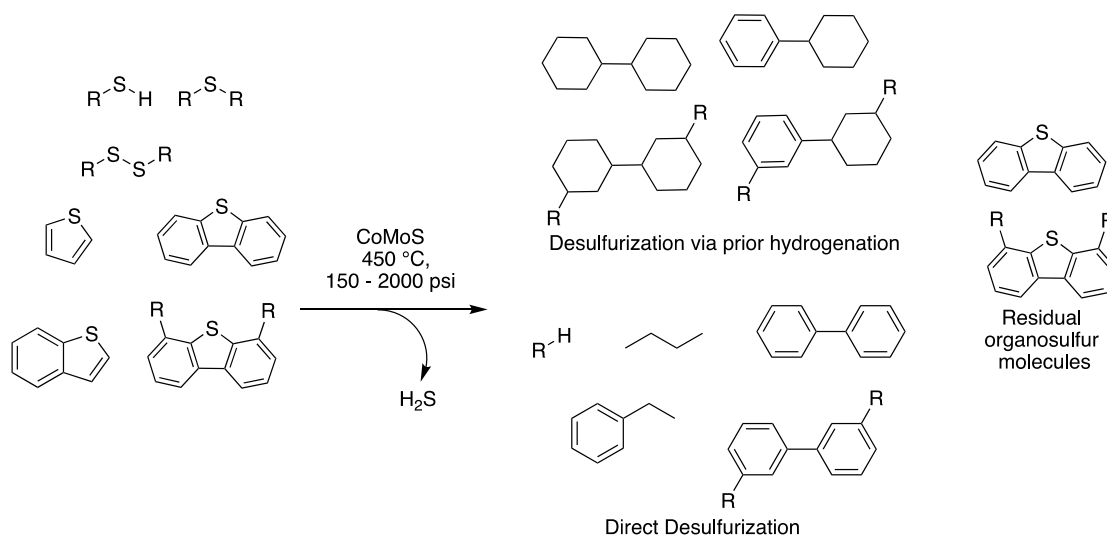
Figure **2.2** Hydrodesulfurization of representative organosulfur molecules over alumina supported CoMoS catalysts.

Simple organosulfur compounds such as thiols, thioethers and simple thiophenes react rapidly under these conditions, but the hydrodesulfurization process struggles to efficiently remove the most refractory benzannulated thiophenic compounds.[112] Dibenzothiophene and its 4,6-dialkyl derivatives, are particularly challenging to desulfurize (Table 2.1), and constitute the majority of the residual sulfur in transportation fuels.[114] The strength of the aromatic C–S bonds in dibenzothiophenes, coupled with the sterically-controlled inaccessibility of the sulfur atom in substituted homologues are responsible for the low reactivity observed. Figure **2.3** illustrates this; dibenzothiophene is desulfurized nearly seven times more slowly than thiophene and the presence of a single alkyl group further slows the rate of desulfurization.[28] For industrial catalysts, prior hydrogenation of aromatic rings is often required before the desulfurization of this class of organosulfur molecules can occur. (Figure **2.2**)

Compound	Structure	Relative rate constant
Thiophene		6.9
2,5-dimethylthiophene		3.5
Dibenzothiophene		1.0
4-Methyldibenzothiophene		0.32
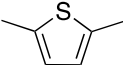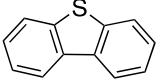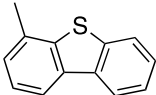
Figure **2.2**: Effect of substitution on the rate of desulfurization of organosulfur molecules[28]

The high concentration of refractory benzannulated thiophenes (60-80 % of total sulfur) in heavy crude oils, such as the Athabasca 'oil-sands' deposits in northern Alberta, requires a very energy intensive and costly remediation process.[28] This lowers the value of the crude and increases the carbon emissions associated the refining process, reflected in the social and economic penalty assessed on heavy, sour (high sulfur) crudes compared to lighter sweet crude oil.[28]

Industrial and academic interest in developing new methodologies for efficient and selective removal of sulfur from refractory thiophenic molecules under mild conditions is understandably intense. Industrial research has largely focused on the modifying the elemental formulation as well as immobilization and activation protocols for supported transition metal species, to develop more active catalysts. This approach is discussed briefly in Chapter 3 of this work. A more academic approach, using discrete transition metal complexes to model the metal-mediated desulfurization is described below.

2.1.2 Commercial catalysts and proposed mechanisms for HDS

It is useful to understand the formulation and reactivity of current hydrotreating catalysts in order to evaluate and appreciate recent attempts to develop more active catalysts. Current hydrotreatment catalysts are prepared by dispersing, then calcining molybdenum and cobalt salts on high surface area γ-alumina. Several metal sulfide phases are then formed by heating the cobalt/molybdenum oxides in a stream of hydrogen mixed with H_2S. *Operando* physical

characterization reveals that the most active of these phases are small MoS crystallites decorated with cobalt atoms, hence CoMoS.[111, 113, 115-116] Other mid-to-late second and third row transition metals, most notably ruthenium, form superior HDS catalysts, but the CoMoS system represents a balance of high activity, long-term stability, and economic viability.[29]

The active sites in the CoMoS catalyst system are found at the edges and corners of MoS crystallites that have been decorated with cobalt atoms.[115-116] At these sites, cobalt and molybdenum atoms are separated by single-atom sulfur bridges. Sulfur atoms are extruded by hydrogenolysis during catalyst activation, generating coordinatively unsaturated surface sites, loosely referred to as vacancies (Figure **2.4**). Organosulfur molecules strongly adsorb to these vacancies, where the C–S bonds undergo hydrogenolysis to liberate the desulfurized molecule and return the catalyst to its original sulfide resting state.
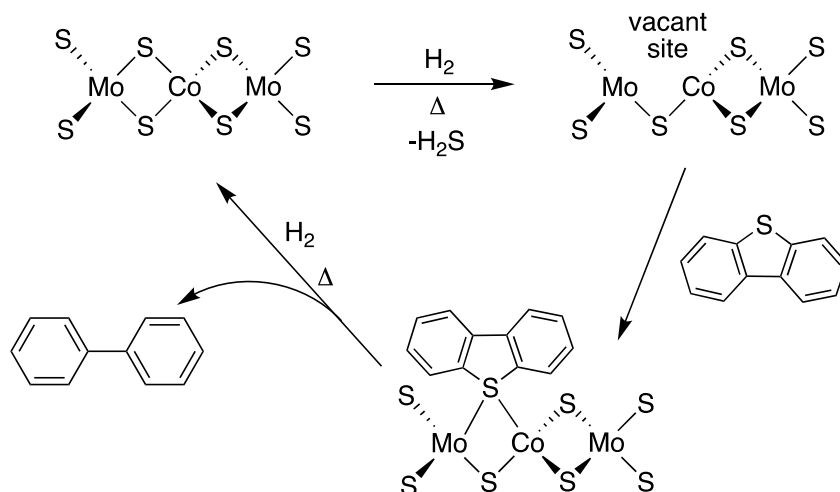
Figure **2.4**: Oversimplified mechanism for desulfurization of DBT over CoMoS catalyst.[28]

The adsorption of the organosulfur compound to the catalyst surface need not be exclusively via the sulfur atom (η^1-S). For dibenzothiophene, (η^2-C=C as well as (η^5/η^6)-arene coordination is common, and leads to hydrogenation of the aromatic rings prior to desulfurization (Figure **2.5**).[28, 111] Coordination of the π-system is especially relevant for 4,6-dialkyl dibenzothiophenes, which are prevented from η^1-sulfur binding by steric crowding.[111]
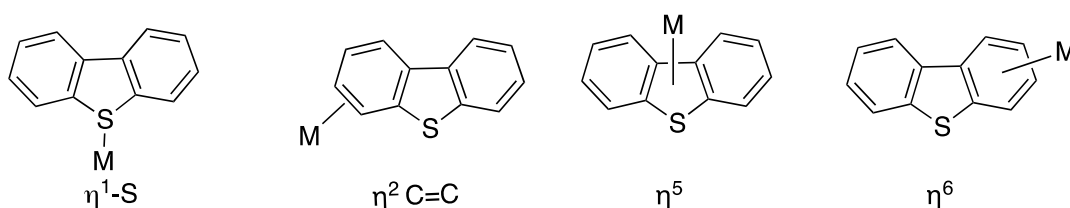
Figure **2.5**: Possible binding modes for DBT to a transition metal atom on the surface of hydrotreating catalysts.

2.1.3 Homogeneous models for stoichiometric HDS under mild conditions

Beginning nearly three decades ago, organometallic compounds have been used to model the active sites in industrial CoMoS hydrotreatment catalysts.[29] Most examples are concerned with the activation/hydrogenolysis of the C–S bonds dibenzothiophenes because they are the most challenging to desulfurize. Second- and third-row transition metals are discussed, but the utilization of earth-abundant and less expensive first-row metals to mediate deep and ultra-deep HDS is the more attractive and relevant strategy.

2.1.3.1 Second- and third-row transition metal organometallic models for HDS

Organomolybdenum compounds are the most obvious molecular analogues of the Mo-based industrial catalyst and, as such, several investigations have been reported. The hetero-polymetallic Mo/Co cluster **25** (Scheme **2.1**), described by Curtis and co-workers, is the most direct homogeneous analogue of the CoMoS industrial catalyst.[117-118] Cluster **25** stoichiometrically desulfurizes *simple* organothiols as well as thiophene, reorganizing in the process to heterocubane cluster **26**, which incorporates the extruded sulfur atom. Under high partial pressure of carbon monoxide (70 atm), cluster **25** can be regenerated by extrusion of carbonyl sulfide.
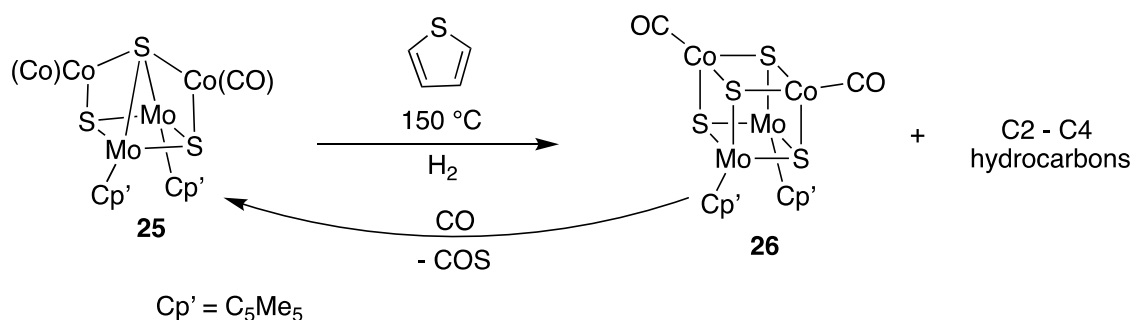
Scheme **2.1**

While this cluster does not react with benzothiophene or DBT, the polymetallic motif offers useful insights into the function of the active sites in industrial catalysts. Experimental and computational probing of potential reaction mechanisms revealed the dramatic lowering of the bond dissociation energy of the C–S bond of a thiol, once coordinated to cluster **25**. The bond dissociation enthalpy of the μ_3-coordinated thiol was found to be only 20-25 kcal/mol, much

less than in the free thiol (Figure **2.6**).[118-119] This strongly argues for use of polymetallic organometallic compounds to model C–S bond activation and in the design of new catalysts.

PhSH   C–S BDE = 73 kcal/mol

$$\begin{array}{c} Ph \\ | \\ S \\ M \diagup \! | \! \diagdown M \\ | \\ M \end{array}$$ C–S BDE = 20–25 kcal/mol
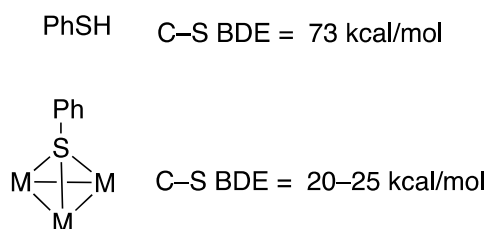
Figure **2.6**: Coordination through 'S' weakens the C–S bond in thiophenol.

Similar polymetallic clusters supported by bridging carbonyl ligands have since been described; notably, rhenium[120] and ruthenium[121] also display comparable reactivity.

Mononuclear complexes readily mediate C–S bond cleavage, but full desulfurization requires transformation to polymetallic intermediates. For example, the mononuclear molybdenum hydride complex **27**, reported by Parkin, *et al.*, inserts into a single C–S bond of DBT to yield thiometallacycle **28**, without subsequent desulfurization (Scheme **2.2**).[122] Complex **27** does desulfurize thiophene and benzothiophene, but uncharacterized *polymetallic* MoS compounds are observed as by-products. (Scheme **2.2**)
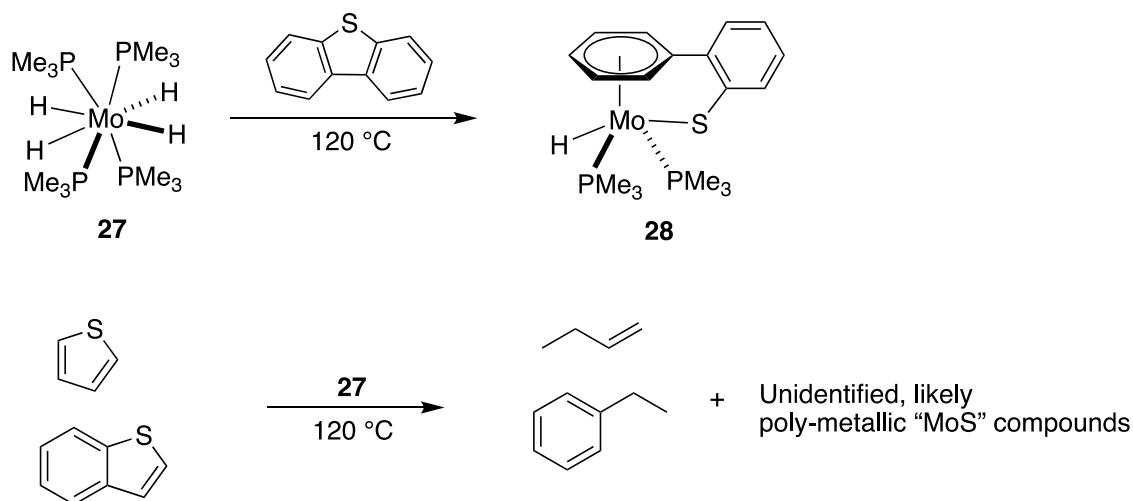
Scheme **2.2**

The analogous low-valent tungsten complex **29** aptly demonstrates the relevance of multi-metallic intermediates in desulfurization.   At least two equivalents of **29** react with DBT to produce binuclear intermediate **3**, which features a fully desulfurized metallacylopentane as well as bridging sulfide (Scheme **2.3**).[123] Exposure of bimetallic **30** to H$_2$ at 60 °C liberates biphenyl and produces an unidentified sulfided tungsten cluster, which could not be recycled.
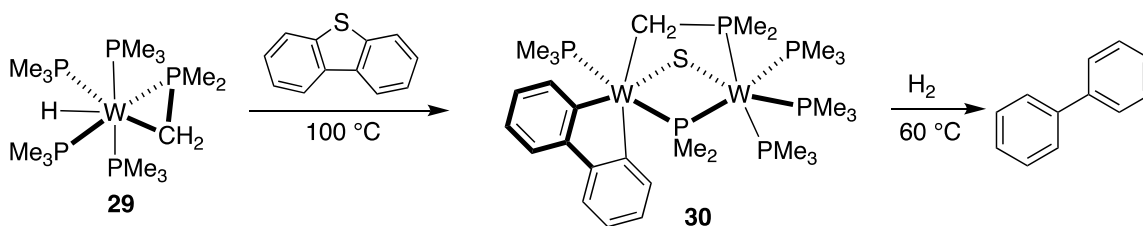
Scheme **2.3**

Further examples, also showing the desulfurization of DBT, highlight the development of polymetallic clusters for the activation of DBT and other challenging molecules. The C–S bonds of DBT are cleaved by reactive organometallic complexes of platinum-group metals stabilized by η^5-cyclopentadienyl or phosphine ligands.[49, 91-92, 124-132]

One notable example is tri-nuclear cyclopentandienyl ruthenium complex **31** (Scheme **2.4**).[131] In principle, this cluster bears close resemblance in structure and function to the purported active site of CoMoS catalysts. The cluster is defined by a small polymetallic core supported by hydride bridges and activates by liberating a small molecule (H_2 rather than H_2S generated from a sulfide), to reveal an open coordination site for binding and transformation of an organosulfur substrate. As shown by the isolation of sulfur-bridged intermediate **32**, the trinuclear core cleaves both C–S bonds in benzothiophene, forming an μ_3–sulfide. Hydrogenolysis at higher pressure liberates the hydrocarbon, but not the bridging sulfide, as required for catalysis.
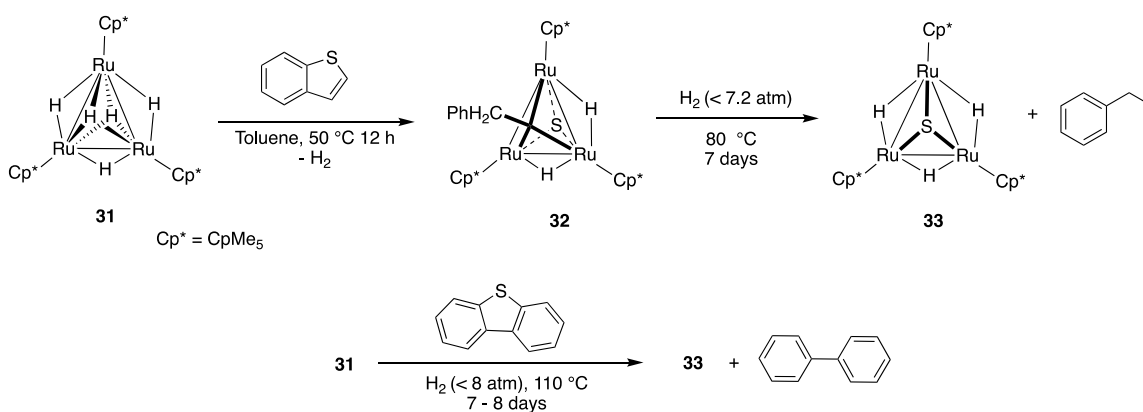
Scheme **2.4**

The diphosphine-supported bimetallic Pt(I) hydride complex **34**, reported by the group of Prof. William D. Jones (Scheme **2.5**),[49] is notable for facile C–S activation. Upon loss of hydrogen, **34** produces a very reactive 14-electron d^{10}-Pt(0) fragment **35**, which inserts readily into the C–S bonds of recalcitrant molecules such as 4,6-Me$_2$-dibenzothiophene. Thiaplatinacycle **36** reacts with a second equivalent of **34** to cleave the second C–S bond, affording the desulfurized hydrocarbon. A recently reported Pd analogue of **34** is equally reactive for stoichiometric HDS of DBT and alkylated derivatives,[124] reinforcing that low-valent, electron-rich metal centers are competent for activating C–S bonds in the most refractory organosulfur molecules.

dippe = 1,2-Bis(diisopropylphosphino)ethane
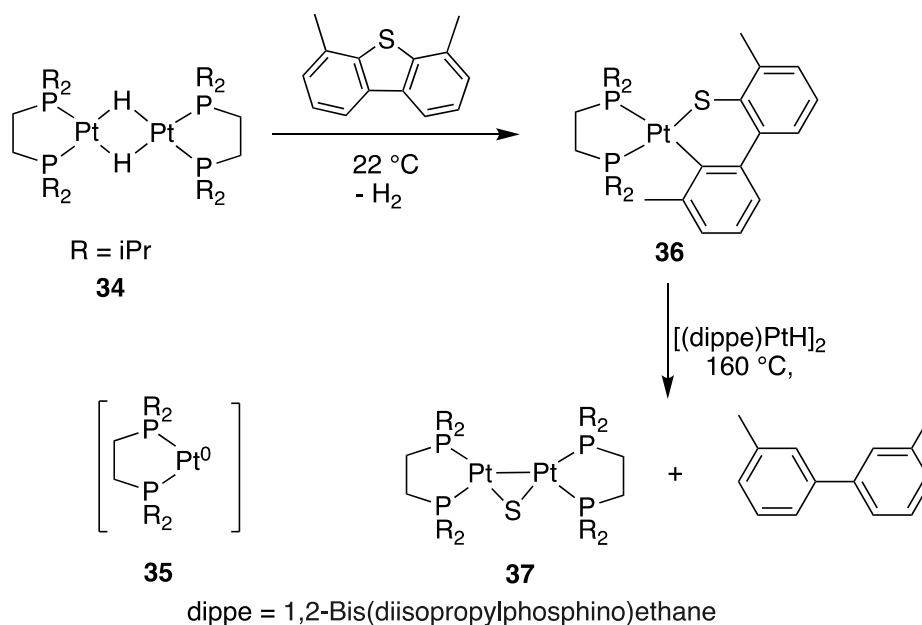
Scheme **2.5**

2.1.3.2 First-row transition metal transition metal organometallic models for HDS

This thesis is primarily concerned with first-row transition metals, thus a few examples of these metals activating C–S bonds are included below. Typically considered to be less active than their heavier congeners[11-12], several research groups have demonstrated that first row metals

functioning as part of a polymetallic unit are fully capable of mediating the most challenging C–S bond activations.

The π-acidic, 12-electron $(CO)_3Mn^+$ fragment, reported by Sweigart and co-workers, activates benzothiophene and dibenzothiophene by coordinating to the six-membered carbocyclic ring (Scheme **2.6**).[91-95] The π-cation complex **38** features a weakened C–S bond, which readily cleaved, oxidizing a low-valent metal center (**39**, Scheme **2.6**).[91, 93] Separately, a single-electron reduction of **38** leads to insertion of a $Mn(CO)_4$ fragment into the C–S bond of DBT, affording polymetallic complex **40** in which manganese is responsible for cooperative activation and cleavage of the C–S bond.[97] Heating **40** under 34 atm (500 psi) of H_2 leads to hydrogenolysis of the Mn–C bond and thiophenolate **41**, which does not evolve further.
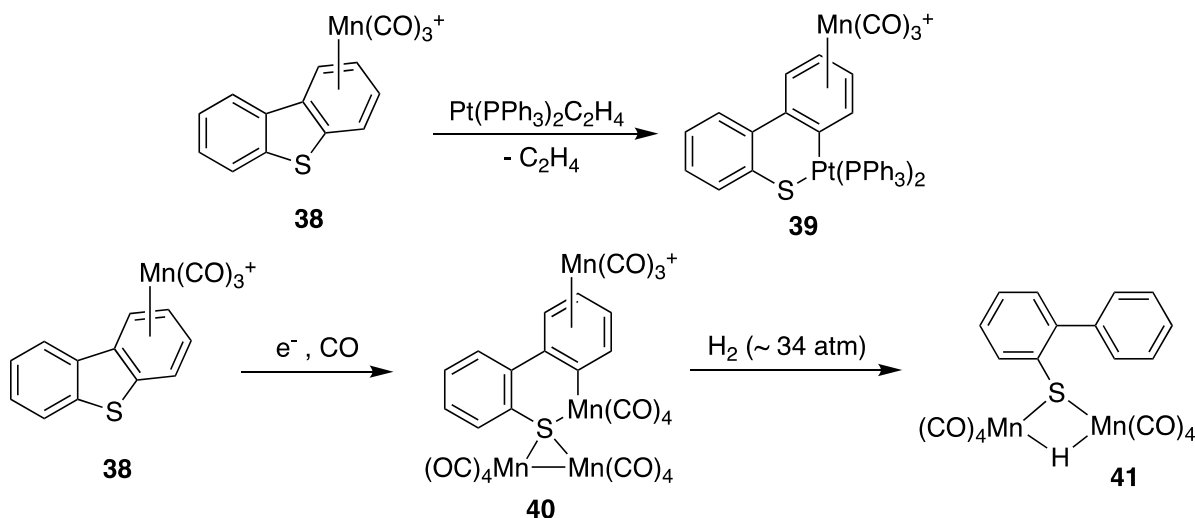
Scheme **2.6**

More electron-rich, low-valent later first-row complexes insert into the C–S bond of DBT without the requirement for pre-coordination of a Lewis acidic fragment or for an external reductant. Cp*Co(C$_2$H$_4$) **42**, for example, forms bimetallic thiacobaltacycle **43** from cooperative insertion of two cobalt centres into one C–S bond of DBT (Scheme **2.7**).[133] While no external π acid is required for this reaction, the crystal structure of **43** suggests η^2-C=C arene bonding to the exocyclic cobalt atom (Co–C$_{ave}$ = 2.12 A); this may represent a secondary activation pathway for C–S bond cleavage. Complex **42** also reacts readily to cleave the C–S bond in other thiophenic compounds.[134-135]
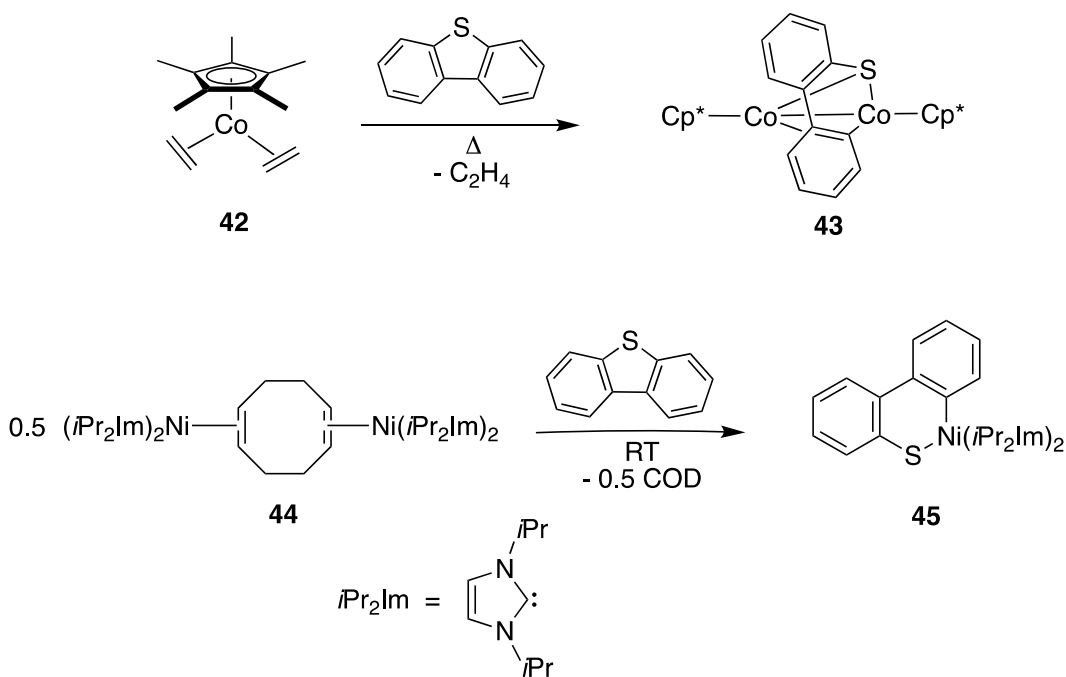
Scheme **2.7**

A similarly electron-rich (NHC)$_2$Ni^0 complex also cleaves the C–S bond of DBT under exceptionally mild conditions. Loss of cyclooctadiene from binuclear complex **44** leads to a reaction between a 14-electron d^{10}-Ni fragment and DBT (Scheme **2.7**).[136] The square planar 16-

electron metallacylce **45** can be isolated in excellent yield, but does not convert further, even upon heating under elevated pressure of hydrogen.

The first reported example of the complete desulfurization of DBT mediated by a first-row metal was also from Jones, et al. (Scheme **2.8**).[49-50] Modelled on his diphosphine Pt and Pd complexes,[49, 124] Ni(I) dimer **1** loses H_2 under ambient conditions to form the now-familiar 14-electron d^{10} intermediate **46**. Exposure of a solution containing **1/46** to DBT leads to rapid, *reversible*, insertion into the C–S bond under ambient conditions, forming the isolable adduct **47**.
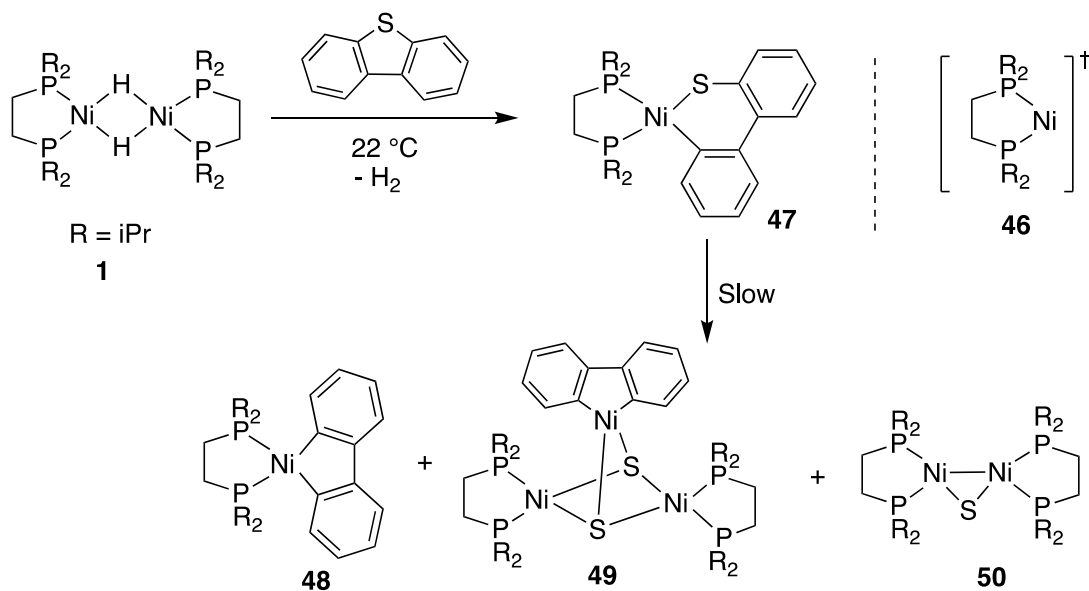
Scheme **2.8**

At room temperature, complex **47** converts over five days to a mixture of organometallic products, including trimetallic sulfide **49**, which features the fully desulfurized hydrocarbon

bound to one Ni, and from which free biphenyl is obtained upon exposure to one atm of H_2 (this is not shown in Scheme **2.8**). The sulfur atom is extruded by at least two equivalents of Ni forming **50**. The Ni–S bonds in sulfides **49** and **50** do not undergo hydrogenolysis, even under high pressure, which impedes the development of a catalytic reaction. Importantly, the C–S bonds of 4,6-dimethyl DBT is also cleaved by **1** albeit under more forceful conditions.

Although a single Ni centre readily inserts into the C–S bond of DBT, the actual desulfurization process clearly involves multi-metallic clusters (e.g., **49** Scheme **2.8**). Computational investigations have revealed the potential existence of a transient trimetallic intermediate, in which the μ_3-sulfur coordination leads to significant weakening of the C–S bond, in line with the observations of Curtis and co-workers.[118, 137]

Pentanuclear Ni cluster **2** is the most recent example of a first-row metal cluster that mediates stoichiometric desulfurization of DBT.[51] This cluster, supported by electron-rich phosphine and bridging hydride ligands, reacts with DBT at ambient temperature, affording slightly greater than one equivalent of the desulfurized hydrocarbon per cluster (Scheme **2.9**). While mechanism of this remarkable transformation is not specified, the isolation of tetranuclear cluster **51**, bearing a μ_4-sulfide ligand, suggests that co-operative desulfurization is again the most reasonable pathway. The independent formation of a related trimetallic nickel sulfide **54** from the reaction of DBT with a low valent nickel precursor **53** further supports this 'polynuclear hypothesis'.
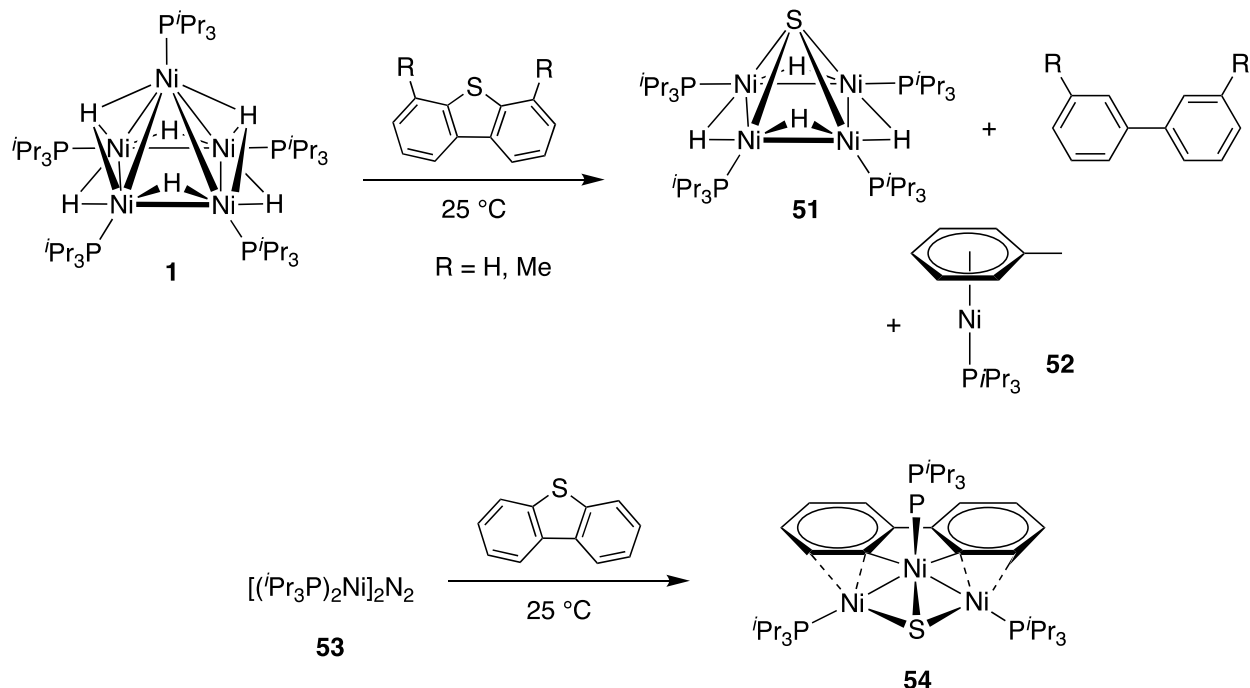
Scheme 2.9

These examples indicate that C–S bond activation in DBT by low-valent polymetallic transition metal complexes is facile. Hydrogenolysis of the metal-carbon bonds to liberate the desulfurized hydrocarbon also occurs readily. Regeneration – desulfurization – of the active transition metal specie(s), however, is inhibited by the thermodynamic stability of the resultant metal sulfides, limiting the metal to a stoichiometric role. Hydrogenolysis of the metal–sulfur bonds in these 'spent' species under mild conditions remains the energetically challenging step for achieving catalytic HDS in homogeneous systems.

2.1.4 Catalytic HDS conditions using homogeneous transition metal complexes

Homogeneous catalytic desulfurization requires a precious metal catalyst or a more reactive reductant, such as stoichiometric Grignard reagent. The (triphos)Ir complex **55** reported by Bianchini and co-workers remains the only example of a discrete molecular complex for catalytic hydrodesulfurization of DBT (Scheme **2.10**).[127] Thermolysis of **55** produces ethane and an Ir(I) intermediate that reacts readily with DBT. Thiairidacyle **56** can be used as a catalyst for HDS, very slowly converting DBT at elevated temperatures and pressure to a mixture of biphenyl and 2-phenylthiphenol. While ground-breaking, this discovery relies on a costly, inefficient iridium catalyst, making it unsuitable for any application.
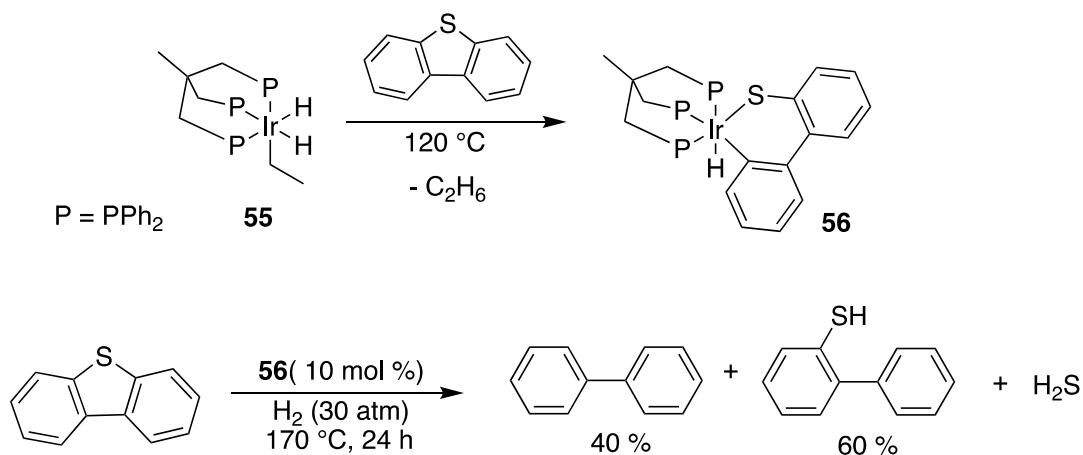
Scheme **2.10**

Alkyl magnesium reagents drive a Ni-catalyzed Kumada-type cross coupling reaction with DBT, forming 2,2'-dialkylbiphenyl as the desulfurized product. The low-valent bimetallic complex **1**,[126, 138] as well as analogous Pd[139] and Pt[126] complexes, are competent for this 'alkylative desulfurization' reaction (Scheme **2.11**). The use of isopropyl Grignard in the desulfurative

coupling reaction leads to *hydro*desulfurization, via β-hydride elimination from a putative *i*Pr–Ni intermediate.[138] A recyclable Ni catalyst for this process is obtained by immobilizing **1** onto a polymeric support,[140] but the reaction suffers from slow rates, high costs, and safety issues from handling pyrophoric Grignard reagents.
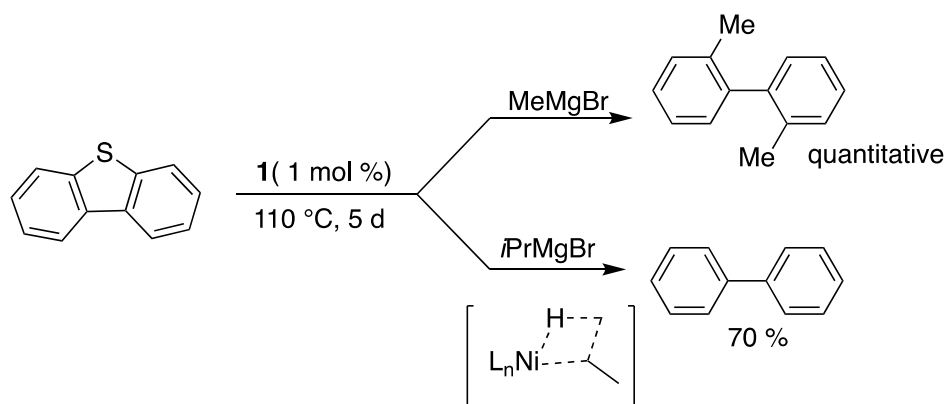
Scheme **2.11**

The Stryker group has recently disclosed cobalt and nickel phosphoranimide catalyst for potassium-hydride promoted desulfurization of refractory organosulfur compounds under very mild conditions (Scheme **2.12**).[45-46, 63, 77-78, 141]
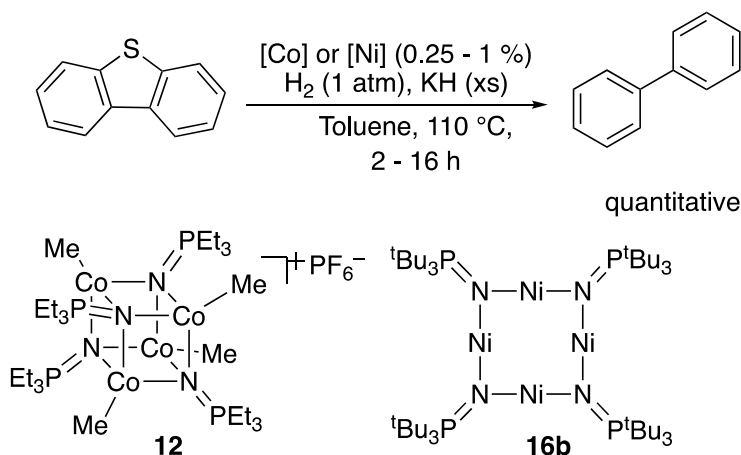
Scheme **2.12**

While sufficient experimental evidence does not exist to a support concrete mechanistic proposals, both Bunquin and Brown suggested reaction pathways consistent with that observed for other first row transition metal complexes. In the case of the **13b**, the C–S bonds of DBT are cleaved via a bimetallic oxidative addition across the electron-rich, co-planar hydridonickel centres (**57,** Scheme 2.**13**). New C–H bonds in the product are formed by reductive elimination from the hydride intermediate **58**. Iteration of this process affords the desulfurized hydrocarbon and the sulfided transition metal cluster **61**. From here, hydrogenolysis of the μ^4-sulfide was expected to liberate H_2S, which is irreversibly scavenged by the KH.[63] Given that earlier examples have highlighted the significant thermodynamic barriers to the hydrogenolysis of the M–S bonds in such systems,[50-51, 121-122, 131, 136] it was clearly naïve to believe that the strongly electron donating phosphoranimide ligand itself could uniquely promote this step.
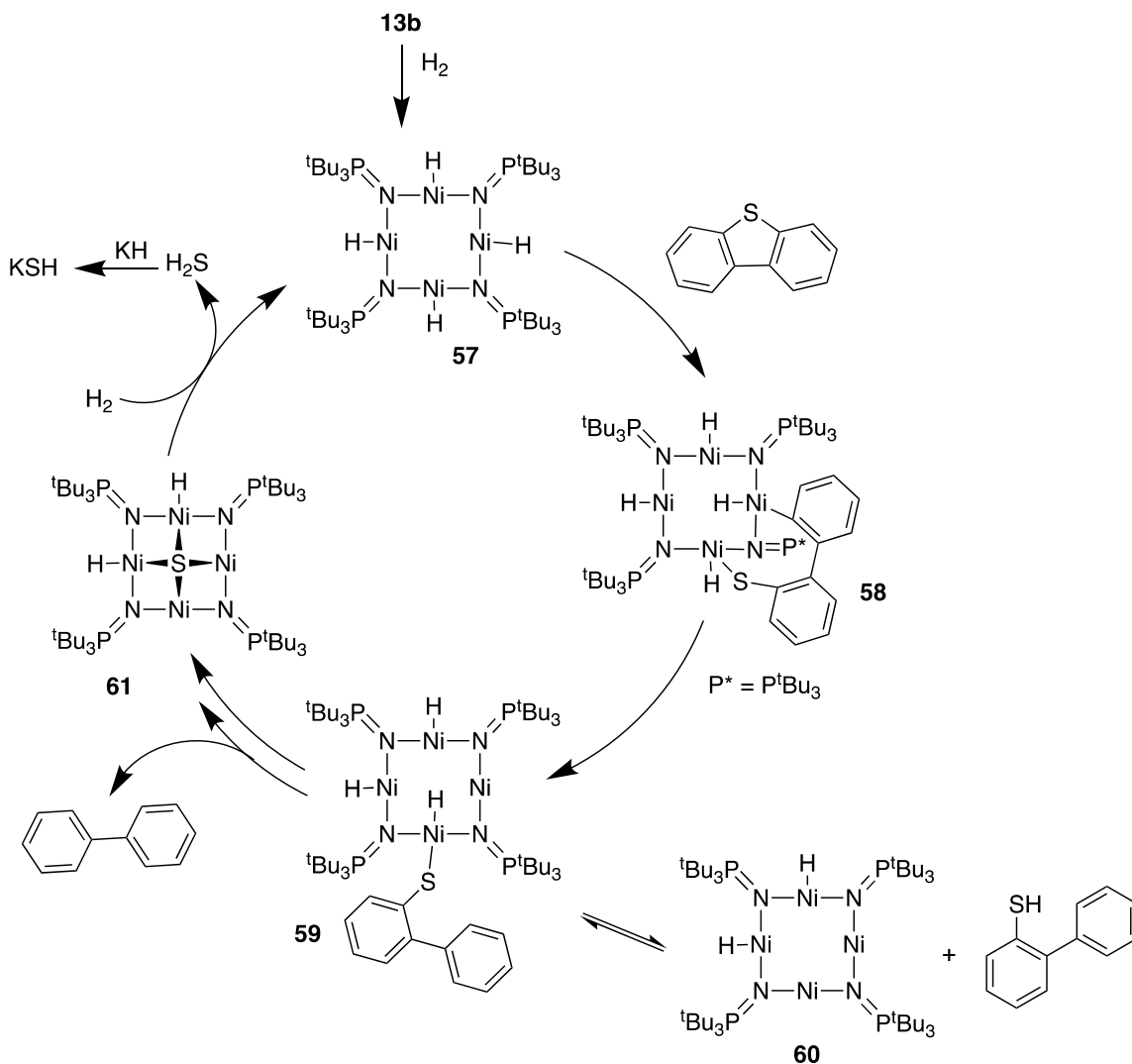
Scheme **2.13**

Specific objectives: Close inspection of the earlier reported control reactions, however, suggests an ambiguous and complex role for the stoichiometric KH.[63, 77] Our objectives were to decipher this role and, ultimately, to design *catalytic* promoters for what were still undefined catalysts. While KH is a highly effective promoter, the expense and challenges associated with handling the highly moisture sensitive reagent severely limit potential applicability. Therefore, the replacement of stoichiometric KH with another, possibly catalytic, additive for

hydrodesulfurization was addressed. Finally, because the Bunquin phosphoranimide precatalyst **13b** requires a capricious, two-step syntheses, where careful control of temperature and reagent stoichiometry is imperative, more robust, easily-accessed nickel precatalyst clusters **23** and **24** were targeted for hydrodesulfurization.

2.2 Results and discussion

2.2.1 Stoichiometric reaction between nickel phosphoranimide clusters and DBT

New nickel phosphoranimide clusters **23** and **24** (Figure **2.7**) react with dibenzothiophene at 110 °C under hydrogen (1 atm) to afford the desulfurized hydrocarbon, but in low isolated yield. Only 0.11-0.15 equivalents of DBT per Ni cluster is transformed to biphenyl (Table **2.1**). Biphenyl is obtained as the exclusive product on acidic workup, indicating that both C–S bonds are cleaved without dissociation of the substrate from the active site. The nickel reagents are apparently transformed under reaction conditions into a more active specie(s), which then reacts with and desulfurizes DBT. This activation step is inefficient, as evidenced by the low conversion of DBT compared to the number of equivalents of Ni present; the majority of the metal atoms are not productive.
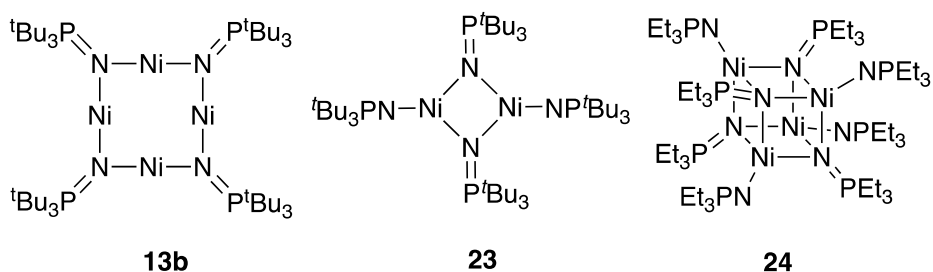
Figure **2.7** Ni precatalyst for hydrodesulfurization

Table **2.1**: Stoichiometric desulfurization of DBT by Ni phosphoranimide precatalysts
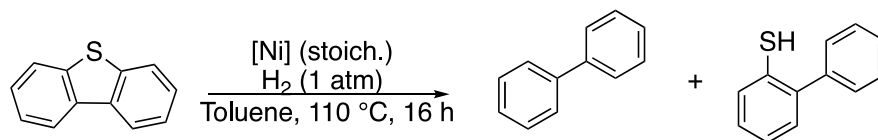
Entry	[Ni]	% Conv.[a,b]	% BP	% BP–SH
1	13b	15	14	0
2	23	12	12	0
3	24	12	11	1

[a]Determined by GC-FID analysis with dodecane as an internal standard. [b] remaining material is DBT or, some conversion to an insoluble material is also observed.

Reactive nickel(0) fragments are often implicated in the C–S bond cleavage step for several homogeneous Ni complexes,[49-51, 136] highlighting the importance of very low-valent active species. The reduction of clusters **23** and **24**, or even **13b**, on exposure to hydrogen, to such low-valent species, most certainly occurs before reaction with DBT.

For **23** or **24**, the initial step in the activation involves the hydrogenolysis of the terminal phosphoranimide, promoted by the strongly basic nitrogen lone pair on this ligand. For **23**, hydrogenolysis forms a transient hydrido Ni cluster **62** (Scheme **2.14**), which can then undergo bimetallic reductive elimination to yield **63** containing two Ni(I) centers. Further evolution of **63** under hydrogen can eventually lead to more reactive Ni(0) fragments. As discussed above, it is the Ni(0) species that appear most relevant to C–S bond cleavage. Zhao, in the Stryker group, has shown that even the coordinatively unsaturated Ni(I) tetramer **13b** must be converted to Ni(0) under hydrogen in order to catalyze the hydrogenation of unsaturated molecules.   The

poor conversion of DBT is therefore easily explained by the slow hydrogenolysis of the M–N

bonds in the nickel clusters to form the active catalyst.
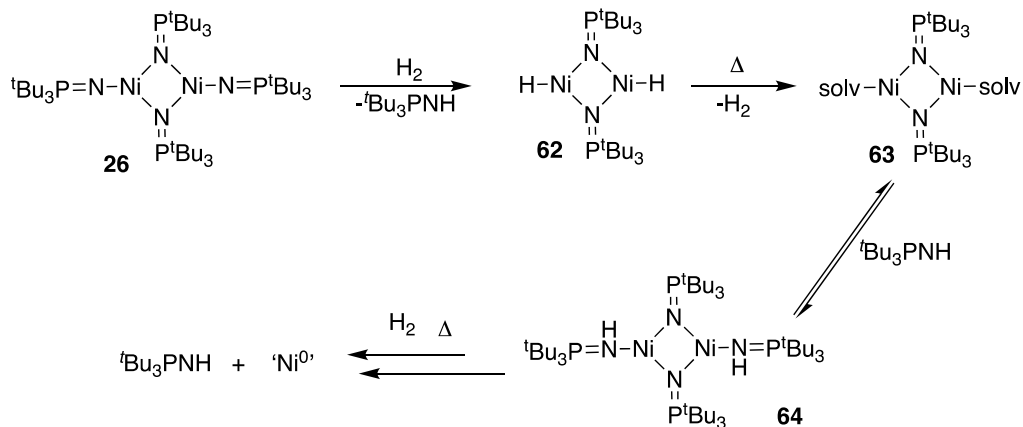
Scheme **2.14**

The free ^{t}Bu$_3$PNH liberated form the hydrogenolysis of the M–N bonds in **23** can also lead to the

suppression of the desulfurization of DBT. The phosphoranimine, is itself a Lewis basic ligand

and reversible coordination of this molecule to the any nickel specie (e.g., **64**, Scheme **2.14**) may

either inhibit substrate coordination or prevent the generation of the true active catalyst.

Hydrogenolysis of the exocyclic phosphoranimide ligand in clusters **23** and **24** was

independently investigated. Solutions (benzene-d$_6$) containing each cluster were exposed to

hydrogen in the absence of DBT, and NMR spectra recorded. The results for **26** are described

here, because its reaction is conveniently monitored by single resonance at 56-57 ppm in the

^{31}P NMR spectrum, diagnostic for the generation of ^{t}Bu$_3$PNH from hydrogenolysis.

No visible colour change is observed when **23** is exposed to hydrogen at room temperature; [31]P

NMR spectroscopy confirms the absence of reaction. On warming to 80 °C, the solution retains

the original yellow/brown colour, but the appearance of a resonance at 56 ppm in the [31]P

spectrum confirmed the activation of H_2 across at least one terminal Ni–N bond (Scheme **2.14**).

Further warming to 110 °C over 24 hours leads to an increase in the intensity of the signal for

tBu$_3$PNH, as well as the appearance of a small amount of a black precipitate, presumably

colloidal Ni(0) *vide infra*. The black solid was found by elemental analysis to contain trace

amounts of carbon, hydrogen and nitrogen from the phosphoranimide ligand. This result

confirms that under hydrogen, the Ni(II) precatalyst transforms slowly to an active low-valent

nickel phase. Similar reactivity was observed by Ting Zhao in the Stryker group, who reported

that tetrameric Ni(I) phosphoranimide complex **13b** react with hydrogen (1 atm, 5 d, RT) to yield

colloidal Ni and ^{t}Bu$_3$PNH.[64]

By using a reagent that reacts rapidly and quantitatively with the terminal phosphoranimide,

the rate of activation of the Ni(II) precatalysts **23** and **25** can be improved. The stable

boraphosphoranimide molecules **65**, first described by Stephan et al, proved helpful in this

regard. Stephan prepared **65** in excellent yields from trimethylsilyl-trialkylphosphoranimides **7**

and a chloroborane **65** (Equation **2.1**).[142]
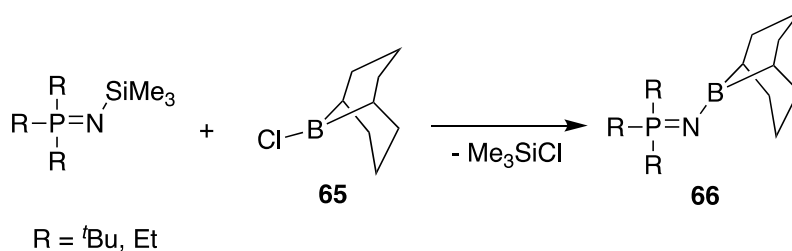
Equation **2.1**

Adapting this strategy, a hydroborane 9-BBN reacted with nickel clusters **23** and **24** generate purported Ni hydride intermediates. While a Ni hydride specie, such as **62**, has not been isolated and characterized, for precatalyst **23**, the addition of 9-BBN produced an immediate change in colour from yellow-brown to green. X-ray diffraction of single crystals obtained from this solution, confirmed the formation of the desired boraphosphoranimide by-product **66a**[142] (Scheme **2.15**, Figure **2.8**).
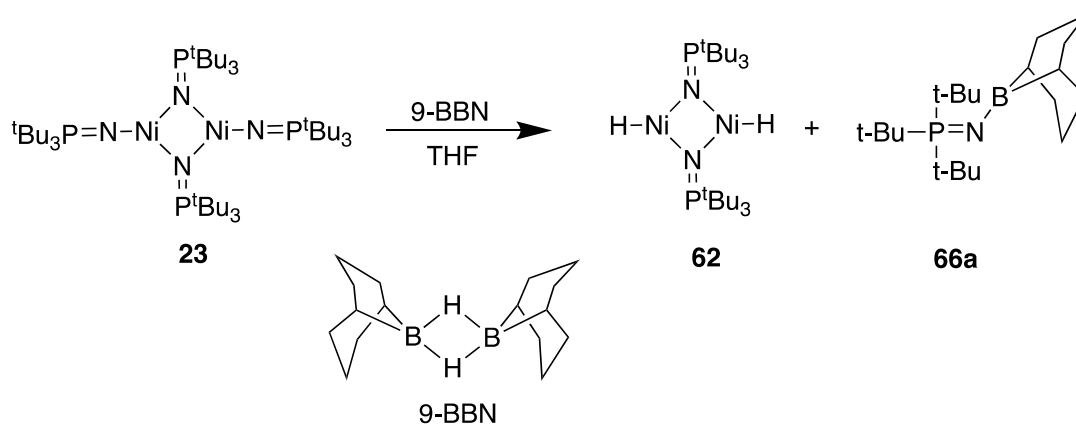
Scheme **2.15**
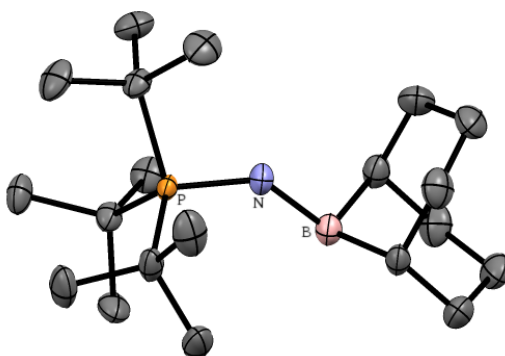
Figure **2.8** ORTEP diagram of [$^{t}Bu_3PN$(9-BBN)] **66a**. The thermal ellipsoids are shown at 30% probability. Hydrogen atoms have been omitted for clarity. R1 = 0.0637, R2 = 0.1896

The use of 9-BBN appears to increase the concentration of active nickel, as evidenced by the significant increase in conversion of DBT to biphenyl under stoichiometric hydrogenolysis conditions. Upon exclusion of hydrogen from this reaction, however, the reactions proceed in nearly identical conversions (Table **2.2**), suggesting that the borane itself mediates the reductive desulfurization of DBT, possibly with the assistance of the nickel catalyst. Unfortunately, this borane desulfurization could not be rendered catalytic; in fact, less than 50% conversion of the DBT to biphenyl is obtained, despite using a stoichiometric amount of nickel and borane.

Table **2.2** 9-BBN enhanced stoichiometric desulfurization of DBT by Ni precatalysts
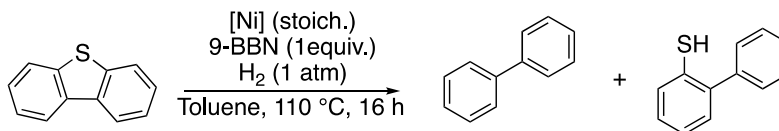
Entry	[Ni]	H$_2$		No H$_2$	
		% BP^a	% BP–SH^a	% BP^a	% BP–SH^a
1	13b	27	3	24	7
2	23	26	6	21	1
3	24	31	5	26	3

^{a}Determined by GC-FID analysis with dodecane as an internal standard.

2.3.2. Catalytic desulfurization of dibenzothiophene promoted by KH

Having established that there is a stoichiometric, albeit inefficient, reaction between DBT and an active catalyst derived from clusters **3** and **4**, catalytic HDS was investigated under conditions of stoichiometric KH. Using protocols previous developed by Bunquin and Houston Brown in the Stryker group, the phosphoranimide clusters were all effective for the desulfurization of DBT

under mild conditions. Near quantitative desulfurization of DBT was observed after 16 h at atmospheric pressure of hydrogen and 110 °C (Equation **2.2**). Under similar conditions in the absence KH, only trace biphenyl is observed.

[Ni] = **23**
88 % **BP** 1% **BP–SH**

[Ni] = **24**
91 % **BP**

[Ni] = **26 or 27 No KH**
trace conversion
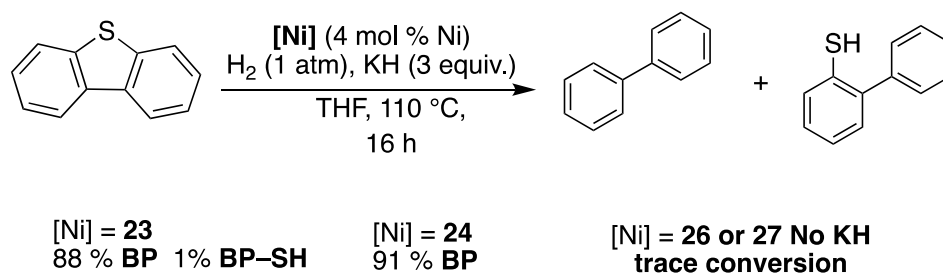
Equation **2.2**

2.3.2.1 Role of KH in catalytic desulfurization of DBT

Potassium hydride provides a dramatic enhancement in the rate of catalyzed HDS, raising questions regarding its true role in the desulfurization reaction. While the phosphoranimide nickel clusters afford only sub-stoichiometric desulfurization of DBT, (see Tables **2.1**, **2.2**, Equation **2.2**), the removal of sulfur is nearly quantitative when potassium hydride is introduced. KH was previously suggested to be purely as a basic scavenger for H_2S, but this is challenged by the fact that, other basic salts are ineffective under the identical reaction conditions. Strong bases such as KO^tBu afford only trace conversion of DBT to biphenyl, (entry 1, Table **2.3**).[143] In fact only bases which had pKa values that approach that of KH provided any promotional effect for HDS (entry 3) Moreover, strong base alone is insufficient; potassium *cations are indispensable*. While KH is an excellent promoter for desulfurization, little more than stoichiometric conversion of DBT is observed using NaH (entry 4).

Table **2.3** Effect of base strength and the identity of the counter ion efficiency of desulfurization
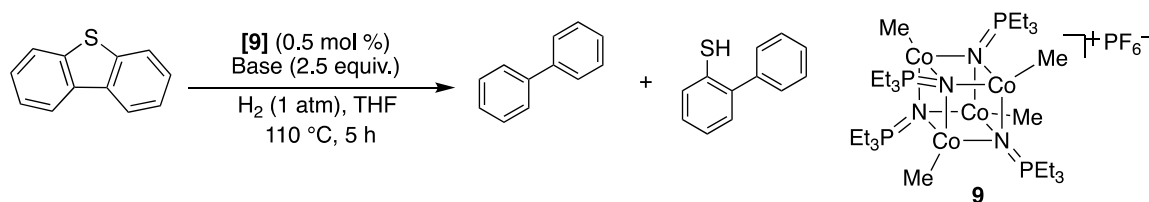
Entry	Scavenger	pKa	% Conversion	% BP	% BP–SH
1	KO^{t}Bu	17	0.64	0.64	-
2	KH	36	62.2	35.4	26.8
3	KDA	36	29.2	6.9	22.3
4	NaH	36	2.0	2	-

Adapted from Vorapattanapong, A.; Stryker, J. M., Unpublished results.

2.3.2.2 Transition metal-free desulfurization of DBT by KH

Having established the powerful reactivity of KH, further control reactions revealed that KH reacts stoichiometrically with DBT in an uncatalyzed reaction. The conversion is slow, but substantial, and does not require hydrogen (Equation **2.3**). Despite some variability in conversion, KH is clearly sufficiently aggressive to cleave C–S bonds under surprisingly mild conditions. In the presence of catalytic amounts of nickel or other first row transition metals the reaction is nearly quantitative. The use of KH was therefore abandoned, in favour of additives which do not have similar 'background' reactions with the substrate.
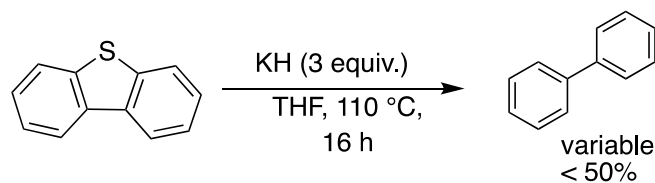
Equation **2.3**

2.3.2.3 Proposed mechanism(s) for the desulfurization of DBT by KH

Potassium hydride is both a strong base and, in some circumstances, an excellent nucleophile; proposals to rationalize its reactivity with DBT are guided by these characteristics. In one possible mechanism, the hydride ion undergoes nucleophilic aromatic substitution (Path **A**, Scheme **2.16**). Hydride addition at the ipso carbon leads to the formation of Meisenheimer-type anionic intermediate **67**, which cleaves the C–S bond to give ring-opened thiophenolate **68.** Depending upon reaction conditions and time, a significant amount of this salt is produced; 2-phenylthiophenol is isolated upon acidic work-up. In the presence of additional KH, a similar reaction of a second equivalent of hydride produces anionic intermediate **69**, which eliminates K_2S to produce biphenyl.
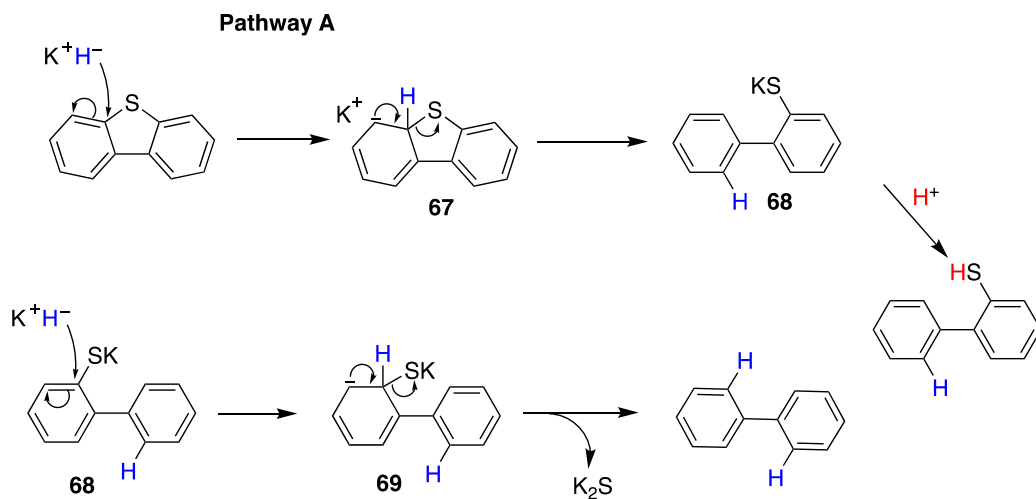
Scheme **2.16**

The formation of anionic σ-adducts such as **71** by hydride addition to an aromatic molecule is not without precedent. However, the reaction generally requires the presence of electron withdrawing groups on the arene ring (e.g., Equation **2.4**).[144-145] While DBT lacks these activating groups, the intervention of a potassium cation–π complex (see Figure **2.9**) may render the aromatic system sufficiently electrophilic for the addition of hydride .
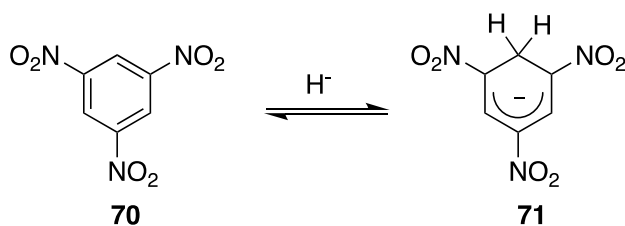
Equation **2.4**

Cation π-complexes involving potassium ions and aromatic systems is an important activating pathway for many processes and transformations, chemical and biological.[146-151] Of the possible modes for binding of DBT and potassium ions – η^6-, η^5- or η^1-S (Figure **2.9**) –computational modeling suggests that η^5-coordination provides the lowest energy path towards nucleophilic substitution by hydride.[152] Cation π -complexes of DBT and their involvement in HDS are discussed exhaustively in Chapter 3 of this work.
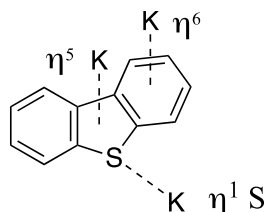
Figure **2.9** Binding modes for K^+ coordination to DBT

The increased acidity of the C–H bonds in DBT due to potassium π-coordination, leads to a second proposed pathway of KH mediated desulfurisation. Here, the basicity of the hydride ion is crucial. Pathway **B** (Scheme **2.17**) involves ortho-deprotonation and ring opening of DBT, generating aryne intermediate **72**, which reacts with additional KH to form carbanion **73** or its regioisomer. Protonation by H_2 (if present) or solvent affords the thiophenolate salt **74**. A second aryne intermediate **75** can be formed by elimination of K_2S. Biphenyl results from further reaction with hydride and a proton source.
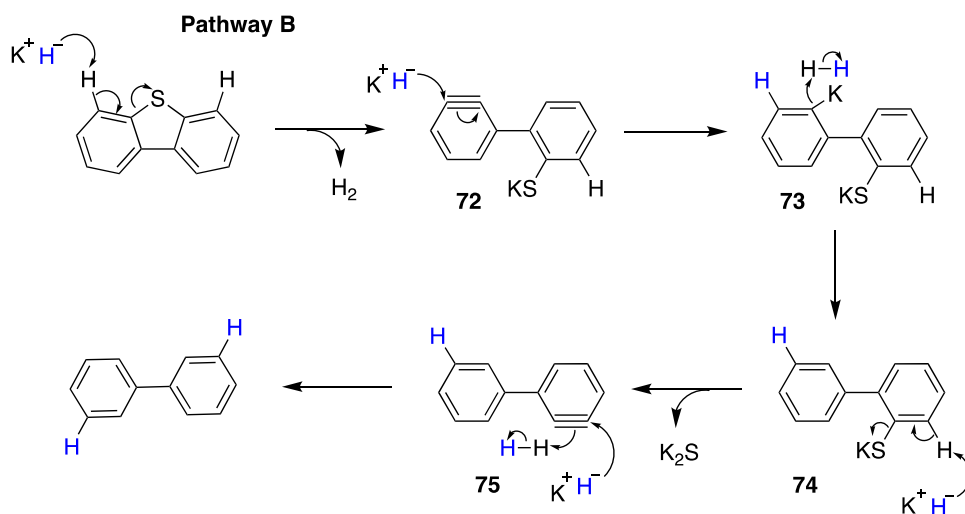
Scheme **2.17**

The use of KNH_2 at slightly higher temperature under hydrogen also desulfurizes DBT, lending further credence to the aryne proposal (Equation **2.5**) The reaction of substituted aromatic systems with amide salts to produce benzyne has been known for over 60 years.[153-155] It is also possible that KH is formed *in situ* from the equilibrium reaction of KNH_2 and H_2, followed by either of the proposed pathways above.
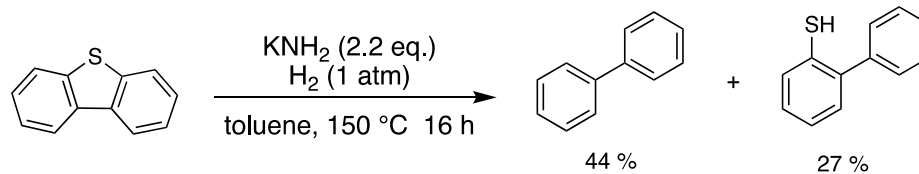
Equation **2.5**

2.2.3 Catalytic desulfurization of dibenzothiophene using KO^{t}Bu and main group hydrides

Although KH is an impractical solution to achieving deep desulfurization on an industrial scale,

there is significant interest in the use of other alkali metal salts for commercial HDS. Since the

1970's, researchers at Exxon Mobil and other petroleum companies have disclosed the use of

stoichiometric alkali metal salts, preferably potassium derivatives, to promote desulfurization of

heavy crude oil at high temperature and hydrogen pressure (Equation **2.6**).[156-167] The conditions

required are harsh (up to 480 °C and 2200 psi H$_2$) and the precipitated sulfide salts must be

captured and recycled, limiting the potential for large scale applications.
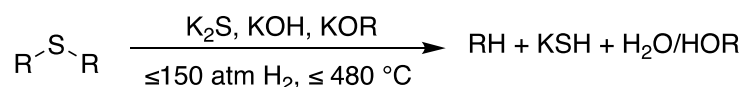
Equation **2.6**

2.2.3.1 KO^{t}Bu/Silane HDS

Using a more aggressive reducing agent in place of hydrogen allows the potassium alkoxide-

promoted desulfurization to proceed under much milder conditions (ca. 170 °C) than listed in

the industrial patents. Previous work in the Stryker group, as a well as a recent report by,

Grubbs, et al., have shown that the combination of KO^{t}Bu and silanes creates a very effective reagent for desulfurization of even the most refractory organosulfur molecules (Equation **2.7**).[63, 168] This combination provides an *in situ* surrogate for KH in the desulfurization process.
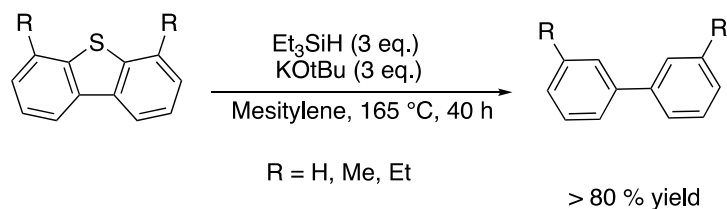
Equation **2.7**

In the presence of the nickel phosphoranimide clusters the rate of the KO^{t}Bu/silane desulfurization is enhanced dramatically compared to the uncatalyzed process. Extensive desulfurization of DBT is obtained in 6 hours at 120 °C in the presence of clusters **13b** and **24** (entry 1 Table **2.4**), compared to the uncatalyzed reaction, which requires over 40 h at 165 °C.[168] The effectiveness of Ni(COD)$_2$ and NiBr$_2$(DME) (entries 3, 4 Table **2.4**) for this transformation *under ligand free conditions* underscores the simplicity of this method and suggests that colloidal Ni(0) is likely the active catalyst.

Table **2.4** Ni catalyzed KO^{t}Bu/silane desulfurization of DBT
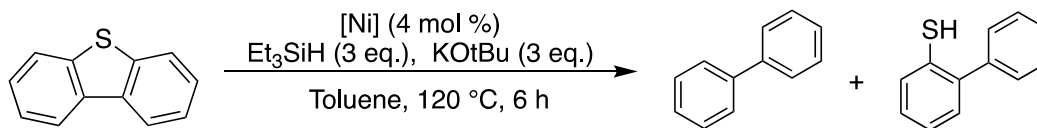
Entry	Catalyst	% Conversion^a	% BP^a	% BP-SH^a
1	13b	94	50	39
2	24	85	45	38
3	Ni(COD)$_2$	100	92	3
4	NiBr$_2$(dme)	100	94	1

^{a}Determined by GC-FID analysis with dodecane as an internal standard.

Grubbs, et al. suggested the intermediacy of organosilyl radicals but we propose that a soluble potassium silicate, K[Et$_3$Si(O^{t}Bu)H] **76** that is formed from ^{t}BuOK and the organosilane, is the active silicon specie under our conditions (*top,* Scheme **2.18**). Anionic **76** is likely aggressive enough to transfer hydride to an intermediate thiametallacycle (e.g., **77**, Scheme **2.18**, center) leading to nickel hydride **78**. Reductive elimination and a second hydride transfer leads to the formation of biphenyl and release of the silyl thioether **81**.
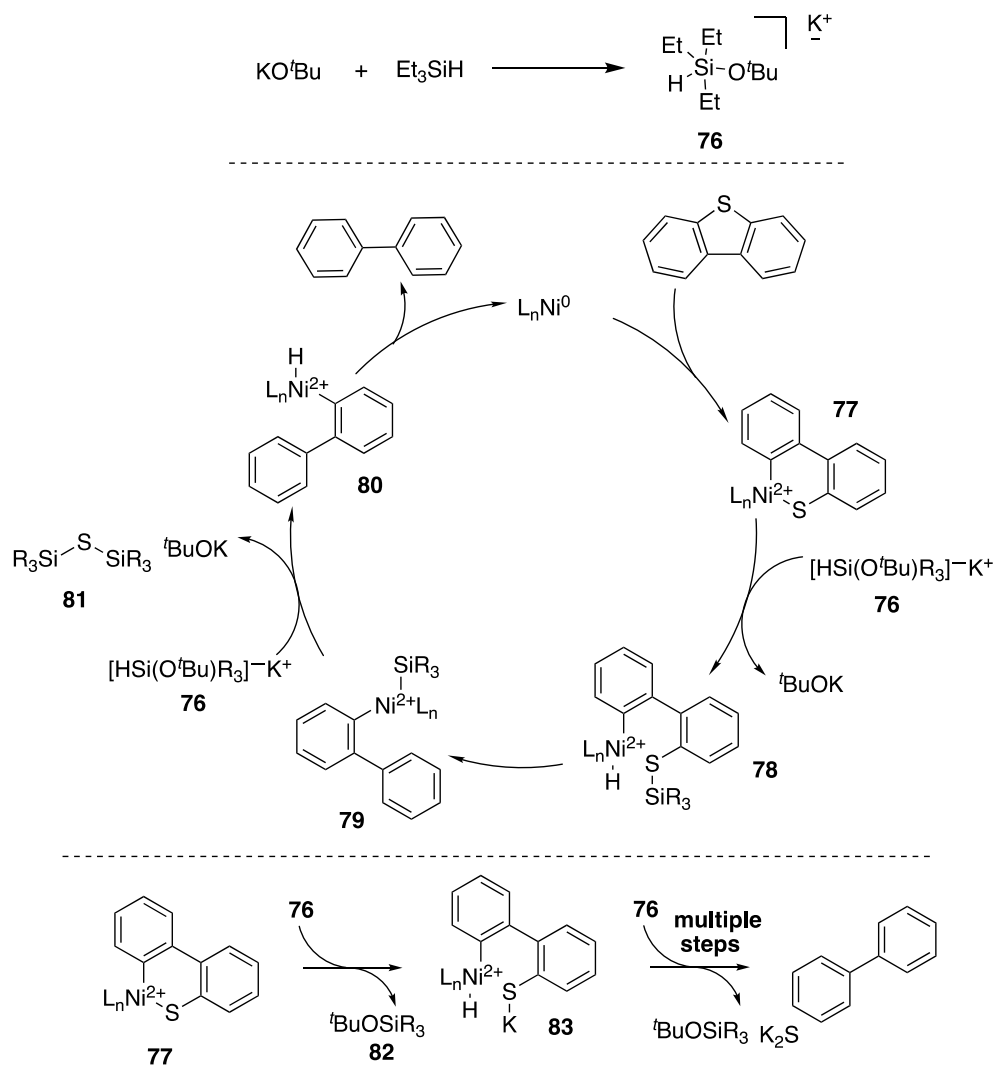
Scheme **2.18**

In a slight variant of this proposed mechanism, trialkyl *tert*-butoxysilane **82** is formed as a by-product of exchange (*bottom,* Scheme **2.18**). The nickel thiophenolate **83** is also an intermediate, with the sulfur extruded as K_2S instead of thiosilylether **81**.

2.2.3.2 KO^tBu/hydroborane HDS

The combination of potassium tert-butoxide and a hydroborane provides an equally convenient means to generate an active KH surrogate for Ni-catalyzed desulfurization (Equation **2.8**). This reaction resembles a typical base-promoted Suzuki-Miyuara cross-coupling reaction between DBT- the electrophilic component, and 9-BBN as the nucleophile. As for typical cross coupling reactions with organoborn reagents, the reaction is very inefficient in the absence of base (see Table **2.2**, above), highlighting the need to generate the organoborohydride **84**, which can more readily deliver hydride in the transmetallation step (Scheme **2.19**).[169-170]

23 (1 mol %)
9-BBN (2.2 eq.)
KOtBu (2.2 eq.)

THF/Toluene, 110 °C, 16 h

42 %   55 %
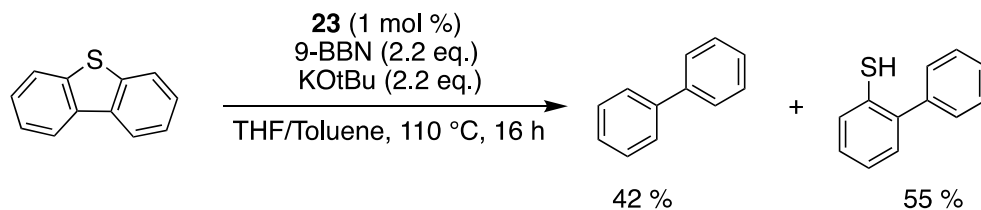
Equation **2.8**
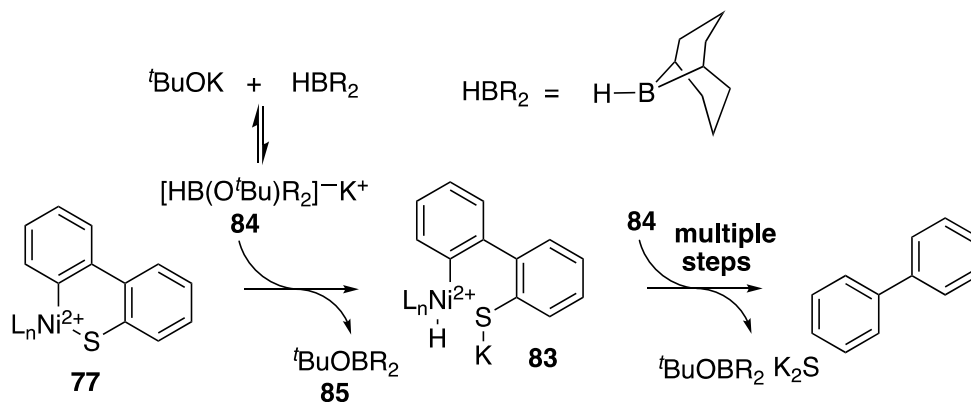
Scheme **2.19**

2.2.4 Catalytic desulfurization of dibenzothiophene using KO^{t}Bu and H$_2$

Inspired by the efficiency of the potassium *tert*-butoxide/main group hydride system for HDS, the use of molecular hydrogen as the terminal reductant was pursued. Highly atom economical and producing easily-managed side products (e.g., H$_2$O, H$_2$S), hydrogen is considered the ideal 'green' reductant for all hydrogenation and hydrotreatment reactions. Although stoichiometr*ic* *tert*-butoxide is known to promote Ni-catalyzed hydrogenolysis of the C–O bonds in aryl ethers at atmospheric pressure,[43-44] the activation and hydogenolysis of C–S bonds, including those in DBT, under similar conditions have not been explored until this investigation.

2.2.4.1 Ambient pressure HDS using KO^{t}Bu/H$_2$

Under atmospheric pressure of H$_2$, KO^{t}Bu does not promote Ni-catalyzed desulfurization of DBT. (Equation **2.9**). Other alkoxide salts are similarly ineffective for HDS, affording at best stoichiometric conversion. Stronger bases/nucleophile (amide, hydride) perform efficiently under these conditions *vide supra* but ^{t}BuO$^-$ is a poor nucleophile, and requires higher temperatures, or an assisting amine ligand, to activate aromatic C–H bonds.[171-172]
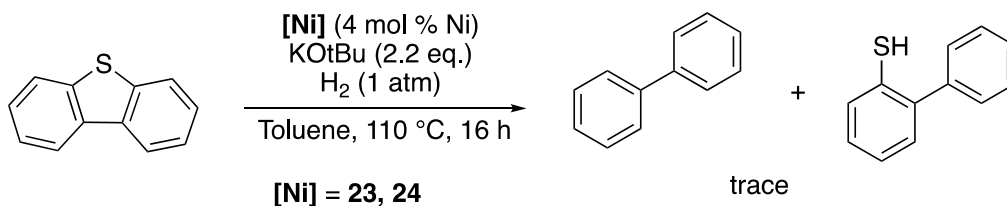
Equation **2.9**

A second challenge to using the ^{t}BuOK/H$_2$ system is the absence of an aggressive hydride source, which drives the transmetallation reaction, cleaving the strong M–S bond (see Schemes

2.18, **2.19**). Direct hydrogenolysis of the M–S bond using only hydrogen is more challenging, generally requiring very high temperature and high hydrogen pressure, as in the industrial CoMoS catalysts.

Two approaches were pursued to compensate for the lower reactivity of the ^{t}BuOK/H$_2$ system: (1) addition of a reducing metal to assist the extrusion of sulfur, and (2) increasing the temperature and hydrogen concentration to promote hydrogenolysis of M–S and M–C bonds, liberating both desulfurized hydrocarbon as well as the sulfur.

2.2.4.2 Catalytic HDS using KO^{t}Bu/H$_2$ promoted by reducing metals

Adding an external reductant such as Mg^0 or Mn^0, was anticipated to promote turnover either by direct reduction of the intermediate metal sulfide, or by single electron transfer to this intermediate, lowering the barrier to hydrogenolysis of the M–S bond. Promoting turnover of soluble Ni catalysts using stoichiometric reducing metals has been described recently by the Weix[173-175] and Shi[176] research groups (Scheme **2.20**).
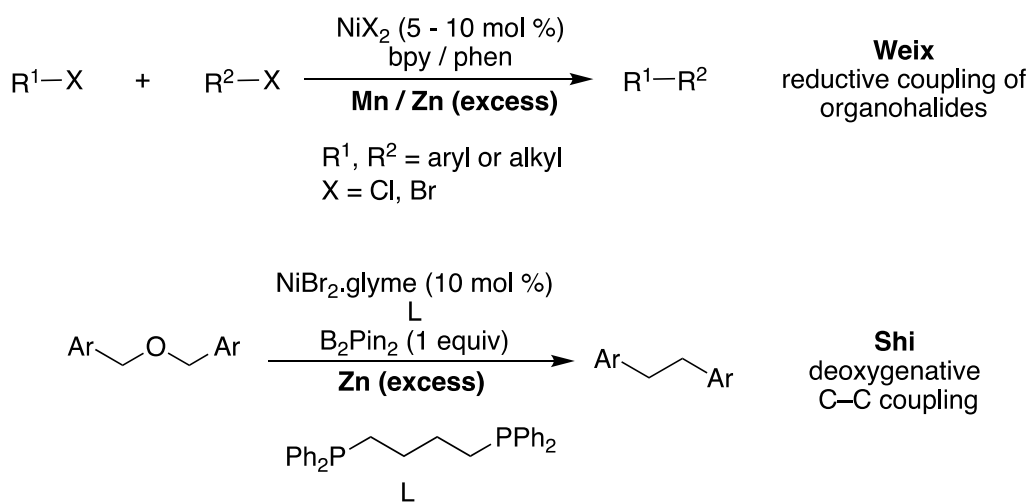
Scheme **2.20**

Super-stoichiometric Mn, Mg or Zn powder has only negligible effect on the conversion of DBT using the Ni precatalyst arising from 9-BBN activation (Equation **2.10**). Shi, et al., observed similar reactivity: the reducing metal alone is not sufficient to extrude the heteroatom and the inclusion of B_2Pin as an 'oxygen acceptor' was essential.
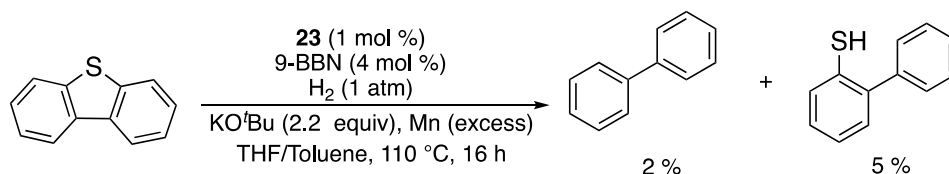
Equation **2.10**

To promote hydrogenolysis, the pressure was increased to 4 atm (60 psi) under otherwise identical reaction conditions. Gratifyingly, a notable improvement was observed in the conversion to biphenyl (Equation **2.11**). Thus, hydrogenolysis of putative M–S bonds can be mediated by hydrogen, at least in conjunction with stoichiometric KO^tBu, and the process responds as expected for a catalytic hydrogenation.
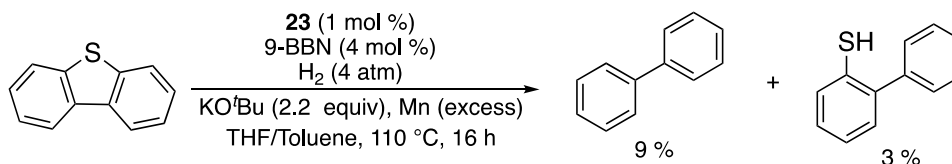
Equation **2.11**

2.2.4.3 Catalytic HDS at elevated temperature and hydrogen pressure

Predictably, at higher temperature and pressure, the conversion of DBT is increased significantly, with near quantitative conversion to a mixture favouring biphenyl over 2-phenylthiophenol obtained at 150 °C under 34 atm of H_2 (Table **2.5**). Under these reaction conditions, *the 9-BBN activator and the reducing metal can be excluded without affecting the extent of desulfurization of DBT*.

Table **2.5** Optimization of catalytic HDS at elevated temperature and hydrogen pressure
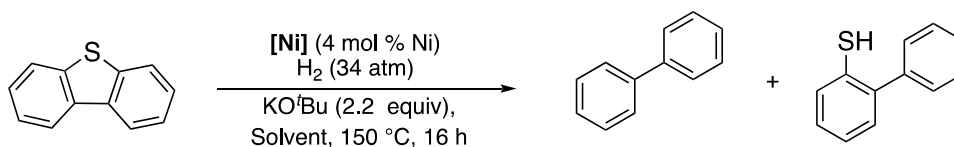
Entry	Catalyst	Solvent	% Conversion[a,b]	% BP[a]	% BP-SH[a]
1	13b	hex	88	10	63
2	13b	thf	99	8	85
3	13b	tol	35	10	22
4	13b	cyclooctane	44	12	24
5	23	hex	93	11	72
6	23	thf	96	14	71
7	23	tol	48	12	23
8	23	cyclooctane	85	36	37
9	24	hex	99	30	65
10	24	thf	96	19	75
11	24	tol	40	19	24
12	24	cyclooctane	80	57	15

[a]Determined by GC-FID analysis with dodecane as an internal standard. [b] Remaining material is DBT or, some conversion to an insoluble material is also observed.

The choice of solvent has profound effect on conversion and product distribution. For all precatalysts, markedly lower conversions were obtained in toluene (*Entries* 3,7,11 Table **2.5**), implicating competitive π-coordination of the Ni catalyst or the potassium cation. By corollary, η^5-or η^6-coordination of DBT to nickel or potassium may be an important step in the activation of the substrate towards C–S bond cleavage. The importance of π-arene complexation for the reaction of DBT[92-95] specifically and nickel catalysis[177-179] in general is well-recognized. Alternatively, toluene coordination may impede the formation of the active catalyst under the reaction conditions.

Using hexane or THF as solvent leads to >80% conversion of DBT, albeit largely to 2-phenylthiophenol rather than hydrocarbon (*Entries* 2-3, 5-6, 10-11 Table **2.5**). The reasons for this are intuitive, yet contradictory. In the presence of the alkoxide, 2-phenylthiophenol is rapidly deprotonated to form the poorly soluble potassium thiophenolate. Further reaction is inhibited by the precipitation of this salt, giving a large quantity of the 2-phenylthiophenol upon acidic work-up. In, THF the thiophenolate may be more soluble, binding to the transition metal through an η^1-S mode. However, competitive coordinative inhibition by THF itself, may suppress re-coordination of the thiophenolate intermediate, inhibiting further C–S bond scission.

Cyclooctane, a high boiling non-coordinating solvent, with greater polarity than hexane, addresses the challenges associated with other solvents. Good conversion is observed, with significantly better selectivity for biphenyl than in reactions performed in other solvent (*Entries* 4, 8, 12 Table **2.5**).

2.2.4.4 Catalyst heterogeneity

The presence of heterogeneous nickel particles as the active catalyst under the forceful reaction is nearly certain. The decomposition of initially homogeneous pre-catalysts to colloidal active phases is common at high temperature and hydrogen pressure,[180] and first-row transition metal complexes are particularly susceptible, suffering from lower bond strengths compared to their heavier analogues.[181] Moreover, colloidal catalysts are implicated in the Ni-catalyzed activation of strong carbon-heteroatom bonds.[41, 44]

The conversion of DBT to biphenyl using Ni(COD)$_2$ as pre-catalyst under ligand-free conditions reinforces the importance of colloidal nickel hydrides in KO^{t}Bu-promoted HDS (Table **2.6**). That catalyst is comparable in efficiency to nickel phosphoranimide precatalysts, again raising the question of whether soluble nickel phosphoranimides are transformed under reaction conditions to dative ligands and nickel nanoparticles, which are the actual desulfurization catalysts.

Table **2.6** Ligand free pre-catalysts for catalytic HDS at elevated temperature and hydrogen pressure
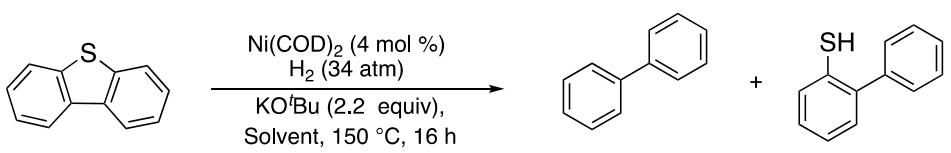
Entry	Solvent	% Conversion^{a,b}	% BP^a	% BP-SH^a
1	hex	79	11	56
2	thf	40	12	17
3	tol	44	27	13

^{a}Determined by GC-FID analysis with dodecane as an internal standard. ^{b} Remaining material is DBT or, some conversion to an insoluble material is also observed.

To evaluate the homogeneity of the catalyst system under the reaction conditions, a mercury puddle test was performed. This is a simple, widely applied, but not entirely conclusive, test of homogeneity for transition metal-catalyzed processes.[182-183] In the presence of excess Hg, conversion fell precipitously for all precatalysts, suggesting that the active catalyst is indeed composed of Ni particles (Table **2.7**).

Table **2.7** Heterogeneity of active catalyst for KO^{t}Bu promote HDS
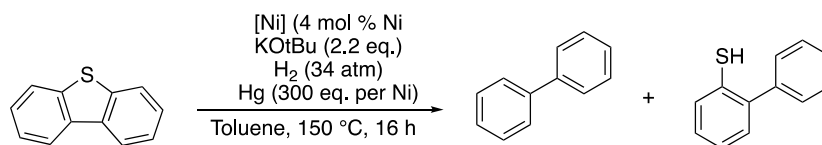
Entry	[Ni]	% Conversion^{a,b}	% BP^a	% BP-SH^a
1	13b	2	1	1
2	23	3	1	2
3	24	1	1	0
4	Ni(COD)$_2$	0	trace	trace

^{a}Determined by GC-FID analysis with dodecane as an internal standard. ^{b} Remaining material is DBT.

The decomposition pathway presumably involves exhaustive hydrogenolysis of the Ni–N bonds in the phosphoranimide clusters. Preliminary computational modelling of the reaction between hydrogen and a tetranuclear nickel phosphoranimide cluster **13b** suggest that heterolytic activation of hydrogen across the M–N bond is facile.[152] Subsequent iterations of this hydrogenolysis are equally favourable, eventually generating a phosphoranimine-supported nickel hydride cluster. Heating leads to ligand dissociation and concomitant loss of dihydrogen,

affording transient Ni atoms, which rapidly agglomerate into nanoparticles. (Scheme **2.21**). The ^{31}P NMR spectra of the filtered liquid phase confirms the presence of the dissociated phosphoranimine $^{t}Bu_3PNH$. Moreover, no catalytically active material remained in the liquid phase; no desulfurization is observed when the liquid is treated with DBT and KO^{t}Bu under typical HDS conditions.

Scheme **2.21**

To further confirm the formation of an *in situ* formed colloidal active catalyst, a sample of a typical reaction mixture was analysed using scanning electron microscopy (SEM). A reaction mixture containing DBT, KO^{t}Bu, and **23**, were heated together at 110 °C under atmospheric pressure of hydrogen for 16 hours, after which an aliquot of the reaction mixture was transferred to a supporting grid and dried then and analysed by SEM.

High-resolution SEM imaging of isolated catalyst confirms the presence of polydisperse nano-particles isolated from the reaction mixtures, averaging about 200 nm in size (Figure **2.10**). Larger, micron-sized aggregates are also visible in the micrographs. The activation and hydrogenolysis of the C–S bonds likely takes place at the surface of these nanoparticles. Energy

dispersive x-ray (EDX) spectroscopic analysis of the particles obtained from the reaction mixture indicates the presence of sulfur and *potassium*, in addition to nickel, implicating this ternary mixture in the composition of the active catalyst for HDS (Figure **2.10**).
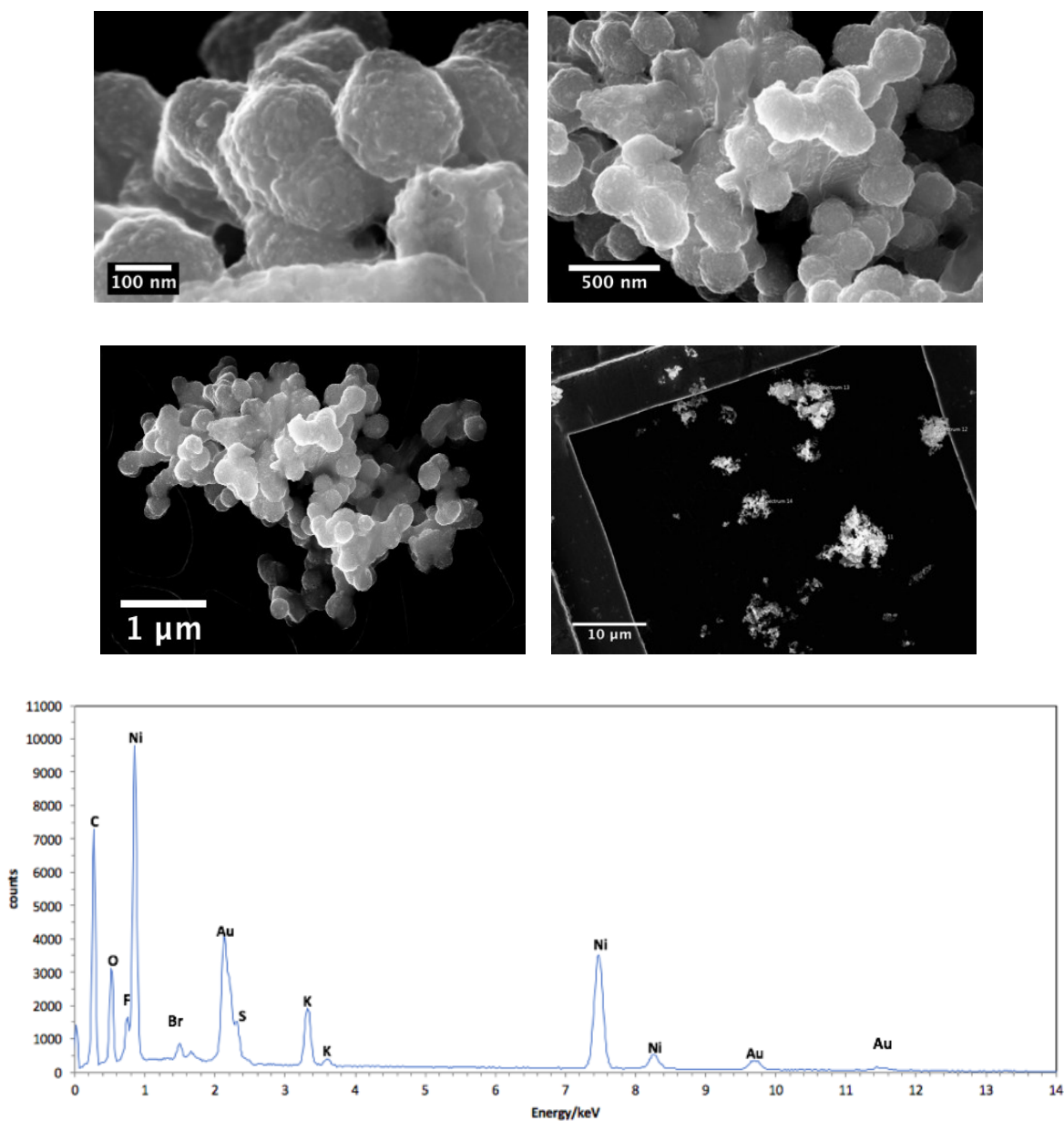
Figure **2.10** High-resolution SEM micrographs and EDX spectrum of the nickel particles formed from the hydrogenolysis precatalyst **23** under reaction conditions. Particles dispersed on carbon grid supported on a gold substrate.

2.3 Conclusions

Nickel phosphoranimide clusters promote the desulfurisation of DBT in the presence of aggressive alkali or main group metal hydrides, affording high yields of biphenyl. Control reactions (and patent literature) suggest that these hydrides, particularly KH, are competent for dibenzothiophene desulfurization in the absence of a transition metal. The mechanism of this reaction is not fully understood, but may proceed through direct nucleophilic aromatic substitution or via *ortho*-deprotonation/elimination.

At elevated temperature and pressure, precatalysts **13b, 23, 24** mediate hydrodesulfurization of DBT in the presence of stoichiometric KO^{t}Bu. The reactions represent the first use of molecular hydrogen as the terminal reductant for deep desulfurization under comparatively mild conditions. Control reactions and characterization by electron microscopy implicate particulate nickel(0) as the active catalyst for the desulfurization of DBT under these conditions.

3. Supported Ni catalysts for potassium-promoted deep hydrodesulfurization

3.1 Introduction and background

3.1.1 Homogeneous and heterogeneous catalysis: a brief comparative overview

The vast majority of catalyzed industrial chemical processes rely on heterogeneous transition metal catalysts.[10, 184] Heterogeneous catalysts are solids, while the reactants they transform exist in the liquid or gas phase. In contrast, for homogeneous systems the catalyst and the reactants exists in the same solution phase. Heterogeneous catalysts are more practical than soluble analogues because they are generally more robust at elevated temperatures and are readily separated from product streams and recycled in subsequent reactions.[184] For these reasons, heterogeneous catalysts are often deployed in flow reactors, where fresh reactant is introduced continuously over a catalyst bed and the product collected without need for separation protocols.[185-186] By contrast, homogeneous catalysts are limited to batch reactions and require extensive work-up to separate the catalysts from the products, increasing the complexity of the process and the volume of waste generated.[187] Often, these soluble transition metal catalysts decompose during the extraction/separation process, requiring multi-step, resource-intensive synthetic protocols to regenerate the active catalysts.[184]

Heterogeneous catalysis is not without challenges, however. Unlike homogeneous transition metal complexes, with uniform, well-defined, active sites, heterogeneous catalysts are most often comprised of transition metal centres in diverse coordination environments, each displaying unique reactivity towards substrate molecules.[188-191] Consequently, controlling

reaction pathway and, hence, product selectivity is challenging.[185, 192-193] Often, only a limited number of the diverse metal sites in heterogeneous catalysts are active for catalysis, principally those at the edges, corners, and faces of small crystallites; the vast majority of the metal atoms are buried in the bulk phase and 'wasted'.[194] As a consequence, high reaction temperatures are often required to compensate for the low concentration of active transition metal sites, among other things.[185] Modelling and probing multiple active sites is often difficult, limiting the opportunities for exploiting clear structure/activity relationships and rational design. A trial and error approach has therefore dominated the preparation and optimization of heterogeneous catalysts.[195]

Some of the challenges are exemplified by the industrial cobalt molybdenum sulfide (CoMoS) hydrotreatment catalysts (Fig. **3.1**). Heterogeneous catalysts are typically prepared from the dispersion of metal salts onto a support – often dehydrated alumina or silica. For CoMoS catalysts, high surface area alumina is impregnated with aqueous solutions of ammonium molybdate and either cobalt or nickel nitrates. Calcining at high temperature removes the solvent and generates transition metal oxides, which are then converted to transition metal sulfides by heating in a H_2/H_2S gas stream.[196] Multiple CoS and MoS domains are formed, but the most active for HDS are small MoS crystallites decorated along the edges and faces with Co atoms.[115-116, 196-197] The generation of active sites involves heating in hydrogen to extrude sulfur atoms from the edge and corner sites of the CoMoS phase, creating vacancies where organosulfur molecules can bind and undergo desulfurization.[113, 196] However, only a limited number of comer and/or edges sites are involved in catalysis; the vast majority of the Co and

Mo in the catalyst is either buried in the bulk phase or resides in other, less-active crystallites. In addition, the corner, edge and face sites of the CoMoS phase are not identical; while some sites are responsible for the direct desulfurization of the organosulfur molecules, others lead the undesirable saturation of aromatic C=C bonds. Rational synthesis of a single, high-activity, high selectivity site for direct hydrodesulfurization is extremely difficult.
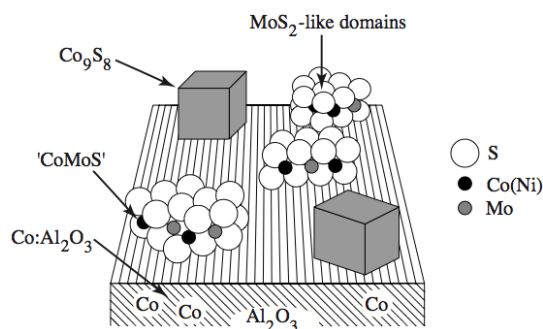
Figure **3.1** Representation of alumina supported CoMoS HDS catalyst[29]

Methods for the precise morphological control of the active CoMoS phases are limited. The most effective approach to improving the activity relies on manipulating the heating rate during sulfidation; this leads to more facile generation of sulfur vacancies at the edges of the resulting slabs of CoMoS, favouring coordination and activation of organosulfur molecules.[196] This approach, however, does not address the large proportion of 'wasted' metal atoms in the catalysts and the high temperatures and hydrogen pressures required to desulfurize refractory organosulfur molecules in petroleum feeds.

Changing the elemental formulation of heterogeneous HDS catalysts can lead to more active systems. The addition of phosphorus-containing precursors for example, has received wide

attention, leading to new cobalt[198], nickel[198-203], molybdenum[204] and tungsten[205] phosphide active phases, which show promising success as catalysts for deep hydrodesulfurization. In addition, there are reports describing selective and highly effective noble metal heterogeneous catalysts for HDS, presumably for specialized applications.[206-211] These modifications, while advantageous, do not address the limitations inherent to the preparation and activation of heterogeneous catalysts.

In contrast, homogeneous organometallic models of heterogeneous HDS catalyst are remarkably efficient at cleaving C–S bonds and even desulfurizing refractory organosulfur molecules under very mild conditions.[29] This highlights the superiority of using *well-defined molecular active sites* in place of traditional heterogeneous systems.

At the molecular level, the elementary steps involved in catalysis are similar for heterogeneous and homogeneous systems.[195] Reactions are initiated by the diffusion of the reactive substrate to a catalyst active site comprised of one or more metal atoms, followed by a bonding interaction (physisorption/chemisorption). After transformation of the substrate via the activation of reactive bonds and the construction of new bonds, the product diffuses from the catalyst(s), regenerating the active site. The major differences: 1) the practicality of heterogeneous systems for product isolation and catalyst recycling and 2) the superior activity and selectivity of homogeneous catalysts as a consequence of the high population of uniform active sites.

3.1.2 Strategies for immobilization of molecular clusters: single-site heterogeneous catalysts

By immobilizing active molecular species on a support, ideal heterogeneous catalysts can be formed, composed of uniform, well-defined, and high-activity sites.[212-217] This approach retains the advantages of homogeneous catalysis in succumbing to rational design through careful modulation of the metal(s) coordination sphere. In addition, the reactivity of substrates with discrete homogeneous catalysts can be evaluated using typical analytical techniques for probing kinetics and mechanisms prior to immobilization.

The grafting of molecular transition metal catalysts to a support can be accomplished by several strategies. One common method involves tethering one or more ligands to silica or a polymer support, followed by exposure to a solution containing the dissolved metal complex (**a**, **b**; Figure **3.2**).[218-221] Strong and persistent metal-ligand bonds are required in order to anchor the metal, and phosphines, NHCs, and amines are often used.[222] A related technique involves copolymerizing a metal functionalized alkene monomer and another simple olefin, resulting in immobilization of the metal complex in an organic polymeric matrix (**c**, Figure **3.2**).[223-224] The use of non-covalent interactions, such as π-stacking, to immobilize transition metal complexes on graphitic supports is also common (**d** Figure **3.2**).[225-226]
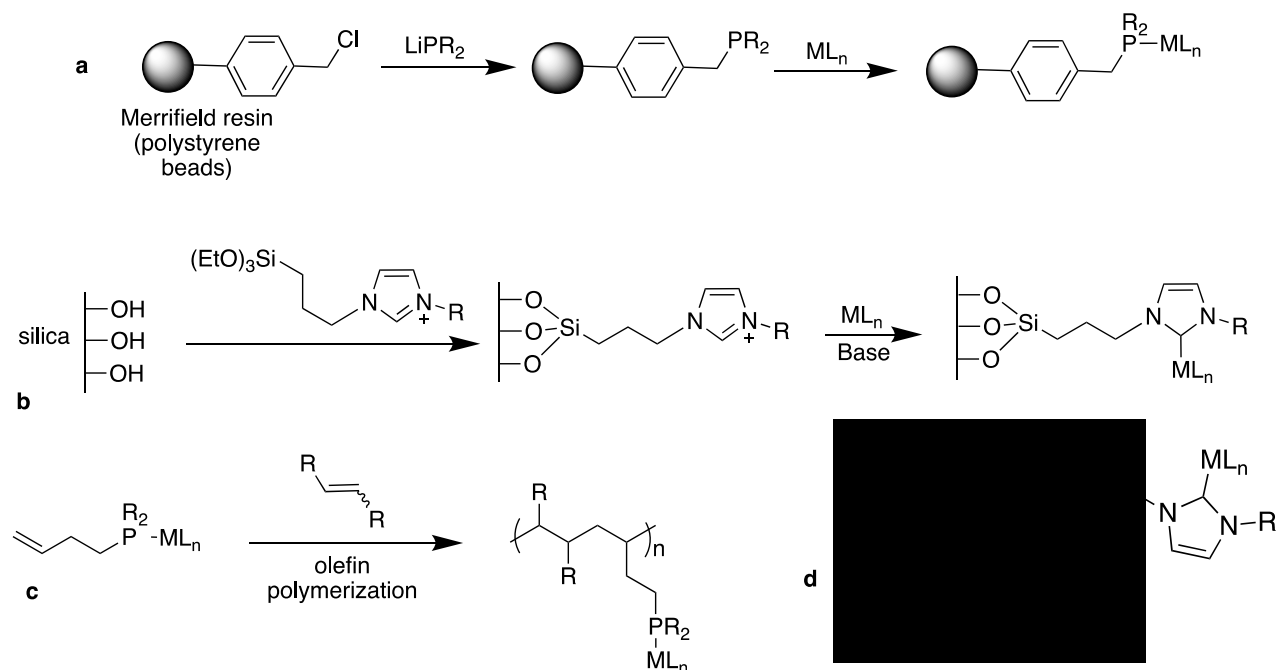
Figure **3.2** Common strategies for Immobilization of transition metal centres for catalysis

An alternative strategy involves exploiting sites on the surface of the support as direct ancillary ligands for transition metal coordination. This strategy takes advantage of the abundance of Brønsted acidic groups, typically hydroxyl, that exist on the surface of oxide supports.[212, 227-231] *Surface organometallic chemistry*, which is the moniker used for this field,[232] usually relies on the presence of an expendable, strongly basic ligand in the coordination sphere of the precatalyst complex. Strongly basic σ-donors, such as alkoxides, amides, and alkyls readily deprotonate surface hydroxyl groups, liberating the protonated form of the ligand and forming a covalent link to the metal via the surface oxygen. (Figure **3.3**)[230] Once bound to the metal centre, the transition metal complex can be used directly in catalysis, or can be subject to

hydrogenation to remove coordinated ligands and yield active sites composed of single atoms or very small polymetallic clusters.[233-235]
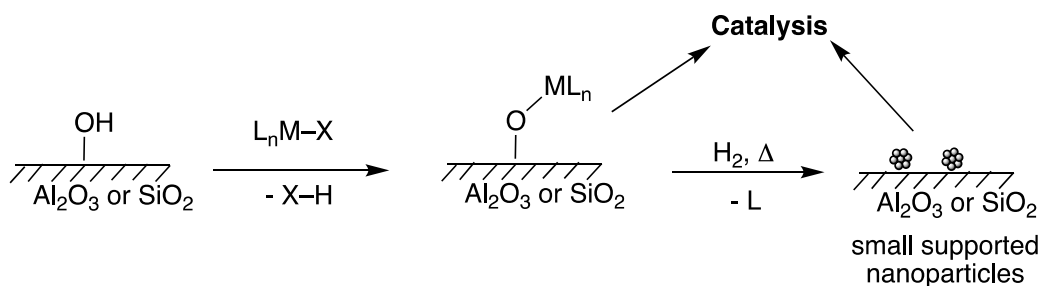
Figure **3.3** Immobilization of metal complexes onto oxide surfaces by protolytic grafting

These supported transition metal catalysts have found wide application. Transformations mediated by surface organometallic species include catalytic hydrogenation, dehydrogenation, oligomerization, polymerization, and olefin metathesis, using a several different transition metal sources.[195, 212, 230] The well-defined active sites afforded through surface organometallic chemistry allow for unprecedented reactivity and selectivity, as well as milder conditions than are common for conventional heterogeneous catalysts.

3.1.3 Features of the surface of silica and alumina

The nature of the surface of the support is essential to ensuring controlled immobilization of organometallic species. Alumina and silica, both widely used supports, have diverse surface chemistry, which can be altered by applying various thermal treatment protocols.[228] For example, bulk alumina is composed of tetrahedral and octahedral aluminum coordinated to oxygen, but at the surface, truncation of the lattice results in three- and four-coordinate

aluminum atoms, along with basic oxygen centers.[227, 231] The dissociation of water molecules over these unstable sites leads to hydroxyl groups with varying coordination modes and acidities;[227] these hydroxyl groups, along with adsorbed water molecules, create a complex hydrophilic surface (Figure **3.4**).[228] Depending on the temperature, thermal treatment can reduce or eliminate the presence of undissociated water molecules, and even remove the majority of the hydroxyl residues. Heating above 500°C creates a partially dehydroxylated alumina surface, decorated with a few isolated hydroxyl groups, along with a large number of Lewis acidic and basic sites (**Figure 3.4**). It is these residual hydroxyl groups and Lewis acidic/basic sites that control the reactivity of organometallic species at the surface of alumina.[236-239]

μ^1 –OH μ^2 –OH μ^3 –OH   Lewis Acidic and basic sites
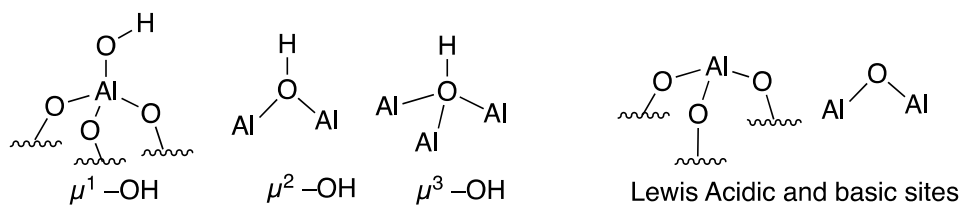
Figure **3.4** Brønsted acidic and Lewis acidic/basic sites on the surface alumina

Compared to alumina, silica presents a simpler bulk structure and surface composition. Tetrahedral SiO_4 units comprise the bulk; truncation of the lattice, followed by stabilisation through chemisorption of water, reveals a surface defined by various silanol groups as wells as siloxane bridges (Figure **3.5**)[228-229, 240] The concentration and relative proportions of the surface silanols control the surface organometallic chemistry.[229] Various protocols have been developed to reduce the density of surface silanols in a very controlled fashion. Upon heating

silica to 200 °C under vacuum, a high concentration of vicinal silanols remain on the surface, but heating to 700 °C produces almost exclusively geminal and isolated silanols.[212, 228-230] This difference controls the number of organometallic species that can be loaded onto the surface, the spatial distribution of the metal atoms, and the secondary reactions that may occur post-grafting.[195, 212, 230]
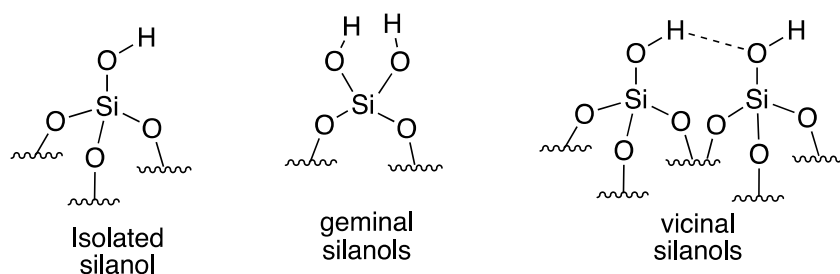
Figure **3.5** Various silanol residues on the surface of silica

Homoleptic bisphosphoranimide clusters **23** and **24** are ideal candidates for immobilization onto well-defined oxide supports. The terminal phosphoranimide ligand is an excellent Brønsted base, and several Lewis basic sites in the clusters are suited to secondary interactions with Lewis acidic sites on the support.

3.2 Results and discussion

3.2.1 Discovery of alumina-supported Ni catalysts for efficient HDS

Dibenzothiophene reacts with hydrogen in the presence of nickel phosphoranimide clusters at 150 °C and 34 atm to yield a mixture of biphenyl and 2-phenylthiophenol. The nickel clusters are converted to nanoparticles, which is the active catalytic species under these conditions. Agglomeration of these particles into less active micron-sized aggregates leads to the low overall yields of desulfurized hydrocarbon (entries 1, 3, 5, 7; Table **3.1**). To suppress this aggregation, high surface area γ-alumina was added to the reaction mixture, both to immobilize the precatalyst *in situ* as well as to act as a dispersant for nickel nanoparticles generated under the reaction conditions. Under otherwise identical conditions, the addition of high surface area, chromatography-grade, basic alumina provided a dramatic improvement in yield of the desulfurization product (entries 2,4,6,8).

The improvement in overall conversion of DBT provided by alumina was especially pronounced for the lowest valent pre-catalysts **13b** and $Ni(COD)_2$ (entries 1-4, Table **3.1**). The decomposition of **13b** to metallic nickel is more facile than that of the Ni(II) analogues **23** and **24**. Consequently, a high concentration of small nickel nanoparticles is obtained from these precursors, and agglomeration into micron-sized active aggregates is rapid. The presence of alumina limits this agglomeration, maintaining a high concentration of active Ni sites. This effect is also apparent in the slightly higher conversions, as well as superior desulfurization selectivity observed using the Ni(II) precursors (Entries 5-8 Table **3.1**).

Table **3.1** Promotional effect of γ-alumina on the nickel catalyzed HDS of DBT

[Ni]@Al$_2$O$_3$ (4 mol % Ni)
KO^{t}Bu (2.2 eq.)
H$_2$ (34 atm)
Additive
Solvent, 150 °C, 16 h
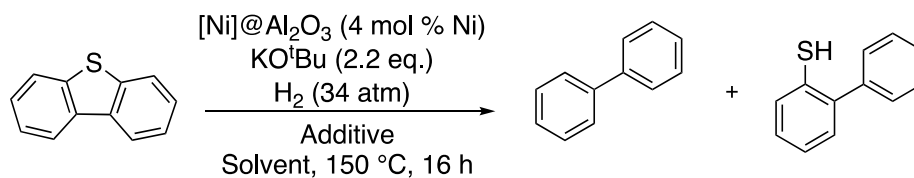
Entry	Catalyst	Solvent	Additive	% Conv.^{a,b}	Yield	
					BP^a	BP-SH^a
1	Ni(COD)$_2$	tol	-	44	27	13
2	Ni(COD)$_2$	tol	Al$_2$O$_3$	94	79	7
3	**13b**	cyclooctane	-	44	12	24
4	**13b**	cyclooctane	Al$_2$O$_3$	91	79	1
5	**23**	cyclooctane	-	85	36	37
6	**23**	cyclooctane	Al$_2$O$_3$	92	74	6
7	**24**	cyclooctane	-	80	57	15
8	**24**	cyclooctane	Al$_2$O$_3$	95	88	1
9	nil	cyclooctane	Al$_2$O$_3$	1	trace	trace
10^c	**24**	cyclooctane	Al$_2$O$_3$	92	84	2

^{a}Determined by GC-FID analysis with dodecane as an internal standard. ^{b} Remaining material is DBT or, some conversion to an insoluble material is also observed. ^{c}KO^{t}Bu purified by sublimation

13b   **23**   **24**
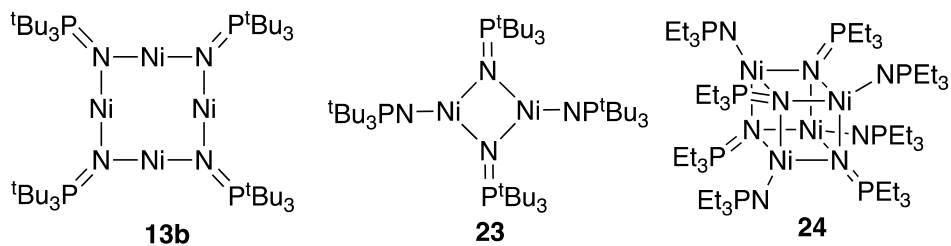
It should be noted that the presence of nickel is essential for the HDS reaction to occur (Entry 9 Table **3.1**). This observation excludes the possibility that adventitious precious metals, entrained in KO*t*Bu or in alumina, are responsible for the catalysis observed. In addition, reactions conducted using KO*t*Bu which was purified by sublimation, return results similar to that obtained using commercially available KO*t*Bu samples (compare entries 8, 10 Table **3.1**). Subsequent experiments were therefore conducted using the commercially available KO*t*Bu without further purification.

3.2.2 Immobilization of nickel phosphoranimide clusters on alumina/silica

The deliberate preparation and isolation of supported HDS pre-catalysts was explored. Protolytic grafting onto alumina or silica surfaces was expected to yield smaller, more stable, highly disperse crystallites, improving the performance of the catalyst.

Exploratory grafting experiments established that immobilization is facile and irreversible. Hydrocarbon solutions of **23** or **24** decolourise rapidly upon exposure to Brockman Activity I basic alumna dried overnight at 180 °C. After 30 seconds, the alumina becomes dyed with the color of the original solution. Extensive washing with hexane/pentane does not lead to visible leaching of the metal complex from the alumina surface. The use of a more polar solvent leads to the desorption of non-covalently-bound clusters from the alumina, but extended stirring leads to re-adsorption of the liberated material onto the surface. Similarly, using THF as the 'grafting solvent', several hours are required for the surface immobilization to be complete, as evidenced by the slow decolorization of the solution.

3.2.3 Characterization of supported pre-catalysts.

The field of surface organometallic chemistry relies on a range of characterization techniques beyond rudimentary visual inspection to probe the grafting of transition metal fragments to metal oxide supports.[212, 230, 232, 241]

3.2.3.1 Stoichiometry of grafting

Among the simplest tools to confirm protolytic grafting is the examination of the supernatant for the presence of the neutral fragment resulting from the reaction.[232] Analysis by NMR spectroscopy (^{31}P and ^{1}H) of the colorless solution reveals the presence of free ^{t}Bu$_3$PNH (Scheme **3.1**), confirming that the reaction proceeds – at least partly – via protonlysis of the terminal phosphoranimide ligands by hydroxyl residues on the surface of the support.
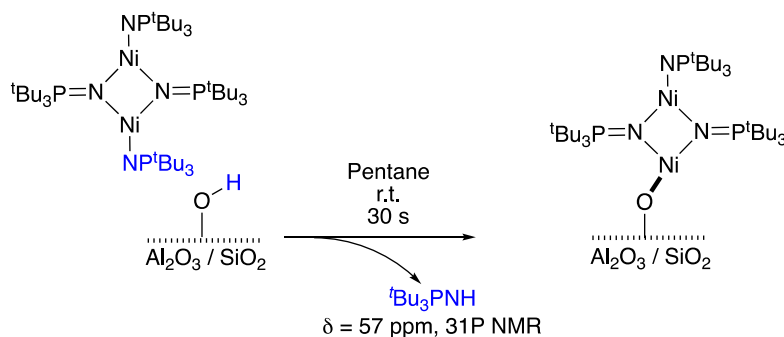
Scheme 3.1

Ordinarily, the total amount of the neutral byproduct recovered indicates the stoichiometry of grafting.[234, 242] In this case, however, less than stoichiometric amounts of the phosphoranimime were recovered, even though visually the grafting reaction appeared complete. This can be attributed to binding of the basic phosphoranimine to Lewis acidic Al^{3+} sites, which are

invariably present on alumina surfaces. (Scheme **3.2**) To test this hypothesis, a hexane solution

of ^{t}Bu$_3$PNH, at a concentration comparable to what would obtain from grafting, was stirred

over alumina for 16 h; less than 40% of the phosphoranimine was recovered after filtration.

Trituration with excess hexane or THF was not sufficient to desorb the amine from the alumina.

Higher temperatures may lead to greater desorption, but this was not explored.
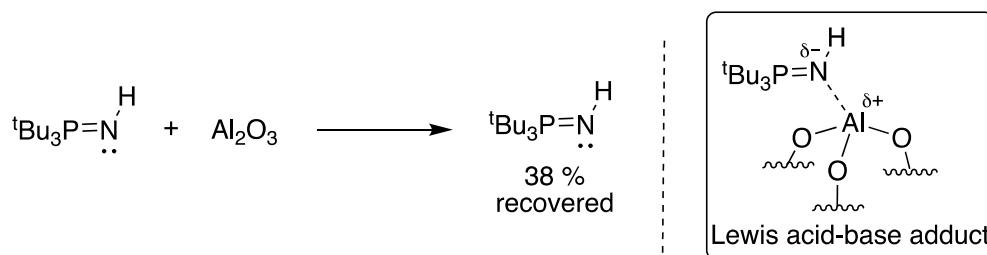
Scheme **3.2**

The binding of the ^{t}Bu$_3$PNH strongly suggests that in addition to the protolytic grafting, further

strong Lewis acid/base interactions are likely to involve the proximal aluminum centres. The

remaining terminal and bridging ^{t}Bu$_3$PN–[Ni] fragments in the metal clusters can bind datively

to Al, further accounting for the low recovery of free ^{t}Bu$_3$PNH. This secondary grafting also

explains how the tetrameric Ni(I) cluster **13b**, which lacks terminal phosphoranimide ligands is

also readily immobilized on alumina, without the evolution of neutral ^{t}Bu$_3$PNH.

3.2.3.2 Spectroscopic monitoring of the grafting process

Infrared spectroscopy offers a useful tool for monitoring the grafting of organometallic

fragment s.[230] For IR monitoring, silica was used as the support because of the well-established

protocols for the preparation and spectroscopic characterization of partially dehydroxylated silica surfaces.[228, 230, 234, 242] In addition, spectral analysis of silica is straightforward, compared to the surface spectra of alumina, which requires DFT modelling to correctly assign absorbances.[227, 231] Silica treated at 700 °C under a high vacuum (10^{-5} Torr) affords a surface with mostly isolated –OH pillars, which display a characteristic sharp IR absorption at 3747 cm^{-1}.[228, 230] For comparison, the surface of silica treated at lower temperatures retains numerous vicinal and germinal –OH groups, characterized by distinct IR absorptions of 3650 cm^{-1} and 3740 cm^{-1} respectively. [228, 230] The surface –OH coverage of silica treated at 700 °C, hitherto referred to as SiO$_{2\text{-}(700)}$, has been determined to be ca. 0.8 OH nm^{-2} by titration using a Grignard reagent.[228, 230, 242] Using this measurement, a stoichiometric amount of the organometallic precursors **23** or **24** can be loaded onto the silica surface, assuming exclusive reactivity at isolated OH groups.

Monitoring the reaction of a stoichiometric amount (per surface OH) of the dimeric Ni cluster **23** and SiO$_{2\text{-}(700)}$ by IR spectroscopy reveals complete disappearance of the absorption associated with surface Si–OH groups (**a**, Figure **3.6**). Concomitant appearance of characteristic absorbances for the hydrocarbon groups of the ligand (**b** and **c**, Fig. **3.6**) confirms the grafting and suggests retention of at least some phosphoranimide ligands in the immobilized organometallic fragment.[230, 242] The evolution of free ^{t}Bu$_3$PNH further confirms that protolytic grafting is the principal mechanism of immobilization of this nickel cluster.
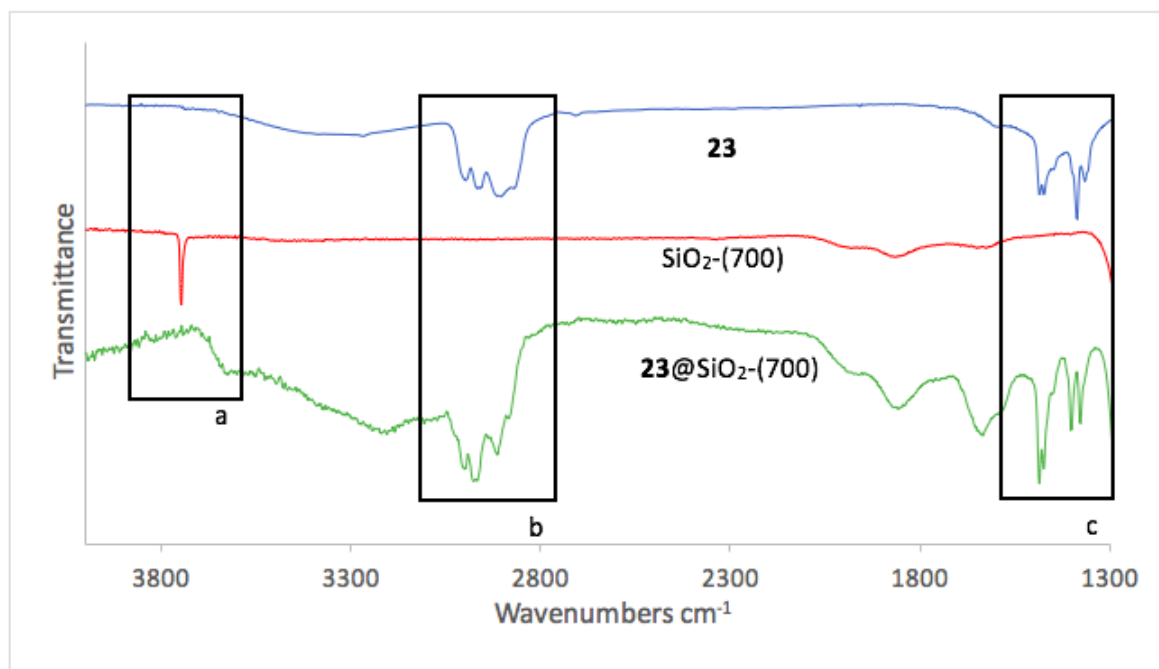
Figure **3.6**. IR monitoring of grafting **23** onto partially dehydroxylated silica

3.2.3.3 TEM imaging of the grafted clusters

Direct visualization of the nickel particles, dispersed on the surface of silica, was possible using electron microscopy. For electron microscopy experiments, SiO_2 nanoparticles (5 -15 nm) and the dehydroxylated $SiO_{2(700)}$ were used as oxide supports, allowing for superior visualization of the immobilized clusters compared to alumina.[234] TEM images reveal the decoration of the silica surface with small (1-2 nm), well-defined, and spatially-isolated Ni nanoparticles (Figure **3.7**). The small particle sizes indicates that only limited aggregation occurs once the precatalysts are grafted to the surface. Spot measurements revealed some particles of less than 0.5 nm in size.
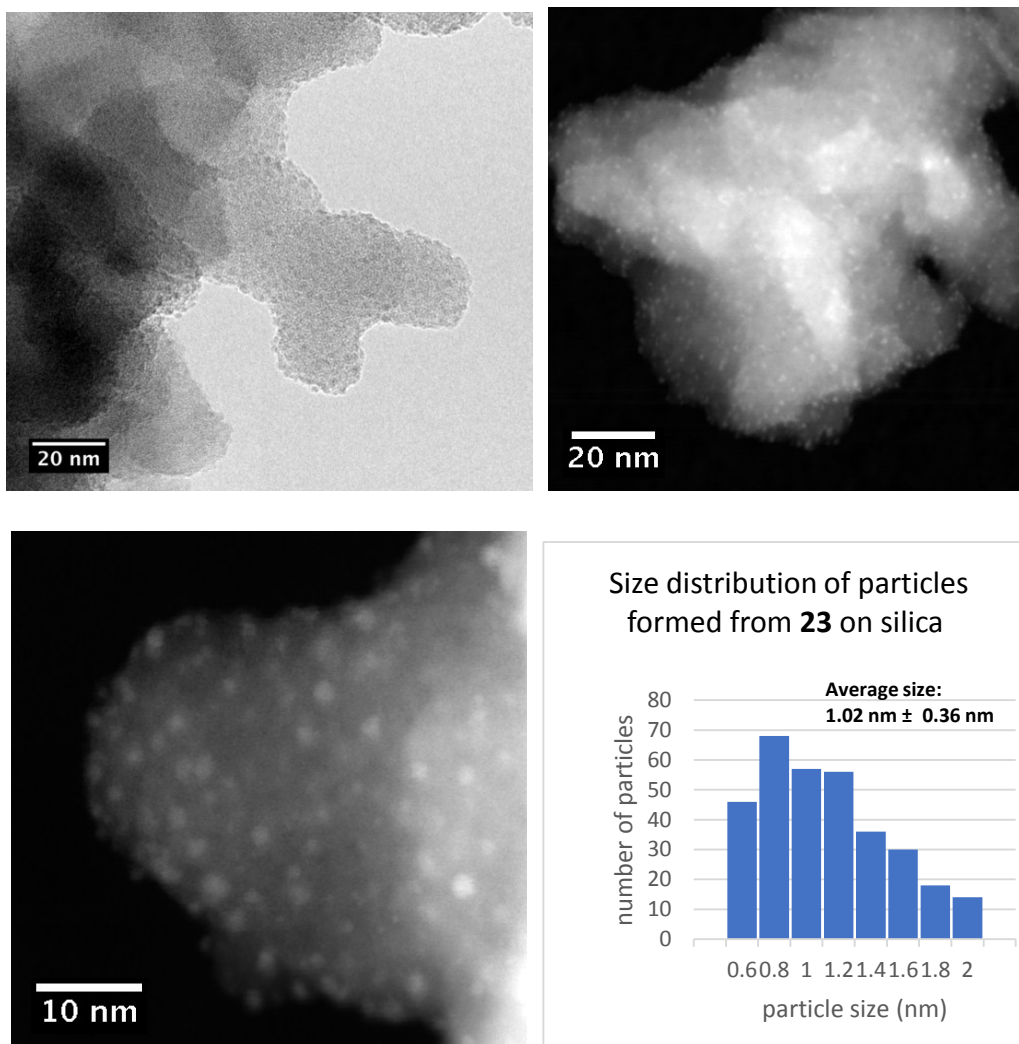
Figure **3.7** TEM micrographs and particle size distribution of solid that result from grafting **23** onto silica.

Energy dispersive X-ray spectroscopy (EDX) of the grafted Ni clusters from precatalyst **23** indicates the presence of nickel, nitrogen, and phosphorous in the immobilized phase (Figure **3.8**). The distribution of the Ni, P and N signals in the EDX map are very strongly correlated, tentatively suggesting some retention of the cluster integrity after grafting.
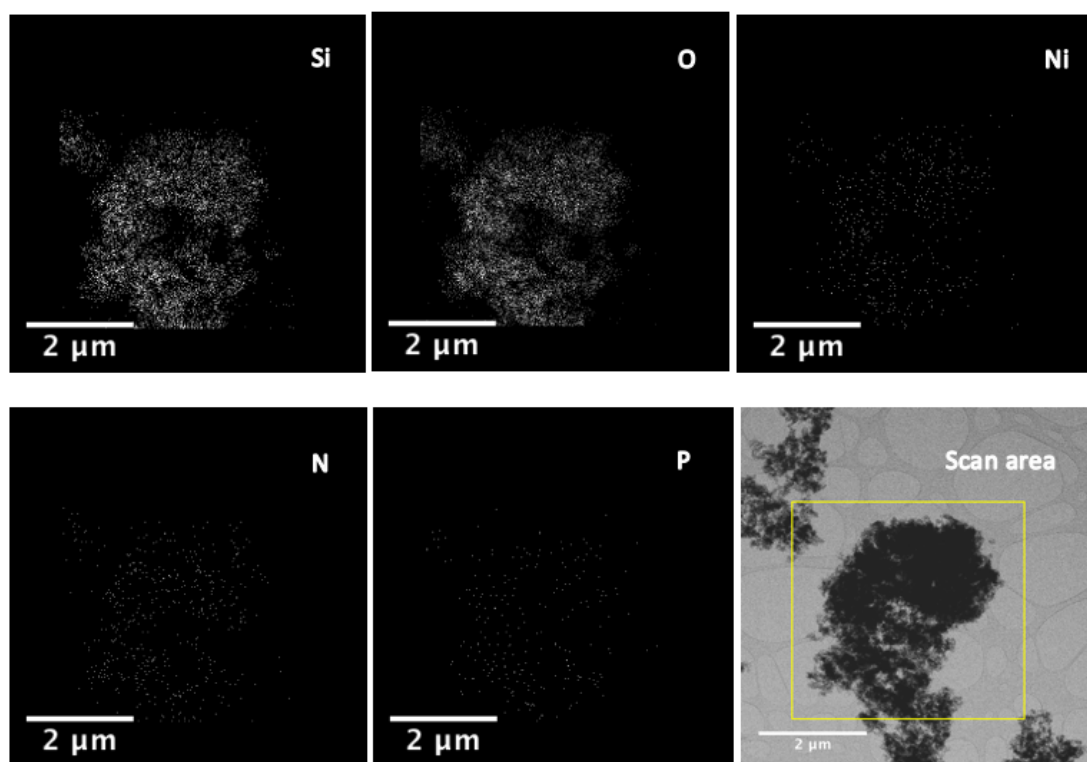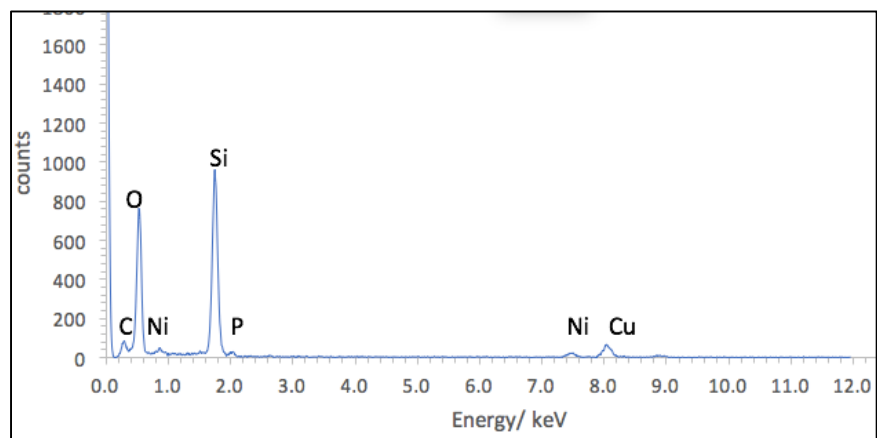
Figure **3.8** EDX spectrum and elemental distribution map of the for **23** grafted onto silica. Particles dispersed on carbon grid supported on a copper substrate.

3.2.4 Immobilized Ni clusters for catalytic hydrodesulfurization of dibenzothiophene

3.2.4.1 Optimization

Alumina-supported clusters **23** and **24** provide superior catalysts for hydrodesulfurization of DBT. Using stoichiometric KO^{t}Bu, the catalytic HDS provides biphenyl in excellent conversion and selectivity (entries 1, 2; Table **3.2**). No hydrogenation of the arene rings is detected (see GC-MS spectrum in appendix) and the reaction proceeds in toluene or THF which, *vide supra*, inhibited reactivity in the absence of an oxide support.

Table **3.2** HDS of DBT over supported Ni catalysts
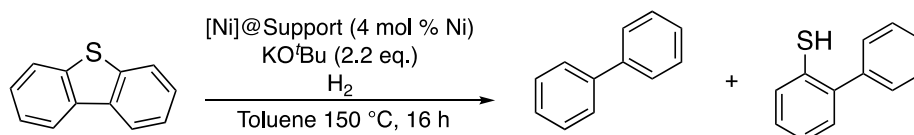
Entry	[Ni]	Support	% Conv.^{a,b}	Yield	
				BP ^{a}	BP-SH ^{a}
1^c	**23**	Al$_2$O$_3$ (basic)	97	91	0
2	**24**	Al$_2$O$_3$ (neutral)	94	87	1
3	**23**	SiO$_2$ (40 -63 µm)	95	84	1
4	**24**	SiO$_2$ (40 -63 µm)	91	81	5
5	**24**	SiO$_{2\ 700}$	93	90	3
6	**24**	SiO$_2$ (5-15 nm)	91	86	2

^{a}Determined by GC-FID analysis with dodecane as an internal standard. ^{b} Remaining material is DBT or, some conversion to an insoluble material is also observed.^{c}90% isolated yield.

The nature of the support does not have any appreciable effect on reactivity. Basic and neutral alumina, as well as silica of varying particle sizes, function similarly as supports (Table **3.2**). Appropriate control reactions confirm the oxide support is inert toward desulfurization, and

suggests that the role of the support is limited to immobilization and dispersion. However, the

Lewis acidic sites on alumina are not always inconsequential in reactions involving supported

catalysts.[228, 243-246] A high concentration of *tert*-butanol in our system has been shown

independently to suppress HDS. Lewis acidic sites on the support can promote catalytic

desulfurization by binding to and sequestering the alcohol as it is produced. Lewis acidic sites

are absent in silica, but alcoholysis of the strained siloxane bridges on the surface can fulfil a

similar function.[247]

Further optimization of the reaction conditions afforded higher rates of desulfurization and

shorter reaction times. Under optimized conditions, the immobilized Ni catalyst requires up to

16 h to approach full desulfurization. Reducing the reaction time without changing the reaction

conditions (Table **3.3**, Entry 1) yields mixtures of biphenyl and 2-phenylthiophenol, as expected.

The high yield of the thiophenol shows that, at least at 150 °C, sequential cleavage of the C–S

bonds occurs, primarily with dissociation of the intermediate 2-phenylthiophenol or its

potassium salt from the catalyst (Scheme **3.3**).
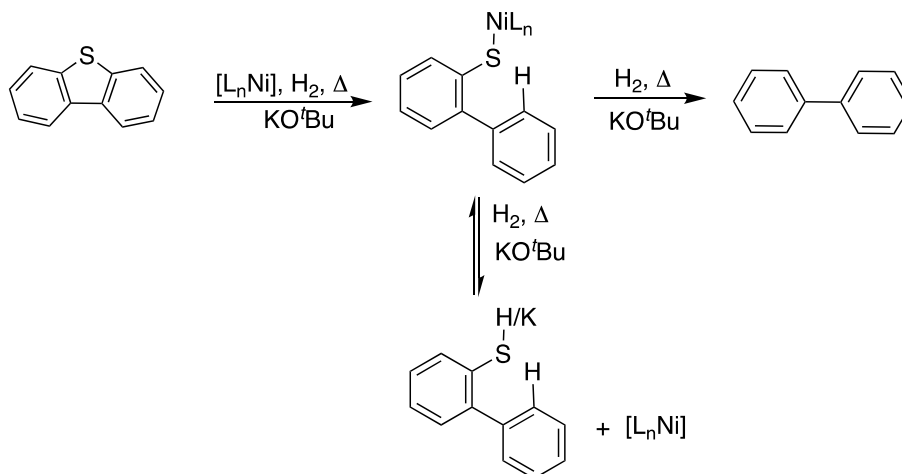
Scheme **3.3**

Predictably, greater conversions and increased selectivity to biphenyl are obtained at higher temperature and when using a higher KO^{t}Bu concentration (Entries 2, 3 Table **3.3**).); nearly quantitative desulfurization is obtained after 4 h. The dependence on KO^{t}Bu suggests that the base is involved either in the activation of the C–S bond or in the regeneration of the active catalysts (or both). The efficiency of the catalyst is maintained at lower hydrogen pressures (10-14 atm; entries 4-6) but a further increase in the reaction temperature to 200 °C was necessary to obtain a high yield of biphenyl under 10 atm. Further reduction of the hydrogen pressure to 1 atm of hydrogen unexpectedly maintained slow conversion of DBT to biphenyl (entry 7). *This represents a rare example of deep desulfurization at ambient pressure using hydrogen as the sole terminal reductant*.

Table **3.3** Optimization of DBT desulfurization in the presence of alumina- supported Ni clusters.
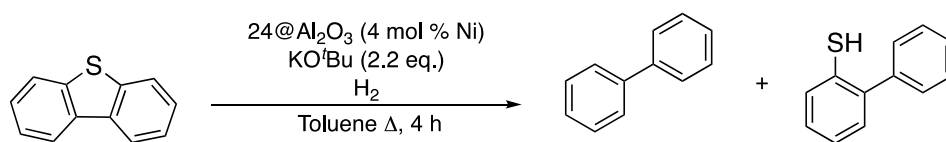
Entry	Time	Pressure	Temp.	% Conv.^{a,b}	Yield	
					BP ^{a}	BP-SH ^{a}
1	4	34	150	61	37	23
2	4	34	175	85	79	2
3^c	4	34	175	99	91	3
4	4	14	175	84	78	1
5	4	14	200	87	83	1
6	4	10	200	79	71	1
7	16	1	150	15	8	7

^{a}Determined by GC-FID analysis with dodecane as an internal standard. ^{b} Remaining material is DBT or, some conversion to an insoluble material is also observed. ^{c}4 equiv KO^{t}Bu.

3.2.4.2 Structural effects of nickel precatalysts

Although a range of nickel sources mediate desulfurization of DBT, the phosphornamide pre-catalysts and Ni(COD)$_2$ are the most efficient under the current conditions (Table **3.4**). The phosphoranimide precatalyst can be conveniently assembled from air and moisture stable salts, and immobilized *in situ* with relatively minor loss of activity (Entry 1, Table **3.4**). Phosphoran-imide-free heterogeneous catalysts prepared from NiBr$_2$ and KO^{t}Bu under hydrogen are also competent for dibenzothiophene HDS, albeit with marked decrease in desulfurization efficiency (Entries 2, 3). The use of NiCl$_2$ is even less efficient, presumably because of low solubility and a corresponding slow production and decomposition of the nickel alkoxide intermediate (Entry 4). Diphosphine-supported NiI$_2$ is also a poor precatalyst (entry 5), presumably due to the stabilization of the nickel precatalyst by the chelating ligand,[49-50] inhibiting decomposition to the Ni particles, which are the active catalyst under these conditions. Conversely, Ni(COD)$_2$ in the absence of a supporting ligand is an excellent precatalyst (entry 6). Although deliberate pre-grafting of Ni(COD)$_2$ onto the support was not explored in this work, the isolation of <5 nm NiO nanoparticles from the grafting of Ni(COD)$_2$ onto silica has been reported.[248] A similar process is believed to occur *in situ* under our grafting conditions.

Table **3.4** Effects of nickel precatalysts on the efficiency of HDS
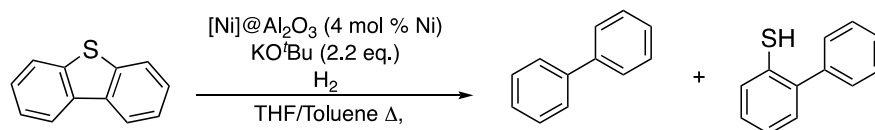
Entry	[Ni]	Time	Pressure	Temp.	% Conv.[a,b]	Yield BP[a]	BP-SH[a]
1	24[c]	16	34	150	93	64	22
2	NiBr$_2$(DME)	16	34	150	95	37	51
3	NiBr$_2$(DME)	4	10	200	66	63	1
4	NiCl$_2$	16	34	150	32	18	13
5	dppeNiI$_2$	16	34	150	4	2	2
6	Ni(COD)$_2$	16	34	150	94	77	8

[a]Determined by GC-FID analysis with dodecane as an internal standard. [b] Remaining material is DBT or, some conversion to an insoluble material is also observed. [c]24prepared in situ from mixing NiBr$_2$(dme) and KNPEt$_3$.

3.2.4.3 Stability of the supported Ni catalyst

While the recyclability of the alumina-supported Ni catalyst has not been assessed, preliminary analysis shows the catalyst continues to turn over after 16 h. The significant amounts of solids formed, as well as the quench and extraction process preclude isolation of the spent catalyst. In lieu of this, the catalyst was challenged with a higher loading of DBT and KO^{t}Bu, effectively reducing the catalyst loading to 1.3 mol%. After heating the mixture for 48 hours, over 80 % the DBT was converted to a mixture of biphenyl and 2-phenylthiophenol. Impaired mass transport, resulting from the precipitation of a copious volume of potassium salts compromises the later stages of the reaction, but clearly the catalyst remains active well beyond 50 C–S bond

cleavages. More insight into the stability and longevity of the supported catalyst will be gained using a continuous flow reactor design for HDS or larger batch reactor equipped with a sampling port.
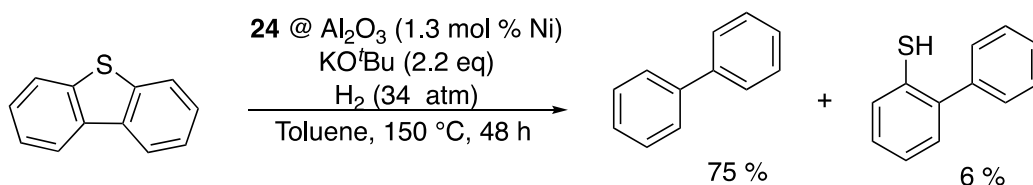
Equation **3.1**

3.2.5 Insights into the kinetics and mechanism of HDS at supported Ni clusters

3.2.5.1 Preliminary kinetic investigations

Rudimentary kinetic information was obtained through monitoring the conversion of DBT over time using parallel reactor runs. The initial consumption of the substrate is rapid; over 50% of the DBT is converted to biphenyl and the 2-phenylthiophenol within the first hour (Figure **3.9**). At 200 °C, the conversion of the 2-phenylthiophenol to the desulfurized hydrocarbon proceeds rapidly, and no buildup of this intermediate is observed. Once the concentration of DBT and alkoxide falls below 40% of the original value, the rate of conversion slows significantly.

Reaction Profile for DBT Desulfurization
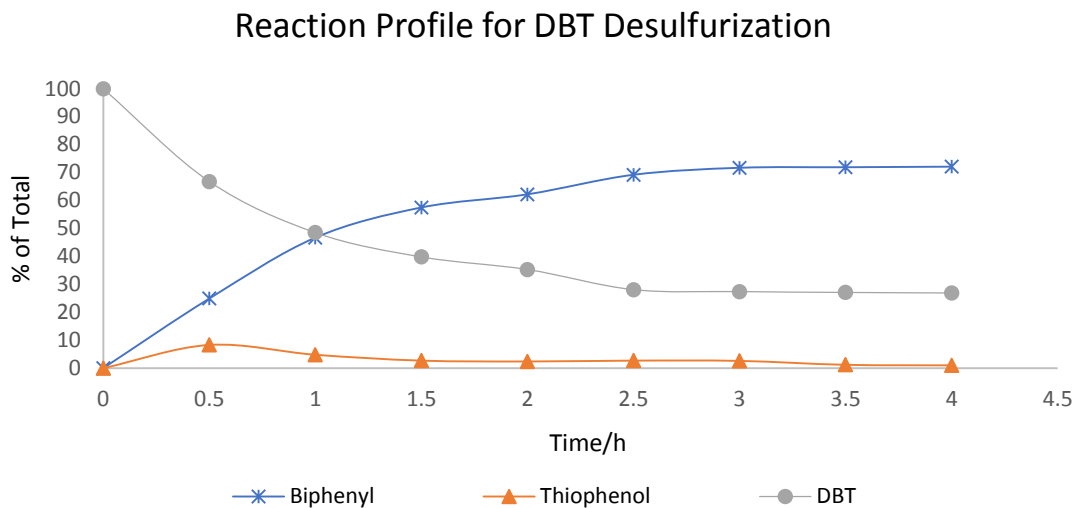
Figure **3.9** Conversion over 4h, of DBT to 4-phenylthiophenol and biphenyl at 200 °C and 14 atm (200 psi) of H_2 using 24@Al_2O_3 as the catalyst.

3.2.5.2 Preliminary proposed mechanism

At this point it is useful to construct a preliminary mechanistic pathway, to represent an idealized version of the HDS process, and to assist in appreciating the information which follows. **88** in Scheme **3.4** represents the nickel clusters, in a low-valent state on alumina. Oxidative addition of a C–S bond DBT forms **89**; a dative interaction between S and a second Ni atom is shown here. Hydrogenolysis of the Ni–C bond followed by a second C–S bond oxidative addition yields **91** featuring the fully desulfurized hydrocarbon. Once this biphenyl is liberated by hydrogenolysis the resting state of the catalyst **92** is apparent. From here, a reaction with KO^{t}Bu can regenerate the active catalyst. KO^{t}Bu thus serves as a stoichiometric scavenger for S, promoting the turn-over of the nickel catalysts. The proposal in Scheme **3.4** is grossly over simplified and the nuances of the reaction are more complex, particularly as it relates to the role of the base, as highlighted in the section that follows.
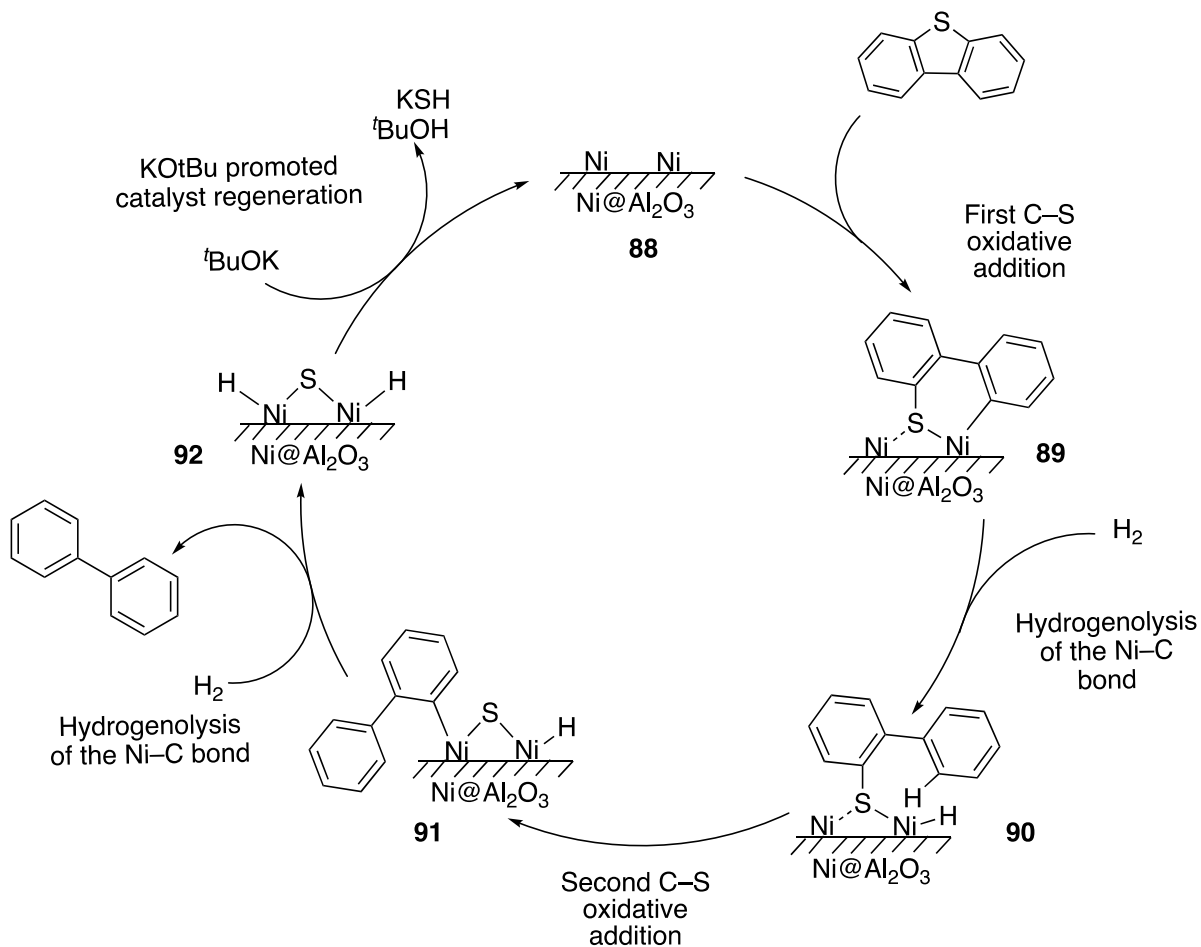
Scheme **3.4**

3.2.5.3 Isotopic substitution

Isotopic substitution clarifies some mechanistic features. Over one hour, the desulfurization of DBT proceeds to greater conversion in the presence of deuterium compared to hydrogen (Scheme **3.5**) This small, inverse isotope effect likely originates with a more facile transfer of deuterium from the weaker Ni–D bond to the stronger hydrocarbon C–D fragment, compared to the case for the Ni–H bond (bottom, Scheme **3.5**). Such inverse KIE's are often observed for the reductive elimination of C–H(D) fragments in organometallic complexes. [249-250] Based on the

mechanism in Scheme **3.4** the formation of the C–H bond is unlikely to be the rate limiting step; stoichiometric reactions in this work and by others[50-51, 121-122, 131, 136] (see chapter 2) all suggest that the extrusion of sulfur form the transition metal is the step with the most significant thermodynamic barrier. In such a case, the faster formation of KS–D vs KS–H from the hydrogenolysis of the Ni–S bond (Scheme **3.5**) may account for the small isotope effect observed.
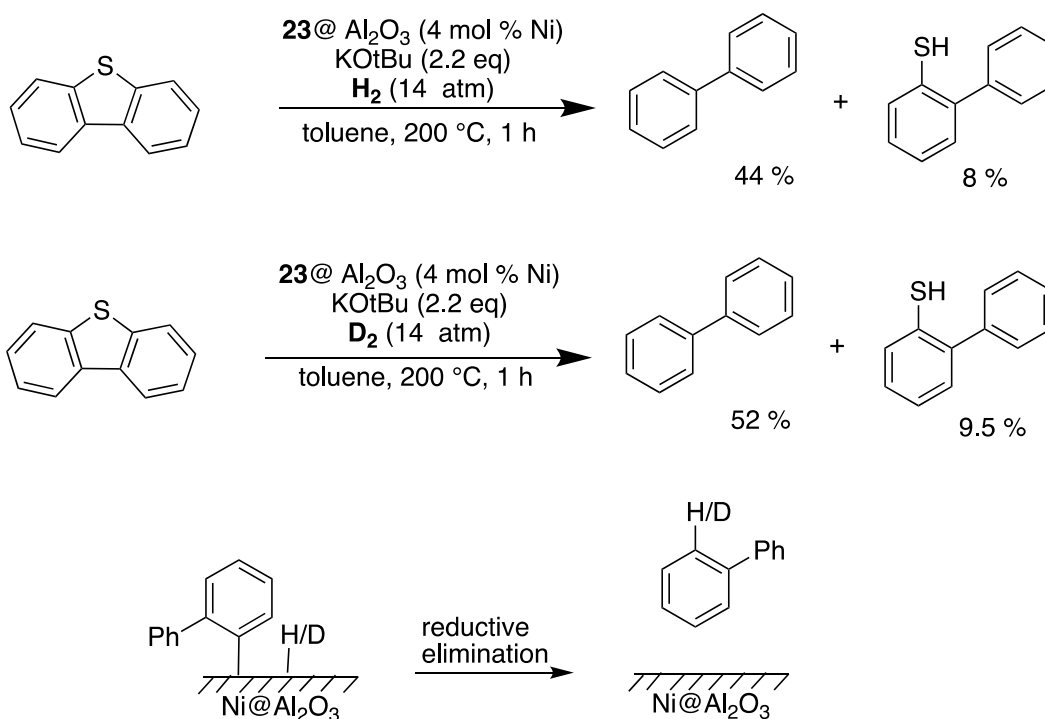
Scheme **3.5**

Analysis of the isolated biphenyl by ^{1}H and ^{2}H NMR spectroscopy confirms the role of hydrogen as the terminal reductant in the Ni-catalyzed HDS. Reactions conducted at 250 psi D_2 over 4 h led to 55% *d*-incorporation at the 2- and 2'-positions. This corresponds to quantitative

incorporation of deuterium in the positions previously bound to sulfur, further revealing that direct hydrogenolysis of the C–Ni bond is the terminal step in the desulfurization reaction (Equation **3.2**). The extra 5% deuterium incorporation is assigned to the product of acid/base exchange involving KO^{t}Bu and D$_2$. Reversible arene deprotonation involving KO^{t}Bu and hydrogen/deuterium is facile at *all* positions of DBT and biphenyl, as shown by extensive H/D exchange at the 3-, 3'- and 4-positions of the recovered biphenyl (Equation **3.2**). This experiment alone does not reveal whether H/D exchange occurs before or after the cleavage of the C–S bond, or whether this process has any implications for the overall mechanism of desulfurization.
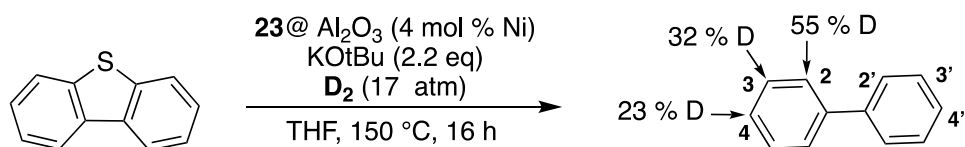
Equation **3.2**

3.2.5.4 Importance of arene deprotonation in the HDS reaction

In the absence of catalyst, KO^{t}Bu alone mediates significant C–H activation, (deuterium incorporation is obtained at all ring positions of DBT), but does not lead to detectable C–S bond cleavage. Quantitative exchange at the more acidic *ortho*-C-H bonds[251] (*top*, Scheme **3.6**) is observed. Similar transition metal-free C–H activation of dibenzothiophene and other aromatic compounds by KO^{t}Bu is well-established and is used widely for the functionalization of arene rings.[172, 252-254] The mechanism of this H/D exchange involves deprotonation the aromatic C–H

bond followed by the quenching of the aryl potassium intermediate with deuterium. This is reminiscent of classic *ortho*-lithiation procedure which forms part of the standard methodology for the preparation of 4-subsitituted and 4,6-disubstituted dibenzothiophenes.[255-259]
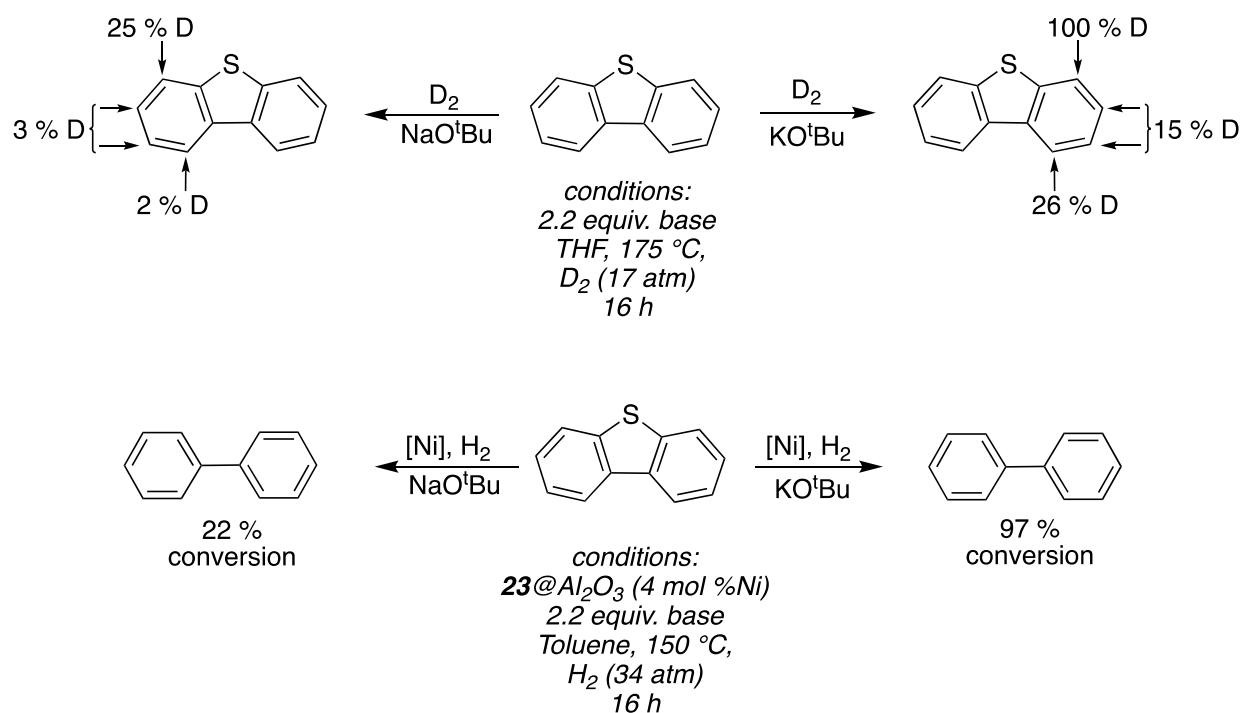
Scheme **3.6**

The strong correlation between the rate of desulfurization and the efficiency of H/D exchange, however, raises the question of whether there is a connection between *ortho*-deprotonation and the C–S bond activation. Considerably slower H/D exchange is observed using NaO^{t}Bu instead of KO^{t}Bu (*top left*, Scheme **3.6**), reflecting the significantly stronger basicity of potassium alkoxides in low polarity media.[260] This mirrors the hydrodesulfurization reactivity in the presence of the Ni catalyst (*bottom left*, Scheme **3.6**). Efficient desulfurization is only observed in the presence of a base that mediates extensive H/D exchange at the *ortho*

positons, suggesting that the deprotonation event is essential for cleavage of the C–S bond. The role of the alkali metal ion in this process is discussed in more detail below.

There is a clear relationship between the pKa of the basic promoter and the extent of hydrodesulfurization. Potassium alkoxides of lower pKa than KO^{t}Bu are less effective (Table **3.5**). While the use of KO^{t}Bu affords near stoichiometric conversion of DBT, only 25% and 17% conversion are observed in the presence of KO^{i}Pr and KOMe, respectively (entries 1-3). Less basic, poorly soluble KOH returns only stoichiometric desulfurization (entry 4).

Table **3.5** Effect of base strength HDS using supported Ni catalysts

Entry	Base	% Conv.^{a,b}	Selectivity	
			BP ^{a}	BP-SH ^{a}
1	KO^{t}Bu	97	100	0
2	KO^{i}Pr	27	42	58
3	KOMe	17	53	47
4	KOH	4	50	50

^{a}Determined by GC-FID analysis with dodecane as an internal standard. ^{b} Remaining material is DBT or, some conversion to an insoluble material is also observed

It is conceivable that *ortho*-deprotonation leads to C–S bond cleavage. Similar to the mechanism suggested for the reaction of KH and DBT (Chapter 2), the intermediacy of an aryne is posited. Deprotonation by KO^{t}Bu, followed by C–S bond cleavage furnishes the aryne (**72**, Scheme **3.7**) which, in the absence of the transition metal, rapidly reverts to the starting

material (Scheme **3.7**). In the presence of the transition metal, the aryne intermediate **72** can be diverted by coordination nickel,[261-263] and hydrogenated to the corresponding arene **74**. At this stage, 2-phenylthiphenol is obtained on acidic work up. A second iteration effectively desulfurizes the organic fragment yielding biphenyl.
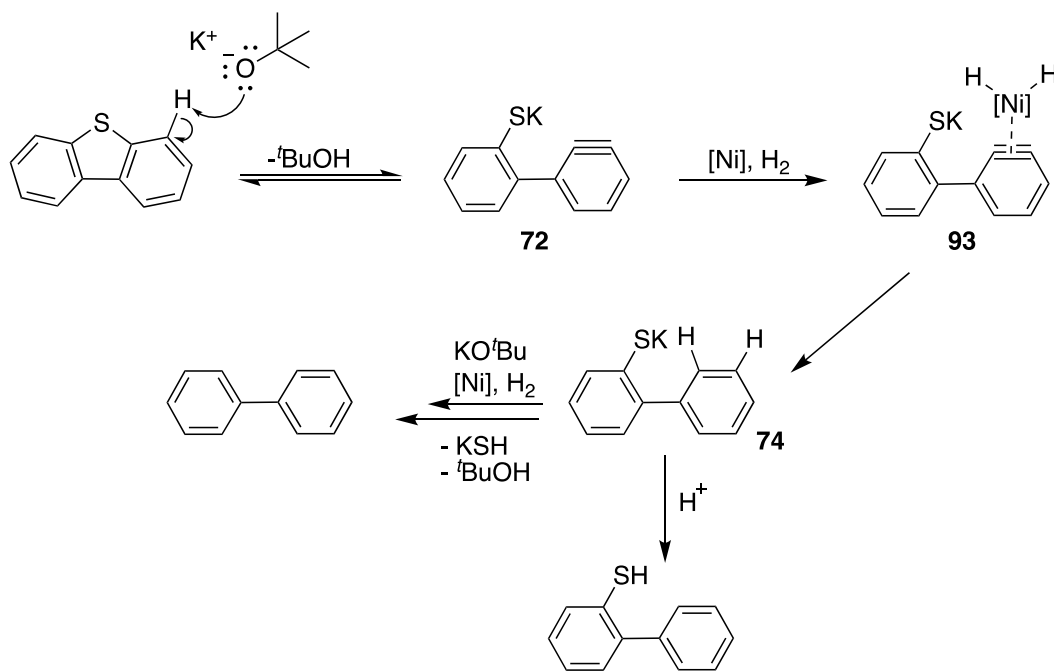
Scheme **3.7**

This hypothesis, is challenged however, by the deuterium incorporation experiments. Hydrogenation of the aryne intermediate **72** according to the mechanism in Scheme **3.7** requires at least 50% deuterium incorporation at the 2,2'- and 3,3'-positions of biphenyl. While this is true at the 2,2'-positions, significantly less than 50 % deuterium appears on the neighboring carbon (Scheme **3.8**).
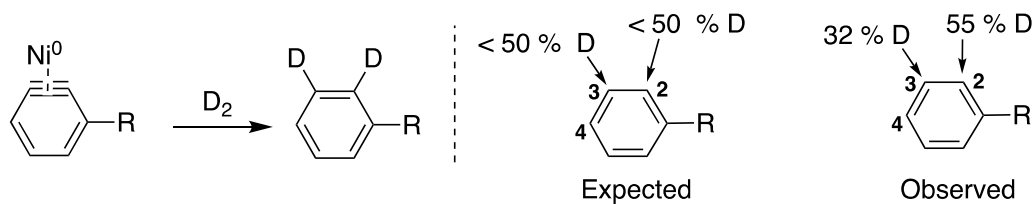
Scheme **3.8**

To probe further the mechanistic connection between the C–S bond cleavage and the deprotonation at the 4- or 6-positions, the relative rates of hydrodesulfurization of unlabeled DBT and 4,6-dideuterio-DBT were compared (Scheme **3.9**). Within experimental error, *no kinetic isotope effect* is observed. While this does not unambiguously exclude reversible ortho-deprotonation as a step in the overall mechanism of alkoxide-promoted catalytic HDS, this process clearly does not control the rate of the desulfurization reaction.
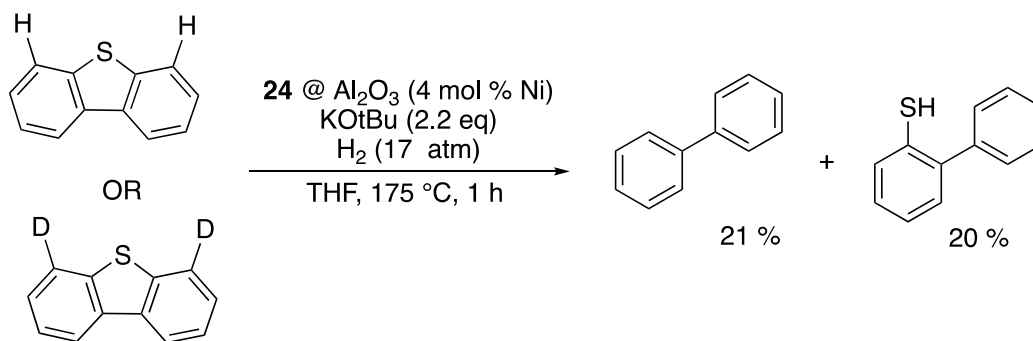
Scheme **3.9**

3.2.5.5 Role of cation-π interactions in the HDS reaction

The identity of the stoichiometric cation in hydrodesulfurization has a profound impact on the rate. As function of the element, hydrodesulfurization rates correlate with the enthalpies of metal-heteroarene π-coordination observed for small cations in solvated systems (Li < Na < K, entries 1-3, Table **3.6**).[151, 264] This trend is reversed for larger cations, however (K > Rb > Cs, entries 3-5).   Cation-π interactions in the gas phase are predicted to follow the order Li > Na > K > Ru > Cs based on the progressively higher charge density for smaller cations, which gives rise to stronger electrostatic interactions with arene.[149] However, in polar solvents, the enthalpic penalty associated with desolvation of the smaller cations is greater than the stabilization afforded by the cation-π interaction,[146-147, 150-151] leading to a reversal of the trend in the strength of π-interactions to K > Na > Li. The use of toluene ensures that the reaction occurs in a relatively non-polar media. Despite this, small clusters of the alkali metal alkoxides[265-266] may mimic solvation effects, i.e., the energy penalty associated with the de-aggregation of the alkoxide is large compared to the enthalpy of the cation-π interaction. The larger K^+ ion, which more readily disaggregates, has the strongest π-binding affinity and, clearly, accelerates the rate of desulfurization.

Using this reasoning, the cesium and rubidium *tert*-butoxide might be expected to be even more efficient promoters, opposite to the observed trend, K > Rb > Cs. This reversal can be partly attributed to the similarities in the desolvation/disaggregation enthalpies of these large cations, so that the strength of the resulting cation-π interaction is largely determined by the charge density, leading to K^+ showing the strongest π-arene interaction.[146]

Table 3.6 Effects of alkali metal cation on HDS of DBT using supported Ni catalysts
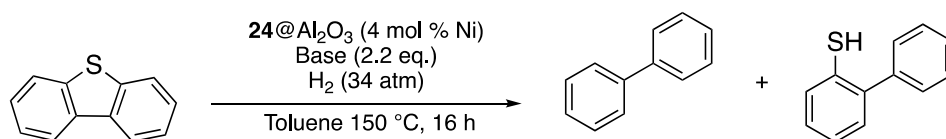
| Entry | Base | % Conv. [a,b] | Selectivity | |
			BP [a]	BP-SH [a]
1	LiO^{t}Bu	5	75	25
2	NaO^{t}Bu	22	100	0
3	KO^{t}Bu	97	100	0
4	RbO^{t}Bu	92	44	56
5	CsO^{t}Bu	55	17	83

[a]Determined by GC-FID analysis with dodecane as an internal standard. [b] Remaining material is DBT or, some conversion to an insoluble material is also observed

Although the potassium effect is pronounced, the precise role binding plays in activating the C–S bond is not clear. One hypothesis is that K$^+$ binding to DBT increases the acidity of the C–H bonds in the resulting cation-π complex. This specific K$^+$ cation-π interaction has been recently invoked as an activating pathway in the dehydrogenative silylation of alkyl indoles catalyzed by KO^{t}Bu (Scheme **3.10**).[151] Alternatively, the cation-π complex may equally activate the C–S bond towards oxidative cleavage by low valent Ni. Further investigations are ongoing.
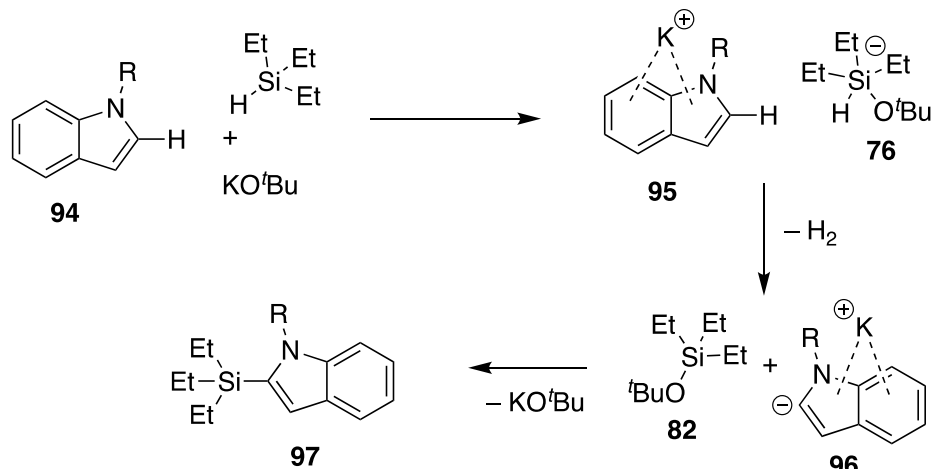
Scheme **3.10** K$^+$ cation π interaction in the KO^{t}Bu catalyzed silylation of alkyl indoles[151]

3.2.5.6 Proposed mechanistic pathways for catalyzed desulfurization

At this point some key elementary steps have emerged from these initial investigation, which taken together, at least partially describe a more plausible mechanism of catalytic desulfurization of DBT using KO^{t}Bu. The key points revealed so far:

1. Hydrogen is the terminal reductant in the hydrogenolysis of C–Ni bonds.

2. Facile *ortho*-deprotonation of DBT precedes C–S bond cleavage, but does not appear to affect the rate of HDS.

3. An aryne intermediate may be involved.

4. Potassium ions coordinating to the DBT affects the acidity of arene C–H bonds and the strength of C–S bonds.

5. KO^{t}Bu may be involved in the turnover of the spent catalyst.

A comprehensive mechanistic picture based on these elementary steps begins with the initial coordination of K$^+$ ions to the π-system DBT and reversible deprotonation of this the cation-π complex by the ^{t}BuO$^-$ (**98**, **99**, Scheme **3.11**). From here two divergent reaction pathways emerge.

In **Pathway A** (Scheme 3.**11**), iterative *ortho*-deprotonation/aryne trapping of **98** affords cleavage of both C–S bonds, generating aryne intermediates **100** and **102**, which are intercepted and hydrogenated by the Ni catalysts. In this pathway, the sulfur atoms form only dative interactions with Ni, and the K$^+$ ions interact with and stabilize a negative charge on the sulfur after C–S bond cleavage. Cation-π interactions are maintained throughout the cycle to reflect the increased acidity of the of all the C–H bonds, as well as any stabilization of the aryne intermediates **100** and **102** by K$^+$ binding. The sulfur atom is finally extruded as K$_2$S. *No transition metal sulfide is involved* and H$_2$S is never generated. The lack of formal Ni–S bonds readily accounts for the ease of regeneration of the active catalyst. In the absence of a sufficient strongly basic K$^+$ salt, the desulfurization cannot be rendered catalytic.
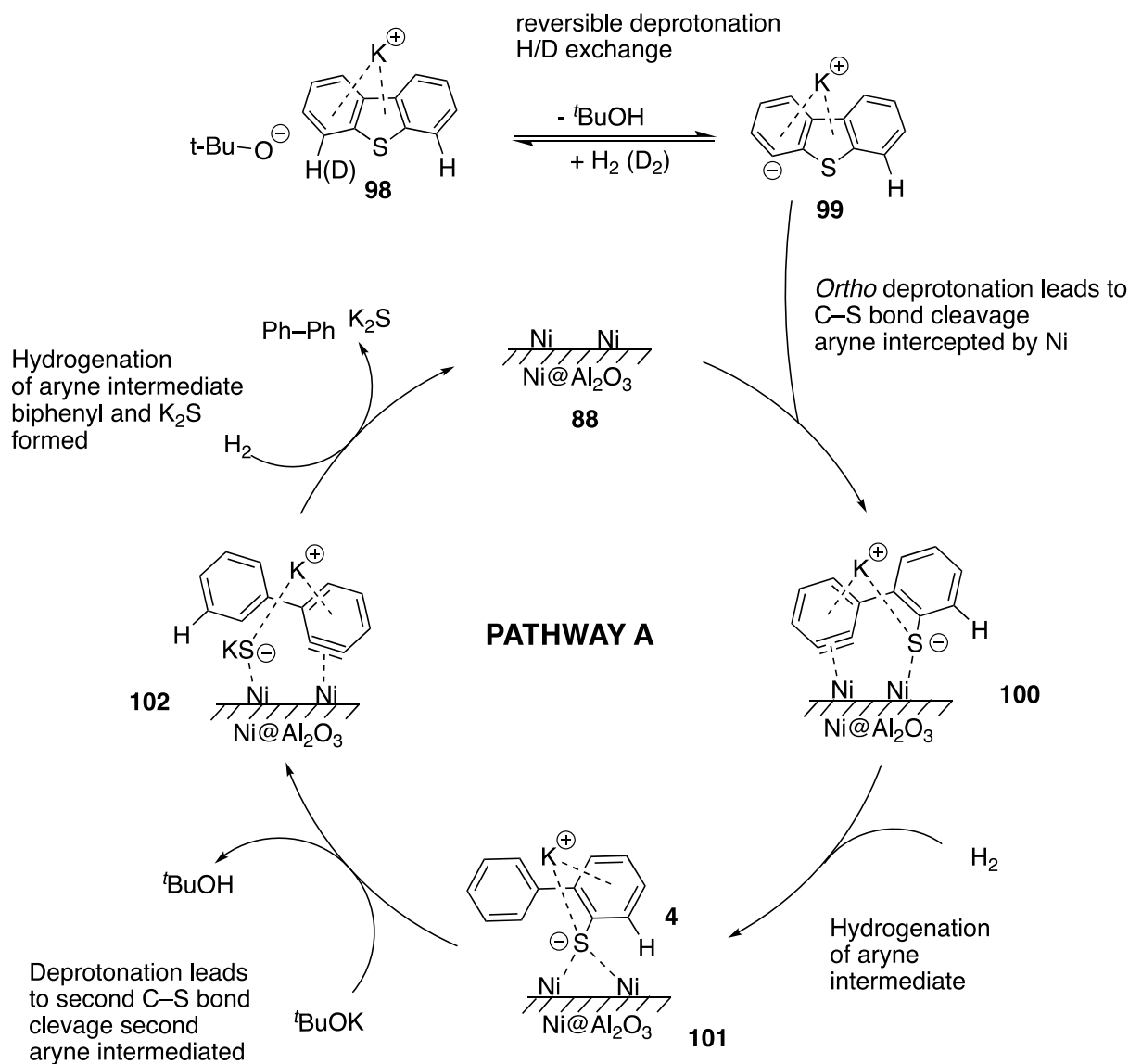
Scheme **3.11**

Pathway **B** (Scheme **3.12**) similarly relies on persistent cation-π interactions. In this proposal, the interaction can be viewed as weakening the C–S bond in **98**, leading to facile oxidative addition at the Ni surface. For simplicity, the oxidative addition can be represented as a mono-metallic process, with only dative interactions of the S with a neighboring Ni atom (e.g., **103**). Nonetheless, a bimetallic oxidative addition is equally possible. One Ni centre in **103** is formally

Ni(II), making a second oxidative addition unlikely; instead, we propose that a σ−bond metathesis pathway is more likely, forming new C–H and Ni–H bonds simultaneously (**104**). Conversely, cooperative bimetallic oxidative addition from **98** affords two adjacent Ni(I) centers (**105**), which can activate H_2 to form organometallic Ni(II) hydride **106**. This series of bimetallic single-electron reactions, instead of a monometallic two-electron process, is a hallmark of Ni catalysis.[17]

In intermediate **104**, the sulfur is formally bound to one Ni atom, but participates in a further dative interaction with another. The combination of the Ni/S dative interaction and activation provided by K^+ cation-π interaction is sufficient to promote the second C–S oxidative cleavage, formally desulfurizing the hydrocarbon fragment. Bimetallic reductive elimination or hydrogenolysis by σ−bond metathesis liberates biphenyl, leaving behind the sulfided Ni cluster **108**.

To regenerate the active catalyst, an equivalent of the KO^{t}Bu is required to displace one of the Ni–S bonds, forming the nickel alkoxide and a Ni–S–K linkage (**109** Scheme **3.12**). The binding of K^+ to the sulfur anion arguably weakens the Ni–S bond, accelerating the hydrogenative extrusion of the sulfur from the metal; in this pathway, sulfur is extruded exclusively as KSH.

Scheme **3.12**

Bianchini and co-workers previously documented a similar role for KO^{t}Bu in the catalytic hydrogenolysis of benzothiophene using a triphos ruthenium complex.[267] In that study, the presence of excess KO^{t}Bu accelerated the cleavage of a Ru–S bond to regenerate the active catalyst (Equation **3.3**).

120
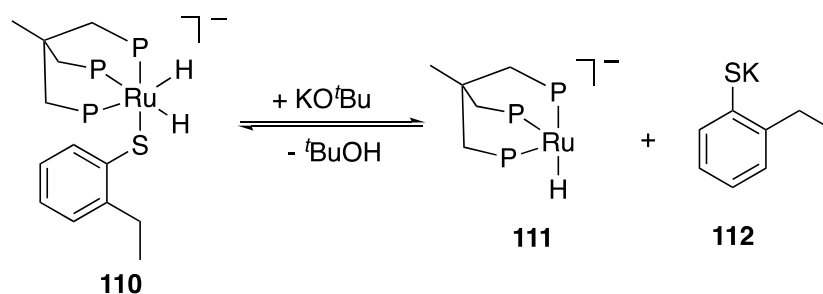
Equation **3.3** KO^{t}Bu promoted dissociation of Ru–S bonds

3.2.5.7 Interactions with the catalyst support – mechanistic implications

The role of the alumina is almost certainly not limited to that of an inert support for the catalyst. Scavenging of *tert*-butyl alcohol by the Lewis acidic sites on the surface of alumina is suspected. Remarkably, the Lewis acidic aluminum sites act cooperatively with the basic O atoms in Al–O–Al bridges to activate methane, producing new Al–CH$_3$ and –OH groups on the surface.[228, 243, 245] Similar surface-assisted C–H activation of DBT may account for some of the enhancement in HDS activity observed using alumina-supported Ni catalysts. Separately, the sulfur lone pair in DBT can coordinate to a proximal Lewis acidic site. This lowers the activation energy for an oxidative cleavage by Ni(0).

3.2.6 Substrate scope – a brief excursion

4,6-Dialkyldibenzothiophenes represent the most challenging organosulfur molecules for conventional hydrotreatment processes, constituting the majority of the remaining organosulfur compounds in ultra-low sulfur fuels. Other researchers in the Stryker group have reported some success in catalytic desulfurization of 4,6-dimethyl and 4,6-diethyl DBT using Co or Ni catalysts in the presence of KH.[77, 143] When KO^{t}Bu is used under standard conditions,

however, no desulfurization of 4,6-dimethyl-DBT is observed. Instead, only H/D exchange at the substituent methyl groups is returned under deuterium pressure, presumably from reversible deprotonation of the benzylic bonds (Scheme **3.13**).
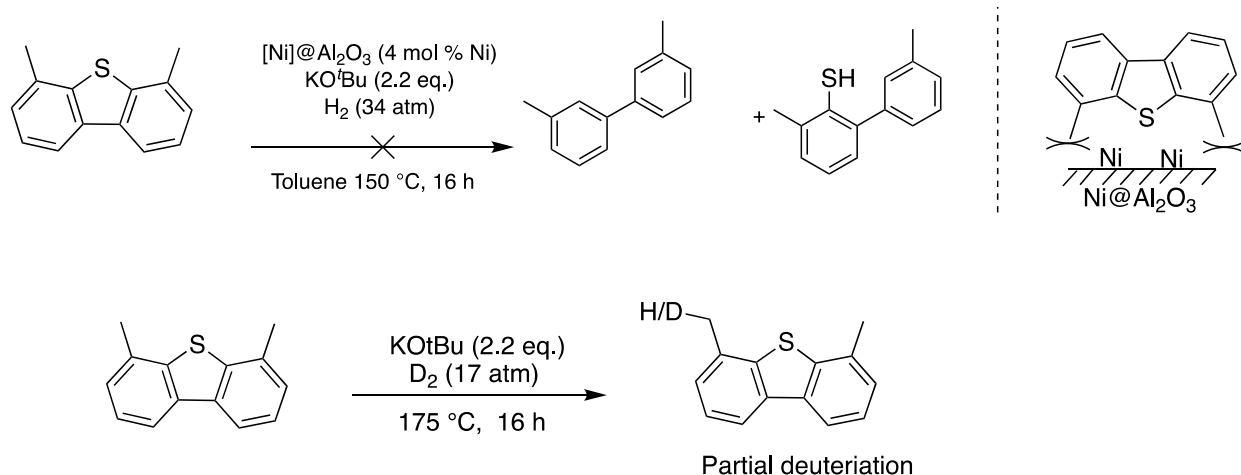
Scheme **3.13** Attempted HDS and H/D exchange in 4,6-dimethyldibenzothiophene.

The absence of the C–S bond cleavage potentially reaffirms the connection between *ortho*-deprotonation and desulfurization of DBT. With the 4- and 6-positions blocked by methyl substituents, this mechanistic pathway becomes unavailable. Conventional HDS pathways, involving oxidative addition at surface active sites, are known to be inhibited by steric effects.

Surprisingly, several other organosulfur compounds are not efficiently desulfurized by the KO^{t}Bu/supported Ni system (Table **3.7**). This contrasts with the facile desulfurization of similar compounds in the presence of KH.[63, 77, 143] Similarly, industrial hydrotreatment catalysts convert simple thiophenic compounds and thioethers to hydrocarbons under less forceful conditions.

Using the KO^{t}Bu/Ni@Al$_2$O$_3$ system, only minimal conversion of 3-hexylthiophene **113** is recorded. The absence of extended π-system for activation by cation-π complex formation can rationalize this reactivity, as can catalyst inhibition by strongly nucleophilic sulfur σ-coordination. The more conjugated benzothiophene **114** (entry 2, Table **3.7**) reacts at a slightly higher rate, but the ring opened thiol dominates the product distribution **114a**, instead of ethylbenzene **114b**.

Although the first C–S bond cleavage proceeds efficiently for simple thioethers and disulfides, complete desulfurization is observed only for thioanisole **115** (entries 1-4, Table **3.7**). Gas phase analysis of this reaction was not conducted; methanethiol may be produced as a primary product. The weaker benzylic C$_{sp3}$–S bond in benzyl phenyl sulfide **116** is cleaved preferentially (entry 4). Similarly, the weak S–S bond of p-tolyl disulfide **117** is readily cleaved under the reaction conditions, but subsequent desulfurization of the 4-methylthiophenol **117a** is very inefficient (entry 5).

Table **3.7** Desulfurization of organosulfur molecules in using the KO^{t}Bu/Ni@Al$_2$O$_3$ system

Entry	Substrate	% Conv.[a]	Product distribution [a]		
1	**113**	7 %	**113a** Hex > 99 %	**113b** Hex trace	
2	**114**	68 %	SH **114a** 81 %	**114b** 19 %	
3	**115**	79 %	SH **115a** trace	**115b** > 99 %	
4	**116**	100 %	SH **116a** 50 %	**116b** 50 %	
5	**117**	77%	SH **117a** 96 %	**117b** 4 %	
6	**118**	67%	SH **118a** 13 %	O **118b** 67 %	**115b** 20 %
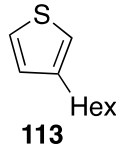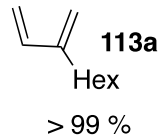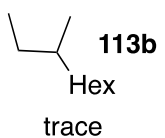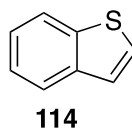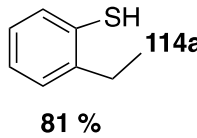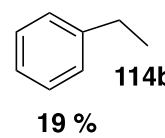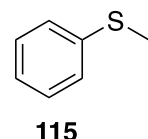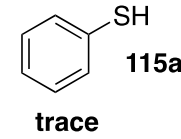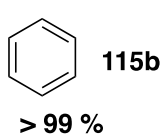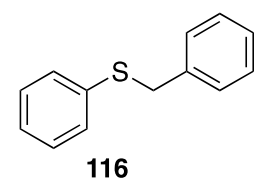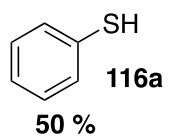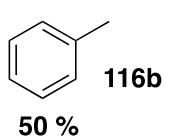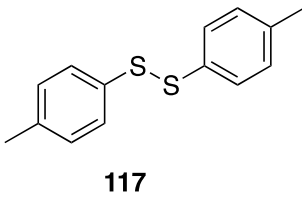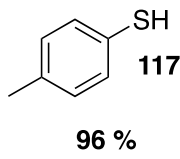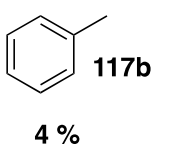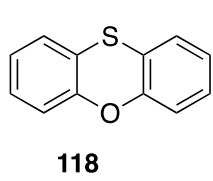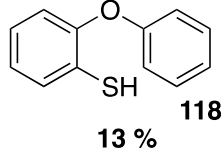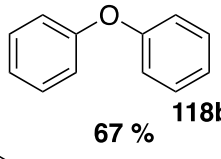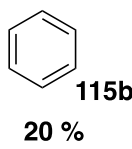
Reaction conditions: 175 °C and 14 atm (200 psi) of H$_2$ using 24@Al$_2$O$_3$ as the catalyst. [a]Conversion and selectivity determined by GCMS analysis.

Only phenoxathiin **118**, which has an extended π-system, is substantially desulfurized under these reaction conditions, giving diphenyl ether **118b** as the major product (entry 6). The presence of benzene in the product mixture results from the activation of both the C–S as well as the C–O bonds indicates that the under appropriate conditions, the Ni/Al$_2$O$_3$/KO^{t}Bu can catalyst can challenge the activation of aryl ethers, a process relevant to biomass valorization.[31, 268]

The current Ni/ KO^{t}Bu protocol may find a niche as a complementary tool to traditional hydrotreatment protocols. Crude petroleum feeds can be desulfurized initially with CoMoS type catalysts. Once a low sulfur feed is obtained, the KO^{t}Bu/Ni could be deployed in secondary desulfurization reactor, to remove dibenzothiophene from the feed. However further optimization is required to achieve catalytic ultra-deep desulfurization using this system.

3.2.7 Alternative K$^+$ salts for HDS

The lower cost and wider availability potassium sulfide and potassium hydroxide, as well as promising technologies for recycling have made these reagents more attractive as stoichiometric additives for desulfurization of dibenzothiophenes (Scheme **3.14**). Initially disclosed over four decades ago, the utility of K$_2$S and KOH has been demonstrated for heavy petroleum processing,[157, 163] but the *uncatalyzed reaction requires prohibitively high temperatures and hydrogen pressures*.

$$R \overset{S}{\diagdown} R \xrightarrow[< 150 \text{ atm } H_2, \; < 480 \; °C]{K_2S \text{ or KOH}} RH + KSH + H_2O$$

$$2 \; Cu^0 + KSH + H_2O \xrightarrow{\Delta} Cu_2S + KOH + H_2 \; \textbf{Regeneration of KOH}$$
$$\overset{\longleftarrow}{\underset{H_2, \; \Delta}{}}$$

$$KSH + KOH \xrightarrow[- H_2O]{\Delta} K_2S \qquad \textbf{Regeneration of } \mathbf{K_2S}$$

Scheme **3.14** Desulfurization under aggressive conditions using recyclable K^+ salts

Potassium hydroxide is inert towards dibenzothiophene HDS under the conditions used in this study. Surprisingly, however, K_2S-mediated desulfurization of DBT is energetically accessible using supported nickel catalysts (entries 1, 2; Table **3.8**). Potassium sulfide has a sufficiently high pKa (ca. 17 in water)[269] that it can behave as a Brønsted base and shows reactivity similar to KO^{t}Bu. The reaction mechanism is presumably similar to that proposed for the alkoxide, producing KSH as the byproduct. The potassium ion effect is readily apparent in the K_2S-promoted desulfurization; Li_2S and Na_2S are completely ineffective (entries 1, 2; Table **3.8**). The influence of cation-π interactions again accounts for the observed reactivity. Optimization of reaction conditions remains in progress, as is further investigation into the mechanism of potassium-promoted hydrogenolysis of nickel sulfide to regenerate the catalyst.

Table **3.8.** Alkali metal sulfide promoted HDS
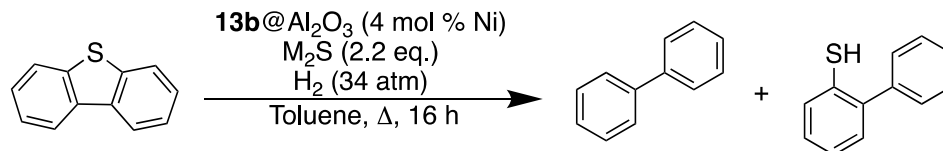
Entry	M$_2$S	Temp (°C)	% BP^a	% BP-SH^a
1	K$_2$S	175	42	1
2	K$_2$S	200	83	0.5
3	Na$_2$S	175	1	1
4	Li$_2$S	175	1	0

^{a}Determined by GC-FID analysis with dodecane as an internal standard.

3.3 Conclusion

Nickel phosphoranimide clusters immobilized on high surface area alumina and silica supports afford more active catalysts for hydrodesulfurization than the use of unsupported precatalysts. Grafting of small Ni clusters onto the support is traced using IR spectroscopy and characterized by S/TEM imaging and EDX analysis. The improved reactivity is, we propose, due to the increased dispersion and stability of the Ni nanoparticles on the surface of the support. Under optimized conditions, near quantitative desulfurization of DBT at hydrogen pressures as low as 10 atm is observed after reaction times of 4 hours. The limited substrate scope is discouraging; significant improvement in catalyst generality is necessary.

A complete mechanistic rationale for the catalyzed desulfurization of DBT has not been ascertained. Several key elementary steps have been proposed, of which K$^+$ cation-π association appears essential; the importance of directed *ortho*-deprotonation by a strong base

is less clear. While the direct involvement of a Ni–S bond during HDS remains unknown, the formation and hydrogenolysis of a Ni–C bond is involved in the overall desulfurization pathway. Unlike catalyzed reactions using KH, hydrogen is the sole reducing agent in the KO^{t}Bu/Ni desulfurization protocol. The stoichiometric alkoxide can be replaced by other, readily recyclable bases, such as K_2S.

4. A copper/molecular sieves system for catalytic deoxygenation of aryl ketones

4.1 Introduction and background

4.1.1 Classical Methods for the deoxygenation of carbonyl compounds

The reductive deoxygenation of carbonyl compounds is useful in synthetic chemistry and in the processing of biomass-derived oxygenates into fuels.[270-272] The classical methods for the conversion of carbonyl groups methylene units include the Clemmeson[273-274] and Wolff-Kishner[275-276] reductions, developed over a century ago (Scheme **4.1**). However, these methods require harsh acidic or basic conditions, and stoichiometric quantities of toxic reagents; they are poorly suited for modern, large scale processes. Using main-group metal hydrides[277-281] or the Monzingo thioketal reduction[282-283] allows milder, safer, reaction conditions, but the chemoselectivity and atom economy of these methods is poor (Scheme **4.1**).

Zn (Hg), HCl, Δ	H$_2$NNH$_2$, KOH, Δ	SH SH Raney Ni, H$_2$	NaBH$_4$, RCOOH
Clemmensen	Wolff-Kishner	Monzingo (thioketal)	
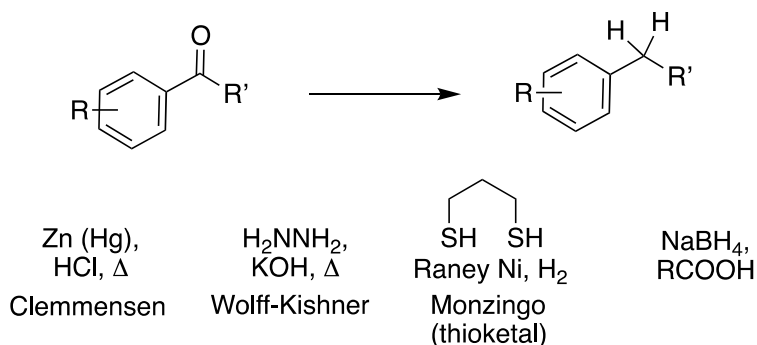
Scheme **4.1**

4.1.2 Deoxygenation of carbonyl compounds by hydrosilanes

Hydrosilanes are more attractive reducing agents; they efficiently and selectively deoxygenate carbonyl compounds under mild conditions in the presence of transition metals or Lewis acid catalyst (Equation **4.1**).[284-293] Moreover, silanes are widely available, relatively inexpensive, and environmentally benign; some, such as polymethylhydrosiloxane (PMHS), demonstrate serviceable tolerance to air and moisture.[294] Palladium and other precious metal catalyst are commonly used in deoxygenative hydrosilylation,[289-293] but several first row metal catalysts are known, including Ni and Co phosphoranimide complexes developed in the Stryker group. [63-64, 295]

R, R' = H, aryl, alkyl
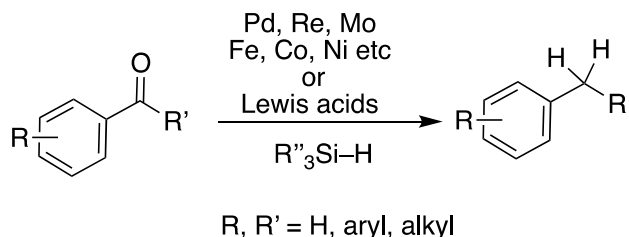
Equation **4.1**

4.1.3 Deoxygenation using hydrogen as the terminal reductant

Molecular hydrogen is the ideal and most atom economical reducing agent for deoxygenation reactions, generating only water as a by-product. However, greater bond strength in the H$_2$ molecule means substantially reduced reactivity compared to silanes and other hydride reagents.[296] The hydrogenation of carbonyl compounds to alcohols is common,[15, 297-300] but the more challenging hydrogenolysis of the C–O bond elicits fewer reports. Of the few examples of

catalytic deoxygenation, heterogeneous precious metal catalysts feature prominently.[98-99, 301-306] These noble metal catalysts, with few exceptions,[98] also hydrogenate the aromatic rings of aryl ketones/aldehydes, leading to complex mixtures of undesired products. (Scheme **4.2**).
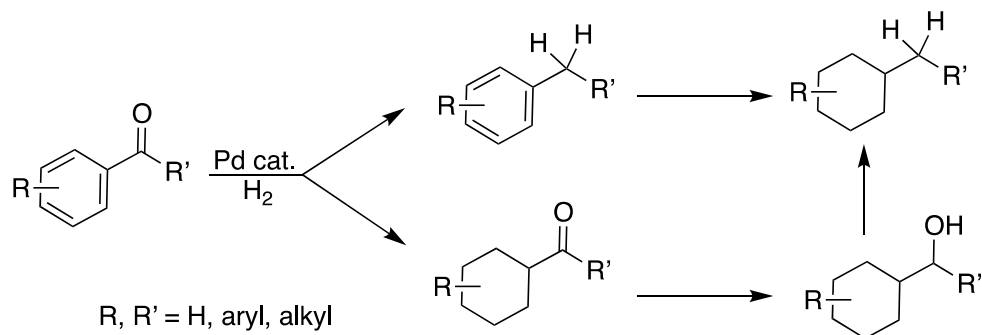
Scheme **4.2**

Inexpensive heterogeneous copper catalysts function using hydrogen to selectively deoxygenate aryl ketones without hydrogenating aromatic rings.[99, 302] Silica-supported copper particles[99] as well as copper-chromium alloy dispersed on alumina[302] are both reported to be excellent catalysts for ketone hydrodeoxygenation. Chromium doping has been suggested to improve the stability and thus longevity of the copper catalyst[302] (Equation **4.2**).
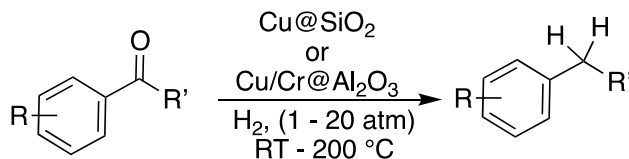
Equation **4.2**

4.1.4 Frustrated Lewis pairs deoxygenation of ketones using H_2

The Stephan and Ashley groups have reported transition metal-free hydrogenation of carbonyl groups using a catalytic amount the powerful Lewis acid B(C$_6$F$_5$)$_3$ **119** in ethereal solvent (*left* Scheme **4.3**).[307-308] In a follow up report, Mahdi and Stephan revealed that either molecular sieves or α-cyclodextrin, form a frustrated Lewis pair with **119**, and that this system smoothly deoxygenates aryl ketones using only H_2 (60 atm) as the reducing agent (*left* Scheme **4.3**).[309] This remarkable transition metal-free protocol for ketone deoxygenation however, depends on very high hydrogen pressure and an expensive the Lewis acid catalyst.
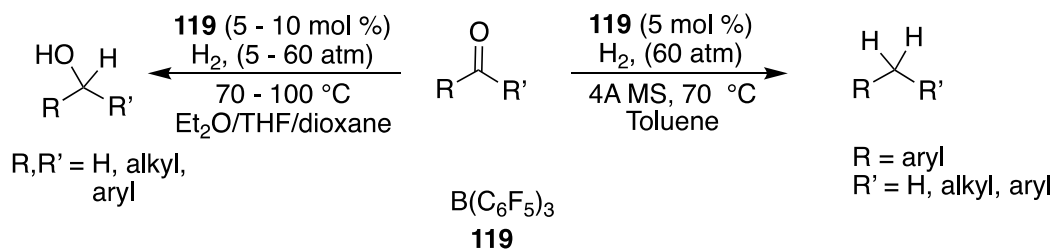
Scheme **4.3**

4.2 Results and Discussion

4.2.1 Nickel/molecular sieves system for deoxygenation of aryl ketones

We questioned whether the addition of molecular sieves to simple transition metal ketone hydrogenation catalysts could lead to similar selectivity for deoxygenation. Transition metals are also well suited to lower the activation energy for the hydrogenolysis of the C–O bond,

potentially reducing the over-pressure of hydrogen required when the reactions are conducted under metal-free conditions.

To test this hypothesis, a catalytic amount of the tetranuclear Ni(I) complex **13b**, which is known to hydrogenate carbonyl compounds,[63-64] was combined with 3 Å molecular sieves and 4-acetylbiphenyl **120** under hydrogen. Heating this reaction mixture to 110 °C for 16 hours under 1 atm of hydrogen leads to partial deoxygenation of the ketone, producing 4-ethylbiphenyl 120**b** (Scheme **4.4**). The alcohol, biphenylethanol **120a**, as well as some arene hydrogenation products were also present in the reaction mixture.
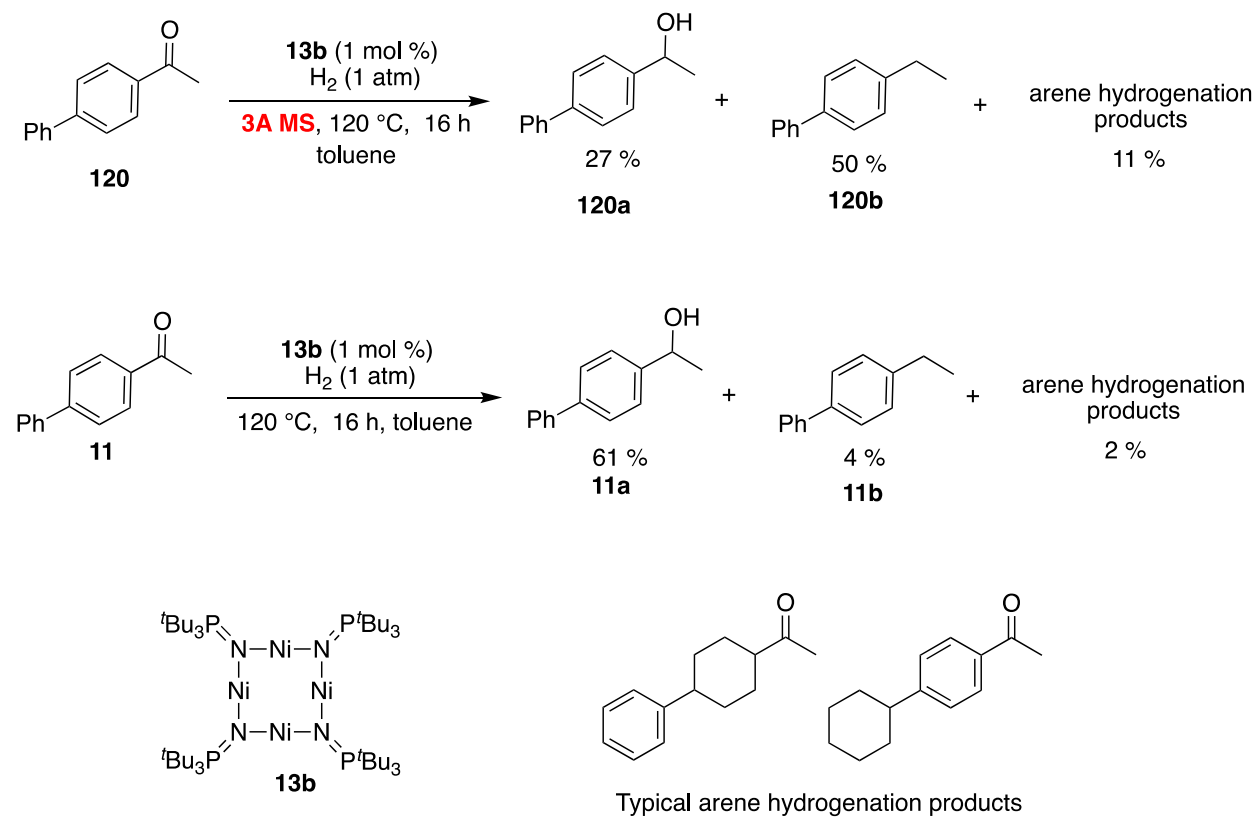
Scheme **4.4**

In contrast, a similar reaction conducted in the absence of molecular sieves was almost exclusively selective for hydrogenation of the **120** to the corresponding alcohol **120a**, with only a trace of the deoxygenated hydrocarbon **120b** present (Scheme **4.4**). The overall conversion, as well as the extent of arene hydrogenation, were also reduced compared to the reaction conducted in the presence of molecular sieves.

4.2.1.1 Role of molecular sieves

The obvious role of the molecular sieves is to scavenge water. Based on the distribution of products seen in Scheme **4.4**, the hydrogenation of the ketone to the alcohol appears to be rapid, followed by a much slower hydrogenolysis of the C–O bond to form water, concomitant with the liberation of a deoxygenated hydrocarbon (Scheme **4.5**). In the absence of the molecular sieves the concentration of water increases, inhibiting the continued functioning of the Ni catalyst. This deactivation of the Ni catalyst prevents further C–O hydrogenolysis or hydrogenation of the ketone, accounting for the small amount of deoxygenation product as well as lower overall conversion of the substrate observed in the absence of molecular sieves.
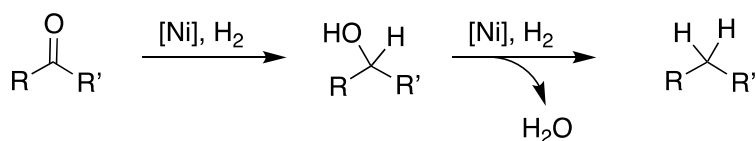
Scheme **4.5**

The pore size of the molecular sieve does not affect the reactivity, 4 Å sieves can be substituted for 3 Å sieves as effective water scavengers in this reaction (*top*, Scheme **4.6**). Surprisingly however, very hygroscopic Activity I alumina does not promote the deoxygenation reaction (*bottom*, Scheme 4.6).
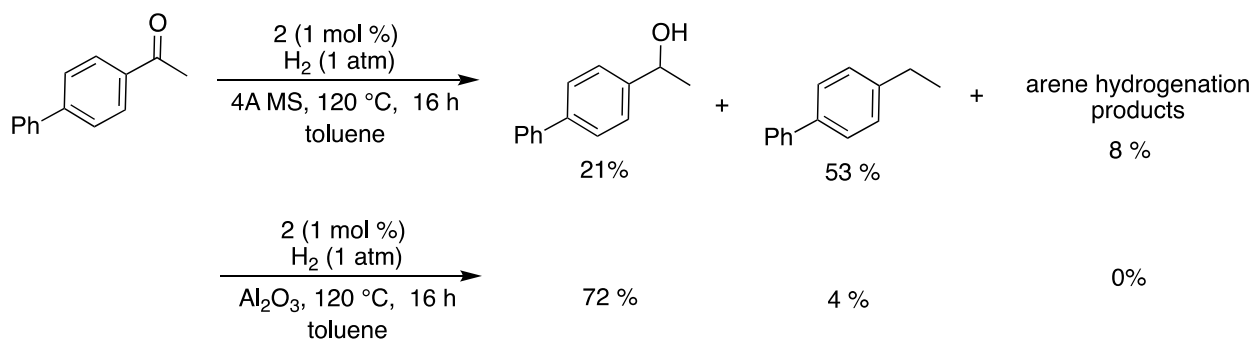
Scheme **4.6**

4.2.1.2 Catalyst heterogeneity and arene hydrogenation

The Ni pre-catalyst is transformed to Ni particles under the reaction conditions, and it is this heterogeneous material that is responsible for the catalytic activity. Addition of excess elemental mercury the reaction mixture leads to nearly complete suppression of the hydrogenation and deoxygenation of the ketone (Table **4.1** entry 2 *c.f.* entry 1).[182] This is unsurprising; the decomposition of **13b** and other phosphoranimide clusters to active Ni nanoparticles has been discussed in Chapter 2.

Nickel bis(phosphoranimide) clusters **23** and **24** (Figure **4.1**) are ineffective for the hydrogenation or deoxygenation (Entries 3, 4 Table **4.1**). These Ni(II) complexes are only slowly

reduced to the active Ni^0 at 120 °C under 1 atm of H_2, accounting for the low yield of both the alcohol and the deoxygenated hydrocarbon.

Table **4.1** Ni catalyzed hydrodeoxygenation of 4-acetyl biphenyl **120**
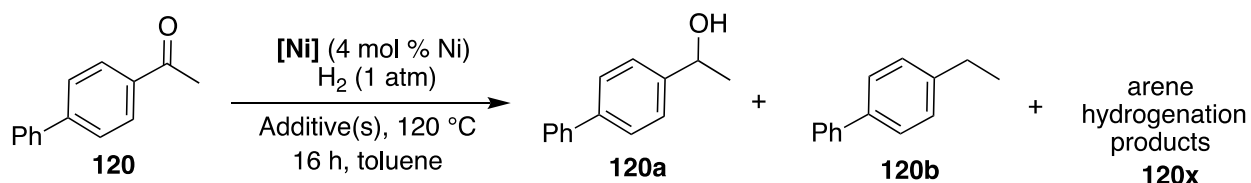
Entry	[Ni] Catalyst	Additive(s)	% Conv[a]	% Yield[a]		
				120a	120b	120x
1	**13b**	3A MS	88	28	50	11
2	**13b**	3A MS/Hg	5	5	0	0
3	**23**	3A MS	11	7	3	1
4	**24**	3A MS	14	10	1	3
5	IPr$_2$Ni[b]	3A MS	80	53	18	9
6	IPr$_2$Ni[b]	3A MS/Hg	46	45	1	0
7	Ni(COD)$_2$	3A MS	85	0	53	32
8	Ni(COD)$_2$	3A MS/Hg	7	7	0	0

[a]Determined by GC-FID analysis. [b]Prepared in situ from Ni(COD)$_2$, IPr.HBF$_4$ and NaO^{t}Bu.
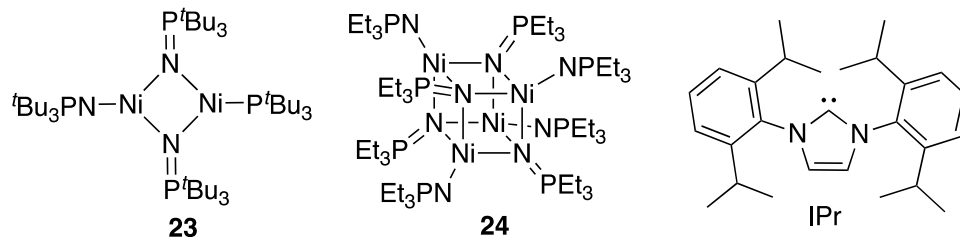
Figure **4.1** Structure of catalysts and ligand for ketone deoxygenation (see Table **4.1**)

136

Soluble Ni complexes such as NHC-supported Ni^0 precatalysts are more suitable for the hydrogenation of the ketone, leading to a higher selectivity for the alcohol (Table **4.1,** entry 5) The NHC ligands are very good σ-donors, forming strong bonds to the transition metal.[310-312] As such, the decomposition of the $(NHC)_2Ni$ complex to form active Ni particles is slow.[313-314] The resulting low concentration accounts for the limited deoxygenation and arene hydrogenation observed using NHC complex. Here again, simple mercury tests are insightful.[182] While the hydrogenation of the ketone by the homogeneous NHC-Ni complex proceeds in the presence of excess mercury, the deoxygenation and arene hydrogenation are completely supressed due to the amalgamation of the Ni particles with mercury (entry 6).

The Ni^0 precatalyst $Ni(COD)_2$ in the absence of additives, afforded the highest yield of deoxygenation (entry 7). In the absence of the NHC ligand, hydrogenation of the cyclooctadiene ligands results in the formation of unsupported Ni atoms, which rapidly agglomerate into nanoparticles.[315] As a result, a high concentration of the active Ni phase is formed, leading to more C–O bond hydrogenolysis. However, this highly efficient catalyst also increases the undesired aromatic hydrogenation of the aryl ketone: 37% of the 4-acetylbiphenyl is recovered as a hexahydro-derivative, with the distal ring saturated (Table **4.1,** entry 7). For this ligand-free Ni catalyst, nearly all reactivity is suppressed in the presence of elemental mercury (entry 8). The degree of aromatic saturation by Ni colloids is unsurprising, yet unacceptably high. Saturation of aromatic compounds by colloidal Ni has been known for nearly a century.[316] Significant back bonding from the electron rich surface disrupts the aromaticity of the ring;

subsequent, hydride transfer to the Ni-arene complex then leads to the saturation of carbocyclic ring.[317]

4.2.1.3 Promoting selective C–O bond hydrogenolysis over arene hydrogenation

To suppress the hydrogenation of the phenyl rings, the catalytic metal was changed to copper for ketone deoxygenation. Several heterogeneous copper catalysts have been reported for the deoxygenation of aryl ketones without associated hydrogenation of aromatic residues.[99, 302] Copper surfaces interact only weakly with the π-system of aromatic rings compared to nickel (and palladium);[318] therefore, copper mediated arene hydrogenation is unlikely. For low-valent copper, the η^{1}- O-carbonyl and similar alcohol interaction are preferred, leading to hydrogenation and/or deoxygenation of the carbonyl group. The reaction of furfural over heterogeneous Cu, Ni and Pd catalysts illustrates this: while Ni and Pd lead to hydrogenation or ring-opening of the furan, the copper catalyst mostly hydrogenates the aldehyde; no hydrogenation of the aromatic ring, and only limited deoxygenation is observed using copper. (Scheme **4.7**).[319]
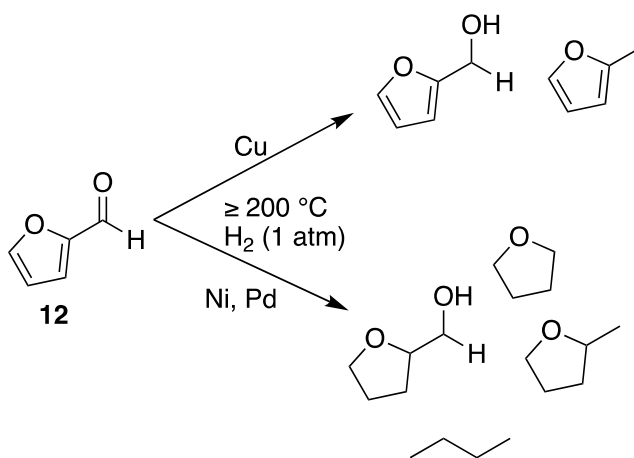
Scheme **4.7**

4.2.2 Copper/molecular sieves system of selective deoxygenation of aryl ketones

Tetranuclear copper(I) complexes **21 and 22**, isostructural with **13b**, do not react with 4-acetylbiphenyl under the standard conditions, returning only starting material, even at 34 atm of hydrogen pressure (Scheme **4.8**). Clusters 21 and 22 are similarly inactive for HDS, as well as olefin hydrogenation reactions (see chapter 1).

No Conversion
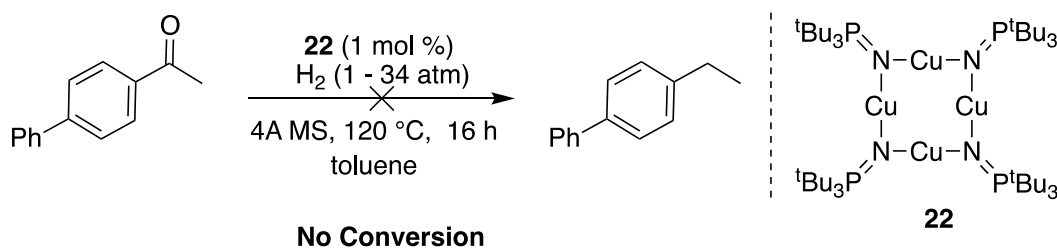
Scheme **4.8**

Conversely, IPrCuO^{t}Bu[320] proved to be an efficient and very convenient precatalyst for the deoxygenation aryl ketones *in the presence of molecular sieves*. N-heterocyclic carbene and phosphine copper hydrides enjoy wide use as mild, chemoselective catalysts for hydrogenation of ketones,[298-300, 320-323] but, remarkably, have not been explored for catalytic ketone deoxygenation. Under one atm of H$_2$, IPrCuO^{t}Bu and molecular sieves show limited activity, producing 6% of a mixture of biphenylethanol **120a**, and biphenylethane **120b** (Entry 1, Table **4.2**). Increasing the pressure of hydrogen to 10 atm, however, affords near-quantitative conversion to the deoxygenated hydrocarbon, 120b (Entry 2). *No hydrogenation of the aromatic rings is observed under these conditions.*

Table **4.2** Copper/molecular sieves system for hydrodeoxygenation of **120**
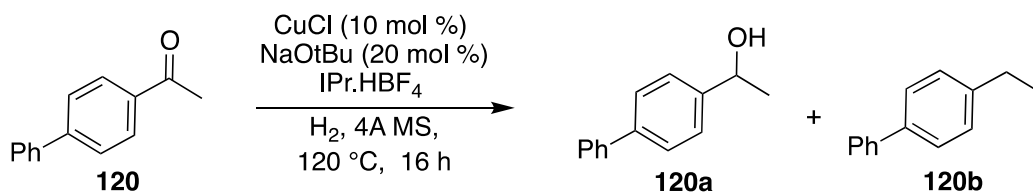
Entry	mol % IPr	Pressure/ atm	Solvent	% Conv.[a]	% Selectivity [a]	
					120a	**120b**
1	10	1	Tol	6	83	17
2	10	10	Tol	99	2	98
3	nil	1	Tol	86	6	94
4	nil	10	Tol	99	1	99

[a]Determined by GC-FID analysis.

The precatalyst mixture of CuCl, IPr.HBF$_4$ and NaO^{t}Bu is expected to generate *in situ*, the active NHC copper(I) hydride catalyst (Scheme **4.9**), for both hydrogenation and deoxygenation. However, visual inspection of the reaction mixture revealed a significant precipitation of metallic Cu, leading to the hypothesis that, as observed for Ni, the active deoxygenation catalyst is a Cu colloid. The over-pressure of hydrogen is required to promote the reduction of the pre-catalyst to the active phase, rather than for the C–O bond hydrogenolysis itself. Moreover, coordination of free NHC, if present, to the surface of the Cu(0) can lead to catalyst 'poisoning';[324] this has been used deliberately, by others, as a strategy for tuning the reactivity and selectivity of heterogeneous catalysts.[234, 325]
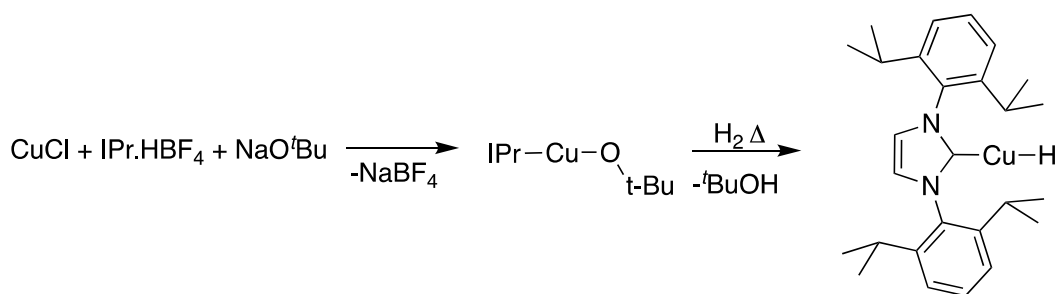
Scheme **4.9**

4.2.2.1 A ligand-free CuOᵗBu precatalyst for ketone deoxygenation

To test this hypothesis, the NHC ligand was excluded from the reaction mixture. At atmospheric pressure of hydrogen, 86% conversion to a 94:6 mixture of **120b**:**120a** was obtained (Entry 3, Table **4.2**). At 10 atm hydrogen, alkane **120b** is obtained nearly quantitatively. Instead of enhancing the reactivity of the copper(I) hydride, the NHC ligand actually suppresses the decomposition, inhibiting the formation of the active colloidal Cu(0) catalyst.[324]

Other heterogeneous Cu(0) catalysts for deoxygenation of aryl ketones have been reported, as noted.[98, 302, 319] These catalysts are typically prepared by the impregnation of silica or alumina with a water-soluble copper salt followed by high temperature calcination and activation at similar temperatures in the presence of hydrogen. By contrast, the colloidal Cu catalyst reported here is conveniently prepared *in situ*, under mild conditions, and from a simple molecular copper precursor CuOᵗBu, which can itself be assembled in situ using commercial CuCl and NaOᵗBu.

The exclusion of the molecular sieves limits the ketone deoxygenation (Equation **4.3**). This highlights that the water produced from C–O bond hydrogenolysis inhibits the activity of the copper particles. Sequestration of water in the pores of the zeolite maintains the catalyst function, allowing high conversion and yield of the deoxygenation product.
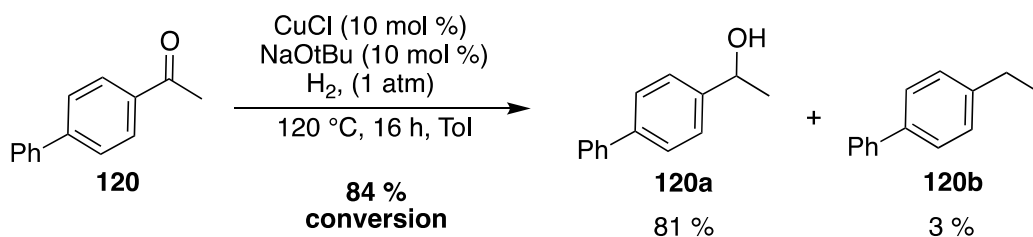
Equation **4.3**

4.2.2.2 Cu/molecular sieves deoxygenation of aryl ketones: substrate scope

Under these unoptimized conditions, the Cu/molecular sieves catalyst system is effective or the deoxygenation of a range of aromatic ketones/aldehydes (**Table 4.3**).   Deoxygenation of electron-deficient ketones is facile compared to more electron-rich analogues. Benzophenone **121** is deoxygenated quantitatively (Entry 1), but acetophenone **122** is converted only to a 90:10 mixture of phenylethanol **122a** and ethylbenzene **122b** (Entry 2). Slightly more electron rich 4-ethylacetophenone **123** is also deoxygenated slowly, yet hydrogenated readily to the alcohol **123a** (Entry 3).

Table **4.3** Hydrogenation and deoxygenation of aryl ketones and aldehydes.
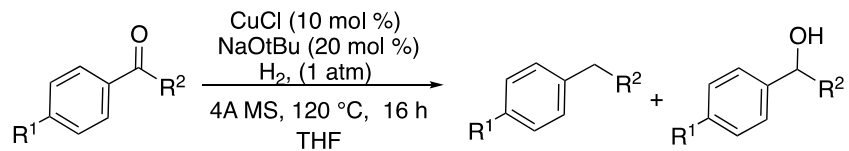
Entry	Substrate	% Conversion	% Selectivity Products	
1	**121**	90	**121a** 0	**121b** 100
2	**122**	100	**122a** 90	**122b** 10
3	**123**	100	**123a** 87	**123b** 13
4	**124**	49	**124a** 38	**124b** 62
5[a]	**125**	70	**125a** 94	**125b** 0
6	**126**	93	**126a** 4	**126b** 96
7	**127**	97 %	**127a** 96	**127b** 4
8	**128**	trace	**128a** trace	**128b** not observed
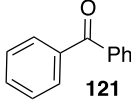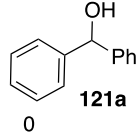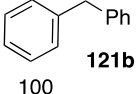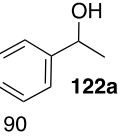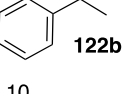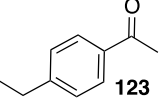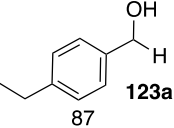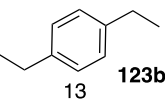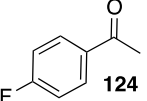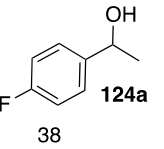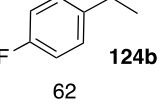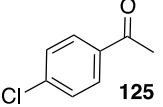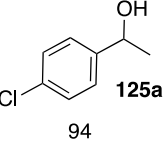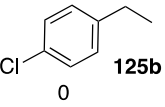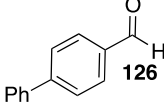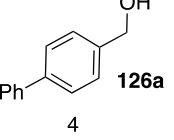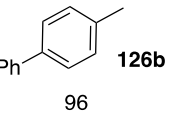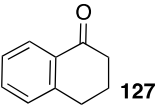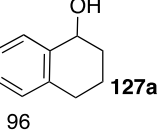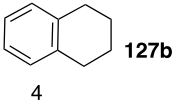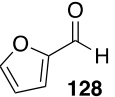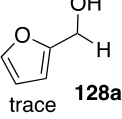
[a]**122b** also observed in the reaction mixture

143

Partial conversion of 4-fluoroacetophenone **124** is observed after 16 h, giving deoxygenated alkane **124b** as the major product (Entry 4). The alcohol **125a** is the major product obtained from 4-chloroacetophenone **125**, but a small amount of dehalogenated phenylethnaol **122a** is also present (Entry 5). During this dehalogenation, the catalyst is converted to CuCl, which is inert, accounting for the absence of deoxygenation.

The aldehyde in biphenyl carboxaldehyde **126** is smoothly deoxygenated to 4-methylbiphenyl **126b**b, but surprisingly, only a trace of the hydrogenation product is obtained from furfural **128**. Furfural, a biomass-derived oxygenate, is relatively electron rich; the Cu/molecular sieves system is biased for the deoxygenation of electron-deficient molecules. Compounding this problem, the oxygen atoms of the furan ring as well as the aldehyde group can form a chelate with the active copper atoms, inhibiting both hydrogenation and deoxygenation.

4.2.2.3 Reaction pathway

The reaction pathway for deoxygenation were assessed briefly using the reduction of 4-acetylbiphenyl **120** by the copper/molecular sieves system. After 4 h under 1 atm hydrogen, the ketone is converted to a mixture of alcohol **120a**, 4-ethylbiphenyl **120b**, and a previously unobserved 4-vinylbiphenyl **120c** (Equation **4.4**). This reveals that the deoxygenation proceeds via sequential reduction, initially to the alcohol, followed by dehydration to the styrene, which is then hydrogenated to alkane. The high concentration of the alcohol after 4 h indicates that

the initial hydrogenation is facile, followed by slower conversion to the alkane, either by direct

hydrogenolysis of the C–O bond, or by a dehydration/hydrogenation pathway.
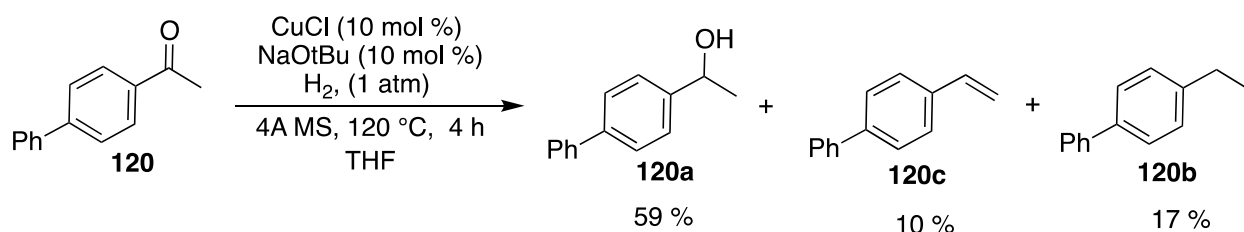
Equation **4.4**

The kinetic profile of the deoxygenation is more clearly illustrated by a series of reactions

performed under 10 atm of H_2 (Figure **4.2** and Table **4.4**). Over the first hour, all of the ketone is

consumed, producing a mixture largely comprised of alcohol **120a** and a small proportion of

alkene **120c**. This highlights that the initial hydrogenation of **120** to the alcohol is rapid,

followed by slow dehydration to 4-phenylstyrene **120c**. Subsequent hydrogenation of the

styrene appears to be facile: no build-up in concentration of this intermediate is observed.

Over the course of the remaining three hours, the consumption of the alcohol **120a** mirrors the

rate of alkane formation of the alkane **120b**, giving after 4 hours, quantitative conversion to

alkane. It is also possible that the 4-phenylstyrene **120c** is only produced in a small quantity

during a short induction period, after which direct hydrogenolysis of the C–O bond in the

alcohol to form the alkane **120b** is the more important reaction pathway.
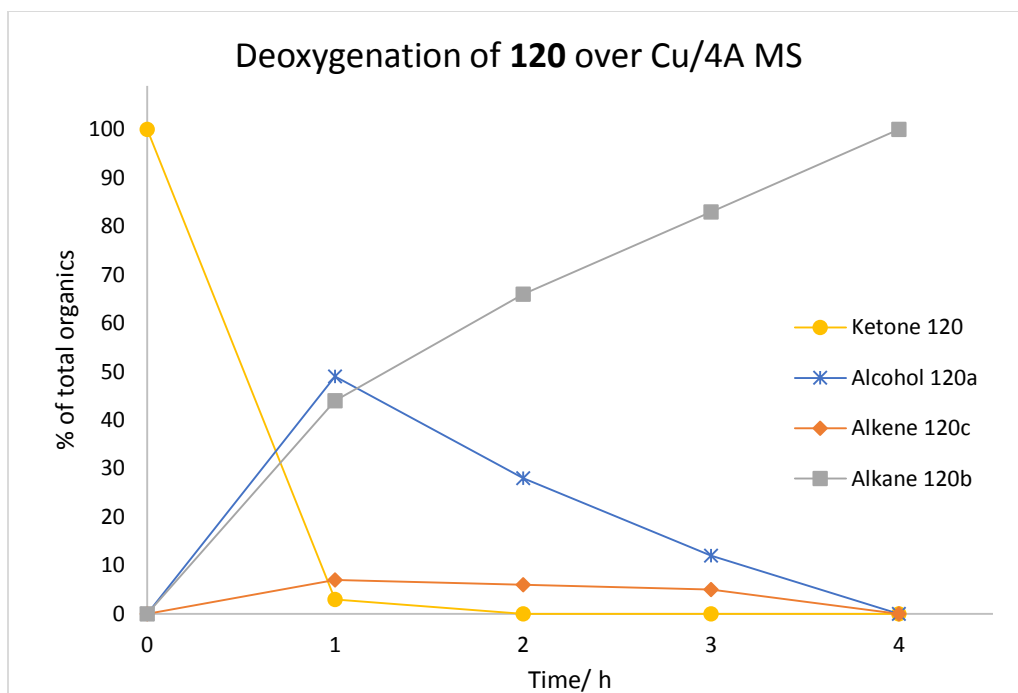
Figure **4.2** Time resolved product distributions from the hydrodeoxygenation of **120** over Cu/molecular sieves (see Table **4.4** below)

Table **4.4** Conversion of **120** to a mixture of products over 4 hours by Cu/molecular sieves.

| | | % of total organics[a] | | | |
Entry	Time/h	ketone	alcohol	alkene	alkane
1	0	100	0	0	0
2	1	3	49	7	44
3	2	0	28	6	66
4	3	0	12	5	83
5	4	0	0	0	100

[a]Determined by GC-FID analysis.

The hydrogenation and subsequent deoxygenation of 4-acetylbiphenyl proceeds at lower temperatures and copper loadings, but with reduced efficiency. At 5 mol % Cu, the majority of the ketone is deoxygenated to the alkane **120b** after 4 hours, but more of the alcohol and alkene are present, compared to the use of 10 mol% Cu. (Entries 1, 2; Table **4.5**). While quantitative conversion of the ketone is maintained using 2.5 mol% Cu, the yield of deoxygenation is substantially lower than at higher Cu loading (Entry 3). Remarkably, quantitative hydrogenation as well as some deoxygenation is still observed using low catalyst loading (2.5 mol % Cu) at only 65 °C (Entry 4). The absence of alkane from the product mixture indicates that at mild temperatures, the hydrogenation of the alkene is slow and direct hydrogenolysis of the C–O bond cannot occur.

Table 4.5 Effect of catalyst loading and reaction temperature efficiency of deoxygenation of **120** by the Cu/molecular sieves system
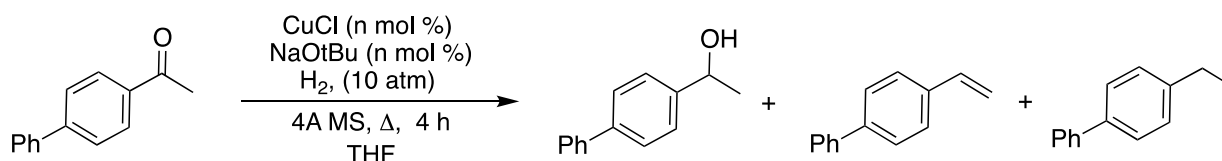
Entry	mol % Cu	Temp/ °C	% of total organics^a			
			ketone	alcohol	alkene	alkane
1	10	120	0	0	0	100
2	5	120	trace	23	5	72
3	2.5	120	trace	57	9	33
4	2.5	65	trace	87	12	trace

^{a}Determined by GC-FID analysis.

4.2.2.4 Hydrogenation of aliphatic ketones – a serious limitation.

Further optimization is required to develop a truly general method for the deoxygenation of carbonyl compounds. While aromatic ketones/aldehydes are deoxygenated with varying levels of success, aliphatic ketones are hydrogenated only to the corresponding alcohol (Scheme **4.10**) and no further. Undecanone **129**, cyclohexanone **130**, cyclococtanone **131** and 2-cyclohexenone **132** are all hydrogenated quantitatively. No C–O bond hydrogenolysis is detected. Both unsaturated bonds in the conjugated π system are completely hydrogenated to alcohol.
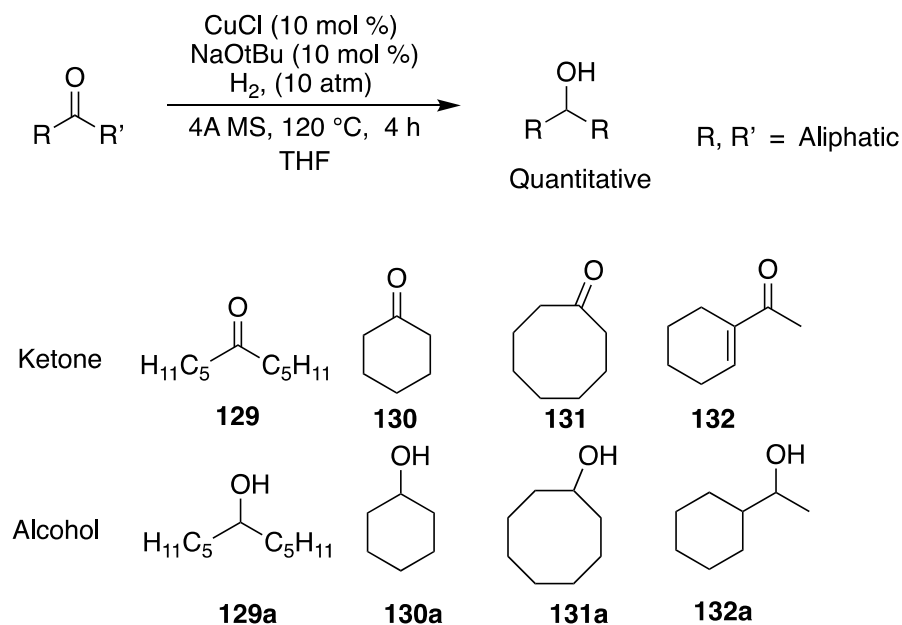
Scheme **4.10**

4.2.2.5 Reaction pathway – a preliminary proposal.

In the absence of rigorous mechanistic analysis, the basic pathway for the deoxygenation can be proposed, based on the products observed. The reaction pathway involves an initial hydrogenation of the ketone to an alcohol which likely exist in equilibrium with a copper bound alkoxide. The C–O bond of the copper alkoxide is then cleaved in either in a homolytic or heterolytic fashion, to form a benzylic radical or a benzylic carbocation respectively (Scheme **4.11**). Both of these purported intermediates are stabilised by the neighboring aromatic ring; aliphatic substrates lack this arene substituent and as such the C–O bonds are not cleaved, as evidenced by the absence of any deoxygenation product when such substrates are used (see Scheme **4.10** above). An olefin can be formed by the loss of a proton from the benzylic carbocation, or by loss of a hydrogen atom from the benzylic radical. Hydrogenation of this olefin, then furnishes the desired alkane as the final product. Alternatively, the transfer of hydride to the carbocation, or of a hydrogen atom the benzylic radical, can lead to the direct formation of the alkane, without the formation of an olefin intermediate. The reaction pathway shown in Scheme **4.11** is highly speculative and over simplified; the actual process will involve multiple copper atoms on the catalyst surface. Furthermore, interactions between the intermediate alcohol and the surface or pores of the molecular sieves may provide some enhancement. This reaction and its mechanism remain under study.
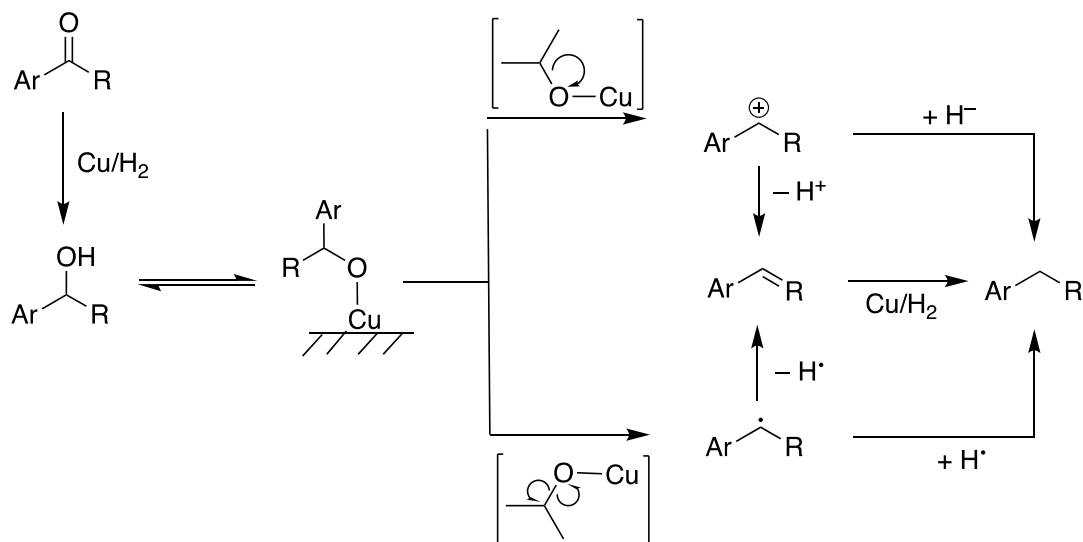
Scheme **4.11**

The hydrogenation to alcohol is facile and can involve either homogeneous or heterogeneous Cu/Ni specie (Scheme **4.11**). The cleavage of the C–O bond is likely the most challenging step.

4.2.3 Hydrogenolysis of C–O bonds in ethers- outlook

From a global perspective, the activation of C–O bonds in ethers a more urgent research priority; depolymerisation and hydrotreatment of lignocellulosic biomass thus remains a principal research goal of the Stryker group. The copper/molecular sieve catalyst/scavenger system described here does not cleave the C–O bond in simple ethers. The development of a transition metal/ molecular sieves catalyst for this deoxygenation reaction is the subject of ongoing investigation. The hydrogenolysis of ether linkages by iron[326] and nickel[43-44] catalysts iron and nickel catalysts is known, but both reactions require an excess of a strong base and complete deoxygenation is not achieved. Heterobimetallic Cu/Fe or Cu/Ni nanoparticles are attractive potential catalyst for these reactions. The synergism between the metals, Fe/Ni for

hydrogenolysis of the ether bond and Cu for deoxygenation, is expected to yield some advantages over monometallic systems. In addition, the use of strong Lewis acids has a promotional effect on C–O hydrogenolysis[43], as such tris(pentafluorophenyl)borane **119**, or alkyl aluminum compounds are obvious potential additives for promoting Cu(Fe/Ni) catalyzed hydrogenolysis of C–O bonds in ethers.

4.3 Conclusion

A simple heterogeneous Cu/molecular sieves catalyst system has been developed for the deoxygenation of aryl ketones using hydrogen under mild conditions. The copper catalyst is conveniently generated in situ from the decomposition of CuO^{t}Bu under hydrogen. The deoxygenation of aryl ketones proceeds by initial hydrogenation, followed by the dehydration of the alcohol produce to yield an alkene. Hydrogenation of this alkene provides the desired product.   An initial substrate survey shows that electron-deficient aryl ketones are deoxygenated readily. Aliphatic ketones are only hydrogenated to the corresponding alcohols. Further research will be conducted to elucidate the mechanism of this transformation, as well as to develop more active monometallic, or heterometallic particles, to achieve higher reaction rates at lower catalyst loadings. Finally, general method for the hydrogenolysis of a variety of C–O bonds remains the target of ongoing research.

5. Conclusion and Future Work

In the preceding chapters I have described the preparation and characterization of a series of polynuclear clusters of first-row transition metals, supported by bridging trialkylphosphoranimide ligands. The manganese, nickel and copper complexes discussed, build on work by Dehnicke, and Stephan, as well earlier research in the Stryker group. As observed by these previous researchers, the oxidation state of the metal and the size of the substituents on the phosphoranimide ligand, control the nuclearity of the polymetallic clusters, allowing the rational design and synthesis of clusters with varying structural motifs. Two-dimensional bi- and tetranuclear complexes of manganese, nickel and copper were obtained using the bulky tri-*tert*-butylphosphoranimide ligand, while the smaller triethylphosphoranimide ligand led to tetrametallic heterocubane clusters of manganese and nickel. The manganese and copper complexes do not catalyze hydrogenation reactions, and only promoted desulfurization in the presence of potassium hydride. Control reactions confirmed that KH, a potent reducing agent, desulfurizes dibenzothiophene in the absence of a transition metal. The presence of catalytic amounts of transition metals, particularly the nickel phosphoranimide clusters, improves the efficiency of this process.

At elevated temperature and pressure, the nickel phosphoranimide clusters [Ni(NP^{t}Bu$_3$)$_2$]$_2$ and [Ni(NPEt$_3$)$_2$]$_4$ promote the hydrogenolysis of the C–S bonds in dibenzothiophene in the presence of stoichiometric potassium *tert*-butoxide. The reactions represent the first use of molecular hydrogen as the terminal reductant for deep desulfurization under relatively mild conditions

(150 °C, as low as 1 atm of H_2). The active catalysts under these conditions are nickel nanoparticles, formed from the exhaustive hydrogenolysis of the Ni–N bonds in the clusters.

Heterogeneous catalysts, displaying improved reactivity and selectivity for hydrodesulfurization, were prepared by protolytic grafting of nickel phosphoranimide clusters onto alumina or silica. While the phosphoranimide ligands served as convenient handles for grafting, and for activation of the clusters by hydrogenolysis, their presence was not essential. Soluble Ni(0) complexes are effective precatalysts for hydrodesulfurization, under these conditions, as are Ni(II) alkoxides, derived *in situ*, from simple nickel halides. The presence of the strongly basic potassium salts is imperative for catalytic hydrodesulfurization. While the precise role of the strong base is not completely understood, the promotional effect of potassium K^+ ions is clear. The cleavage of the C–S bonds assisted by K^+ cation-π interactions with the aromatic rings of dibenzothiophene, as well as potassium-promoted hydrogenolysis of the spent nickel sulfide, are among the roles attributed to potassium in the hydrodesulfurization reaction.

The hydrogenolysis of C–O bonds in aryl ketones is less challenging; a simple and highly convenient, nickel/copper and molecular sieves system accomplishes this catalytic hydrodeoxygenation reaction under mild conditions (120 °C, 1 atm H_2). The active catalysts, for the C–O bond hydrogenolysis, are heterogeneous particles, generated *in situ* from the decomposition of simple molecular precursors; Ni(COD)$_2$ or CuO^{t}Bu are the most effective. The copper catalyst is more selective for promoting the deoxygenation reaction over the

hydrogenation of the arene rings, in the aryl ketones/aldehydes. This method is limited to aryl ketones/aldehydes; aliphatic ketones are only hydrogenated to the corresponding alcohol, and the C–O bonds in aryl ethers are untouched under the reaction conditions.

Several sections of this dissertation provide avenues for future investigation. The magnetic characterization and computational investigation of the manganese complexes remains incomplete. It is anticipated that this will lead to a better understanding of the electronic structure of the compounds, and thus possible activation pathways to promote catalysis. The polynuclear manganese clusters are anticipated to display enhanced reactivity for transformations such as C–H activation, oxidation and hydrosilylation, that are currently catalyzed by mononuclear, manganese complexes.

The activation of the copper clusters for use in hydrotreatment reactions has remained elusive. The clusters may however serve as useful templates for depositing tetranuclear arrays of copper atoms onto a support. Subsequent removal of the phosphoranimide ligands under appropriate thermal conditions can then reveal small, isolated, 'naked' Cu or Cu/Li clusters on the surface of the support, which may prove more active hydrogenation or hydrodeoxygenation reactions.

The stability of the nickel phosphoranimide clusters under reaction conditions needs to be addressed, in order for the polymetallic clusters to function as homogeneous catalysts. One possible strategy for stabilizing these compounds, involves the inclusion of Lewis acidic early

transition metal atoms in the clusters. These electrophilic metal atoms can passivate basic nitrogen atom of the phosphoranimide, reducing the likelihood of exhaustive heterolytic cleavage of the M–N bonds in the cluster, on exposure to hydrogen. The heterometallic clusters produced, will contain adjacent nucleophilic, and electrophilic metal centers, and are expected to provide novel pathways for the binding and activation of substrate molecules.

Beyond attempts to stabilize homogeneous nickel clusters, the rational synthesis of more active heterogeneous nickel catalyst for hydrodesulfurization needs to be addressed. Conventional methods will be used to prepare colloidal nickel particles of varying sizes and morphologies, in order to discover the most efficient catalysts for potassium promoted hydrodesulfurization. In addition, the preparation of potassium doped nickel nanoparticles will be priority. This 'builds in' the potassium promoter into the catalyst, potentially allowing for improved reactivity and more importantly, possibly rendering the process catalytic in potassium. Ultimately the continued use of stoichiometric quantities of any potassium salt, severely limits the viability of these reactions on an industrial scale.

In addition to exploratory small-scale batch reactions, the stability and longevity of these heterogeneous nickel catalysts, must also be assessed in a continuous flow system, in order to more closely mimic industrial reactor designs. As such, switching to a flow reactor is an obvious part of the future work on this project. For reactions requiring added base, the potassium tert-butoxide can be introduced into the flow reactor as part of a solution containing the organosulfur substrate molecules.

More active and promiscuous catalyst for hydrodeoxygenation reactions are required, and this will be addressed in future projects which arise from this research. The homometallic particles of copper and nickel described in this work, are only effective for the deoxygenation of aryl ketones. Heterometallic Cu-Ni particles may provide synergistic effects to more readily promote the hydrogenolysis of C–O bonds in various classes of oxygenated molecules. As such the preparation of binary colloidal particles of these metals, and the exploration of these species as catalyst for hydrodeoxygenation, under mild conditions will form part of the future work on this project. In addition, the exploration of strong Lewis acidic additives to promote the hydrogenolysis of the C–O bonds remains to be to be explored.

6. Experimental

6.1 Foreword

The Stryker group has been interested in the synthesis of first-row transition metal phosphoranimide compounds and their catalytic reactions for over a decade. During this period, several researchers have contributed to the development methods to achieve these goals. As such several the synthetic procedures and analytical methods that appear here, have been reported in previous PhD and MSc theses of former group members, and have been adapted for use in this document.

6.2 Materials, general methods and instrumentation

Unless otherwise stated, all commercially available reagents were purchased from Alfa Aesar/Thermo Fischer Scientific, Strem Chemicals, or Millipore-Sigma and were used without further purification.

All air-sensitive manipulations were performed using standard Schlenk techniques on a vacuum/N_2 (or Ar) double manifold or using an MBraun Labmaster glovebox under nitrogen with O_2 levels maintained below <5 ppm and, typically, <1 ppm. Solvents were rigorously deoxygenated and dried by distillation from Na or CaH_2 under nitrogen or collected from Pure Process Technology solvent purification system under rigorously dry conditions. All glassware was flame-dried, or dried for at least 3 h, in an oven heated to 150 °C, then cooled under vacuum before use.

CHNS elemental analyses, GC-MS and FT-IR analysis were performed by the staff of the University of Alberta Department of Chemistry Analytical and Instrumentation Laboratory. CHNS elemental analyses were performed in duplicate for all samples using a Carlo Erba EA1108 Elemental Analyzer. Air sensitive compounds were added to pre-weighed tin boats in the glove box, which were then folded and submitted for immediate analysis. Samples for CHN analysis were dried on a high vacuum line ($<10^{-5}$ Torr), equipped with a three-stage oil diffusion pump.

IR spectra were recorded on a Nicolet Magna 750 FT-IR Spectrometer, or a Nicolet 8700 FT-IR Spectrometer operating by OMNIC Spectra Software. Sample preparation for air-sensitive IR spectroscopy was done in the glovebox, using a custom cell composed of two KBr salt plates, sealed with a greased O-ring.

The UV-Vis spectra were recorded using an Agilent/HP 8453 UV-Vis spectroscopy system version B.04.01 of UV-Vis ChemStation software.

X-ray crystallography was performed using either a Bruker DB diffractometer or a Bruker PLATFORM diffractometer, both equipped with a SMART APEX II CCD area detectors. Diffraction data collection and crystal structures determinations were completed by the staff of the University of Alberta Department of Chemistry X-ray Crystallography Laboratory.

^{1}H, ^{2}H, and ^{31}P NMR spectra were obtained on Agilent/Varian 400 MHz spectrometers at 27 °C, unless otherwise stated.

Cyclic voltammetry was performed using WaveNow USB potentiostat from Pine Industry Instrumentation. Data processing was performed using Aftermath operating software. In the glove box samples were dissolved in a THF solution containing the electrolyte n-Bu$_4$NPF$_6$. The electrodes were inserted into the solution and the assembly placed in a sealed chamber, with external connections in order maintain an inert atmosphere during measurement. The assembly was removed from the glovebox and connected to the WaveNow USB potentiostat via the external connectors and the CV measurements obtained typically using a scan rate of 0.1V/s.

For heating of reaction mixtures, Ika stir plates with digital temperature control were used along with heavy mineral oil silicone oil baths. Alternatively, aluminum heating blocks, with wells for glass reactors, were fitted to the top of the hot plates. For low temperature reactions, an immersion cooler (Neslab Cryotrol cc-100) was used.

Analyses of reaction products were performed using gas chromatography with flame ionization detection (GC-FID) on an Agilent 6890N gas chromatograph equipped with a HP-5 (5% phenyl)-methylpolysiloxane capillary column (Agilent) or GC-MS analyses were obtained using an Agilent 6850 gas chromatograph equipped with a HP-5 (5% phenyl)-methylpolysiloxane capillary column (Agilent). The mass detectors used were either HP 5870 or 5971 MSD. The MS

library was the NIST/EPA/NIH 2011 Mass Spectral Library and Software package was NIST11. For GC-FID analysis products are identified by referencing to independently prepared, authentic samples, or occasionally by comparison with NMR and GC-MS data. Yields were determined using dodecane as a standard. The calibration curves for DBT, 4-phenylthiophenol and biphenyl were constructed using solutions of varying concentrations of each analyte along with dodecane.

6.3 Experimental procedures for Chapter 1

6.3.1 Synthetic Procedures and Characterization

The phosphoranimide salts LiNP^{t}Bu$_3$ and KNPEt$_3$ were prepared according to previously described in the theses of former members of the Stryker group.[65, 77] [Fe(NP^{t}Bu$_3$)$_2$]$_2$ **11a** and [Co(NP^{t}Bu$_3$)$_2$]$_2$ **11b** were first prepared by Dominique Hebert,[65] then recently reported by Dr Tao Bai.[81]

6.3.1.1 Synthesis of KNP^{t}Bu$_3$ and of NaNP^{t}Bu$_3$

 Inside the dry box, ^{t}Bu$_3$PNH$_2$F[65] (1.12 g, 4.72 mmol) was suspended in approximately 15 mL of THF in a 5-dram vial containing a magnetic stirring bar. A suspension of KH (1.2 g, 30 mmol) and KNH$_2$ (0.8 g, 14.5 mmol) in approximately 5 mL of THF was added rapidly and the resulting mixture was stirred at ambient temperature for 16 hours, yielding a pale brown suspension. The reaction mixture was vacuum filtered through a bed of Celite to remove the solids and the filtrate concentrated *in vacuo*, yielding an off-white solid. This residue was extracted with

approximately 30 mL of benzene and the resulting suspension was filtered through a Celite plug and the solvent was removed from the filtrate under reduced pressure generating a white solid. The product, KNP^{t}Bu$_3$, (0.81 g, 3.17 mmol, 67 %) was dried under high vacuum, and submitted for elemental analysis. Calc'd for C$_{12}$H$_{27}$KNP: C, 56.43; H, 10.66; N, 5.48; Found C, 57.29; H, 11.04; N, 4.98. ^{31}P{^{1}H} NMR (162 MHz, C$_6$D$_6$): δ 16.8

6.3.1.2 Synthesis of NaNP^{t}Bu$_3$

Following the procedure for the synthesis of KNP^{t}Bu$_3$, ^{t}Bu$_3$PNH$_2$F (1.50 g, 6.32 mmol), NaH (1.0 g, 41 mmol) and NaNH$_2$ (0.6 g, 15.3 mmol) were reacted together in THF for 16. At the end of the reaction the product NaNP^{t}Bu$_3$ was isolated as a white solid (0.0.57 g, 2.4 mmol, 38 %) was dried under high vacuum, and submitted for elemental analysis. Calc'd for C$_{12}$H$_{27}$NaNP: C, 60.23; H, 11.37; N, 5.85; Found C, 59.16; H, 11.68; N, 5.11. ^{31}P{^{1}H} NMR (162 MHz, C$_6$D$_6$): δ 23 ppm

6.3.1.3 Synthesis of [MnBr(NP^{t}Bu$_3$)]$_2$ 14a

Inside the glove box, MnBr$_2$ [96 mg, 0.45 mmol) was suspended in approximately 10 mL of THF in a 5-dram vial containing a magnetic stirring bar. A suspension of LiNP^{t}Bu$_3$ (100 mg, 0.45 mmol) in approximately 7 mL of THF was added. After overnight and orange solution is formed. The solvent was then removed under reduced pressure and the residue extracted with approximately 10 mL of toluene and the resulting solution was filtered through a celite plug. The solution was cooled to -35 °C for 30 minutes to ensure the precipitation of any remaining

LiBr. The solution was filtered, while cold, through a plug of celite. This was repeated until no more white precipitate-LiBr was formed, following which the solvent removed under reduced pressure, leaving an orange solid. The product [MnBr(NP^{t}Bu$_3$)]$_2$ **14a** (80 mg, 0.12 mmol, 51%) was dried under high vacuum, and submitted for elemental analysis. Calcd for C$_{24}$H$_{54}$N$_2$Mn$_2$P$_2$Br$_2$: C, 41.04; H, 7.75; N, 3.49. Found C, 42.15; H, 8.03; N, 4.04. X-ray quality crystals were obtained by cooling a THF solution of **14a** to -35 °C.

6.3.1.4 Synthesis of [MnCl(NP^{t}Bu$_3$)]$_2$ 14b

Following the procedure for the synthesis of [MnBr(NP^{t}Bu$_3$)]$_2$ **14a** MnCl$_2$ (56 mg, 0.44 mmol) was reacted with LiNP^{t}Bu$_3$ (100 mg, 0.45 mmol) in THF. After stirring overnight an orange-pink solution was formed. The product [MnCl(NP^{t}Bu$_3$)]$_2$ (99 mg, 0.16 mmol 74 %) was isolated as an orange-pink solid.   C$_{24}$H$_{54}$N$_2$Mn$_2$P$_2$Cl$_2$ C, 46.99; H, 8.87; N, 4.57. Found C, 46.45; H, 8.36; N, 4.72.

6.3.1.5 Synthesis of [MnMe(NP^{t}Bu$_3$)]$_2$ 15

Inside the glove box, MnBr$_2$ [200 mg, 0.93 mmol) was suspended in approximately 10 mL of THF in a Schleck flask containing a magnetic stirring bar. The flask was capped with a rubber septum, removed from the glove box then connected to Schleck line. The suspension was cooled to -78 °C using dry ice/acetone bath and MeLi (1.6 M, 0.52 mL, 0.84 mmol) was added slowly via syringe. After stirring for 4 hours, a pale orange solution developed. A THF suspension of LiNP^{t}Bu$_3$ (187 mg, 0.84 mmol) was then added via canula, and the reaction mixture stirred for a further 16 hours. The temperature was maintained at   -78 °C using an immersion cooler. After stirring overnight, a deep orange solution formed. The solvent was

then removed under reduced pressure, while the reaction mixture warmed to room temperature. The Schlenk flask was then pumped into the glovebox and the residue extracted with approximately 10 mL of toluene, then the resulting solution was filtered through a celite plug. The orange solution was cooled to -35 °C for 30 minutes to ensure the precipitation of any remaining LiBr. The solution was filtered, while cold. This was repeated until no more white precipitate-LiBr was formed, following which the solvent removed under reduced pressure, leaving an orange solid. The product [MnMe(NP^{t}Bu$_3$)]$_2$ **14a** (104 mg, 0.18 mmol, 43 %) was dried under vacuum, and submitted for elemental analysis. Calcd for C$_{26}$H$_{60}$N$_2$Mn$_2$P$_2$: C, 54.54; H, 10.56; N, 4.89. Found C, 53.91; H, 11.02; N, 4.95. X-ray quality crystals were obtained by cooling a toluene solution of **15** to -35 °C.

6.3.1.6 Synthesis of [Mn(NP^{t}Bu$_3$)$_2$]$_2$ 16

Inside the glove box, MnBr$_2$ (96 mg, 0.45 mmol) was suspended in approximately 10 mL of THF in a 5-dram vial containing a magnetic stirring bar. A suspension of LiNP^{t}Bu$_3$ (200 mg, 0.89 mmol) in approximately 7 mL of THF was added rapidly forming an orange solution initially, which becomes green after stirring overnight. The mixture was stirred at ambient temperature for 16 hours, after which the solvent was removed under reduced pressure. The residue was extracted with approximately 10 mL of pentane and the resulting green solution was filtered through a celite plug. The solvent was removed from the filtrate under reduced pressure and a pale green solid was obtained. The solid was re-dissolved in approximately 10 mL pentane and the resulting solution cooled to -35 °C for 30 minutes to ensure the precipitation of any remaining LiBr. The solution was filtered, while cold, through a plug of celite and the solvent

removed from the filtrate under reduced pressure. The product $[Mn(NP^tBu_3)_2]_2$ (155 mg, 0.16 mmol, 71%) was dried under high vacuum, and submitted for elemental analysis. Calcd for $C_{48}H_{108}N_4Mn_2P_4$: C, 59.12; H, 11.16; N, 5.75. Found C, 58.73; H, 10.99; N, 5.64. X-ray quality crystals were obtained by cooling a pentane solution of **16** to -35 °C.

6.3.1.7 Synthesis of [MnMe(NPEt₃)]₄ 8a[52]

Inside the glove box, $MnCl_2$ (73 mg, 0.58 mmol) was suspended in approximately 5 mL of THF in a 5-dram vial containing a small stir bar. A solution of KNPEt₃ (100 mg, 0.58 mmol) in approximately 7 mL of THF was added forming an orange solution after stirring overnight. The mixture was stirred at room temperature for 16 hours then filtered through a Celite plug to remove a white solid. The solvent was removed under reduced pressure to yield an orange solid which was re-dissolved in dioxane. Separately Me₂Mg•dioxane (100 mg, 0.71 mmol) was dissolved 5 mL of dioxane. The Me₂Mg•dioxane solution was added drop-wise over five minutes to the orange solution prepared earlier; a black suspension developed immediately. After stirring for a further 16 hours, solvent was removed from the black suspension under reduced pressure, and the residue extracted with pentane. The pentane suspension was filtered through Celite. A pink solution was collected. Removal of pentane under reduced pressure, yielded a pink solid. The product [MnMe(NPEt₃)]₄ **8a** (69 mg, 0.08 mmol, 59%) was dried under high vacuum, and submitted for elemental analysis. Calcd for $C_{28}H_{72}N_4Mn_4P_4$: C, 41.59; H, 8.98; N, 6.93. Found C, 42.03; H, 8.79; N, 6.68.

6.3.1.8 Synthesis of [Mn(NPEt$_3$)$_2$]$_4$ 17

Inside the glove box, MnCl$_2$ (73 mg, 0.58 mmol) was suspended in approximately 10 mL of THF in a 5-dram vial containing a magnetic stirring bar. A solution of KNPEt$_3$ (200 mg, 1.17 mmol) in approximately 7 mL of THF was added rapidly forming a pink solution which darkens slightly overnight. The mixture was stirred at ambient temperature for 16 hours, after which the solvent was removed under reduced pressure. The residue was extracted with approximately 10 mL of hexane and the resulting solution was filtered through Celite. The solvent was removed from the filtrate under reduced pressure and a purple waxy solid was obtained. The solid was re-dissolved in approximately 10 mL pentane and the resulting solution cooled to -35 °C for 30 minutes to ensure the precipitation of any remaining KBr. The solution was then filtered, while cold, through a plug of celite and the solvent removed from the filtrate under reduced pressure, leaving pink waxy solid. The product, [Mn(NPEt$_3$)$_2$]$_4$ **17** (118 mg, 0.09 mmol, 64%), was dried under high vacuum, and submitted for elemental analysis. Calcd for C$_{48}$H$_{120}$N$_8$Mn$_4$P$_8$: C, 45.14; H, 9.47; N, 8.77. Found C, 43.75; H, 9.31; N, 8.96.

6.3.1.9 solation of [MnH(NPEt$_3$)(9-BBN)]$_4$ 18

Inside the glove box [MnH(NPEt$_3$)(9-BBN)]$_4$ **18** (50 mg, 0.04 mmol) was dissolved in approximately 5 mL of hexane in a 5 dram vial containing a magnetic stirring bar. A solution of 9-BBN dimer (39 mg, 0.16 mmol) in approximately 1 mL of THF was added rapidly leading to the pink solution darkening slightly. The mixture was stirred at ambient temperature for 16 hours, after which the solvent was removed under reduced pressure. The pink residue was extracted

with approximately 10 mL of pentane and the resulting solution was filtered through a celite plug. On cooling to -35 °C, single crystals of **18** were obtained and submitted for X-ray diffraction. **18** could not be separated from a second white pentane soluble by product, as such no elemental composition was determined.

6.3.1.10 Synthesis of [Cu$_4$(NP^{t}Bu$_3$)$_4$Li$_2$] 21

Inside the glove box, CuBr$_2$ (200 mg, 0.89 mmol) was suspended in approximately 10 mL of THF in a 5-dram vial containing a magnetic stirring bar cooled to -35 °C in the glove box freezer. A suspension of LiNP^{t}Bu$_3$ (140 mg, 0.62 mmol) in approximately 7 mL of THF also cooled to -35 °C was added dropwise over 1 hour forming dark green solution. The mixture was stirred briefly then allowed to stand for 16 hours in the freezer at -35 °C. 1 % Na/Hg (4.2 g 1.86 mmol of Na) was added to the green solution and the mixture stirred for a further 16 hours. The solvent was removed and the residue extracted with approximately 10 mL of pentane and the resulting yellow pentane solution cooled to -35 °C. The product precipitated as pale-yellow crystals which were characterized by x ray crystallography. [Cu$_4$(NP^{t}Bu$_3$)$_4$Li$_2$] **21** (75 mg, 0.06 mmol, 43%) was dried under high vacuum, and submitted for elemental analysis. Calcd for C$_{48}$H$_{108}$N$_4$P$_4$Cu$_4$Li$_2$: C, 50.87; H, 9.61; N, 4.94. Found C, 51.36; H, 9.92; N, 5.08. ^{1}H (400 MHz C$_6$D$_6$) NMR δ 1.53 ppm (d, J$_{P-H}$ = 12 Hz) ^{31}P (162 MHz C$_6$D$_6$) δ 49 ppm NMR ^{7}Li{^{1}H} (155 MHz C$_6$D$_6$) δ 1.35 ppm

6.3.1.11 Synthesis of [Cu₄(NPᵗBu₃)₄] 22

Following the procedure for the synthesis [Cu$_4$(NP^{t}Bu$_3$)$_4$] **22** was prepared in 67 % from CuBr$_2$ (200 mg, 0.89 mmol) and KNP^{t}Bu$_3$ (158 mg, 0.62 mmol) Single crystals were obtained by cooling a concentrated pentane solution to -35 °C. [Cu$_4$(NP^{t}Bu$_3$)$_4$Li$_2$] **22** was dried under high vacuum, and submitted for elemental analysis. Calcd for C$_{48}$H$_{108}$N$_4$P$_4$Cu$_4$: C, 51.50; H, 9.72; N, 5.00. Found C, 52.16; H, 9.84; N, 5.15. ^{1}H (400 MHz C$_6$D$_6$) NMR δ 1.54 ppm (d, J$_{P–H}$ = 12Hz)

6.3.1.11 Synthesis of [Ni(NPᵗBu₃)₂]₂ 23

Inside the glove box, NiCl$_2$ (173 mg, 1.33 mmol) was suspended in approximately 10 mL of THF in a 5-dram vial containing a magnetic stirring bar. A suspension of LiNP^{t}Bu$_3$ (595 mg, 2.66 mmol) in approximately 7 mL of THF was added rapidly forming a yellow solution, which darkens to deep yellow/brown overnight. The mixture was stirred at ambient temperature for 16 hours, after which the solvent was removed under reduced pressure. The residue was extracted with approximately 10 mL of pentane and the resulting solution was filtered through a celite plug to separate a grey solid (largely LiCl) which was discarded. The solvent was removed from the filtrate under reduced pressure and a brown solid was obtained. The solid was re-dissolved in approximately 10 mL pentane and the resulting solution cooled to -35 °C for 30 minutes to ensure the precipitation of any remaining LiCl. The solution was filtered, while cold, through a plug of celite and the solvent removed from the filtrate under reduced pressure, leaving a brown solid. The product [Ni(NP^{t}Bu3)$_2$]$_2$ (506 mg, 0.51 mmol, 77%) was

dried under high vacuum, and submitted for elemental analysis. Calcd for $C_{48}H_{108}N_4Ni_2P_4$: C, 58.67; H, 11.08; N, 5.70. Found C, 58.42; H, 11.08; N, 5.32.

6.3.1.13 Synthesis of [Ni(NPEt₃)₂]₄ 24

Inside the glove box, NiBr₂(DME) (315 mg, 1.02 mmol) was suspended in approximately 10 mL of THF in a 5-dram vial containing a magnetic stirring bar. A solution of KNPEt₃ (350 mg, 2.04 mmol) in approximately 7 mL of THF was added rapidly forming dark brown solution, which becomes deep purple overnight. The mixture was stirred at ambient temperature for 16 hours, after which the solvent was removed under reduced pressure. The residue was extracted with approximately 10 mL of hexane and the resulting solution was filtered through a celite plug to separate a grey solid (largely KBr) which was discarded. The solvent was removed from the filtrate under reduced pressure and a purple waxy solid was obtained. The solid was re-dissolved in approximately 10 mL pentane and the resulting solution cooled to -35 °C for 30 minutes to ensure the precipitation of any remaining KBr. The solution was then filtered, while cold, through a plug of celite and the solvent removed from the filtrate under reduced pressure, leaving a purple waxy solid. The product, [Ni(NPEt₃)₂]₄, (170 mg, 0.13 mmol, 52%), was dried under high vacuum, and submitted for elemental analysis. Calcd for $C_{48}H_{120}N_8Ni_4P_8$: C, 44.62; H, 9.36; N, 8.76. Found C, 42.54; H, 8.75; N, 8.43.

6.3.2 Preparation of solutions for UV-Vis spectroscopy

Solutions for UV-vis spectroscopy were prepare in the glove box, by dissolving 1.5 mg each **11a**, **11b**, **16** and **23** in 20 mL portions of THF. Approximately 1 mL of a sample solution was transferred to a re-sealable quartz cuvette, equipped with a Teflon valve. The cuvette was sealed and removed from the glovebox, and the UV-Vis spectra the sample recorded. The overlay of the spectra for all the complexes is shown below.

Figure 6.1
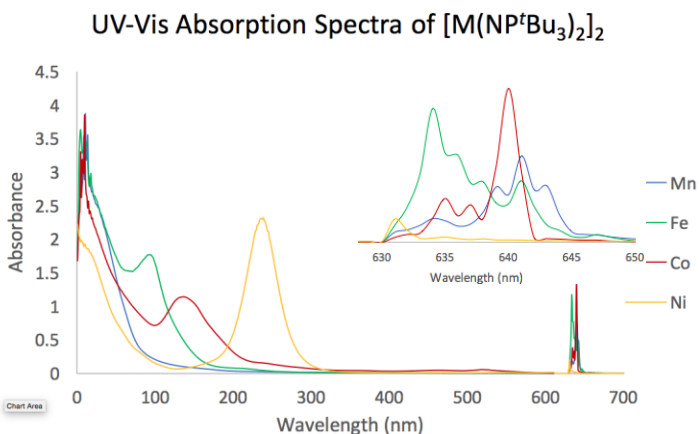
6.4 Experimental procedures for Chapter 2

6.4.1 General considerations and methods

All catalytic hydrodesulfurisation reactions were set up in a glove box. A Schlenk tube, fitted with a Teflon stopcock, was used for reactions conducted at atmospheric pressure, while glass lined steel autoclaves with Swagelok fittings were used for high pressure reactions. After removal from the glove box, hydrogen was introduced into the reaction vessel using Schlenk

techniques, or via a Swagelok system for high pressure reactions. All reactions were performed with clean Teflon-coated magnetic stirring bars. Dried and degassed solvents were used in all experiments.

For brevity, general procedures are presented for groups of reactions conducted in a similar manner, with specific modifications to these procedures listed as necessary. For some repetitive reactions, such as substrate scope, catalyst screening and optimization experiments, a condensed general procedure is presented, and the reader is referred to the original table in the thesis, where the results appear.

6.4.2 Activation of nickel precatalyst

6.4.2.1 Reaction between [Ni(NP^{t}Bu$_3$)$_2$]$_2$ 23 and hydrogen.

Inside the glove box 5 mg of [Ni(NP^{t}Bu$_3$)$_2$]$_2$ **23** was dissolved in benzene-d$_6$ (2 mL) in a re-sealable NMR tube. The NMR tube was removed from the glovebox and degassed on a vacuum line by 3 freeze-pump-thaw cycles. The NMR tube was then backfilled with 1 atm of hydrogen at room temperature, then resealed. Finally, the tube was heated in an oil bath to 80°C for 2 hours and then 110 °C for 24 h. The ^{31}P spectra at each stage of the process:

At room temperature before exposure to H$_2$ - No signal
At room temperature after exposure to H$_2$ -   No signal
After heating 80 °C for 2 hours -   single resonance δ 57 ppm
After heating 110 °C for 24 hours-   δ 57 ppm Increased intensity

The reaction was repeated with 200 mg of [Ni(NP^{t}Bu$_3$)$_2$]$_2$ **23** in benzene using a Schlenk tube.

After heating to 110 °C for 24 under hydrogen a black precipitate (6 mg) formed. The solution

was decanted and the black precipitate (11 mg) dried and submitted for submitted for elemental analysis. Found C, 3.04; H, 0.25; N, 0.19

6.4.2.2 Reaction between [Ni(NP^{t}Bu$_3$)$_2$]$_2$ 23 and 9-BBN.

Inside the glove box [Ni(NP^{t}Bu$_3$)$_2$]$_2$ **23** (50 mg, 0.05 mmol) was dissolved in 5 mL of hexane and a solution of 9-BBN dimer (25 mg, 0.10 mmol) in 1 mL of THF was added rapidly, a dark green colour developed immediately. The mixture was stirred at ambient temperature for 16 hours, after which the solvent was removed under reduced pressure. The green solid was extracted with 5 mL of pentane and the resulting solution was filtered through a celite plug. On cooling to -35 °C, single crystals of **66a**[142] were obtained and submitted for X-ray diffraction. The organometallic products could not be separated from **66a** based on differential solubility.

6.4.3 Hydrodesulfurization Experiments.

6.4.3.1 General procedure for HDS reactions at 1 atm of H$_2$

Inside the glove box, a re-sealable glass reactor (Schlenk tube) containing a Teflon coated magnetic stirring bar was charged with appropriate reagents and a solvent (8 mL). The reactor was sealed with a Teflon valve, removed from the glovebox, and degassed on a vacuum line by 3 freeze-pump-thaw cycles. The reactor was backfilled with 1 atm of hydrogen at room temperature, then resealed and placed in a preheated oil bath/metal block on a magnetic stirring plate, which was set to 1200 rpm and stirred a prescribed time. After cooling the reactor to room temperature, the hydrogen was vented and the reaction mixture was

quenched with 10% HCl (5 mL), then extracted with diethyl ether. The organic fraction was collected, dried with MgSO$_4$, and filtered through a plug of Florisil. Dodecane (25 L) was added as an internal standard and the resulting solution diluted with diethyl ether to 25 mL in a volumetric flask. 1 mL of this final solution was then transferred to a GC sample vial and submitted for GC analysis. The analysis of reaction products was performed using gas chromatography with flame ionization detection (GC-FID) on an Agilent 6890N gas chromatograph equipped with a HP-5 (5% phenyl)-methylpolysiloxane capillary column (Agilent). The concentration of dibenzothiophene, 2-phenylthiophenol and biphenyl were determined by reference an appropriate calibration curve.

6.4.3.2 Stoichiometric reaction between Ni pre-catalysts, DBT and H$_2$.

Following the general procedure for HDS reactions at 1 atm of H$_2$, DBT (100 mg, 0.54 mmol), the nickel precatalyst (0.54 mmol of Ni), and toluene (8 mL) were reacted with hydrogen for 16 hours. The reactor was cooled and the products extracted and submitted for GC analysis The results appear in Table **2.1**

6.4.3.3 Stoichiometric reaction between Ni precatalysts, 9-BBN, DBT and H$_2$

Following the general procedure for HDS reactions at 1 atm of H$_2$, DBT (50 mg, 0.54 mmol), the nickel precatalyst (0.54 mmol of Ni), 9-BBN dimer (131 mg 0.54 mmol) and toluene (8 mL) were reacted together with hydrogen at 110 °C for 16 hours. The reactor was cooled and the products extracted and submitted for GC analysis. Results appear in Table **2.2**

6.4.3.4 Mn, Ni and Cu catalyzed HDS of DBT at 1 atm of H$_2$ in the presence of KH

Following the general procedure for HDS reactions at 1 atm of H$_2$, DBT (100 mg, 0.54 mmol), a precatalyst (4 mol % metal), KH (65.0 mg 1.63 mmol) and THF/toluene (8 mL) were reacted together with hydrogen at 110 °C for 16 hours. The reactor was then cooled and the products extracted and submitted for GC analysis.

Table **6.1** Metal-catalyzed, KH mediated desulfurization of DBT

Entry	Precatalyst [M]	mmol [M]^a	Solvent	% Yield BP	% Yield BP-SH
1	[MnMe(NP^{t}Bu$_3$)]$_2$ **15**	0.0108	Tol	19	28
2	[Mn (NP^{t}Bu$_3$)$_2$]$_2$ **16**	0.0108	Tol	23	31
3	[MnMe(NPEt$_3$)]$_4$ **8a**	0.0054	Tol	20	36
4	[Mn(NPEt$_3$)$_2$]$_4$ **17**	0.0054	Tol	14	43
5	[(Cu(NP^{t}Bu$_3$)$_4$Li$_2$] **21**	0.0054	Tol	11	37
6	[Cu(NP^{t}Bu$_3$)]$_4$ **22**	5.4 x 10^{-3}	Tol	18	29
7	[Ni(NP^{t}Bu$_3$)$_2$]$_2$ **23**	1.08 X 10^{-2}	THF	88	1
8	[Ni(NPEt$_3$)$_2$]$_4$ **24**	5.4 x 10^{-3}	THF	91	0

^{a}The loading of the precatalysts were adjusted to achieve that 4 mol % metal atoms

6.4.3.5 Transition metal free HDS of DBT by KH

Inside the glove box, a re-sealable glass reactor (Schlenk tube) containing a Teflon coated magnetic stirring bar was charged with DBT (100 mg, 0.54 mmol), and KH (65 mg 1.63 mmol) and THF (8 mL). The reactor was sealed and remove from the glove box and heated at 110 °C

for 16 hours. **No hydrogen was added to the reactor**. After 16 hours, the reactor was cooled and the products extracted and submitted for GC analysis according to the general procedure for HDS reactions, above. The yield of biphenyl and 4-phenylthiophenol is variable. The best conversion obtained was 55 % biphenyl and 38 % 4-phenylthiophenol.

6.4.3.6 Transition metal free HDS of DBT using KNH$_2$/H$_2$

Following the general procedure for HDS reactions at 1 atm of H$_2$, DBT (100 mg, 0.54 mmol), and KNH$_2$ (90 mg 1.63 mmol) and toluene (8 mL) were reacted together with hydrogen at 150 °C for 16 hours. After 16 hours, the reactor was cooled and the products extracted and submitted for GC analysis. Biphenyl 44 % and 4-phenylthiophenol 25 % were obtained.

6.4.3.7 Ni catalyzed desulfurization of DBT using KO^{t}Bu/Et$_3$SiH

Inside the glove box, a re-sealable glass reactor (Schlenk tube) containing a Teflon coated magnetic stirring bar was charged with DBT (100 mg, 0.54 mmol), a precatalyst (4 mol % Ni), KO^{t}Bu (181 mg 1.63 mmol), and triethylsilane (190 mg, 1.63 mmol) and toluene (8 mL). The reactor was sealed and remove from the glove box and heated at 120 °C for 16 hours. *No hydrogen was included in the reaction*. The reactor was then cooled and the products extracted and submitted for GC analysis. The results appear in Table **2.4**

6.4.3.8 Ni catalyzed desulfurization of DBT using KO^{t}Bu/9-BBN

Inside the glove box, a re-sealable glass reactor (Schlenk tube) containing a Teflon coated magnetic stirring bar was charged with DBT (100 mg, 0.54 mmol), [Ni(NP^{t}Bu$_3$)$_2$]$_2$ **23** (5.3 mg, 5.4

x10^{-3}mmol) KO^{t}Bu (181 mg 1.63 mmol), and triethyl silane (190 mg, 1.63 mmol) and toluene (8 mL). The reactor was sealed and remove from the glove box and heated at 120 °C for 16 hours. *No hydrogen was included in the reaction*. The reactor was then cooled and the products extracted and submitted for GC analysis according to the procedures above. Yield: Biphenyl 42 % and 4-phenylthiophenol 55 % were present in the organic fraction.

6.4.3.9 Attempt at Ni catalyzed desulfurization of DBT using KO^{t}Bu and H$_2$

Following the general procedure for HDS reactions at 1 atm of H$_2$, DBT (100 mg, 0.54 mmol), a Ni phosphoranimide precatalyst (0.021 mmol of Ni, 4 mol % Ni), KO^{t}Bu (133 mg 1.19 mmol), 9-BBN (5.2 mg, 2.16 x 10^{-2} mmol) and toluene (8 mL) were combined together with hydrogen and the reaction mixture heated for to 110 °C 16 hours. The reactor was then cooled and the products extracted and submitted for GC analysis. Only trace conversion of DBT is observed under these conditions.

6.4.3.10 Attempt at Ni catalyzed desulfurization of DBT using KO^{t}Bu , H$_2$ and a reducing metal.

Following the general procedure for HDS reactions at 1 atm of H$_2$, DBT (100 mg, 0.54 mmol), [Ni(NP^{t}Bu$_3$)$_2$]$_2$ **23** (10.6 mg, 1.08 x10^{-2} mmol), KO^{t}Bu (133 mg 1.19 mmol), 9-BBN (5.2 mg, 2.16 x 10^{-2} mmol), and a reducing metal (200 mg) were added to a glass reactor along with toluene (8 mL). The mixture was combined together with hydrogen and the reaction mixture heated for to 110 °C 16 hours. The reactor was then cooled and the products extracted and submitted for GC analysis.

Table **6.2** Limited promotional effect of reducing metal on HDS

Entry	Metal	mmol Mg/Mn/Zn	% Conv.	% Yield BP	% Yield BP-SH
1	Mg	8.33	4	2	2
2	Mn	3.70	3	2	6
3	Zn	3.07	6	1	1

6.4.3.11 General procedure for Ni catalyzed hydrodesulfurization of DBT at elevated pressure using unsupported Ni catalysts.

Inside the glove box, a glass-lined steel autoclave equipped with a Teflon coated magnetic stir bar was charged with dibenzothiophene (100 mg, 0.54 mmol), KO^{t}Bu (134 mg, 1.19 mmol) and the nickel precatalyst (0.021 mmol of Ni), along with solvent (8 mL). The reactor was sealed, removed from the glovebox, purged three times and pressurized with hydrogen. The sealed autoclave was then placed in a preheated oil bath on a magnetic stirring plate set to 1200 rpm. After the indicated reaction time, the autoclave was cooled rapidly by submerging in cold water, and the excess pressure vented. The glass liner was removed from the autoclave and the reaction mixture quenched with 10 % HCl solution (5 mL), then extracted with diethyl ether. The organic fraction was collected and dried with MgSO$_4$, and filtered through a plug of Florisil. Dodecane (25 ⌀L) was added as an internal standard and the resulting solution diluted with diethyl ether to 25 mL in a volumetric flask. The concentration of dibenzothiophene, 2-

phenylthiophenol and biphenyl were determined by GC analysis, with reference to a calibration curve.

6.4.3.12 Ni catalyzed desulfurization of DBT using KO^{t}Bu and H$_2$ (at elevated pressure) promoted by a reducing metal.

Following the general procedure for reactions elevated pressure, DBT (100 mg, 0.54 mmol), [Ni(NP^{t}Bu$_3$)$_2$]$_2$ **23** (10.6 mg, 1.08 x10^{-2} mmol), KO^{t}Bu (133 mg 1.19 mmol), 9-BBN (5.2 mg, 2.16 x 10^{-2} mmol), and manganese (225 mg, 4.2 mmol) were added to a glass lined autoclave along with toluene (8 mL). The reactor was pressurized to 60 psi (4 atm) with hydrogen and the reaction mixture heated for to 110 °C 16 hours. The reactor was cooled and the excess hydrogen vented. The products were extracted and submitted for GC analysis according to the general procedure above. Yield: biphenyl 9 %, 4-phenylthiophenol 3 %.

6.4.3.13 Optimization of Ni catalyzed desulfurization of DBT using KO^{t}Bu, at elevated pressure of H$_2$ (500 psi)

Following the general procedure for reactions elevated pressure, dibenzothiophene (100 mg, 0.54 mmol), KO^{t}Bu (134 mg, 1.19 mmol) and the nickel precatalyst (0.021 mmol of Ni), along with solvent (8 mL) were added to a glass lined autoclave. The reactor was pressurized to 500 psi (34 atm) with hydrogen and the reaction mixture heated to 150 °C for 16 hours. The reactor was cooled and the excess hydrogen vented. The products were extracted and submitted for GC analysis

Table **6.3** Optimization of reaction conditions for 'homogeneous' HDS at elevated pressure

Entry	Catalyst	Solv.	Additive[a]	% Conv.	Yield BP	Yield BP-SH	DBT Recovered	% unrecovered
1	Ni(COD)$_2$	hex	-	79	11	56	21	11
2	Ni(COD)$_2$	thf	-	40	12	17	60	11
3	Ni(COD)$_2$	tol	-	44	27	13	56	4
4	Ni(COD)$_2$	tol	Al$_2$O$_3$	94	79	7	6	8
5	**13b**	hex	-	83	10	63	17	10
6	**13b**	thf	-	99	8	85	1	6
7	**13b**	tol	-	35	10	22	65	3
8	**13b**	cyclooct.	-	44	12	24	56	8
9	**13b**	cyclooct.	Al$_2$O$_3$	91	79	1	9	11
10	**23**	hex	-	93	11	72	7	10
11	**23**	thf	-	96	19	75	4	3
12	**23**	tol	-	48	12	23	52	12
13	**23**	cyclooct.	-	85	36	37	15	12
14	**23**	cyclooct.	Al$_2$O$_3$	92	74	6	8	13
15	**24**	hex	-	99	30	65	1	4
16	**24**	thf	-	96	19	75	4	1
17	**24**	tol	-	45	19	24	55	2
18	**24**	cyclooct.	-	80	57	15	20	7
19	**24**	cyclooct.	Al$_2$O$_3$	95	88	1	5	6
20	**24**[b]	cyclooct.	Al$_2$O$_3$	92	84	2	4	10
21	**24**[c]	cyclooct.	Al$_2$O$_3$	82	79	6	10	5
22	nil	cyclooct.	Al$_2$O$_3$	1	trace	trace	99	-

[a]130 mg of Al$_2$O$_3$ used as an additive. [b]KO^{t}Bu purified by sublimation. [c]2 mol % Ni.

6.4.3.14 Mercury test for homogeneity

The general procedure above for Ni catalyzed hydrodesulfurization of DBT at elevated pressure was followed, but with excess mercury (1.5 g, 7.48 mmol, 356 equiv Hg per Ni) added to the reaction mixture. The autoclave was pressurized with hydrogen to 34 atm and heated for 16 h, after which the suspension was decanted from the mercury puddle and the reaction quenched,

extracted, and analyzed according to the general procedure above. All reactions were suppressed significantly as shown in Table **2.7**

6.4.3.15 Preparation of SEM samples for unsupported heterogeneous catalysts

The general procedure for HDS at atmospheric pressure was followed using dibenzothiophene (100 mg, 0.54 mmol), KO^{t}Bu (134 mg, 1.19 mmol) and precatalyst 23 (20 mg 0.021 mmol). After heating to 110 °C for 16 h, the hydrogen was evacuated on a Schlenk manifold and the reactor returned to the glovebox. Two drops of the reaction mixture were deposited on a TEM grid (ultra-thin carbon film on lacey carbon support film, 300 mesh, gold) and the solvent allowed to evaporate. The grid was dried for 3 h, then submitted in a sealed vial under nitrogen for immediate analysis. The grid was removed from the vial and exposed momentarily to air before being place under high vacuum for analysis. SEM analysis was performed by staff at University of Alberta nanoFAB Fabrication and Characterization Centre using a Zeiss Sigma field emission scanning electron microscope (FESEM).

6.5 Experimental procedures for Chapter 3

6.5.1 Preparation of Alumina and SiO$_2$ for grafting.

Chromatography grade silica, and Brockman activity I neutral alumina were dried at 180 °C for at least 16 h before use. Brockman activity I, basic alumina was heated in air at 560 °C for 4 h, then maintained at the same temperature under vacuum for 12 h. SiO$_2$-700 was prepared according to literature procedures from fumed silica (Millipore-Sigma 0.4 – 0.5 ⬛m).[230, 242] Silica

nanoparticles were obtained from Millipore-Sigma chemical company and dried at 180 °C for at least 16 h before use.

6.5.2 Immobilization of 13b, 23 and 24 onto alumina and silica.

6.5.2.1 General procedure for Immobilization of 13b, 23 and 24 onto alumina and silica

Inside the glove box, a pentane solution (10 mL) containing a nickel phosphoranimide precatlyst was added rapidly to a pentane slurry of alumina/silica at ambient temperature. The resulting slurry was stirred for 30 minutes, with decolorization typically occurring after 1 minute. The resulting coloured solid, was collected by filtration, was washed with pentane, then dried *in vacuo*. The filtrate and washings were combined and the pentane removed under reduced pressure, and any residue dissolved in benzene-d_6 for NMR analysis.

6.5.2.2 Grafting of 13b onto SiO_2 or Al_2O_3

The general procedure above was followed using **13b** (45.8 mg 0.041 mmol) and alumina/silica (954 mg), A green solid was obtained and no resonance corresponding to $^tBu_3PNH$ was present in the ^{31}P NMR spectrum. Calcd for 4.58 wt % 2@Al_2O_3: C, 2.40; H, 0.45; N, 0.23. Found C, 2.86; H, 0.69; N, 0.26.

6.5.2.3 Grafting of 23 onto SiO₂ or Al₂O₃

The general procedure above was followed using **23** (40 mg 0.04 mmol) and alumina/silica (960 mg), A light brown solid was obtained and resonance at 57 ppm corresponding to ^{t}Bu₃PNH was present in the ^{31}P NMR spectrum. Calcd for 4 wt % 23@Al₂O₃: C, 2.41; H, 0.45; N, 0.23. Found C, 2.59; H, 0.68; N, 0.27.

6.5.2.4 Grafting of 24 onto SiO₂ or Al₂O₃

The general procedure above was followed using **24** (52 mg 0.04 mmol) on alumina/silica (948 mg) forming a dark brown free-flowing solid. Calcd for 5.2 wt % 24@Al₂O₃: C, 2.28; H, 0.48; N, 0.44. Found C, 2.47; H, 0.59; N, 0.53.
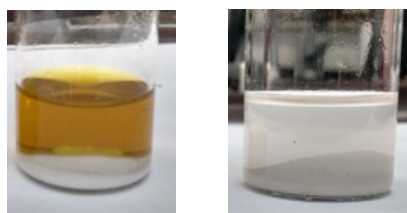
Figure **5.2** Photograph showing a typical grafting experiment immediately after adding a yellow-brown pentane solution of **23** to alumina (left), and the same vial after stirring for 1 minute (right).

6.5.2.5 Recovery of ^{t}Bu₃PNH from alumina

Inside the glove box a solution of ^{t}Bu₃PNH (25 mg, 0.11 mmol) in 10 mL hexane was added to Activity I basic alumina (1.5 g) and the resulting slurry stirred for 16 hours. The slurry was then vacuum filtered and the alumina rinsed with 3 X 10 mL of hexane. The filtrate and the washings

were combined and the hexane removed under vacuum to yield a small amount of a white solid $^{t}Bu_3PNH$ (9.5 mg 38 % recovery).

6.5.2.6 Monitoring the grafting of 23 onto SiO$_{2-700}$ by IR spectroscopy

First, the IR spectra of freshly prepared sample of SiO$_2$-700 as well as that for **23** were recorded under air and moisture free conditions, using a custom cell composed of two KBr salt plates, sealed with a greased O-ring. The procedure for grafting **23** (19 mg 0.019 mmol) onto SiO$_2$-700 (0.34 OH/g 150 mg, 0.038 mmol OH) was followed, and the IR spectrum of the light brown solid formed was recorded. The overlay of the spectra is shown in Figure **3.6**

6.5.2.7 Preparation of TEM samples of silica-grafted Ni pre-catalysts.

Inside the glove box, a yellow-brown pentane solution (10 mL) containing 3 (19 mg 0.019 mmol) was added rapidly to a pentane slurry of silica powder (150 mg, 5-15 nm silica particles) at ambient temperature. A purple slurry was obtained which was stirred for 16 h. The slurry was filtered through a fritted disc, and the separated purple powder was washed with pentane. 2 mg of the powder was suspended in fresh pentane (20 mL) and stirred vigorously. Two drops of this mixture were deposited on a TEM grid (ultra-thin carbon film on lacey carbon support film, 300 mesh, gold) and the solvent allowed to evaporate. The grid was dried for 3 h, then submitted in a sealed vial under nitrogen for immediate analysis. The grid was removed from the vial and exposed momentarily to air before being place under high vacuum for analysis. TEM analysis was performed on a JEOL JEM-ARM200cF S/TEM, which is equipped with a cold

Field-Emission Gun (cFEG) and a probe Cs corrector. Figures **3.7** and **3.8** display the images of the silica-supported Ni clusters, as well as the elemental composition data from EDX.

6.5.3 Synthesis of alkali metal alkoxides

Potassium isopropoxide. KO^{i}Pr was prepared by adding KH (1000 mg 24.9 mmol) and dry deoxygenated 2-propanol (3.8 mL 49.9 mmol) to toluene (15 mL) at room temperature. The reaction mixture was stirred for 16 h, then filtered. The volatiles were removed under reduced pressure, yielding an off-white solid. The solid was dried under high vacuum, affording a white powder (2053 mg, 84 %). Calcd for C_3H_7KO : C, 36.70; H, 7.19. Found C, 37.51; H, 7.38.

KOMe was prepared similarly from KH (1000 mg 24.9 mmol) dry deoxygenated 2-methanol (2.0 mL 49.9 mmol), affording the expected product as a white powder (1125 mg 65 %) Calcd for CH_3KO : C, 17.13; H, 4.31. Found C, 18.21; H, 4.88.

CsO^{t}Bu and RbO^{t}Bu were synthesized from metallic Cs or Rb and dry, deoxygenated tert-butanol according to literature procedures.[327-328]   CsOtBu: 84 % yield. Calcd for C_4H_9CsO : C, 23.32; H, 4.40. Found C, 24.41; H, 4.60. RbOtBu: 81 % yield. Calcd for C_4H_9RbO : C, 30.30; H, 7.72. Found C, 31.37; H, 5.91.

6.5.4. Hydrodesulfurization experiments

6.5.4.1 General procedure for Ni-catalyzed hydrodesulfurization of DBT at elevated pressure using pre-supported catalysts.

Inside the glove box, a glass lined steel autoclave equipped with a Teflon coated magnetic stirring bar was charged with dibenzothiophene (100mg, 0.54 mmol), KO^{t}Bu (134 mg, 1.19 mmol) and a supported nickel catalyst (0.021 mmol of Ni), For **23@Al$_2$O$_3$** 260 mg of the pre-supported catalyst was added to achieve approximately 0.021 mmol of Ni, while only 130 mg of **24@Al$_2$O$_3$** was used to achieve the same catalyst loading. The reaction was subsequently performed following the general procedure for Ni catalyzed hydrodesulfurization of DBT at elevated pressure described earlier. Tables **3.2** and **3.3** display results for HDS using these supported Ni catalysts under various reaction conditions.

6.5.4.2 Ni-catalyzed hydrodesulfurization of DBT at elevated pressure using in situ supported catalysts.

In Table **3.4** various nickel sources are explored as HDS catalyst. Dibenzothiophene (100 mg, 0.54 mmol), KO^{t}Bu (134 mg, 1.19 mmol) and the nickel precatalyst (0.021 mmol of Ni), alumina (130 mg), along with THF/Toluene 2:6 (8 mL) were added to a glass lined autoclave. The reactor was pressurized with hydrogen and the reaction mixture heated for to the prescribed time. The reactor was cooled and the excess hydrogen vented. The products were extracted and submitted for GC analysis. The results appear in Table **3.4**

24 was prepared in situ from KNPEt$_3$ (7.19 mg, 0.042 mmol) and NiBr$_2$(DME) (6.5 mg, 0.021 mmol). All the other Ni salts and Ni(COD)$_2$ were added directly to the reactor without further treatment.

6.5.4.3 Evaluation of the longevity of the alumina supported catalysts.

Inside the glove box a glass lined steel autoclave equipped with a Teflon coated magnetic stirring bar was charged with dibenzothiophene (300 mg, 1.62 mmol), KO^{t}Bu (402 mg, 2.57 mmol) and 4@Al$_2$O$_3$ (130 mg, 0.021 mmol of Ni), along with 15 mL of toluene. The autoclave was sealed and removed from the glove box and pressurized to 34 atm with hydrogen, then placed in a pre-heated oil bath at 150 °C for 48 h. The reaction was then quenched and the products extracted and analysed by GC. Yield: 75 % biphenyl, 6 % 4-phenylthiophenol

6.5.4.4 Monitoring the conversion of DBT to 4-phenylthiophenol and biphenyl over time

Because the microreactor design does not allow sampling aliquots from an ongoing reaction, the conversion over time was determined using eight identical reaction mixtures heated to the same temperature for increasing amounts of time. DBT was added to 8 separate glass lined autoclaves, each containing KO^{t}Bu and 4@Al$_2$O$_3$. Each reactor was pressurized to 200 psi of H$_2$ and then placed in a pre-heated oil bath (200 °C) for a specific amount of time (0.5, 1.0, 1.5, 2.0, 2.5, 3.0, 3.5, 4.0 h), then cooled rapidly by immersion in cold water and subjected to analysis by quantitative GC. The results are shown in table **6.8** below and also appear in Figure **3.9**

Table **6.4** Conversion over 4h, of DBT to 4-phenylthiophenol and biphenyl at 200 °C and 14 atm (200 psi) of H$_2$

Time (h)	% of total organics		
	BP	BP-SH	DBT
0	0	0	100
0.5	24.9	8.3	66.8
1.0	46.7	4.8	48.5
1.5	57.5	2.7	39.8
2.0	62.2	2.4	35.3
2.5	69.2	2.7	28.1
3.0	71.7	2.6	27.4
3.5	71.9	1.2	27.1
4.0	72.1	1	26.9

6.5.4.5 Determination of deuterium incorporation into biphenyl recovered from Ni-catalyzed hydrodesulfurization of DBT

Inside the glove box, a glass-lined steel autoclave equipped with a Teflon coated magnetic stir bar was charged with dibenzothiophene (100 mg, 0.54 mmol), KO^{t}Bu (134 mg, 1.19 mmol) and the nickel catalyst (3@Al$_2$O$_3$ 0.021 mmol of Ni), along with THF (8 mL). The reactor was pressurized to 17 atm (250 psi) of D$_2$ and 175 °C for 16 h. After GC analysis to determine the distribution of products, a 10 % NaOH solution (5 mL) was added to convert 2-phenylthiophenol to a water-soluble thiophenolate salt. The mixture was again extracted with diethyl ether. The organic fraction was collected, dried over MgSO$_4$, and filtered through a plug of celite; GC analysis confirmed the presence of biphenyl. The volatiles were removed under reduced pressure to yield a white solid. A small portion of the solid was dissolved in CH$_2$Cl$_2$ and the ^{2}H NMR spectrum recorded. A second portion of the solid (11 mg) was dissolved in CD$_2$Cl$_2$ along with hexamethyldisiloxane (5.3 mg), and the ^{1}H NMR spectrum recorded. The ratio of the

integral for each proton compared to hexamethyldisiloxane was used to determine the proportion of protium remaining at each position.

Figure **6.3** ^{1}H and ^{2}H NMR spectra of biphenyl recovered from HDS of DBT under D$_2$, showing deuterium incorporation into final product.
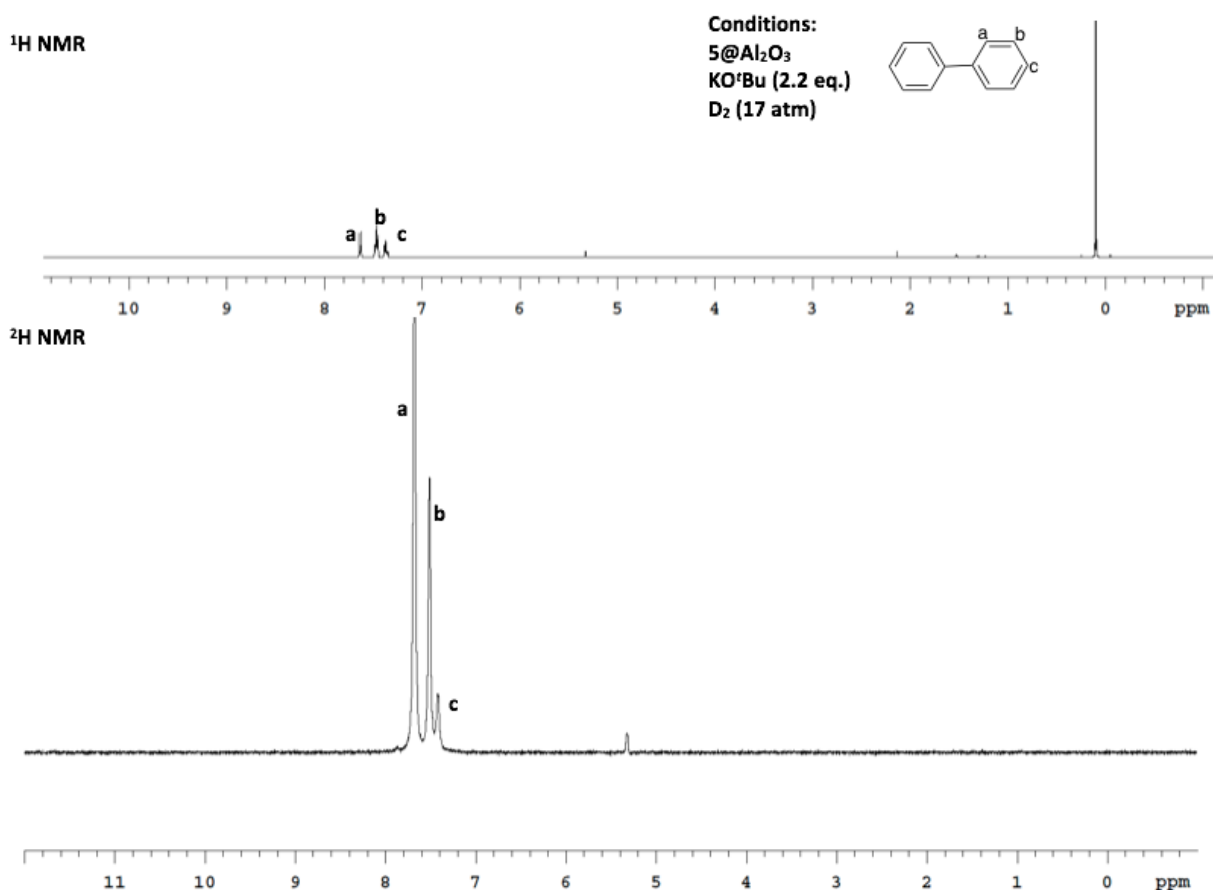
6.5.4.6 Determination of H/D exchange in DBT mediated by KO^{t}Bu and NaO^{t}Bu

The procedure used for the determination of deuterium incorporation into biphenyl was followed using KO^{t}Bu (134 mg, 1.19 mmol) and DBT (100 mg 0.54 mmol), but with the exclusion of catalyst from the reaction mixture. GC analysis revealed only trace (<1%) conversion to

biphenyl or 2-phenylthiophenol. The ^{1}H and ^{2}H NMR spectra were recorded and are displayed below (Figure **6.4**). NMR analysis confirms complete isotopic substitution at the 4- and 6-positions of DBT as well as partial H/D exchange at all other positions. The isolated 4,6-deuterio DBT was used for further experiments described below. In a second experiment NaO^{t}Bu (114 mg, 1.19 mmol) was substituted for KO^{t}Bu (Figure **6.5**).

Figure **6.4** ^{1}H and ^{2}H NMR spectrum of showing H/D exchange on DBT in the presence of KO^{t}Bu and D$_2$
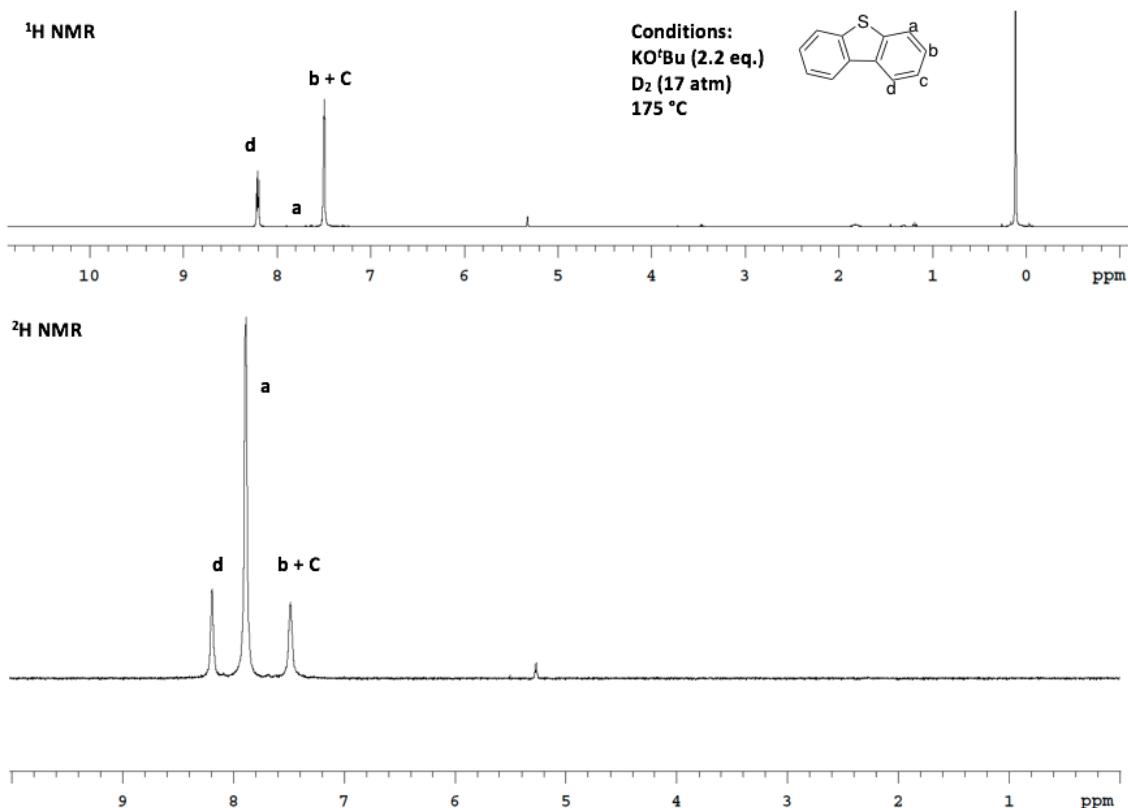
Figure **6.5** ^{1}H and ^{2}H NMR spectrum of showing H/D exchange on DBT in the presence of

NaO^{t}Bu and D$_2$
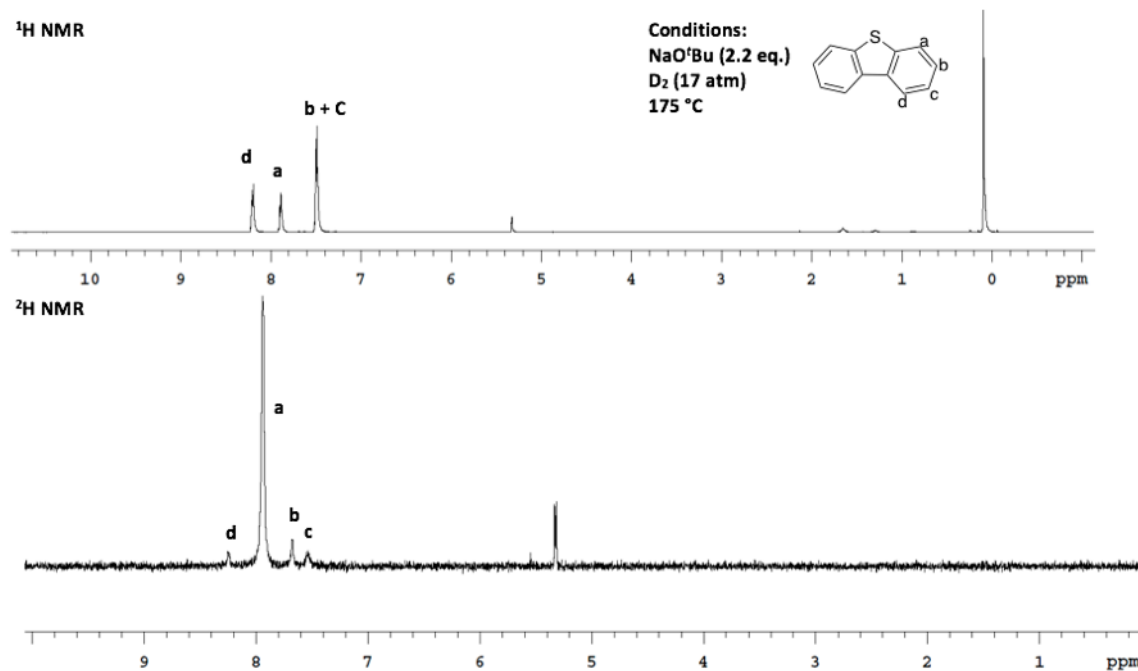
6.5.4.7 Comparison of the rate of desulfurization of DBT using H$_2$ and D$_2$

Following the general procedure for Ni catalyzed hydrodesulfurization of DBT at elevated pressure and temperature, DBT was added to two separate glass-lined autoclaves, each containing KO^{t}Bu and precatalyst **24**@alumina. Both reactors were pressurized to 14 atm (200 psi) one with H$_2$ and the other with D$_2$ labelled **A** and **B** respectively. The reactors were then heated to 200 °C in an oil bath for 1 h, then cooled rapidly by immersion in cold water, and the products isolated and analyzed as described above. Conversion for hydrogen **A**: 44% biphenyl, 8 % 4-phenylthiophenol. Conversion for deuterium **B**: 52% biphenyl, 9.5% 4-phenylthiophenol

6.5.4.8 Comparison of the rate of desulfurization of DBT and 4,6-DBT-d$_2$

Following the general procedure for desulfurization at elevated temperatures, DBT and 4,6-DBT-d$_2$ were added to individual glass-lined autoclaves, each containing KO^{t}Bu and precatalyst 4@alumina. Each reactor was pressurized to 17 atm (250 psi) of H$_2$ and heated to 175 °C in an oil bath for 1 h, then cooled rapidly by immersion in cold water. Isolation and quantitative GC analyses were conducted as previously described. For both reactions, the conversions were similar: 21% biphenyl, 20 % 4-phenylthiophenol

6.5.4.9 Substrate scope.

Following the general procedure for HDS at elevated temperature, an organosulfur compound (0.54 mmol), KO^{t}Bu (134 mg, 1.19 mmol) and **24**@Al$_2$O$_3$ (130 mg, 0.021 mmol of Ni) were added to a glass lined autoclave and the reactor pressurized to 200 psi of H$_2$ and heated to 175 °C for 4 hours. The products were isolated as previously described, and identified/quantified by GC-MS analysis. The results appear in Table **3.7**

6.5.4.10 Effect of base strength and alkali-cation identity on HDS

These reactions were conducted using the general procedure for HDS of DBT at elevated temperature using pre-supported catalyst. Inside the glove box, a glass lined steel autoclave equipped with a Teflon coated magnetic stirring bar was charged with dibenzothiophene (100mg, 0.54 mmol), a **base** (1.19 mmol) and **24**@Al$_2$O$_3$ (130 mg 0.021 mmol of Ni). KO^{i}Pr, KOMe, KOH, LiO^{t}Bu, NaO^{t}Bu, RbO^{t}Bu and CsO^{t}Bu were in turn substituted for KO^{t}Bu as the base. The reactor was charged with 500 psi of hydrogen and heated to 150 °C for 16 hours.

Isolation and quantitative GC analyses were conducted as previously described.

Table **6.5** Effect of base strength and alkali-cation identity on HDS of DBT

Entry	Base	Conv. (%)	Yield 1a (%)	Yield 1b (%)
1	LiO^{t}Bu	5	3	1
2	NaO^{t}Bu	22	19	0
3	KO^{t}Bu	97	88	1
4	RbO^{t}Bu	92	28	64
5	CsO^{t}Bu	55	9	46
6	KO^{i}Pr	27	10	14
7	KOMe	17	9	8
8	KOH	4	1	1

6.5.4.11 Alkali metal sulfides as promoters for HDS

These reactions were conducted using the general procedure for HDS of DBT at elevated temperature using pre-supported catalyst. DBT (100mg, 0.54 mmol), a **M₂S** (1.19 mmol) and **24**@Al$_2$O$_3$ (130 mg 0.021 mmol of Ni). Li$_2$S Na$_2$S K$_2$S were in turn substituted for KO^{t}Bu as the base. The reactor was charged with 500 psi of hydrogen and heated to the specified temperature for 16 hours. The results appear in Table **3.8**

6.6 Experimental procedures for Chapter 4

6.6.1 Precatalysts

The syntheses of **[Ni(NP^{t}Bu$_3$)]$_4$ 13b**, **[Cu(NP^{t}Bu$_3$)]$_4$ 22**, **[Ni(NP^{t}Bu$_3$)$_2$]$_2$ 23**, and **[Ni(NPEt$_3$)$_2$]$_2$ 24** are described earlier in this chapter.

6.6.2 General procedure for deoxygenation of 4-acetylbiphenyl at 1 atmosphere of hydrogen in the presence of molecular sieves

Inside the glove box, a resealable glass reactor (Schlenk tube) containing a Teflon coated magnetic stirring bar was charged with a 4-acetylbiphenyl (100 mg, 0.51 mmol), a catalyst, 3A or 4A molecular sieves (200 mg) and a solvent (8 mL). The reactor was sealed with a Teflon valve, removed from the glovebox, and degassed on a vacuum line by 3 freeze-pump-thaw cycles. The reactor was backfilled with 1 atm of hydrogen at room temperature, resealed and placed in a preheated oil bath/metal block on a magnetic stirring plate, which was set to 1200 rpm and stirred a prescribed time. After cooling the reactor to room temperature, the hydrogen was vented and the reaction mixture was quenched with distilled water, then extracted with diethyl ether. The organic fraction was collected, dried with MgSO$_4$, and filtered through a plug of Florisil. 1 mL of this final solution was then transferred to a GC sample vial and submitted for GC analysis.

6.6.3 General procedure for deoxygenation of 4-acetylbiphenyl at elevated pressure of H_2 in the presence of molecular sieves

Inside the glove box, a glass-lined steel autoclave equipped with a Teflon coated magnetic stir bar was charged with a ketone or aldehyde (0.51 mmol), catalyst (typically 0.051 mmol metal), 3 A or 4 A molecular sieves (200 mg) and a solvent (8 mL). The reactor was sealed, removed from the glovebox, purged three times and pressurized with hydrogen. The sealed autoclave was then placed in a preheated oil bath on a magnetic stirring plate set to 1200 rpm. After the indicated reaction time, the autoclave was cooled rapidly by submerging in cold water, and the excess pressure vented. The glass liner was removed from the autoclave and the reaction mixture quenched with distilled water, then extracted with diethyl ether. The extraction and analysis of the reaction products were conducted according to the general procedure above.

6.6.4 Deoxygenation of 4-acetylbiphenyl at 1 atm H_2 in the presence of 3A molecular sieves using [Ni(NPtBu₃)]₄ 13b

The general procedure 6.6.2 above was followed using 4-acetylbiphenyl (100 mg, 0.51 mmol), **13b** (5.6 mg, 0.0051 mmol), 3 A molecular sieves (200 mg) and toluene (8 mL). GC yields 27 % 1-(4-biphenyl)ethanol, 50 % 4-ethylbiphenyl, 11 % arene hydrogenation products.

6.6.5 Deoxygenation of 4-acetylbiphenyl at 1 atm H_2 in the absence of molecular sieves using 13b

The general procedure **6.6.2** above was followed using 4-acetylbiphenyl (100 mg, 0.51 mmol), **13b** (5.6 mg, 0.0051 mmol), and toluene (8 mL). No molecular sieves were added to this

reaction. GC-MS yields 61 % 1-(4-biphenyl)ethanol, 4 % 4-ethylbiphenyl, 2 % arene hydrogenation products.

6.6.6 Deoxygenation of 4-acetylbiphenyl at 1 atm H_2 in the presence of 4A molecular sieves using 13b

The general procedure **6.6.2** above was followed using 4-acetylbiphenyl (100 mg, 0.51 mmol), **13b** (5.6 mg, 0.0051 mmol), 4A molecular sieves (200 mg) and toluene (8 mL). GC yields 21 % 1-(4-biphenyl)ethanol, 53 % 4-ethylbiphenyl, 8 % arene hydrogenation products.

6.6.7 Deoxygenation of 4-acetylbiphenyl at 1 atm H_2 in the presence of Activity I alumina using 13b

The general procedure **6.6.2** above was followed using 4-acetylbiphenyl (100 mg, 0.51 mmol), **13b** (5.6 mg, 0.0051 mmol), alumina (200 mg) and toluene (8 mL). GC yields 21 % 1-(4-biphenyl)ethanol, 72 % 4-ethylbiphenyl, 4 % arene hydrogenation products.

6.6.8 Optimization of nickel catalyst and catalyst heterogeneity

The general procedure above was followed using 4-acetylbiphenyl (100 mg, 0.51 mmol), a **nickel catalyst** (0.02 mmol Ni), 3A molecular sieves (200 mg) and toluene (8 mL). Nickel catalysts used were: **13b** (5.61 mg, 0.0051 mmol), **23** (9.8 mg, 0.01 mol), **24** (6.7 mg, 0.0051 mmol), Ni(COD)$_2$(5.6 mg, 0.02 mmol). IPr$_2$Ni was prepared in situ from IPr.HBF$_4$ (19 mg 0.04 (mmol), Ni(COD)$_2$ (5.6 mg, 0.02 mmol) and NaO^{t}Bu (5 mg, 0.05 mmol) For precatalysts 13b, IPr$_2$Ni and Ni(COD)$_2$ a second reaction was conducted in the presence of mercury (1.5 g, 350 equivalents per Ni). Results are listed in **Table 4.1**

6.6.9 Deoxygenation of 4-acetylbiphenyl at 1 atm H$_2$ in the presence of 4A molecular sieves using [Cu(NPtBu$_3$)]$_4$ 22

The general procedure **6.6.2** above was followed using 4-acetylbiphenyl (100 mg, 0.51 mmol),

22 (5.8 mg, 0.0051 mmol), 4A molecular sieves (200 mg) and toluene (8 mL). No conversion was

detected by GC.

6.6.10 Deoxygenation of 4-acetylbiphenyl at 1 atm or at elevated H$_2$ pressure using 4A molecular sieves and IPrCuO^{t}Bu or CuO^{t}Bu

The general procedures **6.6.2/6.6.3** above were followed using 4-acetylbiphenyl (100 mg, 0.51

mmol), a copper catalyst (0.051 mmol Cu), 4A molecular sieves (200 mg) and toluene (8 mL).

For reactions at elevated pressure, 150 ps1 (10 atm) of hydrogen was used. IPrCuO^{t}Bu was

prepared in situ from IPr.HBF$_4$ (24 mg 0.051 (mmol), CuCl (5 mg, 0.051 mmol) and NaO^{t}Bu (10

mg, 0.102 mmol). For the ligand, free reactions CuO^{t}Bu was prepared from CuCl (5 mg, 0.051

mmol) and NaO^{t}Bu (10 mg, 0.102 mmol). Results appear in **Table 4.2**

6.6.11 Deoxygenation of 4-acetylbiphenyl at 1 atmosphere hydrogen pressure in the absence molecular sieves using CuO^{t}Bu

The general procedure **6.6.2** above was followed using 4-acetylbiphenyl (100 mg, 0.51 mmol),

a CuO^{t}Bu (0.051 mmol) and toluene (8 mL). CuO^{t}Bu was prepared in situ from CuCl (5 mg, 0.051

mmol) and NaO^{t}Bu (5 mg, 0.051 mmol) GC yields 81 % 1-(4-biphenyl)ethanol, 3 % 4-

ethylbiphenyl.

6.6.12 Substrate scope: Deoxygenation of various aryl ketones/aldehydes at 1 atm H_2 in the presence of 4A molecular sieves using CuO^tBu

The general procedure **6.6.2** above was followed using   a ketone/aldehyde (0.51 mmol), CuO^tBu (0.051 mmol), 4A molecular sieves (200 mg) and THF (8 mL). CuO^tBu was prepared in situ from CuCl (5 mg, 0.051 mmol) and NaO^tBu (5 mg, 0.051 mmol) Yields were determined by GC-MS analysis. Using THF avoided the presence of ambiguous aromatic signals GC-MS data arising from toluene. Results are listed in Table **4.3**

6.6.13 Kinetic experiments

6.6.13.1 Deoxygenation of 4-acetylbiphenyl at 1 atm H_2 in the presence molecular sieves using CuO^tBu over 1 hour.

The general procedure above was followed using 4-acetylbiphenyl (100 mg, 0.51 mmol), a CuO^tBu (0.051 mmol) 4A molecular sieves (200 mg) and toluene (8 mL). CuO^tBu was prepared in situ from CuCl (5 mg, 0.051 mmol) and NaO^tBu (5 mg, 0.051 mmol). The reaction was stopped after 1 hour and the products identified by GC analysis according to the procedures above. The results appear in Equation **4.4**

6.6.13.2 Monitoring the conversion of 4-acetylbiphenyl over time in the presence of 4A molecular sieves using CuO^tBu

Because the microreactor design does not allow sampling aliquots from an ongoing reaction, the conversion over time was determined using four identical reaction mixtures heated to the same temperature for increasing amounts of time. Following the general procedure for deoxygenation of ketone/aldehyde at elevated pressure of hydrogen in the presence of molecular sieves 4 acetylbiphenyl was added to four separate glass lined autoclaves, each

containing CuCl, NaOtBu, and 4 A molecular sieves. Each reactor was pressurized to 150 psi (10 atm) of H_2 and then placed in a pre-heated oil bath (120 °C) for a specific amount of time (1.0, 2.0, 3.0, 4.0 h), then cooled rapidly by immersion in cold water. Yields were determined by GC analysis. Results are displayed on Figure **4.2** and Table **4.4**

6.6.14 Hydrogenation of aliphatic ketones at 1 atm H_2 in the presence of 4A molecular sieves using CuO^tBu

Following the general procedure **6.6.3** above, an aliphatic ketone (0.51 mmol), CuO^tBu (0.051 mmol), 4A molecular sieves (200 mg) and THF (8 mL) were added to a glass lined autoclaves. The reactor was pressurized to 150 psi (10 atm) of H_2 heated for 4 hours Yields were determined by GC-MS analysis and the results are listed in Scheme **4.10**

References

1. Noyori, R. *Angew. Chem. Int. Ed.* **2002**, *41*, 2008-2022.
2. Sharpless, K. B. *Angew. Chem. Int. Ed.* **2002**, *41*, 2024-2032.
3. Knowles, W. S. *Angew. Chem. Int. Ed.* **2002**, *41*, 1998-2007.
4. Grubbs, R. H. *Angew. Chem. Int. Ed.* **2006**, *45*, 3760-3765.
5. Schrock, R. R. *Angew. Chem. Int. Ed.* **2006**, *45*, 3748-3759.
6. Chauvin, Y. *Angew. Chem. Int. Ed.* **2006**, *45*, 3740-3747.
7. Suzuki, A. *Angew. Chem. Int. Ed.* **2011**, *50*, 6722-6737.
8. Negishi, E.-i. *Angew. Chem. Int. Ed.* **2011**, *50*, 6738-6764.
9. Full Text of Alfred Nobel's Will. https://www.nobelprize.org/alfred_nobel/will/will-full.html (accessed October 30, 2017).
10. Hagen, J., Homogeneously Catalyzed Industrial Processes. In *Industrial Catalysis*, Wiley-VCH Verlag GmbH & Co. KGaA: 2015; pp 47-80.
11. Chirik, P. J.; Gunnoe, T. B. *ACS Catalysis* **2015**, *5*, 5584-5585.
12. Chirik, P.; Morris, R. *Acc. Chem. Res.* **2015**, *48*, 2495-2495.
13. Chirik, P. J. *Acc. Chem. Res.* **2015**, *48*, 1687-1695.
14. Li, Y.-Y.; Yu, S.-L.; Shen, W.-Y.; Gao, J.-X. *Acc. Chem. Res.* **2015**, *48*, 2587-2598.
15. Morris, R. H. *Chem. Soc. Rev.* **2009**, *38*, 2282-2291.
16. Gaillard, S.; Renaud, J.-L. *ChemSusChem* **2008**, *1*, 505-509.
17. Tasker, S. Z.; Standley, E. A.; Jamison, T. F. *Nature* **2014**, *509*, 299-309.
18. Miao, J.; Ge, H. *Eur. J. Org. Chem.* **2015**, *2015*, 7859-7868.
19. Chirik, P. J. *Angew. Chem. Int. Ed.* **2017**, *56*, 5170-5181.
20. Han, F.-S. *Chem. Soc. Rev.* **2013**, *42*, 5270-5298.
21. Astruc, D., Bio-Organometallic Chemistry: Enzymatic Catalysis. In *Organometallic Chemistry and Catalysis*, Springer Berlin Heidelberg: Berlin, Heidelberg, 2007; pp 441-456.
22. McEvoy, J. P.; Brudvig, G. W. *Chem. Rev.* **2006**, *106*, 4455-4483.
23. Beck, R.; Shoshani, M.; Johnson, S. A. *Angew. Chem.* **2012**, *124*, 11923-11926.
24. Hu, S.; Shima, T.; Hou, Z. *Nature* **2014**, *512*, 413-415.
25. Shoshani, M. M.; Johnson, S. A. *Nat. Chem* **2017**.
26. Shima, T.; Hu, S.; Luo, G.; Kang, X.; Luo, Y.; Hou, Z. *Science* **2013**, *340*, 1549-1552.
27. Araake, R.; Sakadani, K.; Tada, M.; Sakai, Y.; Ohki, Y. *J. Am. Chem. Soc.* **2017**, *139*, 5596-5606.
28. Gray, M. R., *Upgrading Oilsands Bitumen and Heavy Oil*. The University of Alberta Press: Edmonton, 2015.
29. Sánchez-Delgado, R. A., *Organometallic Modeling of the Hydrodesulfurization and Hydrodenitrogenation Reactions*. Springer Netherlands: 2006.
30. Hagen, J., Refinery Processes and Petrochemistry. In *Industrial Catalysis*, Wiley-VCH Verlag GmbH & Co. KGaA: 2015; pp 299-318.
31. Gallezot, P. *Chem. Soc. Rev.* **2012**, *41*, 1538-1558.
32. Huber, G. W.; Iborra, S.; Corma, A. *Chem. Rev.* **2006**, *106*, 4044-4098.

33.   Luterbacher, J. S.; Martin Alonso, D.; Dumesic, J. A. *Green Chemistry* **2014**, *16*, 4816-4838.

34.   Chheda, J. N.; Huber, G. W.; Dumesic, J. A. *Angew. Chem. Int. Ed.* **2007**, *46*, 7164-7183.

35.   Wenkert, E.; Michelotti, E. L.; Swindell, C. S. *J. Am. Chem. Soc.* **1979**, *101*, 2246-2247.

36.   Wenkert, E.; Ferreira, T. W.; Michelotti, E. L. *J. Chem. Soc., Chem. Commun.* **1979**, 637-638.

37.   Okamura, H.; Miura, M.; Takei, H. *Tetrahedron Lett.* **1979**, *20*, 43-46.

38.   Tobisu, M.; Shimasaki, T.; Chatani, N. *Angew. Chem. Int. Ed.* **2008**, *47*, 4866-4869.

39.   Zarate, C.; Manzano, R.; Martin, R. *J. Am. Chem. Soc.* **2015**, *137*, 6754-6757.

40.   Wang, C.; Ozaki, T.; Takita, R.; Uchiyama, M. *Chem. Eur. J.* **2012**, *18*, 3482-3485.

41.   Barbero, N.; Martin, R. *Org. Lett.* **2012**, *14*, 796-799.

42.   Álvarez-Bercedo, P.; Martin, R. *J. Am. Chem. Soc.* **2010**, *132*, 17352-17353.

43.   Sergeev, A. G.; Hartwig, J. F. *Science* **2011**, *332*, 439-443.

44.   Sergeev, A. G.; Webb, J. D.; Hartwig, J. F. *J. Am. Chem. Soc.* **2012**, *134*, 20226-20229.

45.   Brown, H. J. S.; Stryker, J. M.; Hebert, D. M. Catalysts for hydrodesulfurization. U.S. Patent 9,458,395 B2, Oct 4, 2016.

46.   Bunquin, J. C.; Stryker, J. M. Transition metal catalysts for hydrodesulfurization. U.S. Patent 9,120,984 B2, 2015.

47.   Puddephatt, R. J., Metal Clusters in Catalysis – An Overview. In *Metal Clusters in Chemistry*, Wiley-VCH Verlag GmbH: 2008; pp 604-615.

48.   Sánchez-Delgado, R. A. *J. Mol. Catal.* **1994**, *86*, 287-307.

49.   Vicic, D. A.; Jones, W. D. *Organometallics* **1998**, *17*, 3411-3413.

50.   Vicic, D. A.; Jones, W. D. *J. Am. Chem. Soc.* **1997**, *119*, 10855-10856.

51.   Shoshani, M. M.; Johnson, S. A. *Inorg. Chem.* **2015**, *54*, 11977-11985.

52.   Dehnicke, K.; Krieger, M.; Massa, W. *Coord. Chem. Rev.* **1999**, *182*, 19-65.

53.   Sundermann, A.; Schoeller, W. W. *J. Am. Chem. Soc.* **2000**, *122*, 4729-4734.

54.   Hawkeswood, S. B.; Stephan, D. W. *Inorg. Chem.* **2003**, *42*, 5429-5433.

55.   Honeyman, C. H.; Lough, A. J.; Manners, I. *Inorg. Chem.* **1994**, *33*, 2988-2993.

56.   Stephan, D. W.; Stewart, J. C.; Guérin, F.; Courtenay, S.; Kickham, J.; Hollink, E.; Beddie, C.; Hoskin, A.; Graham, T.; Wei, P.; Spence, R. E. v. H.; Xu, W.; Koch, L.; Gao, X.; Harrison, D. G. *Organometallics* **2003**, *22*, 1937-1947.

57.   LePichon, L.; Stephan, D. W.; Gao, X.; Wang, Q. *Organometallics* **2002**, *21*, 1362-1366.

58.   Mai, H.-J.; zu Köcker, R. M.; Wocadlo, S.; Massa, W.; Dehnicke, K. *Angew. Chem.* **1995**, *107*, 1349-1350.

59.   Mai, H. J.; Kang, H. C.; Wocadlo, S.; Massa, W.; Dehnicke, K. *Z. Anorg. Allg. Chem.* **1995**, *621*, 1963-1968.

60.   Riese, U.; Faza, N.; Harms, K.; Massa, W.; Neumüller, B.; Dehnicke, K. *Phosphorus, Sulfur, and Silicon and the Related Elements* **1997**, *124*, 315-321.

61.   Krieger, M.; Gould, R. O.; Pebler, J.; Dehnicke, K. *Z. Anorg. Allg. Chem.* **1998**, *624*, 781-786.

62.   Riese, U.; Harms, K.; Neumüller, B.; Dehnicke, K. *Z. Anorg. Allg. Chem.* **1998**, *624*, 1279-1284.

63.   Bunquin, J. C. Empowering the Base Metals: Rational Design of Homogeneous Catalysts

for Hydrotreatment, and Reduction of Organic Unsaturates. University of Alberta, Edmonton, Alberta, 2013.

64. Zhao, T. Phosphoranimide-supported Nickel Clusters for Hydrotreatment. University of Alberta, Edmonton, Alberta, 2016.

65. Hebert, D. M.; Hamilton, R.; Stryker, J. M., Unpublished results

66. Camacho-Bunquin, J.; Ferguson, M. J.; Stryker, J. M. *J. Am. Chem. Soc.* **2013**, *135*, 5537-5540.

67. Clavier, H.; Nolan, S. P. *Chem. Commun.* **2010**, *46*, 841-861.

68. Tolman, C. A. *J. Am. Chem. Soc.* **1970**, *92*, 2956-2965.

69. Bilbrey, J. A.; Kazez, A. H.; Locklin, J.; Allen, W. D. *J. Comput. Chem.* **2013**, *34*, 1189-1197.

70. Stephan, D. W. *Organometallics* **2005**, *24*, 2548-2560.

71. Coville, N. J.; Loonat, M. S.; White, D.; Carlton, L. *Organometallics* **1992**, *11*, 1082-1090.

72. Ferguson, G.; Roberts, P. J.; Alyea, E. C.; Khan, M. *Inorg. Chem.* **1978**, *17*, 2965-2967.

73. Staudinger, H.; Meyer, J. *Helv. Chim. Acta* **1919**, *2*, 635-646.

74. Birkofer, L.; Kim, S. M. *Chem. Ber.* **1964**, *97*, 2100-2101.

75. Courtenay, S.; Wei, P.; Stephan, D. W. *Can. J. Chem.* **2003**, *81*, 1471-1476.

76. Gröb, T.; Chitsaz, S.; Harms, K.; Dehnicke, K. *Z. Anorg. Allg. Chem.* **2002**, *628*, 473-479.

77. Brown, H. Mixed-Valence First-Row Metal Clusters for Catalytic Hydrodesulfurization and Hydrodeoxygenation. University of Alberta, Edmonton, Alberta, 2013.

78. Brown, H. J. S.; Stryker, J. M.; Hebert, D. M. Mixed-valent transition metal-phosphoranimide catalysts. U.S. Patent 9,000,198 B2, Apr 7, 2015.

79. Bunquin, J. C.; Stryker, J. M. Transition metal catalysts for hydrogenation and hydrosilylation. U.S. Patent 9,120,741 B2, Sep 1, 2015.

80. Bunquin, J. C.; Stryker, J. M. Transition metal catalysts for C—O hydrogenolysis and hydrodeoxygenation. U.S. Patent 9,051,229 B2, Jun 9, 2015.

81. Bai, T.; Janes, T.; Song, D. *Dalton Trans* **2017**, *46*, 12408-12412.

82. Carney, J. R.; Dillon, B. R.; Thomas, S. P. *Eur. J. Org. Chem.* **2016**, *2016*, 3912-3929.

83. Jacobsen, E. N.; Zhang, W.; Muci, A. R.; Ecker, J. R.; Deng, L. *J. Am. Chem. Soc.* **1991**, *113*, 7063-7064.

84. McGarrigle, E. M.; Gilheany, D. G. *Chem. Rev.* **2005**, *105*, 1563-1602.

85. Liu, W.; Groves, J. T. *Acc. Chem. Res.* **2015**, *48*, 1727-1735.

86. Trovitch, R. J. *Synlett* **2014**, *25*, 1638-1642.

87. DiBiase Cavanaugh, M.; Gregg, B. T.; Cutler, A. R. *Organometallics* **1996**, *15*, 2764-2769.

88. van Putten, R.; Uslamin, E. A.; Garbe, M.; Liu, C.; Gonzalez-de-Castro, A.; Lutz, M.; Junge, K.; Hensen, E. J. M.; Beller, M.; Lefort, L.; Pidko, E. A. *Angew. Chem. Int. Ed.* **2017**, *56*, 7531-7534.

89. Elangovan, S.; Topf, C.; Fischer, S.; Jiao, H.; Spannenberg, A.; Baumann, W.; Ludwig, R.; Junge, K.; Beller, M. *J. Am. Chem. Soc.* **2016**, *138*, 8809-8814.

90. Kallmeier, F.; Irrgang, T.; Dietel, T.; Kempe, R. *Angew. Chem. Int. Ed.* **2016**, *55*, 11806-11809.

91. Li, H.; Carpenter, G. B.; Sweigart, D. A. *Organometallics* **2000**, *19*, 1823-1825.

92. Zhang, X.; Dullaghan, C. A.; Watson, E. J.; Carpenter, G. B.; Sweigart, D. A. *Organometallics* **1998**, *17*, 2067-2075.

93. Dullaghan, C. A.; Zhang, X.; Greene, D. L.; Carpenter, G. B.; Sweigart, D. A.; Camiletti, C.; Rajaseelan, E. *Organometallics* **1998**, *17*, 3316-3322.

94. Dullaghan, C. A.; Zhang, X.; Walther, D.; Carpenter, G. B.; Sweigart, D. A.; Meng, Q. *Organometallics* **1997**, *16*, 5604-5606.

95. Dullaghan, C. A.; Carpenter, G. B.; Sweigart, D. A.; Choi, D. S.; Lee, S. S.; Chung, Y. K. *Organometallics* **1997**, *16*, 5688-5695.

96. Pauling, L. *Proc. Natl. Acad. Sci. U.S.A* **1976**, *73*, 4290-4293.

97. Zhang, X.; Dullaghan, C. A.; Carpenter, G. B.; Sweigart, D. A.; Meng, Q. *Chem. Commun.* **1998**, 93-94.

98. Gong, S. W.; He, H. F.; Zhao, C. Q.; Liu, L. J.; Cui, Q. X. *Synth. Commun.* **2012**, *42*, 574-581.

99. Zaccheria, F.; Ravasio, N.; Ercoli, M.; Allegrini, P. *Tetrahedron Lett.* **2005**, *46*, 7743-7745.

100. Deutsch, K. L.; Shanks, B. H. *Appl. Catal., A* **2012**, *447-448*, 144-150.

101. Massey, A. G., Copper. In *The Chemistry of Copper, Silver and Gold*, Pergamon: 1973; pp 1-78.

102. Robinson, T. P.; Price, R. D.; Davidson, M. G.; Fox, M. A.; Johnson, A. L. *Dalton Trans* **2015**, *44*, 5611-5619.

103. Tsui, E. Y.; Tran, R.; Yano, J.; Agapie, T. *Nat Chem* **2013**, *5*, 293-299.

104. Morimoto, Y.; Kotani, H.; Park, J.; Lee, Y.-M.; Nam, W.; Fukuzumi, S. *J. Am. Chem. Soc.* **2011**, *133*, 403-405.

105. Zhao, T.; Hamilton, R. J.; Camacho-Bunquin, J.; Ferguson, M. J.; McDonald, R.; Stryker, J. M., Manuscript in preparation. 2017.

106. Cornella, J.; Zarate, C.; Martin, R. *Chem. Soc. Rev.* **2014**, *43*, 8081-8097.

107. Rosen, B. M.; Quasdorf, K. W.; Wilson, D. A.; Zhang, N.; Resmerita, A.-M.; Garg, N. K.; Percec, V. *Chem. Rev.* **2011**, *111*, 1346-1416.

108. Amster, E. D.; Haim, M.; Dubnov, J.; Broday, D. M. *Environ. Pollut.* **2014**, *186*, 20-28.

109. Diesel Fuel Standards and Rulemakings. https://www.epa.gov/diesel-fuel-standards/diesel-fuel-standards-and-rulemakings (accessed Sep 3, 2017).

110. Sulphur in Diesel Fuel Regulations
. https://www.ec.gc.ca/energie-energy/default.asp?lang=En&n=7A8F92ED-1 (accessed August 30, 2017).

111. Topsøe, H.; Clausen, B. S.; Massoth, F. E., Hydrotreating Catalysis. In *Catalysis: Science and Technology*, Anderson, J. R.; Boudart, M., Eds. Springer: Berlin, Heidelberg, 1996; pp 1-269.

112. Angelici, R. J., Hydrodesulfurization & Hydrodenitrogenation. In *Encyclopedia of Inorganic Chemistry*, John Wiley & Sons, Ltd: 2006.

113. Prins, R., Hydrotreating. In *Handbook of Heterogeneous Catalysis*, Wiley-VCH Verlag GmbH & Co. KGaA: 2008.

114. Xiao, J.; Wang, X.; Chen, Y.; Fujii, M.; Song, C. *Ind. Eng. Chem. Res.* **2013**, *52*, 15746-15755.

115. Topsøe, H. *Appl. Catal., A* **2007**, *322*, 3-8.

116. Lauritsen, J. V.; Kibsgaard, J.; Olesen, G. H.; Moses, P. G.; Hinnemann, B.; Helveg, S.; Nørskov, J. K.; Clausen, B. S.; Topsøe, H.; Lægsgaard, E. *J. Catal.* **2007**, *249*, 220-233.

117. Curtis, M. D. *Appl. Organomet. Chem.* **1992**, *6*, 429-436.

118. Curtis, M. D. *J. Cluster Sci.* **1996**, *7*, 247-262.

119. Curtis, M. D.; Druker, S. H. *J. Am. Chem. Soc.* **1997**, *119*, 1027-1036.
120. Reynolds, M. A.; Guzei, I. A.; Angelici, R. J. *Inorg. Chem.* **2003**, *42*, 2191-2193.
121. Chehata, A.; Oviedo, A.; Arévalo, A.; Bernès, S.; García, J. J. *Organometallics* **2003**, *22*, 1585-1587.
122. Sattler, A.; Janak, K. E.; Parkin, G. *Inorg. Chim. Acta* **2011**, *369*, 197-202.
123. Sattler, A.; Parkin, G. *J. Am. Chem. Soc.* **2011**, *133*, 3748-3751.
124. Munjanja, L.; Brennessel, W. W.; Jones, W. D. *Organometallics* **2015**, *34*, 1716-1724.
125. Grochowski, M. R.; Brennessel, W. W.; Jones, W. D. *Organometallics* **2009**, *28*, 2661-2667.
126. Torres-Nieto, J.; Arévalo, A.; García, J. J. *Organometallics* **2007**, *26*, 2228-2233.
127. Bianchini, C.; Jimenez, M. V.; Meli, A.; Moneti, S.; Vizza, F.; Herrera, V.; Sanchez-Delgado, R. A. *Organometallics* **1995**, *14*, 2342-2352.
128. Garcia, J. J.; Maitlis, P. M. *J. Am. Chem. Soc.* **1993**, *115*, 12200-12201.
129. Garcia, J. J.; Mann, B. E.; Adams, H.; Bailey, N. A.; Maitlis, P. M. *J. Am. Chem. Soc.* **1995**, *117*, 2179-2186.
130. Jones, W. D.; Dong, L. *J. Am. Chem. Soc.* **1991**, *113*, 559-564.
131. Matsubara, K.; Okamura, R.; Tanaka, M.; Suzuki, H. *J. Am. Chem. Soc.* **1998**, *120*, 1108-1109.
132. Myers, A. W.; Jones, W. D. *Organometallics* **1996**, *15*, 2905-2917.
133. Jones, W. D.; Chin, R. M. *J. Organomet. Chem.* **1994**, *472*, 311-316.
134. Jones, W. D.; Chin, R. M. *Organometallics* **1992**, *11*, 2698-2700.
135. Chan, N. H.; Roache, J. H.; Jones, W. D. *Inorg. Chim. Acta* **2015**, *437*, 36-40.
136. Schaub, T.; Backes, M.; Plietzsch, O.; Radius, U. *Dalton Trans* **2009**, 7071-7079.
137. Palmer, M. S.; Harris, S. *Organometallics* **2000**, *19*, 2114-2124.
138. Torres-Nieto, J.; Arévalo, A.; García-Gutiérrez, P.; Acosta-Ramírez, A.; García, J. J. *Organometallics* **2004**, *23*, 4534-4536.
139. Torres-Nieto, J.; Arévalo, A.; García, J. J. *Inorg. Chem.* **2008**, *47*, 11429-11434.
140. Torres-Nieto, J.; García, J. J. *J. Organomet. Chem.* **2009**, *694*, 780-784.
141. Bunquin, J. C.; Stryker, J. M. Transition metal-phosphoranimide catalysts. U.S. Patent 8,901,334 B2, Dec. 2, 2014.
142. Holthausen, M. H.; Mallov, I.; Stephan, D. W. *Dalton Trans* **2014**, *43*, 15201-15211.
143. Vorapattanapong, A.; Stryker, J. M., Unpublished results.
144. Artamkina, G. A.; Egorov, M. P.; Beletskaya, I. P. *Chem. Rev.* **1982**, *82*, 427-459.
145. Meisenheimer, J. *Justus Liebigs Annalen der Chemie* **1902**, *323*, 205-246.
146. Kumpf, R. A.; Dougherty, D. A. *Science* **1993**, *261*, 1708-1710.
147. Dongqiang, Z.; Bruce, E. H.; Mark, A. S.; Elizabeth, R. C. *J. Environ. Qual.* **2004**, *33*, 276-284.
148. Unkelbach, C.; Rosenbaum, H. S.; Strohmann, C. *Chem. Commun.* **2012**, *48*, 10612-10614.
149. Dougherty, D. A. *Acc. Chem. Res.* **2013**, *46*, 885-893.
150. Lu, Q.; Oh, D. X.; Lee, Y.; Jho, Y.; Hwang, D. S.; Zeng, H. *Angewandte Chemie (International ed. in English)* **2013**, *52*, 3944-3948.

151. Banerjee, S.; Yang, Y.-F.; Jenkins, I. D.; Liang, Y.; Toutov, A. A.; Liu, W.-B.; Schuman, D. P.; Grubbs, R. H.; Stoltz, B. M.; Krenske, E. H.; Houk, K. N.; Zare, R. N. *J. Am. Chem. Soc.* **2017**, *139*, 6880-6887.

152. Spilebout, F.; Stoyanov, S.; Kovalenko, A., Unpublished computational results.

153. Heaney, H. *Chem. Rev.* **1962**, *62*, 81-97.

154. Bunnett, J. F. *J. Chem. Educ.* **1961**, *38*, 278.

155. Roberts, J. D.; Simmons, H. E.; Carlsmith, L. A.; Vaughan, C. W. *J. Am. Chem. Soc.* **1953**, *75*, 3290-3291.

156. Soto, J. L.; Raterman, M.; Leta, D. P.; Vann, W. D.; Han, L.; McConnachie, J. M.; Bielenberg, J. R.; Baird, W. C.; Bearden, R. Desulfurization process using alkali metal reagent. U.S. Patent 8,696,890 B2, Apr 15, 2014.

157. Leta, D. P.; McConnachie, J. M.; Baird, W. C.; Vann, W. D.; Soto, J. L. Heavy oil conversion process with in-situ potassium sulfide generation. U.S. Patent 8,673,132 B2, Mar 18, 2014.

158. McConnachie, J. M.; Leta, D. P.; Bielenberg, J. R.; Wright, C. A.; Brown, L. D. Desulfurization of heavy hydrocarbons and conversion of resulting hydrosulfides utilizing copper metal. U.S. Patent 8,398,848 B2, Mar 19, 2013.

159. Leta, D. P.; McConnachie, J. M.; Bielenberg, J. R.; Wright, C. A.; Brown, L. D. Desulfurization of heavy hydrocarbons and conversion of resulting hydrosulfides utilizing copper sulfide. U.S. Patent 8,968,555 B2, Mar 3, 2013.

160. Brons, G. Process for upgrading heavy oil using alkaline earth metal hydroxide. U.S. Patent 5,871,637, Feb 16, 1999.

161. Brons, G. B.; Myers, R.; Bearden, R. Continuous in-situ combination process for upgrading heavy oil. U.S. Patent 5,935,421 Aug 10, 1997.

162. Baird, W. C.; Bearden, R.; Ledford, T. H. Hydroconversion with group IA, IIA metal compounds. U.S. Patent 4,127,470, Nov 28, 1978.

163. Baird, W. C.; Bearden, R. Hydroconversion of residua with potassium sulfide. U.S. Patent 4,1195,28, Oct 10, 1978.

164. Baird, W. C. Hydroconversion and desulfurization process. U.S. Patent 4,087,349, May 2, 1978.

165. Baird, W. C.; Bearden, R. Combined desulfurization and hydroconversion with alkali metal hydroxides. U.S. Patent 4,003,823, Jan 18, 1977.

166. Hardesty, D. E.; Rodgers, T. A. Molten salt hydroconversion process. U.S. Patent 3,677,932, Jul 18, 1972.

167. Thomsen, A. M. Method of processing mineral oils with alkali metals or their compounds. U.S. Patent 2,950,245, Aug 23, 1960.

168. Toutov, A. A.; Salata, M.; Fedorov, A.; Yang, Y.-F.; Liang, Y.; Cariou, R.; Betz, K. N.; Couzijn, E. P. A.; Shabaker, J. W.; Houk, K. N.; Grubbs, R. H. *Nat. Energy* **2017**, *2*, 17008.

169. Matos, K.; Soderquist, J. A. *J. Org. Chem.* **1998**, *63*, 461-470.

170. Braga, A. A. C.; Morgon, N. H.; Ujaque, G.; Maseras, F. *J. Am. Chem. Soc.* **2005**, *127*, 9298-9307.

171. Barham, J. P.; Coulthard, G.; Emery, K. J.; Doni, E.; Cumine, F.; Nocera, G.; John, M. P.; Berlouis, L. E. A.; McGuire, T.; Tuttle, T.; Murphy, J. A. *J. Am. Chem. Soc.* **2016**, *138*, 7402-7410.

172. Cuthbertson, J.; Gray, V. J.; Wilden, J. D. *Chem. Commun.* **2014**, *50*, 2575-2578.
173. Prinsell, M. R.; Everson, D. A.; Weix, D. J. *Chem. Commun.* **2010**, *46*, 5743-5745.
174. Everson, D. A.; Jones, B. A.; Weix, D. J. *J. Am. Chem. Soc.* **2012**, *134*, 6146-6159.
175. Everson, D. A.; Weix, D. J. *J. Org. Chem.* **2014**, *79*, 4793-4798.
176. Cao, Z.-C.; Shi, Z.-J. *J. Am. Chem. Soc.* **2017**, *139*, 6546-6549.
177. Tobisu, M.; Chatani, N. *Acc. Chem. Res.* **2015**, *48*, 1717-1726.
178. Sontag, S. K.; Bilbrey, J. A.; Huddleston, N. E.; Sheppard, G. R.; Allen, W. D.; Locklin, J. *J. Org. Chem.* **2014**, *79*, 1836-1841.
179. Yoshikai, N.; Matsuda, H.; Nakamura, E. *J. Am. Chem. Soc.* **2008**, *130*, 15258-15259.
180. van Leeuwen, P. W. N. M.; Chadwick, J. C., Elementary Steps. In *Homogeneous Catalysts*, Wiley-VCH Verlag GmbH & Co. KGaA: 2011; pp 1-49.
181. Tudela, D. *J. Chem. Educ.* **2000**, *77*, 1410.
182. Whitesides, G. M.; Hackett, M.; Brainard, R. L.; Lavalleye, J. P. P. M.; Sowinski, A. F.; Izumi, A. N.; Moore, S. S.; Brown, D. W.; Staudt, E. M. *Organometallics* **1985**, *4*, 1819-1830.
183. Widegren, J. A.; Finke, R. G. *J. Mol. Catal. A: Chem.* **2003**, *198*, 317-341.
184. Hagen, J., In *Industrial Catalysis*, Wiley-VCH Verlag GmbH & Co. KGaA: 2015; pp 1-16.
185. Dumesic, J. A.; Huber, G. W.; Boudart, M., Principles of Heterogeneous Catalysis. In *Handbook of Heterogeneous Catalysis*, Wiley-VCH Verlag GmbH & Co. KGaA: 2008.
186. Dingerdissen, U.; Martin, A.; Herein, D.; Wernicke, H. J., The Development of Industrial Heterogeneous Catalysis. In *Handbook of Heterogeneous Catalysis*, Wiley-VCH Verlag GmbH & Co. KGaA: 2008.
187. Cole-Hamilton, D. J. *Science* **2003**, *299*, 1702-1706.
188. Liu, G.; Zhao, Z.-J.; Wu, T.; Zeng, L.; Gong, J. *ACS Catalysis* **2016**, *6*, 5207-5214.
189. Sattler, J. J. H. B.; Ruiz-Martinez, J.; Santillan-Jimenez, E.; Weckhuysen, B. M. *Chem. Rev.* **2014**, *114*, 10613-10653.
190. Lwin, S.; Wachs, I. E. *ACS Catalysis* **2014**, *4*, 2505-2520.
191. Wachs, I. E.; Roberts, C. A. *Chem. Soc. Rev.* **2010**, *39*, 5002-5017.
192. The State of the Working Catalyst. In *Modern Heterogeneous Catalysis*, Wiley-VCH Verlag GmbH & Co. KGaA: 2017; pp 117-143.
193. van Santen, R. A., Chemical Bonding and Reactivity of Transition Metal Surfaces. In *Modern Heterogeneous Catalysis*, Wiley-VCH Verlag GmbH & Co. KGaA: 2017; pp 209-291.
194. Taylor, H. S., The Heterogeneity of Catalyst Surfaces for Chemisorption. In *Advances in Catalysis*, Frankenburg, W. G.; Komarewsky, V. I.; Rideal, E. K., Eds. Academic Press: 1948; Vol. 1, pp 1-26.
195. Pelletier, J. D. A.; Basset, J.-M. *Acc. Chem. Res.* **2016**, *49*, 664-677.
196. Topsøe, H.; Clausen, B. S.; Massoth, F. E., Hydrotreating catalysis. In *Catalysis*, Springer: 1996; pp 1-269.
197. Lauritsen, J.; Helveg, S.; Lægsgaard, E.; Stensgaard, I.; Clausen, B.; Topsøe, H.; Besenbacher, F. *J. Catal.* **2001**, *197*, 1-5.
198. Robinson, W. R. A. M.; van Gestel, J. N. M.; Korányi, T. I.; Eijsbouts, S.; van der Kraan, A. M.; van Veen, J. A. R.; de Beer, V. H. J. *J. Catal.* **1996**, *161*, 539-550.

199. Sawhill, S. J.; Layman, K. A.; Van Wyk, D. R.; Engelhard, M. H.; Wang, C.; Bussell, M. E. *J. Catal.* **2005**, *231*, 300-313.
200. Phillips, D. C.; Sawhill, S. J.; Self, R.; Bussell, M. E. *J. Catal.* **2002**, *207*, 266-273.
201. Lee, Y.-K.; Oyama, S. T. *Appl. Catal., A* **2017**.
202. Layan Savithra, G. H.; Muthuswamy, E.; Bowker, R. H.; Carrillo, B. A.; Bussell, M. E.; Brock, S. L. *Chem. Mater.* **2013**, *25*, 825-833.
203. Danforth, S. J.; Liyanage, D. R.; Hitihami-Mudiyanselage, A.; Ilic, B.; Brock, S. L.; Bussell, M. E. *Surf. Sci.* **2016**, *648*, 126-135.
204. Stinner, C.; Prins, R.; Weber, T. *J. Catal.* **2000**, *191*, 438-444.
205. Clark, P.; Li, W.; Oyama, S. T. *J. Catal.* **2001**, *200*, 140-147.
206. Niquille-Röthlisberger, A.; Prins, R. *J. Catal.* **2006**, *242*, 207-216.
207. Ishihara, A.; Dumeignil, F.; Lee, J.; Mitsuhashi, K.; Qian, E. W.; Kabe, T. *Appl. Catal., A* **2005**, *289*, 163-173.
208. Röthlisberger, A.; Prins, R. *J. Catal.* **2005**, *235*, 229-240.
209. Ziaei-Azad, H.; Semagina, N. *Appl. Catal., B* **2016**, *191*, 138-146.
210. Wang, H.; Iglesia, E. *ChemCatChem* **2011**, *3*, 1166-1175.
211. Shen, J.; Semagina, N. *ChemCatChem* **2016**, *8*, 2565-2571.
212. Copéret, C.; Chabanas, M.; Petroff Saint-Arroman, R.; Basset, J.-M. *Angew. Chem. Int. Ed.* **2003**, *42*, 156-181.
213. Gladysz, J. A. *Chem. Rev.* **2002**, *102*, 3215-3216.
214. Fraile, J. M.; García, J. I.; Mayoral, J. A. *Chem. Rev.* **2009**, *109*, 360-417.
215. Jones, C. W. *Top. Catal.* **2010**, *53*, 942-952.
216. Wang, Z.; Chen, G.; Ding, K. *Chem. Rev.* **2009**, *109*, 322-359.
217. Bond, G. C. *Chem. Soc. Rev.* **1991**, *20*, 441-475.
218. Buchmeiser, M. R. *Chem. Rev.* **2009**, *109*, 303-321.
219. Zhong, R.; Lindhorst, A. C.; Groche, F. J.; Kühn, F. E. *Chem. Rev.* **2017**, *117*, 1970-2058.
220. Sommer, W. J.; Weck, M. *Coord. Chem. Rev.* **2007**, *251*, 860-873.
221. Ranganath, K. V. S.; Onitsuka, S.; Kumar, A. K.; Inanaga, J. *Catal. Sci. Technol.* **2013**, *3*, 2161-2181.
222. Hübner, S.; de Vries, J. G.; Farina, V. *Adv. Synth. Catal.* **2016**, *358*, 3-25.
223. Mastrorilli, P.; Nobile, C. F. *Coord. Chem. Rev.* **2004**, *248*, 377-395.
224. Corkum, E. G.; Kalapugama, S.; Hass, M. J.; Bergens, S. H. *RSC Advances* **2012**, *2*, 3473-3476.
225. Sabater, S.; Mata, J. A.; Peris, E. *ACS Catalysis* **2014**, *4*, 2038-2047.
226. Zhao, Q.; Chen, D.; Li, Y.; Zhang, G.; Zhang, F.; Fan, X. *Nanoscale* **2013**, *5*, 882-885.
227. Digne, M.; Sautet, P.; Raybaud, P.; Euzen, P.; Toulhoat, H. *J. Catal.* **2002**, *211*, 1-5.
228. Rascon, F.; Wischert, R.; Coperet, C. *Chem. Sci.* **2011**, *2*, 1449-1456.
229. Zhuravlev, L. T. *Colloids Surf., A* **2000**, *173*, 1-38.
230. Copéret, C.; Comas-Vives, A.; Conley, M. P.; Estes, D. P.; Fedorov, A.; Mougel, V.; Nagae, H.; Núñez-Zarur, F.; Zhizhko, P. A. *Chem. Rev.* **2016**, *116*, 323.
231. Digne, M.; Sautet, P.; Raybaud, P.; Euzen, P.; Toulhoat, H. *J. Catal.* **2004**, *226*, 54-68.
232. Basset, J. M.; Ugo, R., On the Origins and Development of "Surface Organometallic Chemistry". In *Modern Surface Organometallic Chemistry*, Wiley-VCH Verlag GmbH & Co. KGaA: 2009; pp 1-21.

233. Boukebbous, K.; Merle, N.; Larabi, C.; Garron, A.; Darwich, W.; Laifa, E. A.; Szeto, K.; De Mallmann, A.; Taoufik, M. *New J. Chem.* **2017**, *41*, 427-431.

234. Fedorov, A.; Liu, H.-J.; Lo, H.-K.; Copéret, C. *J. Am. Chem. Soc.* **2016**, *138*, 16502-16507.

235. Foley, H. C.; DeCanio, S. J.; Tau, K. D.; Chao, K. J.; Onuferko, J. H.; Dybowski, C.; Gates, B. C. *J. Am. Chem. Soc.* **1983**, *105*, 3074-3082.

236. Burwell, R. L. *J. Catal.* **1984**, *86*, 301-314.

237. Wegener, S. L.; Marks, T. J.; Stair, P. C. *Acc. Chem. Res.* **2012**, *45*, 206-214.

238. Joubert, J.; Delbecq, F.; Sautet, P.; Roux, E. L.; Taoufik, M.; Thieuleux, C.; Blanc, F.; Copéret, C.; Thivolle-Cazat, J.; Basset, J.-M. *J. Am. Chem. Soc.* **2006**, *128*, 9157-9169.

239. Toscano, P. J.; Marks, T. J. *J. Am. Chem. Soc.* **1985**, *107*, 653-659.

240. Legrand, A. P.; Editor, *The Surface Properties of Silicas*. Wiley: 1998; p 470 pp.

241. Lamberti, C.; Zecchina, A.; Groppo, E.; Bordiga, S. *Chem. Soc. Rev.* **2010**, *39*, 4951-5001.

242. Le Roux, E.; Taoufik, M.; Chabanas, M.; Alcor, D.; Baudouin, A.; Copéret, C.; Thivolle-Cazat, J.; Basset, J.-M.; Lesage, A.; Hediger, S.; Emsley, L. *Organometallics* **2005**, *24*, 4274-4279.

243. Valla, M.; Wischert, R.; Comas-Vives, A.; Conley, M. P.; Verel, R.; Copéret, C.; Sautet, P. *J. Am. Chem. Soc.* **2016**, *138*, 6774.

244. Coperet, C. *Chem. Rev.* **2010**, *110*, 656-680.

245. Wischert, R.; Copéret, C.; Delbecq, F.; Sautet, P. *Angew. Chem. Int. Ed.* **2011**, *50*, 3202-3205.

246. Gribov, E. N.; Zavorotynska, O.; Agostini, G.; Vitillo, J. G.; Ricchiardi, G.; Spoto, G.; Zecchina, A. *PCCP* **2010**, *12*, 6474-6482.

247. Smith, R. C.; Kellum, G. E. *Anal. Chem.* **1966**, *38*, 647-648.

248. Zhu, K.; D'Souza, L.; Richards, R. M. *Appl. Organomet. Chem.* **2005**, *19*, 1065-1069.

249. Buchanan, J. M.; Stryker, J. M.; Bergman, R. G. *J. Am. Chem. Soc.* **1986**, *108*, 1537-1550.

250. Jones, W. D. *Acc. Chem. Res.* **2003**, *36*, 140-146.

251. Whisler, M. C.; MacNeil, S.; Snieckus, V.; Beak, P. *Angew. Chem. Int. Ed.* **2004**, *43*, 2206-2225.

252. Yanagisawa, S.; Ueda, K.; Taniguchi, T.; Itami, K. *Org. Lett.* **2008**, *10*, 4673-4676.

253. Liu, W.-B.; Schuman, D. P.; Yang, Y.-F.; Toutov, A. A.; Liang, Y.; Klare, H. F. T.; Nesnas, N.; Oestreich, M.; Blackmond, D. G.; Virgil, S. C.; Banerjee, S.; Zare, R. N.; Grubbs, R. H.; Houk, K. N.; Stoltz, B. M. *J. Am. Chem. Soc.* **2017**, *139*, 6867-6879.

254. Toutov, A. A.; Liu, W.-B.; Betz, K. N.; Fedorov, A.; Stoltz, B. M.; Grubbs, R. H. *Nature* **2015**, *518*, 80-84.

255. Gilman, H.; Morton, J. W., The Metalation Reaction with Organolithium Compounds. In *Organic Reactions*, John Wiley & Sons, Inc.: 2004.

256. Snieckus, V. *Chem. Rev.* **1990**, *90*, 879-933.

257. Meille, V.; Schulz, E.; Lemaire, M.; Faure, R.; Vrinat, M. *Tetrahedron* **1996**, *52*, 3953-3960.

258. Campaigne, E.; Hewitt, L.; Ashby, J. *J. Heterocycl. Chem.* **1969**, *6*, 553-557.

259. Gilman, H.; Jacoby, A. L. *J. Org. Chem.* **1938**, *03*, 108-119.

260. Stanton, M. G.; Allen, C. B.; Kissling, R. M.; Lincoln, A. L.; Gagné, M. R. *J. Am. Chem. Soc.* **1998**, *120*, 5981-5989.

261. Sumida, Y.; Sumida, T.; Hashizume, D.; Hosoya, T. *Org. Lett.* **2016**, *18*, 5600-5603.

262. Bennett, M. A.; Kopp, M. R.; Wenger, E.; Willis, A. C. *J. Organomet. Chem.* **2003**, *667*, 8-15.

263. Bennett, M. A.; Wenger, E. *Chem. Ber.* **1997**, *130*, 1029-1042.

264. Lu, Q.; Oh, D. X.; Lee, Y.; Jho, Y.; Hwang, D. S.; Zeng, H. *Angew. Chem. Int. Ed.* **2013**, *52*, 3944-3948.

265. Caine, D., Potassium tert-Butoxide. In *Encyclopedia of Reagents for Organic Synthesis*, John Wiley & Sons, Ltd: 2001.

266. Stanton, M. G.; Gagné, M. R. *J. Am. Chem. Soc.* **1997**, *119*, 5075-5076.

267. Bianchini, C.; Meli, A.; Moneti, S.; Vizza, F. *Organometallics* **1998**, *17*, 2636-2645.

268. Corma, A.; Iborra, S.; Velty, A. *Chem. Rev.* **2007**, *107*, 2411-2502.

269. Stumm, W.; Morgan, J. J., *Aquatic Chemistry: Chemical Equilibria and Rates in Natural Waters*. 3rd ed.; John Wiley & Sons: New York, 1996.

270. Alonso, D. M.; Wettstein, S. G.; Dumesic, J. A. *Chem. Soc. Rev.* **2012**, *41*, 8075-8098.

271. Alotaibi, M. A.; Kozhevnikova, E. F.; Kozhevnikov, I. V. *Chem. Commun.* **2012**, *48*, 7194-7196.

272. King, A. E.; Brooks, T. J.; Tian, Y.-H.; Batista, E. R.; Sutton, A. D. *ACS Catalysis* **2015**, *5*, 1223-1226.

273. Clemmensen, E. *Berichte der deutschen chemischen Gesellschaft* **1914**, *47*, 681-687.

274. Clemmensen, E. *Berichte der deutschen chemischen Gesellschaft* **1913**, *46*, 1837-1843.

275. Kishner, N. *Russian Journal of Physical Chemistry* **1911**, *43*.

276. Wolff, L. *Justus Liebigs Annalen der Chemie* **1912**, *394*, 86-108.

277. Hutchins, R. O.; Maryanoff, B.; Milewski, C. *J. Am. Chem. Soc.* **1971**, *93*, 1793-1794.

278. Gribble, G. W.; Kelly, W. J.; Emery, S. E. *Synthesis* **1978**, 763-765.

279. Gribble, G. W.; Kelly, W. J.; Emery, S. E. *Synthesis* **1978**, *1978*, 763-765.

280. Hutchins, R. O.; Natale, N. R. *J. Org. Chem.* **1978**, *43*, 2299-2301.

281. Srikrishna, A.; Viswajanani, R.; Sattigeri, J. A.; Yelamaggad, C. V. *Tetrahedron Lett.* **1995**, *36*, 2347-2350.

282. Wolfrom, M. L.; Karabinos, J. V. *J. Am. Chem. Soc.* **1944**, *66*, 909-911.

283. Hauptmann, H.; Walter, W. F. *Chem. Rev.* **1962**, *62*, 347-404.

284. West, C. T.; Donnelly, S. J.; Kooistra, D. A.; Doyle, M. P. *J. Org. Chem.* **1973**, *38*, 2675-2681.

285. Fry, J. L.; Orfanopoulos, M.; Adlington, M. G.; Dittman, W. P.; Silverman, S. B. *J. Org. Chem.* **1978**, *43*, 374-375.

286. Chandrasekhar, S.; Reddy, C. R.; Babu, B. N. *J. Org. Chem.* **2002**, *67*, 9080-9082.

287. Rahaim, R. J.; Maleczka, R. E. *Org. Lett.* **2011**, *13*, 584-587.

288. Sakai, N.; Nagasawa, K.; Ikeda, R.; Nakaike, Y.; Konakahara, T. *Tetrahedron Lett.* **2011**, *52*, 3133-3136.

289. Wang, H.; Li, L.; Bai, X.-F.; Shang, J.-Y.; Yang, K.-F.; Xu, L.-W. *Adv. Synth. Catal.* **2013**, *355*, 341-347.

290. Fernandes, T. A.; Bernardo, J. R.; Fernandes, A. C. *ChemCatChem* **2015**, *7*, 1177-1183.

291. Mamillapalli, N. C.; Sekar, G. *Adv. Synth. Catal.* **2015**, *357*, 3273-3283.

292. Volkov, A.; Gustafson, K. P. J.; Tai, C.-W.; Verho, O.; Bäckvall, J.-E.; Adolfsson, H. *Angew. Chem. Int. Ed.* **2015**, *54*, 5122-5126.

293. Sousa, S. C. A.; Fernandes, T. A.; Fernandes, A. C. *Eur. J. Org. Chem.* **2016**, *2016*, 3109-3112.

294. Lavis, J. M.; Maleczka, R. E.; Chandrasekaran, V.; Collier, S. J., Polymethylhydrosiloxane. In *Encyclopedia of Reagents for Organic Synthesis*, John Wiley & Sons, Ltd: 2001.

295. Mitton, S.; Stryker, J. M., Unpublished results.

296. Luo, Y.-R., Comprehensive Handbook of Chemical Bond Energies. CRC Press 2007
.

297. Noyori, R.; Ohkuma, T. *Angew. Chem. Int. Ed.* **2001**, *40*, 40-73.

298. Mahoney, W. S.; Stryker, J. M. *J. Am. Chem. Soc.* **1989**, *111*, 8818-8823.

299. Chen, J.-X.; Daeuble, J. F.; Brestensky, D. M.; Stryker, J. M. *Tetrahedron* **2000**, *56*, 2153-2166.

300. Chen, J.-X.; Daeuble, J. F.; Stryker, J. M. *Tetrahedron* **2000**, *56*, 2789-2798.

301. Wang, W.; Yang, Y.; Luo, H.; Hu, T.; Liu, W. *Catal. Commun.* **2011**, *12*, 436-440.

302. Ma, J.; Liu, S.; Kong, X.; Fan, X.; Yan, X.; Chen, L. *Res. Chem. Intermed.* **2012**, *38*, 1341-1349.

303. Vannice, M. A.; Poondi, D. *J. Catal.* **1997**, *169*, 166-175.

304. Cano, M.; Benito, A. M.; Maser, W. K.; Urriolabeitia, E. P. *New J. Chem.* **2013**, *37*, 1968-1972.

305. Bejblová, M.; Zámostný, P.; Červený, L.; Čejka, J. *Appl. Catal., A* **2005**, *296*, 169-175.

306. Kogan, V.; Aizenshtat, Z.; Neumann, R. *Angew. Chem. Int. Ed.* **1999**, *38*, 3331-3334.

307. Mahdi, T.; Stephan, D. W. *J. Am. Chem. Soc.* **2014**, *136*, 15809-15812.

308. Scott, D. J.; Fuchter, M. J.; Ashley, A. E. *J. Am. Chem. Soc.* **2014**, *136*, 15813-15816.

309. Mahdi, T.; Stephan, D. W. *Angew. Chem. Int. Ed.* **2015**, *54*, 8511-8514.

310. Arduengo, A. J. *Acc. Chem. Res.* **1999**, *32*, 913-921.

311. Bourissou, D.; Guerret, O.; Gabbaï, F. P.; Bertrand, G. *Chem. Rev.* **2000**, *100*, 39-92.

312. Lummiss, J. A. M.; Higman, C. S.; Fyson, D. L.; McDonald, R.; Fogg, D. E. *Chem. Sci.* **2015**, *6*, 6739-6746.

313. Crudden, C. M.; Allen, D. P. *Coord. Chem. Rev.* **2004**, *248*, 2247-2273.

314. Hopkinson, M. N.; Richter, C.; Schedler, M.; Glorius, F. *Nature* **2014**, *510*, 485-496.

315. Ely, T. O.; Amiens, C.; Chaudret, B.; Snoeck, E.; Verelst, M.; Respaud, M.; Broto, J.-M. *Chem. Mater.* **1999**, *11*, 526-529.

316. Bancroft, W. D.; George, A. B. *J. Phys. Chem.* **1930**, *35*, 2219-2225.

317. Brooks, B. C.; Brent Gunnoe, T.; Dean Harman, W. *Coord. Chem. Rev.* **2000**, *206-207*, 3-61.

318. Orita, H.; Itoh, N. *Surf. Sci.* **2004**, *550*, 177-184.

319. Sitthisa, S.; Resasco, D. E. *Catal. Lett.* **2011**, *141*, 784-791.

320. Jurkauskas, V.; Sadighi, J. P.; Buchwald, S. L. *Org. Lett.* **2003**, *5*, 2417-2420.

321. Jordan, A. J.; Lalic, G.; Sadighi, J. P. *Chem. Rev.* **2016**, *116*, 8318-8372.

322. Shimizu, H.; Igarashi, D.; Kuriyama, W.; Yusa, Y.; Sayo, N.; Saito, T. *Org. Lett.* **2007**, *9*, 1655-1657.

323. Deutsch, C.; Krause, N.; Lipshutz, B. H. *Chem. Rev.* **2008**, *108*, 2916-2927.

324. Ott, L. S.; Campbell, S.; Seddon, K. R.; Finke, R. G. *Inorg. Chem.* **2007**, *46*, 10335-10344.

325. Zhukhovitskiy, A. V.; MacLeod, M. J.; Johnson, J. A. *Chem. Rev.* **2015**, *115*, 11503-11532.

326. Ren, Y.; Yan, M.; Wang, J.; Zhang, Z. C.; Yao, K. *Angew. Chem. Int. Ed.* **2013**, *52*, 12674-12678.

327. Clegg, W.; Kennedy, A. R.; Klett, J.; Mulvey, R. E.; Russo, L. *Eur. J. Inorg. Chem.* **2012**, 2989-2994.

328. Chisholm, M. H.; Drake, S. R.; Naiini, A. A.; Streib, W. E. *Polyhedron* **1991**, *10*, 337-345.

Appendix

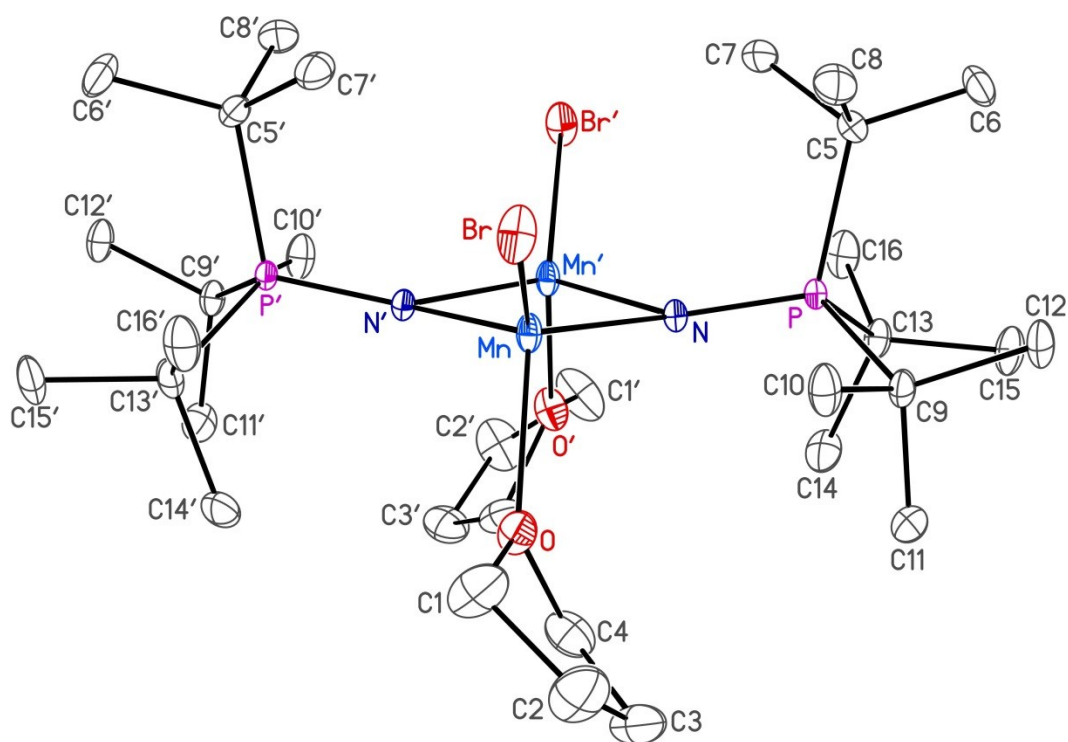Select X-Ray Crystallography Data

STRUCTURE REPORT

XCL Code:	JMS1336	**Date:**	22 October 2013
Compound:	$[Mn_2Br_2(NP^tBu_3)_2(OC_4H_8)_2]$		
Formula:	$C_{32}H_{70}Br_2Mn_2N_2O_2P_2$		
Supervisor:	J. M. Stryker	**Crystallographer:**	M. J. Ferguson

Figure Legends

Figure 1.   Perspective view of the [$Mn_2Br_2(NP^tBu_3)_2(OC_4H_8)_2$] molecule showing the atom labelling scheme. Primed atoms related to unprimed ones by 2-fold rotation axis at (0, y, $^1/4$). Non-hydrogen atoms are represented by Gaussian ellipsoids at the 30% probability level. Hydrogen atoms are not shown.
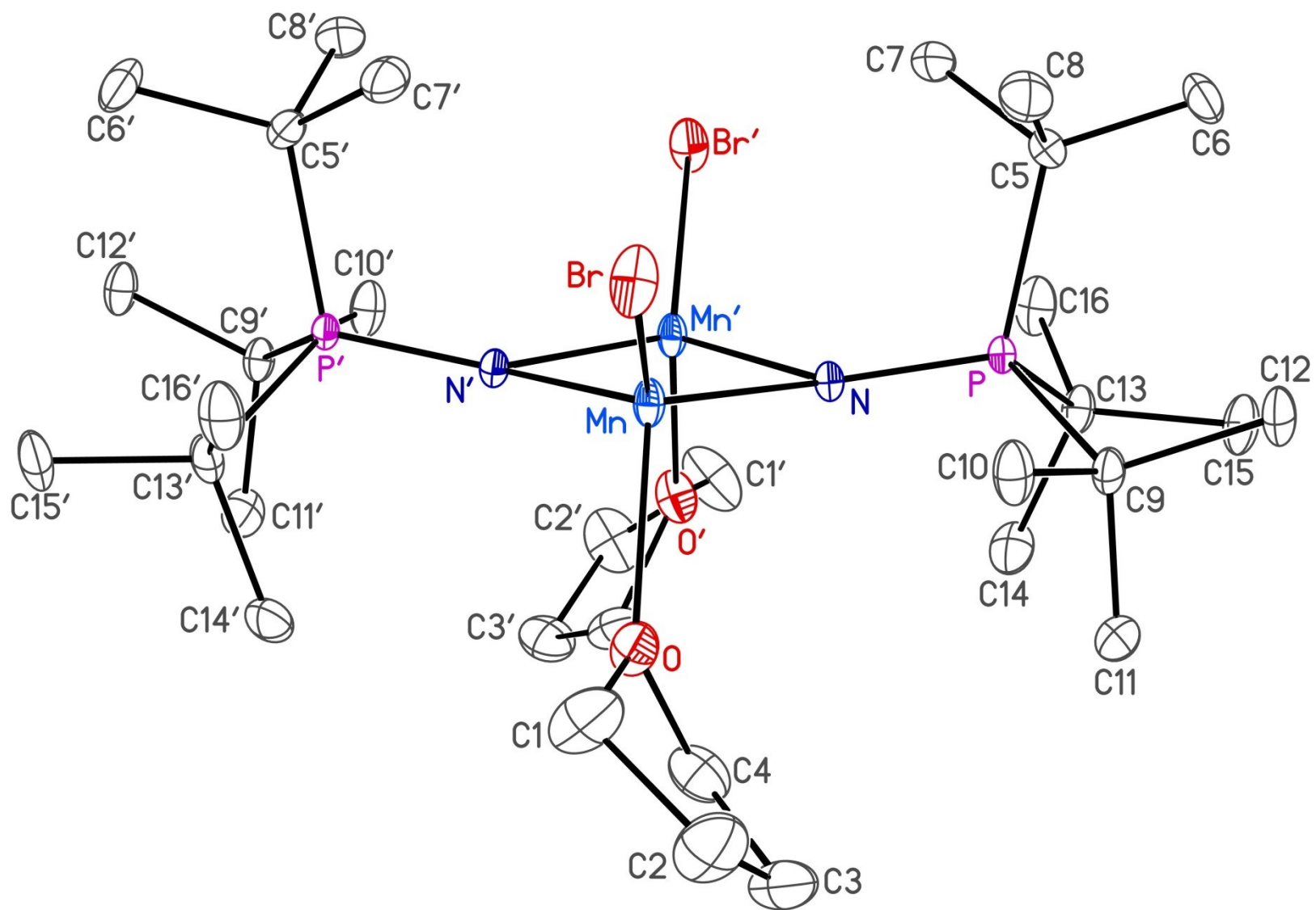
Table 1. Crystallographic Experimental Details

A. Crystal Data

formula	$C_{32}H_{70}Br_2Mn_2N_2O_2P_2$
formula weight	846.54
crystal dimensions (mm)	$0.37 \times 0.34 \times 0.24$
crystal system	monoclinic
space group	$C2/c$ (No. 15)
unit cell parameters[a]	
a (Å)	21.5341 (19)
b (Å)	8.7436 (8)
c (Å)	21.4810 (19)
β (deg)	104.3715 (9)
V (Å³)	3918.0 (6)
Z	4
ρ_{calcd} (g cm⁻³)	1.435
μ (mm⁻¹)	2.795

B. Data Collection and Refinement Conditions

diffractometer	Bruker D8/APEX II CCD[b]
radiation (λ [Å])	graphite-monochromated Mo Kα (0.71073)
temperature (°C)	−100
scan type	ω scans (0.3°) (20 s exposures)
data collection 2θ limit (deg)	55.00
total data collected	16924 ($-27 \leq h \leq 27$, $-11 \leq k \leq 11$, $-27 \leq l \leq 27$)
independent reflections	4476 (R_{int} = 0.0097)
number of observed reflections (NO)	4259 [$F_o^2 \geq 2\sigma(F_o^2)$]
structure solution method	intrinsic phasing (SHELXT[c])
refinement method	full-matrix least-squares on F^2 (SHELXL–2013[c])
absorption correction method	Gaussian integration (face-indexed)
range of transmission factors	0.6285–0.4344
data/restraints/parameters	4476 / 0 / 190
goodness-of-fit (S)[d] [all data]	1.072
final R indices[e]	
R_1 [$F_o^2 \geq 2\sigma(F_o^2)$]	0.0286
wR_2 [all data]	0.0737
largest difference peak and hole	1.446 and −1.454 e Å⁻³

[a]Obtained from least-squares refinement of 9832 reflections with 4.78° < 2θ < 55.00°.

[b]Programs for diffractometer operation, data collection, data reduction and absorption correction were those supplied by Bruker.

Table 1. Crystallographic Experimental Details (continued)

[c]Sheldrick, G. M. *Acta Crystallogr.* **2008**, *A64*, 112–122.

[d]$S = [\Sigma w(F_o^2 - F_c^2)^2/(n - p)]^{1/2}$ (n = number of data; p = number of parameters varied; $w = [\sigma^2(F_o^2) + (0.0333P)^2 + 9.7229P]^{-1}$ where $P = [\text{Max}(F_o^2, 0) + 2F_c^2]/3$).

[e]$R_1 = \Sigma||F_o| - |F_c||/\Sigma|F_o|$; $wR_2 = [\Sigma w(F_o^2 - F_c^2)^2/\Sigma w(F_o^4)]^{1/2}$.

STRUCTURE REPORT

XCL Code: JMS1348 **Date:** 16 December 2013

Compound: [Mn$_2$Me$_2$(NP^{t}Bu$_3$)$_2$]

Formula: C$_{26}$H$_{60}$Mn$_2$N$_2$P$_2$

Supervisor: J. M. Stryker **Crystallographer:** M. J. Ferguson
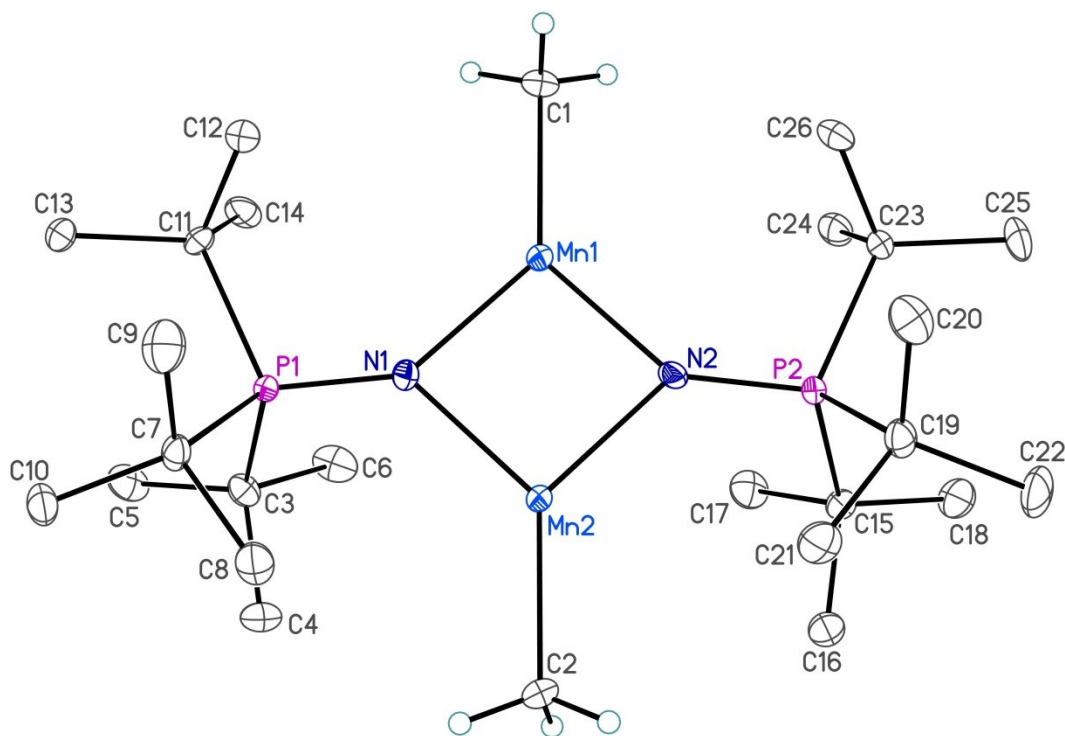
Figure Legends

Figure 1.   Perspective view of the $[Mn_2Me_2(NP^tBu_3)_2]$ molecule showing the atom labelling scheme. Non-hydrogen atoms are represented by Gaussian ellipsoids at the 30% probability level. Hydrogen atoms are shown with arbitrarily small thermal parameters for the Mn–CH$_3$ groups, and are not shown for the *t*-butyl groups.
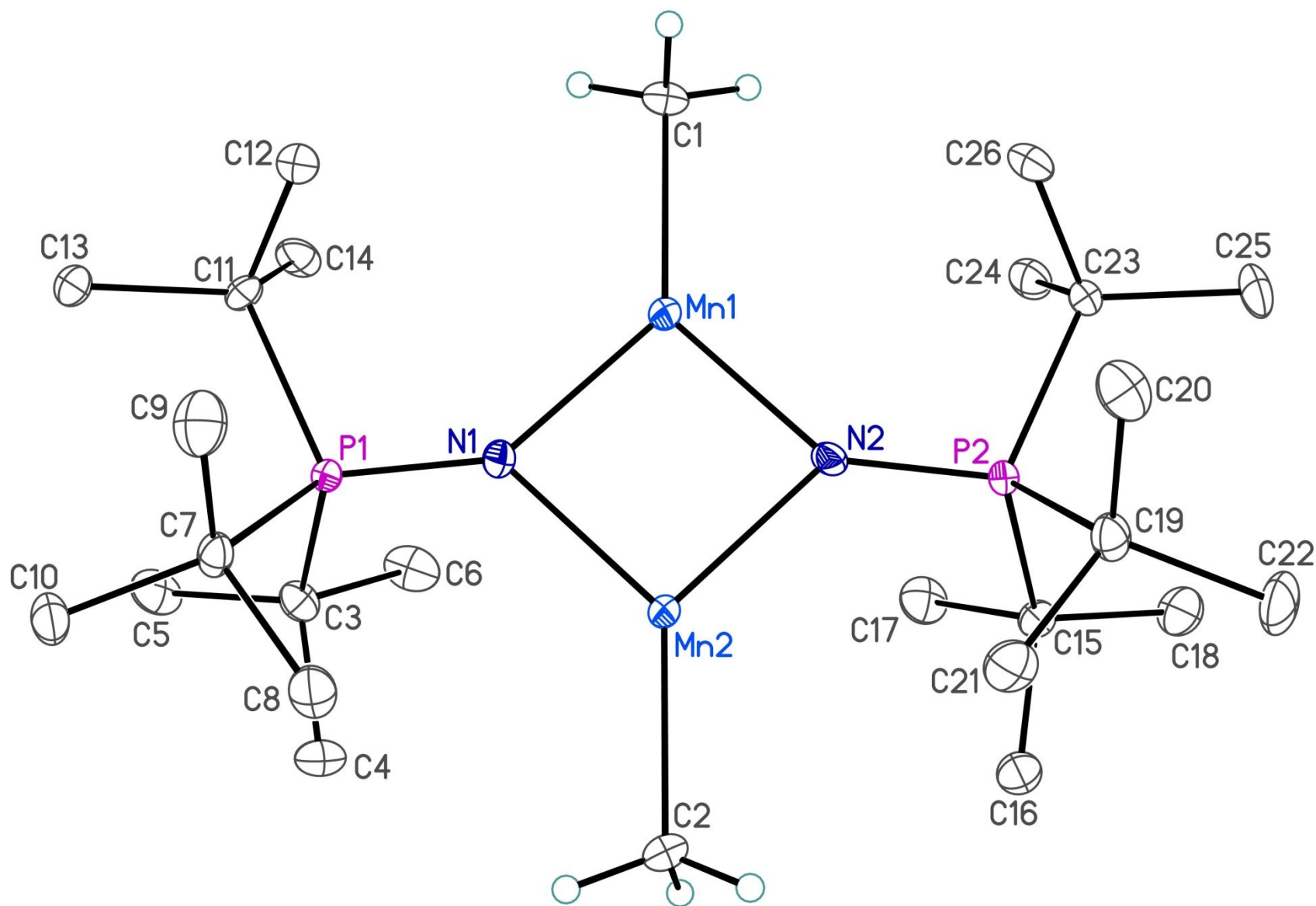
Table 1. Crystallographic Experimental Details

A. Crystal Data

formula	$C_{26}H_{60}Mn_2N_2P_2$
formula weight	572.58
crystal dimensions (mm)	$0.32 \times 0.16 \times 0.06$
crystal system	monoclinic
space group	$P2_1$ (No. 4)
unit cell parameters[a]	
$\quad a$ (Å)	11.0088 (13)
$\quad b$ (Å)	12.5124 (15)
$\quad c$ (Å)	11.4066 (13)
$\quad \beta$ (deg)	101.6764 (14)
$\quad V$ (Å^3)	1538.7 (3)
$\quad Z$	2
ρ_{calcd} (g cm^{-3})	1.236
μ (mm^{-1})	0.940

B. Data Collection and Refinement Conditions

diffractometer	Bruker D8/APEX II CCD[b]
radiation (λ [Å])	graphite-monochromated Mo Kα (0.71073)
temperature (°C)	−100
scan type	ω scans (0.3°) (20 s exposures)
data collection 2θ limit (deg)	52.63
total data collected	12062 ($-13 \leq h \leq 13$, $-15 \leq k \leq 15$, $-14 \leq l \leq 14$)
independent reflections	6183 (R_{int} = 0.0290)
number of observed reflections (*NO*)	5768 [$F_o^2 \geq 2\sigma(F_o^2)$]
structure solution method	intrinsic phasing (*SHELXT*[c])
refinement method	full-matrix least-squares on F^2 (*SHELXL–2013*[c])
absorption correction method	Gaussian integration (face-indexed)
range of transmission factors	0.9665–0.7653
data/restraints/parameters	6183 / 0 / 310
Flack absolute structure parameter[d]	0.15(3)
goodness-of-fit (*S*)[e] [all data]	1.139
final *R* indices[f]	
$\quad R_1$ [$F_o^2 \geq 2\sigma(F_o^2)$]	0.0446
$\quad wR_2$ [all data]	0.1199
largest difference peak and hole	0.882 and −0.451 e Å^{-3}

[a]Obtained from least-squares refinement of 9296 reflections with 4.70° < 2θ < 52.12°.

Table 1. Crystallographic Experimental Details (continued)

[b]Programs for diffractometer operation, data collection, data reduction and absorption correction were those supplied by Bruker.

[c]Sheldrick, G. M. *Acta Crystallogr.* **2008**, *A64*, 112–122.

[d]Flack, H. D. *Acta Crystallogr.* **1983**, *A39*, 876–881; Flack, H. D.; Bernardinelli, G. *Acta Crystallogr.* **1999**, *A55*, 908–915; Flack, H. D.; Bernardinelli, G. *J. Appl. Cryst.* **2000**, *33*, 1143–1148. The Flack parameter will refine to a value near zero if the structure is in the correct configuration and will refine to a value near one for the inverted configuration. The value observed herein is indicative of racemic twinning, and was accommodated during the refinement (using the *SHELXL-2013* TWIN instruction [see reference *c*]).

[e]$S = [\Sigma w(F_o^2 - F_c^2)^2/(n - p)]^{1/2}$ (n = number of data; p = number of parameters varied; $w = [\sigma^2(F_o^2) + (0.0436P)^2 + 2.5134P]^{-1}$ where $P = [\text{Max}(F_o^2, 0) + 2F_c^2]/3$).

[f]$R_1 = \Sigma||F_o| - |F_c||/\Sigma|F_o|$; $wR_2 = [\Sigma w(F_o^2 - F_c^2)^2/\Sigma w(F_o^4)]^{1/2}$.

STRUCTURE REPORT

**XCL Code:**   JMS1466   **Date:** 30 October 2014

Compound: $[Mn_2(Me)_2(NP^tBu_3)_2(THF)]$

**Formula:** $C_{30}H_{68}Mn_2N_2OP_2$

Supervisor: J. M. Stryker   **Crystallographer:** M. J. Ferguson
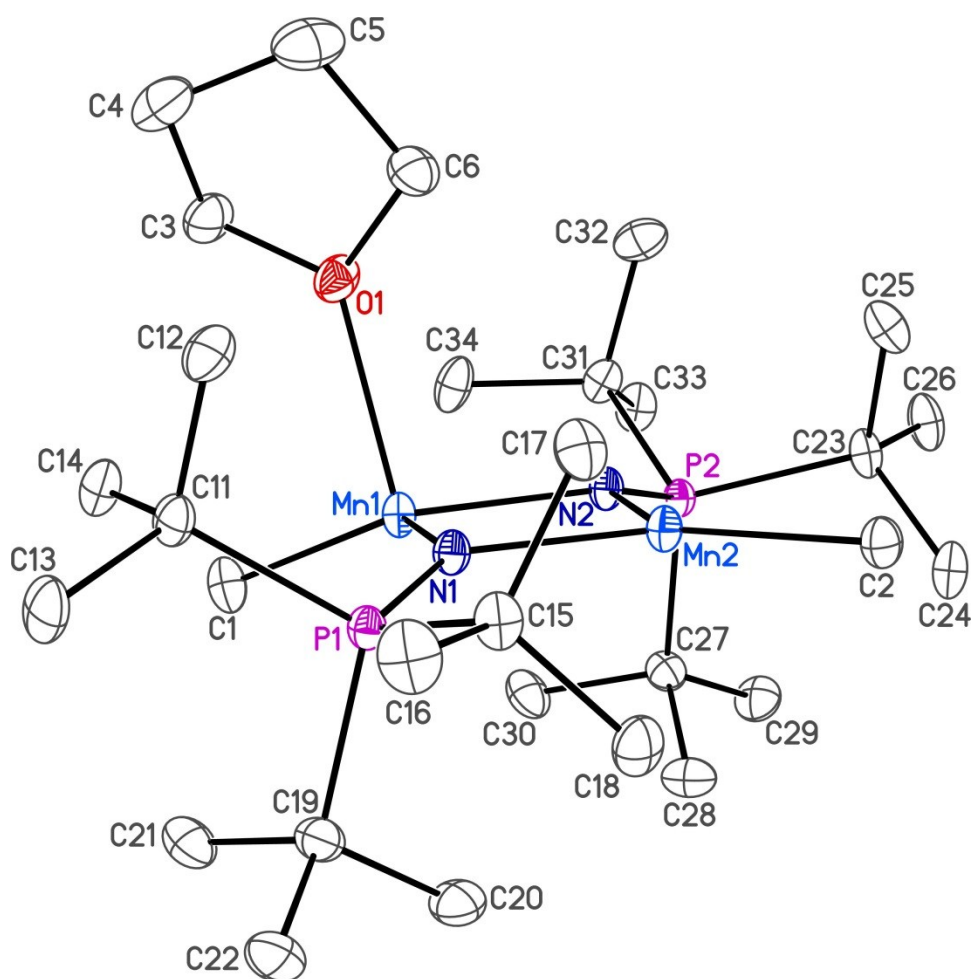
Figure Legends

Figure 1. Perspective view of the [Mn$_2$(Me)$_2$(NP^{t}Bu$_3$)$_2$(THF)] molecule showing the atom labelling scheme. Non-hydrogen atoms are represented by Gaussian ellipsoids at the 30% probability level. Hydrogen atoms are not shown.
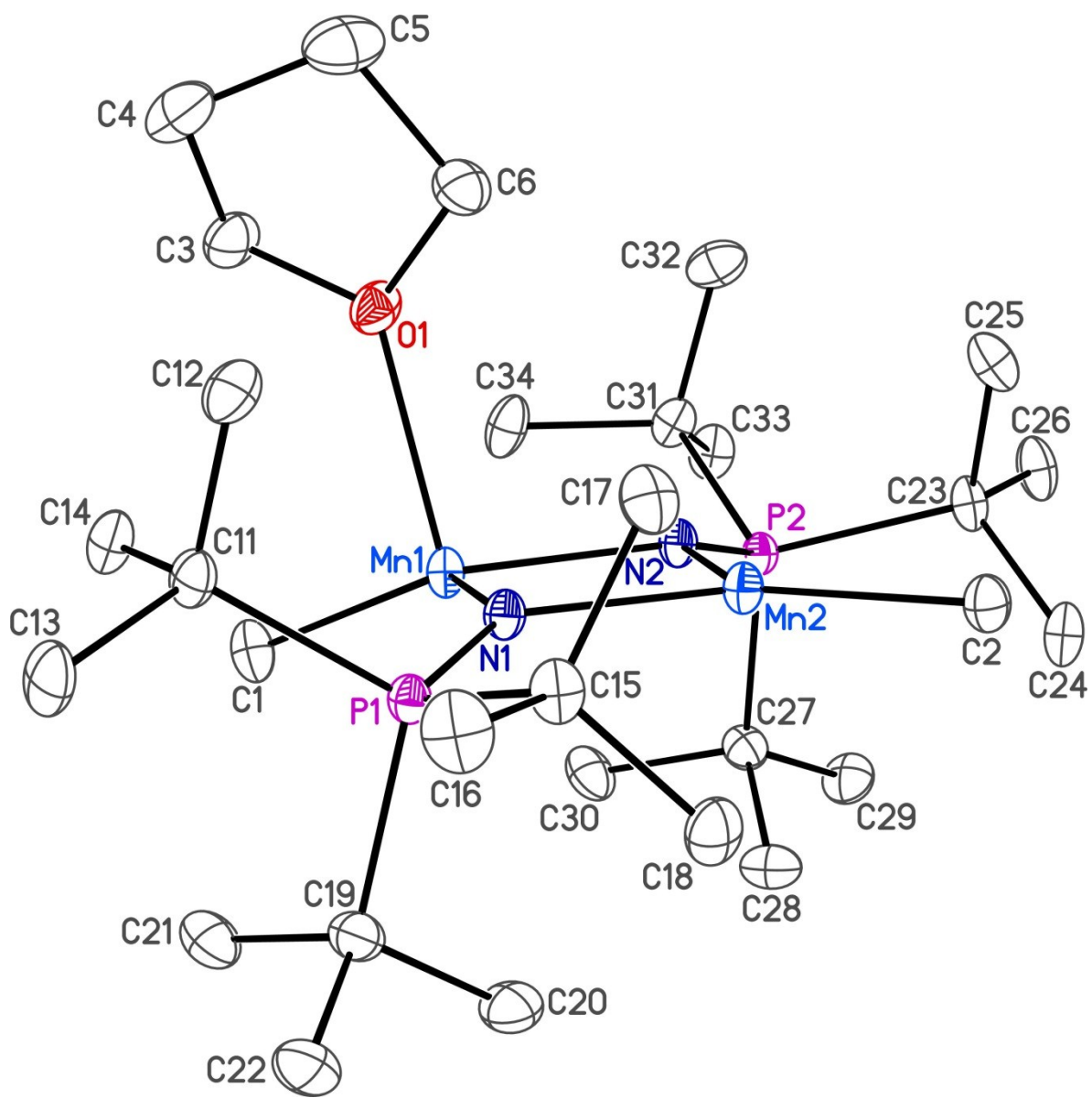
Table 1. Crystallographic Experimental Details

A. Crystal Data

formula	$C_{30}H_{68}Mn_2N_2OP$
formula weight	644.68
crystal dimensions (mm)	$0.28 \times 0.22 \times 0.18$
crystal system	triclinic
space group	$P\bar{1}$ (No. 2)
unit cell parameters[a]	
$\quad a$ (Å)	8.6367 (5)
$\quad b$ (Å)	11.3369 (6)
$\quad c$ (Å)	19.2422 (11)
$\quad \alpha$ (deg)	77.6633 (6)
$\quad \beta$ (deg)	80.7192 (7)
$\quad \gamma$ (deg)	78.5571 (6)
$\quad V$ (Å^3)	1790.02 (17)
$\quad Z$	2
ρ_{calcd} (g cm^{-3})	1.196
μ (mm^{-1})	0.818

B. Data Collection and Refinement Conditions

diffractometer	Bruker D8/APEX II CCD[b]
radiation (λ [Å])	graphite-monochromated Mo Kα (0.71073)
temperature (°C)	−100
scan type	ω scans (0.3°) (20 s exposures)
data collection 2θ limit (deg)	55.58
total data collected	16274 (-11 $\leq h \leq$ 11, -14 $\leq k \leq$ 14, -25 $\leq l \leq$ 25)
independent reflections	8344 (R_{int} = 0.0203)
number of observed reflections (*NO*)	6971 [$F_o^2 \geq 2\sigma(F_o^2)$]
structure solution method	intrinsic phasing (*SHELXT-2014*[c])
refinement method	full-matrix least-squares on F^2 (*SHELXL–2014*[c])
absorption correction method	Gaussian integration (face-indexed)
range of transmission factors	0.9361–0.8257
data/restraints/parameters	8344 / 0 / 354
goodness-of-fit (*S*)[d] [all data]	1.047
final *R* indices[e]	
$\quad R_1$ [$F_o^2 \geq 2\sigma(F_o^2)$]	0.0311
$\quad wR_2$ [all data]	0.0837
largest difference peak and hole	0.503 and −0.257 e Å^{-3}

[a]Obtained from least-squares refinement of 9911 reflections with 4.66° < 2θ < 55.08°.

Table 1. Crystallographic Experimental Details (continued)

[b]Programs for diffractometer operation, data collection, data reduction and absorption correction were those supplied by Bruker.

[c]Sheldrick, G. M. *Acta Crystallogr.* **2008**, *A64*, 112–122.

[d]$S = [\Sigma w(F_o^2 - F_c^2)^2/(n - p)]^{1/2}$ (n = number of data; p = number of parameters varied; $w = [\sigma^2(F_o^2) + (0.0402P)^2 + 0.4992P]^{-1}$ where $P = [\text{Max}(F_o^2, 0) + 2F_c^2]/3$).

[e]$R_1 = \Sigma||F_o| - |F_c||/\Sigma|F_o|$; $wR_2 = [\Sigma w(F_o^2 - F_c^2)^2/\Sigma w(F_o^4)]^{1/2}$.

STRUCTURE REPORT

XCL Code: JMS1426   **Date:** 14 May 2014

Compound: $[Mn_2(NP^tBu_3)_4] \cdot C_4H_8O$

Formula: $C_{52}H_{116}Mn_2N_4OP_4$ ($C_{48}H_{108}Mn_2N_4P_4 \cdot C_4H_8O$)

Supervisor: J. M. Stryker   **Crystallographer:** M. J. Ferguson
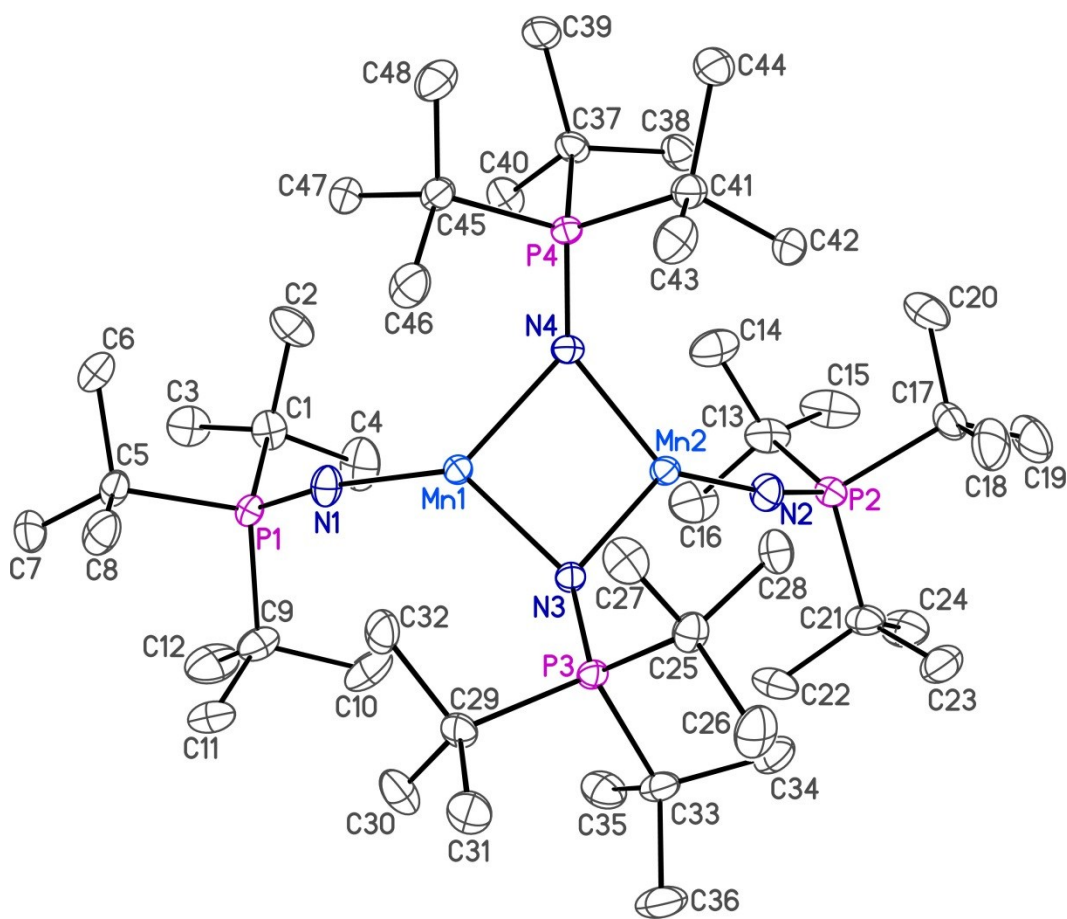
Figure Legends

Figure 1.   Perspective view of the [Mn$_2$(NP^{t}Bu$_3$)$_4$] molecule showing the atom labelling scheme. Non-hydrogen atoms are represented by Gaussian ellipsoids at the 30% probability level. Hydrogen atoms are not shown.

Figure 2.   Alternate view of the molecule.
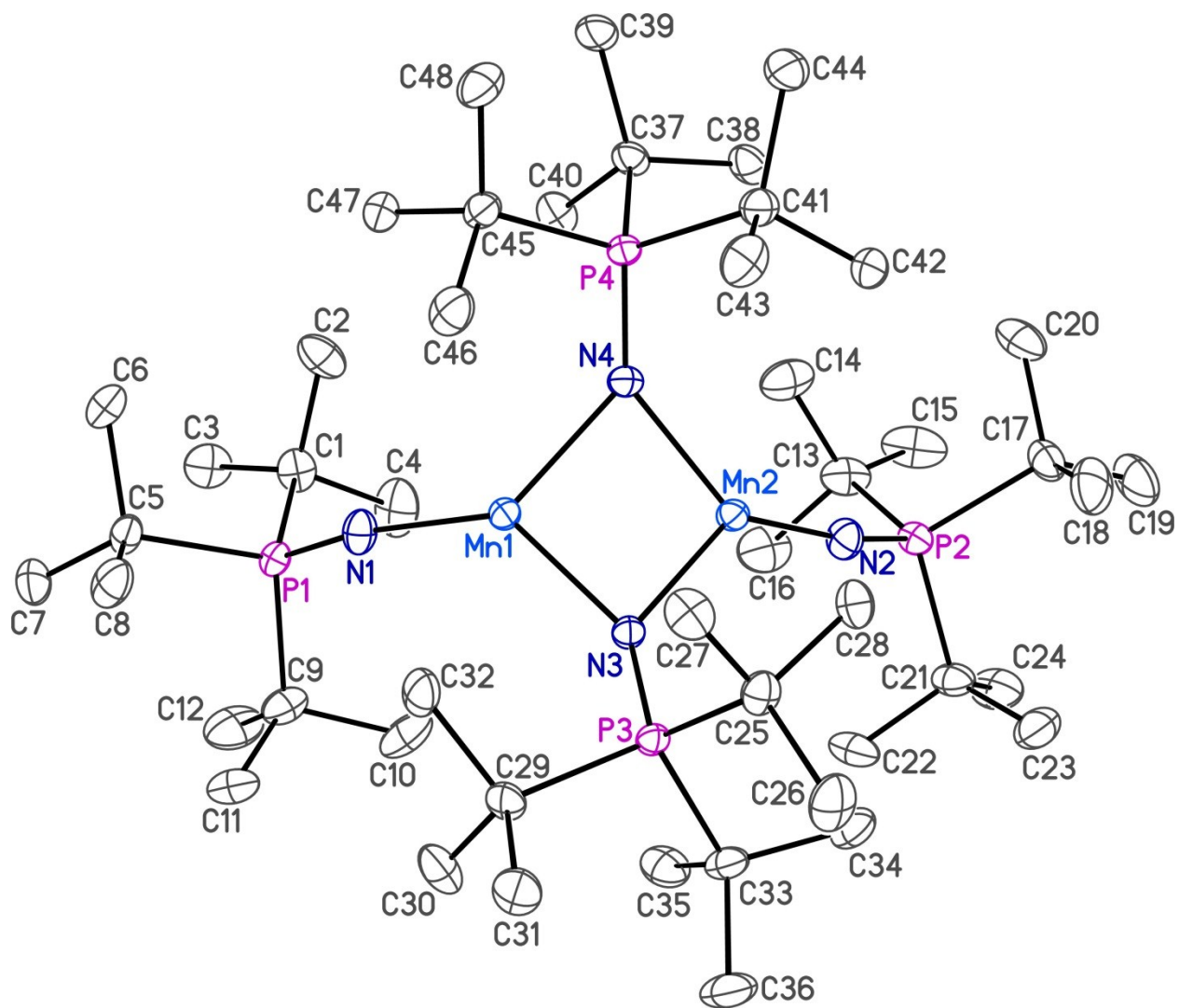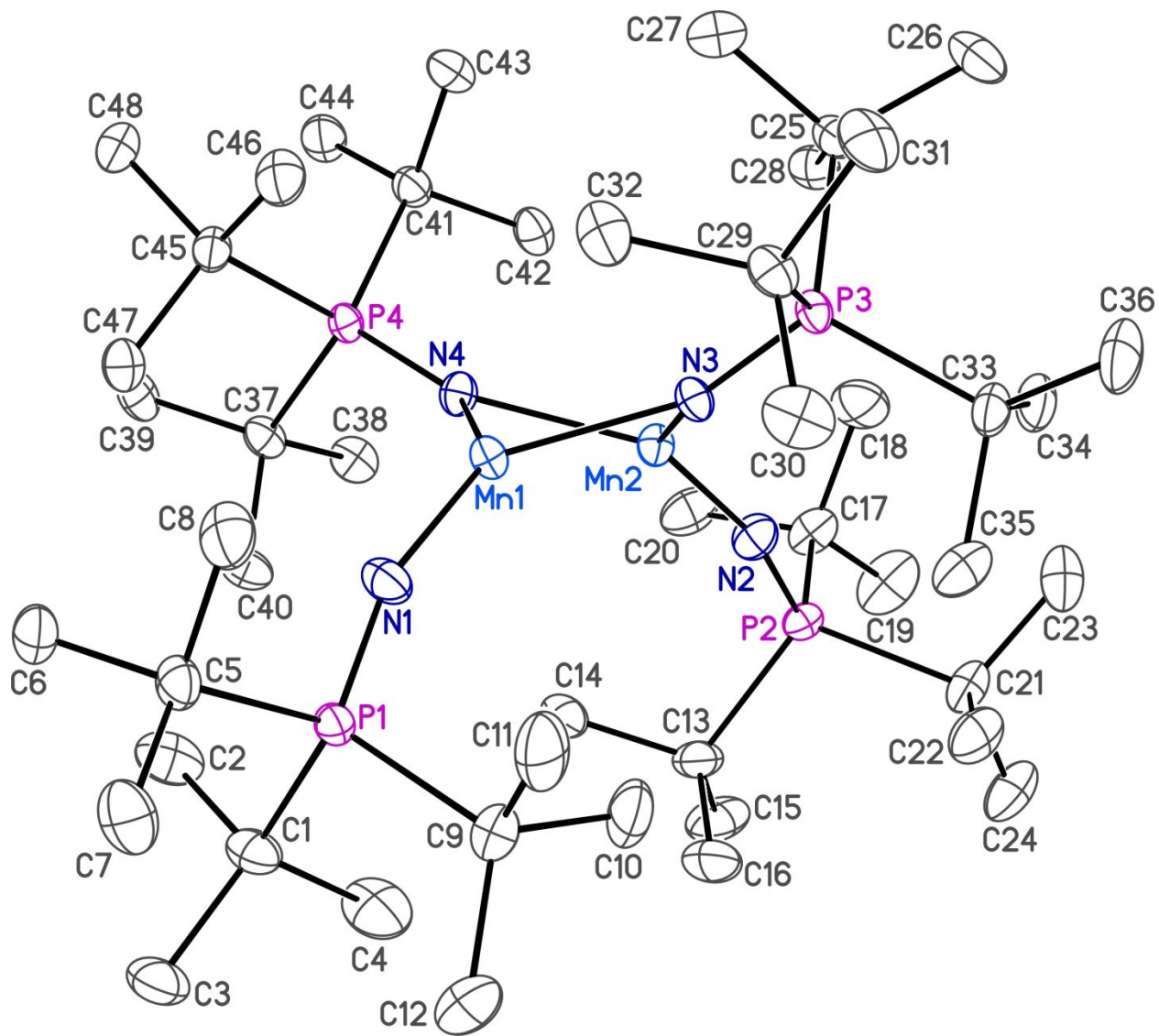
Table 1. Crystallographic Experimental Details

A. Crystal Data

formula	$C_{52}H_{116}Mn_2N_4OP_4$
formula weight	1047.24
crystal dimensions (mm)	$0.39 \times 0.32 \times 0.24$
crystal system	orthorhombic
space group	*Pbca* (No. 61)
unit cell parameters[a]	
$\quad a$ (Å)	29.3862 (9)
$\quad b$ (Å)	12.5383 (4)
$\quad c$ (Å)	33.2379 (11)
$\quad V$ (Å^3)	12246.6 (7)
$\quad Z$	8
ρ_{calcd} (g cm^{-3})	1.136
μ (mm^{-1})	0.553

B. Data Collection and Refinement Conditions

diffractometer	Bruker D8/APEX II CCD[b]
radiation (λ [Å])	graphite-monochromated Mo Kα (0.71073)
temperature (°C)	−100
scan type	ω scans (0.3°) (20 s exposures)
data collection 2θ limit (deg)	52.84
total data collected	94961 (-36 $\leq h \leq$ 36, -15 $\leq k \leq$ 15, -41 $\leq l \leq$ 41)
independent reflections	12571 (R_{int} = 0.0854)
number of observed reflections (*NO*)	8994 [$F_o^2 \geq 2\sigma(F_o^2)$]
structure solution method	intrinsic phasing (*SHELXT*[c])
refinement method	full-matrix least-squares on F^2 (*SHELXL–2013*[c])
absorption correction method	Gaussian integration (face-indexed)
range of transmission factors	0.9282–0.8446
data/restraints/parameters	12571 / 21[d] / 599
goodness-of-fit (*S*)[e] [all data]	1.021
final *R* indices[f]	
$\quad R_1$ [$F_o^2 \geq 2\sigma(F_o^2)$]	0.0434
$\quad wR_2$ [all data]	0.1158
largest difference peak and hole	0.977 and −0.408 e Å^{-3}

[a]Obtained from least-squares refinement of 9972 reflections with 4.44° < 2θ < 43.24°.

[b]Programs for diffractometer operation, data collection, data reduction and absorption correction were those supplied by Bruker.

(continued)

Table 1. Crystallographic Experimental Details (continued)

[c]Sheldrick, G. M. *Acta Crystallogr.* **2008**, *A64*, 112–122.

[d]The disordered solvent tetrahydrofuran had the following distance restraints applied: O–C, 1.43(1) Å; C–C, 1.53(1) Å; C̲–O–C̲, 2.34(2); O̲–C–C̲, 2.42(2) Å; C̲–C–C̲, 2.50(2) Å. An anti-bumping restraint of 2.2(2) Å was applied to H5SB⋯H48B.

[e]$S = [\Sigma w(F_o^2 - F_c^2)^2/(n - p)]^{1/2}$ (n = number of data; p = number of parameters varied; $w = [\sigma^2(F_o^2) + (0.0470P)^2 + 11.6029P]^{-1}$ where $P = [\text{Max}(F_o^2, 0) + 2F_c^2]/3$).

[f]$R_1 = \Sigma||F_o| - |F_c||/\Sigma|F_o|$; $wR_2 = [\Sigma w(F_o^2 - F_c^2)^2/\Sigma w(F_o^4)]^{1/2}$.

STRUCTURE REPORT

XCL Code: JMS1453   **Date:**   7 November 2017

Compound: $[Mn_4(NPEt_3)_4Cl(9\text{-}BBN\text{-}H_2)_3]$

Formula: $C_{48}H_{108}B_3ClMn_4N_4P_4$

Supervisor: J. M. Stryker   **Crystallographer:**   M. J. Ferguson
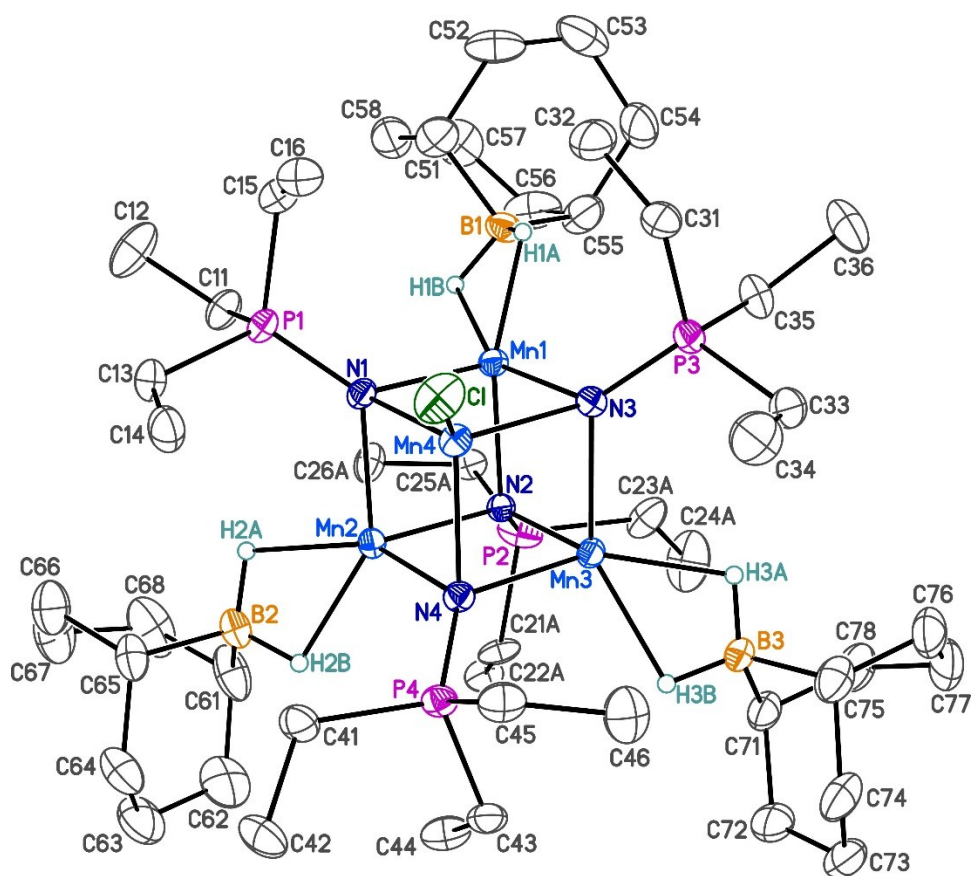
Figure Legends

Figure 1.   Perspective view of the $[Mn_4(NPEt_3)_4Cl(9\text{-}BBN\text{-}H_2)_3]$ molecule showing the atom labelling scheme. Only the major orientation of the disordered PEt_3 group is shown for clarity. Non-hydrogen atoms are represented by Gaussian ellipsoids at the 30% probability level. Hydrogen atoms are shown with arbitrarily small thermal parameters for the BH_2 groups, and are not shown for the remaining groups.
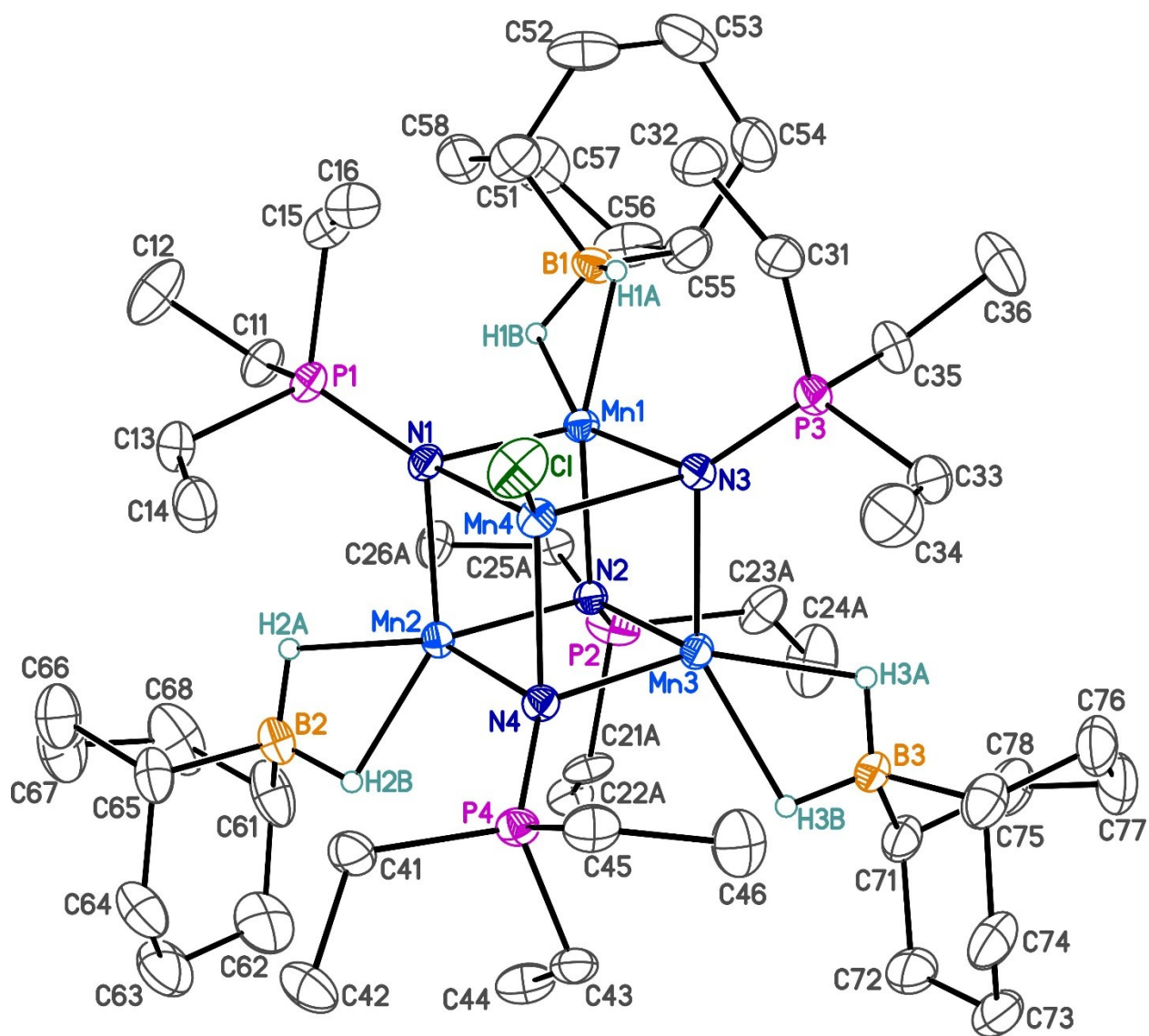
Table 1. Crystallographic Experimental Details

A. Crystal Data

formula	$C_{48}H_{108}B_3ClMn_4N_4P_4$
formula weight	1152.90
crystal dimensions (mm)	$0.33 \times 0.19 \times 0.15$
crystal system	monoclinic
space group	$P2_1$ (No. 4)
unit cell parameters[a]	
a (Å)	12.3750 (5)
b (Å)	19.9882 (9)
c (Å)	12.9679 (6)
β (deg)	109.0047 (5)
V (Å^3)	3032.8 (2)
Z	2
ρ_{calcd} (g cm^{-3})	1.262
μ (mm^{-1})	0.997

B. Data Collection and Refinement Conditions

diffractometer	Bruker D8/APEX II CCD[b]
radiation (λ [Å])	graphite-monochromated Mo Kα (0.71073)
temperature (°C)	-100
scan type	ω scans (0.3°) (20 s exposures)
data collection 2θ limit (deg)	53.01
total data collected	24853 ($-15 \leq h \leq 15$, $-25 \leq k \leq 25$, $-16 \leq l \leq 16$)
independent reflections	12542 (R_{int} = 0.0284)
number of observed reflections (*NO*)	11318 [$F_o^2 \geq 2\sigma(F_o^2)$]
structure solution method	intrinsic phasing (*SHELXT-2014*[c])
refinement method	full-matrix least-squares on F^2 (*SHELXL–2014*[d])
absorption correction method	Gaussian integration (face-indexed)
range of transmission factors	0.8753–0.6640
data/restraints/parameters	12542 / 56[e] / 616
Flack absolute structure parameter[f]	0.024(15)
goodness-of-fit (*S*)[g] [all data]	1.039
final *R* indices[h]	
R_1 [$F_o^2 \geq 2\sigma(F_o^2)$]	0.0326
wR_2 [all data]	0.0808
largest difference peak and hole	0.487 and -0.616 e Å^{-3}

[a]Obtained from least-squares refinement of 9899 reflections with 4.44° < 2θ < 51.58°.

[b]Programs for diffractometer operation, data collection, data reduction and absorption correction were those supplied by Bruker.

Table 1. Crystallographic Experimental Details (continued)

[c]Sheldrick, G. M. *Acta Crystallogr.* **2015**, *A71*, 3–8. (*SHELXT-2014*)

[d]Sheldrick, G. M. *Acta Crystallogr.* **2015**, *C71*, 3–8. (*SHELXL-2014*)

[e]The P–C distances within the disordered PEt$_3$ group were restrained to be approximately equal by use of the *SHELXL* **SADI** instruction; the C–C distances were similarly restrained. Additionally, the rigid bond restraint was applied to the carbon atoms of the major component by use of the **RIGU** instruction. The B–H distances were also restrained by use of **SADI**.

[f]Flack, H. D. *Acta Crystallogr.* **1983**, *A39*, 876–881; Flack, H. D.; Bernardinelli, G. *Acta Crystallogr.* **1999**, *A55*, 908–915; Flack, H. D.; Bernardinelli, G. *J. Appl. Cryst.* **2000**, *33*, 1143–1148. The Flack parameter will refine to a value near zero if the structure is in the correct configuration and will refine to a value near one for the inverted configuration. The value observed herein is indicative of racemic twinning, and was accomodated during the refinement (using the *SHELXL-2014* TWIN instruction [see reference *d*]).

[g]$S = [\Sigma w(F_o^2 - F_c^2)^2/(n - p)]^{1/2}$ (*n* = number of data; *p* = number of parameters varied; $w = [\sigma^2(F_o^2) + (0.0427P)^2 + 0.1833P]^{-1}$ where $P = [\text{Max}(F_o^2, 0) + 2F_c^2]/3$).

[h]$R_1 = \Sigma||F_o| - |F_c||/\Sigma|F_o|$; $wR_2 = [\Sigma w(F_o^2 - F_c^2)^2/\Sigma w(F_o^4)]^{1/2}$.

STRUCTURE REPORT

XCL Code:	JMS1345	**Date:**	9 December 2013

Compound: [Cu$_5$Br$_3$(NP^{t}Bu$_3$)$_2$(NHP^{t}Bu$_3$)]•PhMe

Formula: C$_{43}$H$_{90}$Br$_3$Cu$_5$N$_3$P$_3$ (C$_{36}$H$_{82}$Br$_3$Cu$_5$N$_3$P$_3$•C$_7$H$_8$)

Supervisor:	J. M. Stryker	**Crystallographer:**	M. J. Ferguson
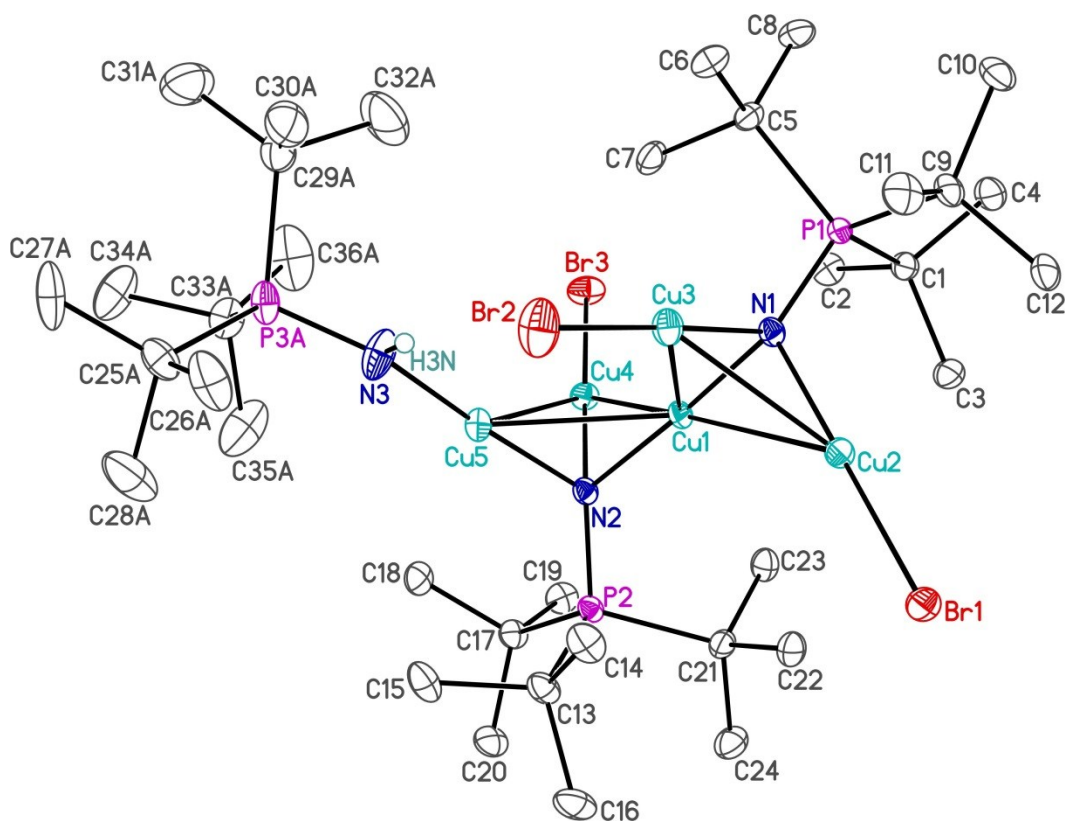
Figure Legends

Figure 1.   Perspective view of the $[Cu_5Br_3(NP^tBu_3)_2(NHP^tBu_3)]$ molecule showing the atom labelling scheme. Only the major orientation of the disordered tri-*tert*-butylphosphoranimine group is shown for clarity. Non-hydrogen atoms are represented by Gaussian ellipsoids at the 30% probability level. Hydrogen atoms are shown with arbitrarily small thermal parameters for the N–H group, and are not shown for the remaining groups.

Figure 2.   Alternate view of the molecule.
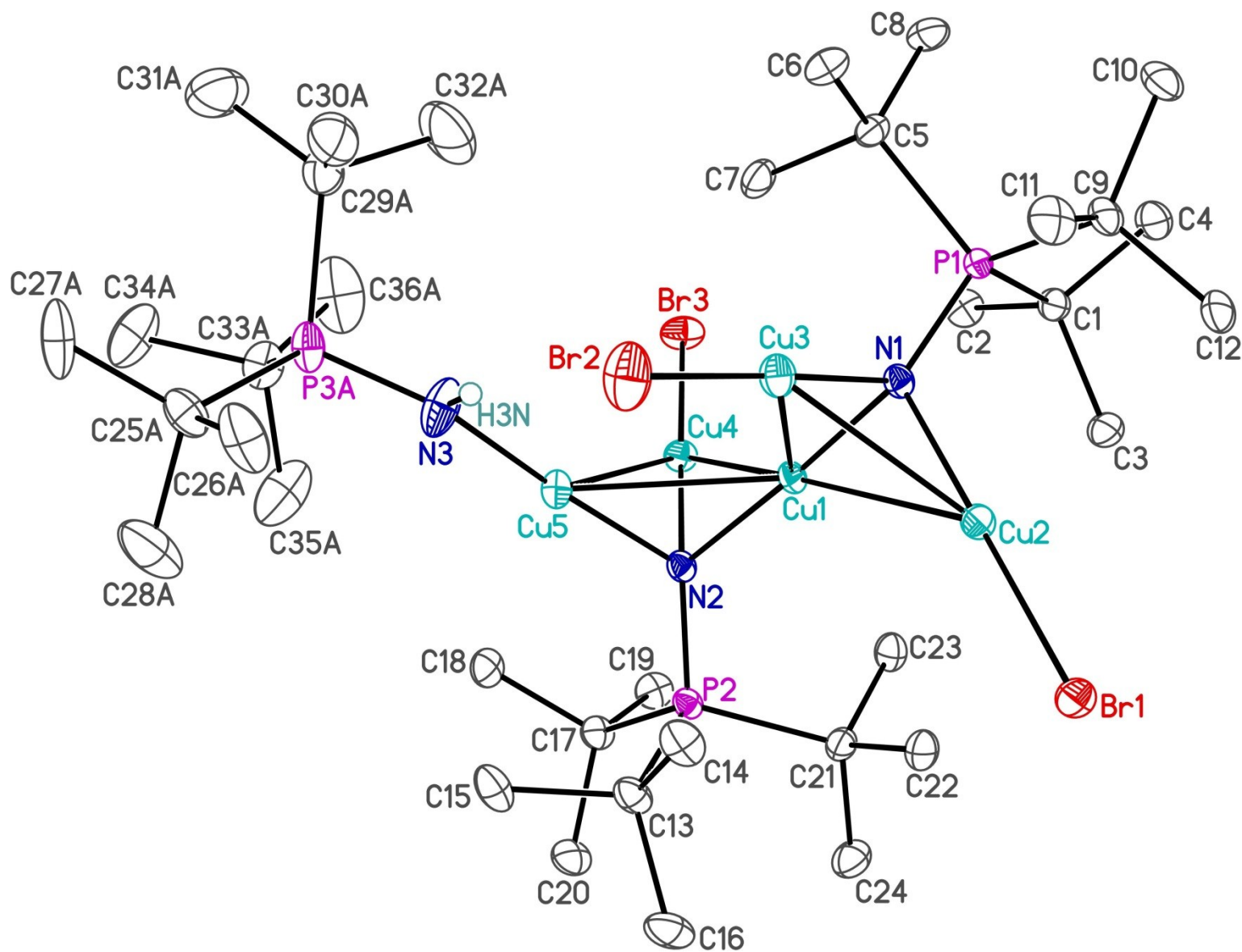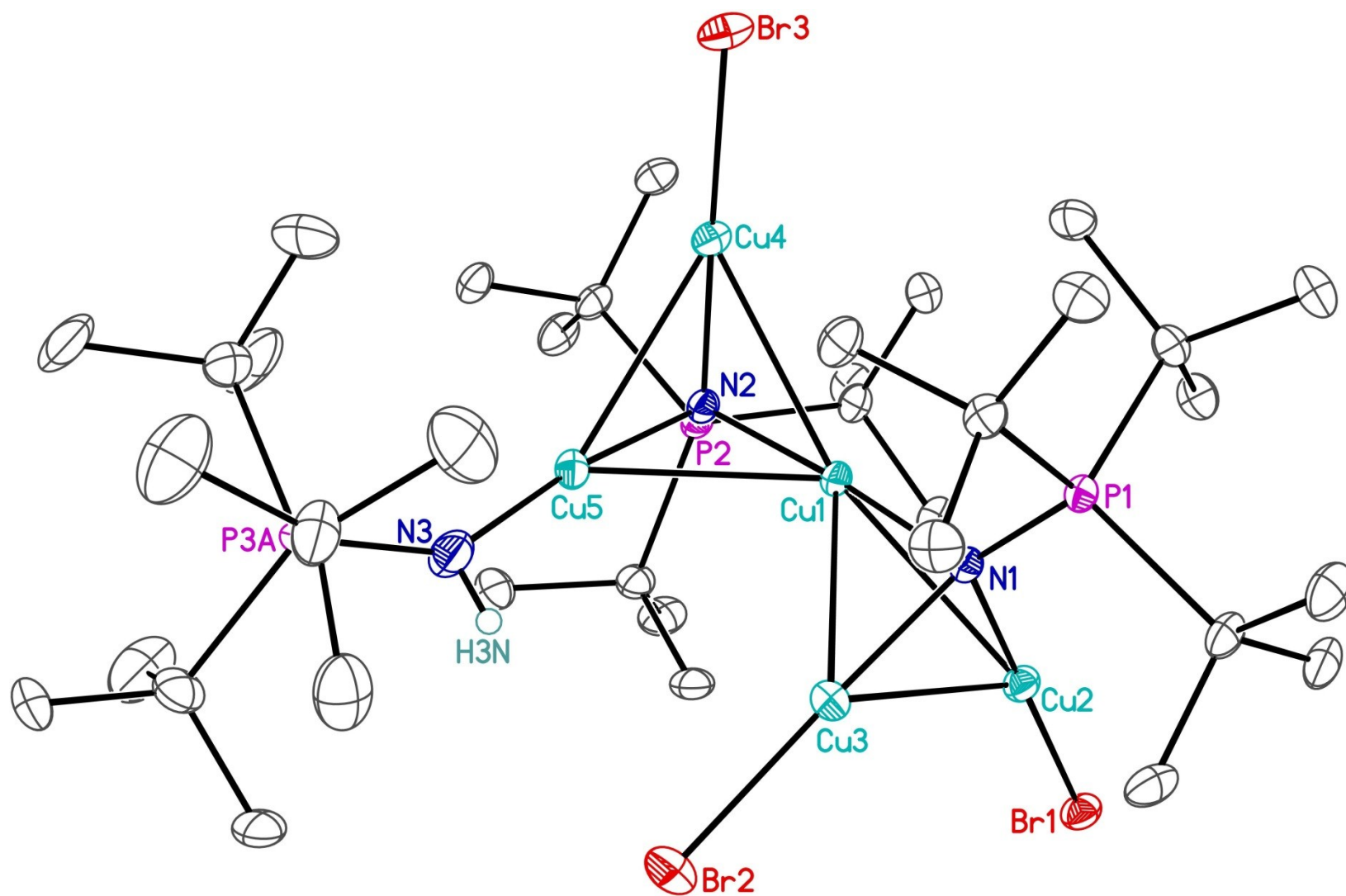
Table 1. Crystallographic Experimental Details

A. Crystal Data

formula	$C_{43}H_{90}Br_3Cu_5N_3P_3$
formula weight	1299.51
crystal dimensions (mm)	$0.32 \times 0.15 \times 0.08$
crystal system	triclinic
space group	$P\bar{1}$ (No. 2)
unit cell parameters[a]	
$\quad a$ (Å)	11.9925 (4)
$\quad b$ (Å)	14.7485 (5)
$\quad c$ (Å)	18.2496 (6)
$\quad \alpha$ (deg)	108.7647 (4)
$\quad \beta$ (deg)	101.7417 (4)
$\quad \gamma$ (deg)	106.2588 (4)
$\quad V$ (Å^3)	2776.81 (16)
$\quad Z$	2
ρ_{calcd} (g cm^{-3})	1.554
μ (mm^{-1})	4.159

B. Data Collection and Refinement Conditions

diffractometer	Bruker D8/APEX II CCD[b]
radiation (λ [Å])	graphite-monochromated Mo Kα (0.71073)
temperature (°C)	-100
scan type	ω scans (0.3°) (20 s exposures)
data collection 2θ limit (deg)	54.98
total data collected	24888 ($-15 \leq h \leq 15$, $-19 \leq k \leq 18$, $-23 \leq l \leq 23$)
independent reflections	12670 (R_{int} = 0.0145)
number of observed reflections (*NO*)	10947 [$F_o^2 \geq 2\sigma(F_o^2)$]
structure solution method	intrinsic phasing (*SHELXT*[c])
refinement method	full-matrix least-squares on F^2 (*SHELXL–2013*[c])
absorption correction method	Gaussian integration (face-indexed)
range of transmission factors	0.7896–0.3735
data/restraints/parameters	12670 / 0 / 619
goodness-of-fit (*S*)[d] [all data]	1.098
final *R* indices[e]	
$\quad R_1$ [$F_o^2 \geq 2\sigma(F_o^2)$]	0.0253
$\quad wR_2$ [all data]	0.0728
largest difference peak and hole	1.117 and -0.463 e Å^{-3}

[a]Obtained from least-squares refinement of 9828 reflections with 4.58° < 2θ < 54.90°.

(continued)

Table 1. Crystallographic Experimental Details (continued)

[b]Programs for diffractometer operation, data collection, data reduction and absorption correction were those supplied by Bruker.

[c]Sheldrick, G. M. *Acta Crystallogr.* **2008**, *A64*, 112–122.

[d]$S = [\Sigma w(F_o^2 - F_c^2)^2/(n - p)]^{1/2}$ (n = number of data; p = number of parameters varied; $w = [\sigma^2(F_o^2) + (0.0409P)^2 + 0.5015P]^{-1}$ where $P = [\text{Max}(F_o^2, 0) + 2F_c^2]/3$).

[e]$R_1 = \Sigma||F_o| - |F_c||/\Sigma|F_o|$; $wR_2 = [\Sigma w(F_o^2 - F_c^2)^2/\Sigma w(F_o^4)]^{1/2}$.

STRUCTURE REPORT

XCL Code: JMS1339   **Date:** 19 November 2013

Compound: $[Cu_4(NP^tBu_3)_4Li_2(OC_4H_8)_2]$

Formula: $C_{56}H_{124}Cu_4Li_2N_4O_2P_4$

Supervisor: J. M. Stryker   **Crystallographer:** M. J. Ferguson
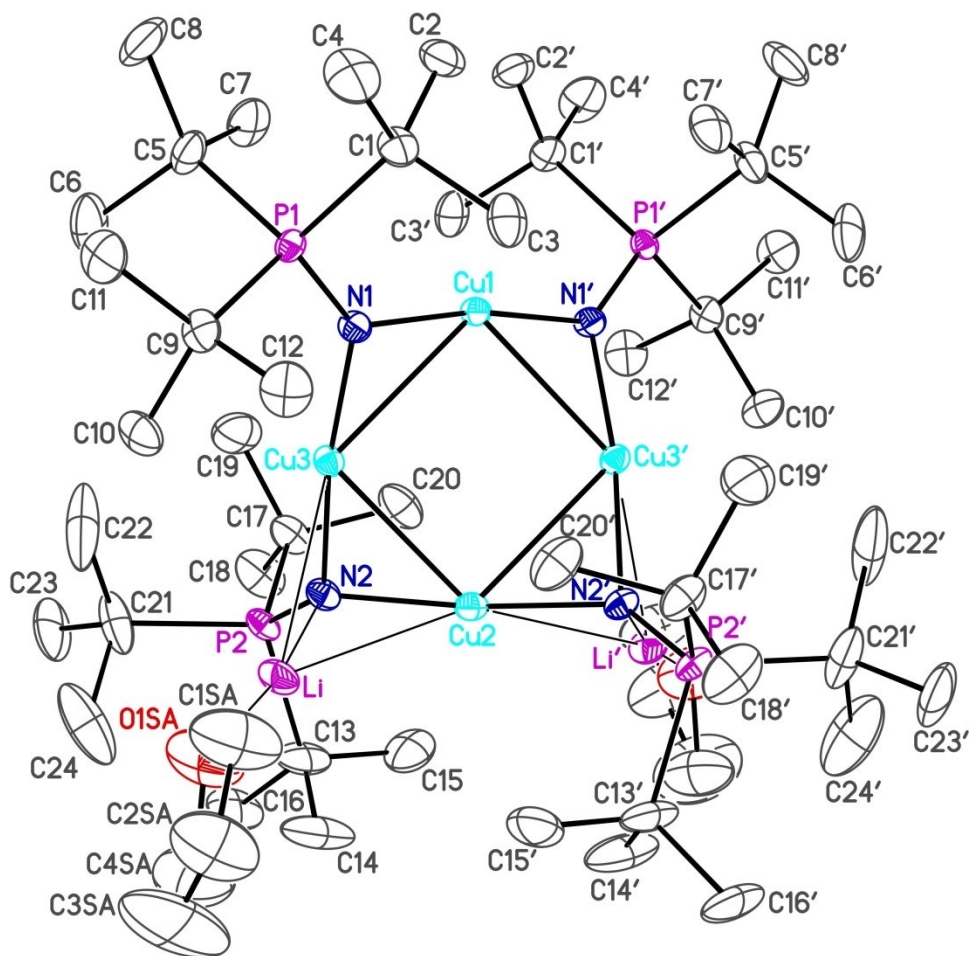
Figure Legends

Figure 1.   Perspective view of the $[Cu_4(NP^tBu_3)_4Li_2(OC_4H_8)_2]$ molecule showing the atom labelling scheme.   Only the major orientation (79%) of the disordered tetrahydrofuran molecule is shown. Primed atoms are related to unprimed ones by the 2-fold rotation axis at ($^1/_2$, y, $^1/_4$). Non-hydrogen atoms are represented by Gaussian ellipsoids at the 30% probability level. Hydrogen atoms are not shown.

Figure 2.   Alternate view of the molecule.
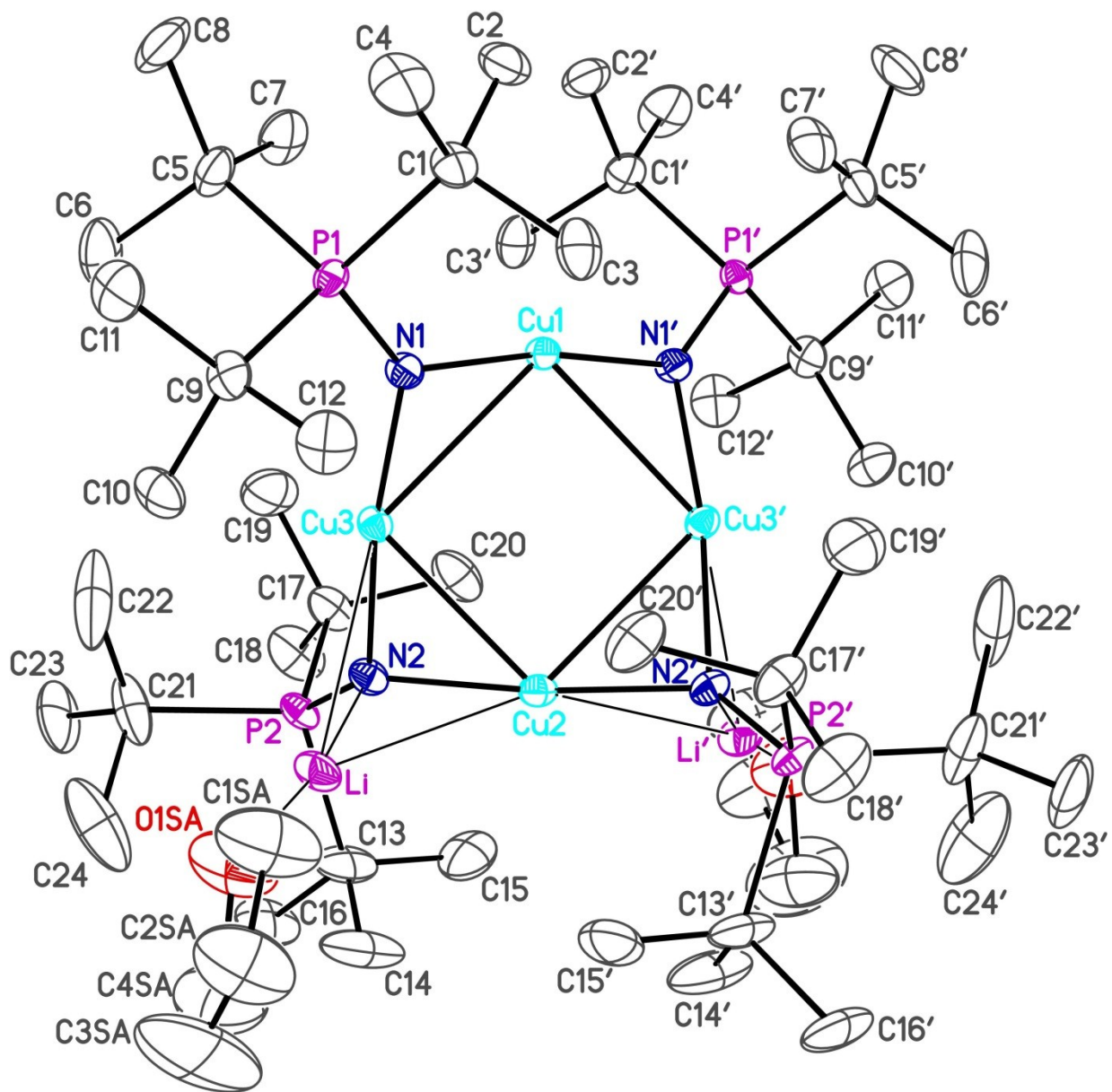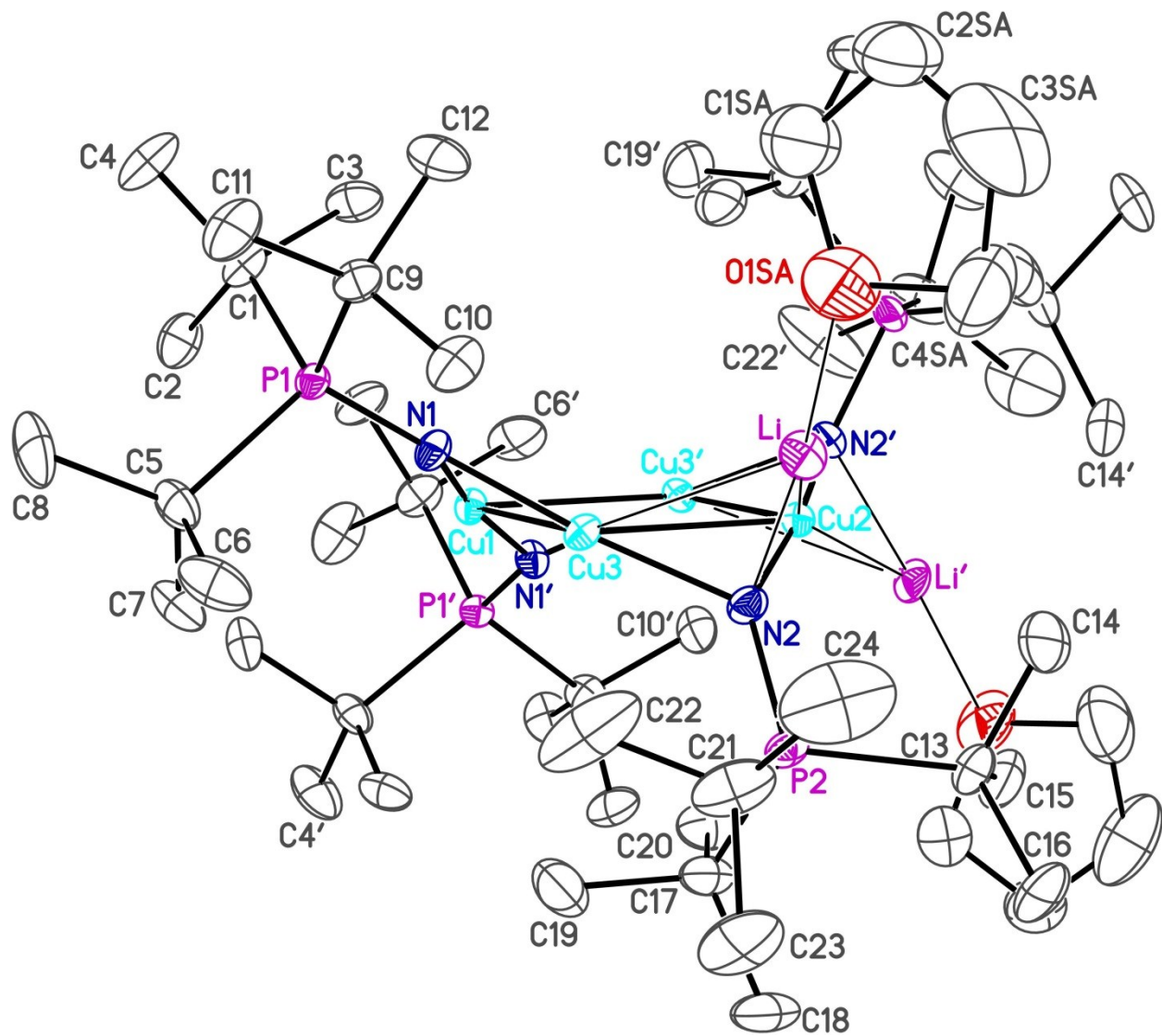
Table 1. Crystallographic Experimental Details

A. Crystal Data

formula	$C_{56}H_{124}Cu_4Li_2N_4O_2P_4$
formula weight	1277.50
crystal dimensions (mm)	$0.51 \times 0.43 \times 0.35$
crystal system	monoclinic
space group	$C2/c$ (No. 15)
unit cell parameters[a]	
$\quad a$ (Å)	23.4162 (9)
$\quad b$ (Å)	12.8971 (5)
$\quad c$ (Å)	23.6950 (9)
$\quad \beta$ (deg)	113.5896 (4)
$\quad V$ (Å^3)	6557.9 (4)
$\quad Z$	4
ρ_{calcd} (g cm^{-3})	1.294
μ (mm^{-1})	1.417

B. Data Collection and Refinement Conditions

diffractometer	Bruker D8/APEX II CCD[b]
radiation (λ [Å])	graphite-monochromated Mo Kα (0.71073)
temperature (°C)	-100
scan type	ω scans (0.3°) (10 s exposures)
data collection 2θ limit (deg)	54.91
total data collected	28733 ($-30 \leq h \leq 30$, $-16 \leq k \leq 16$, $-30 \leq l \leq 30$)
independent reflections	7510 (R_{int} = 0.0109)
number of observed reflections (*NO*)	6936 [$F_o^2 \geq 2\sigma(F_o^2)$]
structure solution method	direct methods (*SHELXS–2013*[c])
refinement method	full-matrix least-squares on F^2 (*SHELXL–2013*[c])
absorption correction method	Gaussian integration (face-indexed)
range of transmission factors	0.7241–0.6045
data/restraints/parameters	7510 / 11[d] / 365
goodness-of-fit (*S*)[e] [all data]	1.044
final *R* indices[f]	
$\quad R_1$ [$F_o^2 \geq 2\sigma(F_o^2)$]	0.0281
$\quad wR_2$ [all data]	0.0812
largest difference peak and hole	0.548 and -0.369 e Å^{-3}

[a]Obtained from least-squares refinement of 9752 reflections with 4.68° < 2θ < 54.90°.

[b]Programs for diffractometer operation, data collection, data reduction and absorption correction were those supplied by Bruker.

Table 1. Crystallographic Experimental Details (continued)

[c]Sheldrick, G. M. *Acta Crystallogr.* **2008**, *A64*, 112–122.

[d]The following distance restraints were applied to the minor component of the disordered tetrahydrofuran molecule: O–C, 1.43(1) Å; C–C, 1.53(1) Å; O1SB⋯C2SB, O1SB⋯C3SB, 2.42(2) Å; C1SB⋯C4SB, 2.34(2) Å; C1SB⋯C3SB, C2SB⋯C4SB, 2.50(2) Å.

[e]$S = [\Sigma w(F_o^2 - F_c^2)^2/(n - p)]^{1/2}$ (n = number of data; p = number of parameters varied; $w = [\sigma^2(F_o^2) + (0.0432P)^2 + 8.6444P]^{-1}$ where $P = [\text{Max}(F_o^2, 0) + 2F_c^2]/3$).

[f]$R_1 = \Sigma||F_o| - |F_c||/\Sigma|F_o|$; $wR_2 = [\Sigma w(F_o^2 - F_c^2)^2/\Sigma w(F_o^4)]^{1/2}$.

STRUCTURE REPORT

XCL Code: JMS1722

Date: 3 November 2017

Compound: [$^{t}Bu_3PNH(9\text{-}BBN)$]

Formula: $C_{20}H_{43}BNP$

Supervisor: J. M. Stryker

Crystallographer: M. J. Ferguson
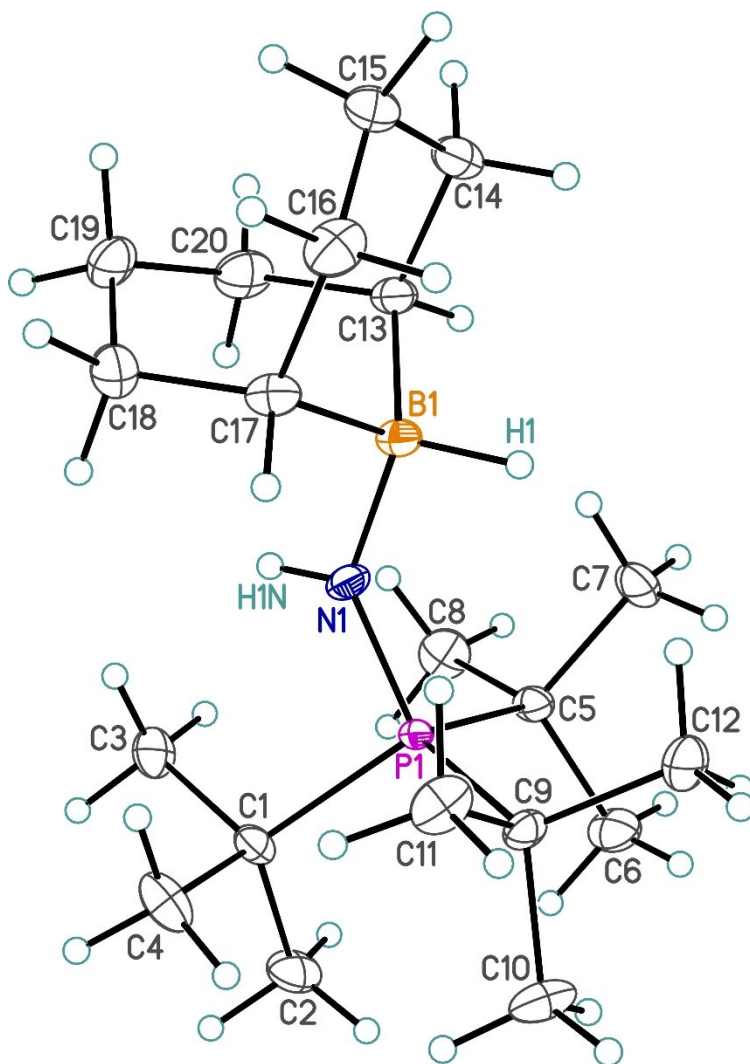
Figure Legends

Figure 1.   Perspective view of one of two crystallographically-independent [^{t}Bu$_3$PNH(9-BBN)] molecules (molecule A) showing the atom labelling scheme. Non-hydrogen atoms are represented by Gaussian ellipsoids at the 30% probability level. Hydrogen atoms are shown with arbitrarily small thermal parameters.

Figure 2.   Alternate view of the second independent molecule (molecule B). Only the N–H and B–H hydrogen atoms are shown; the remaining hydrogen atoms have been removed for clarity.
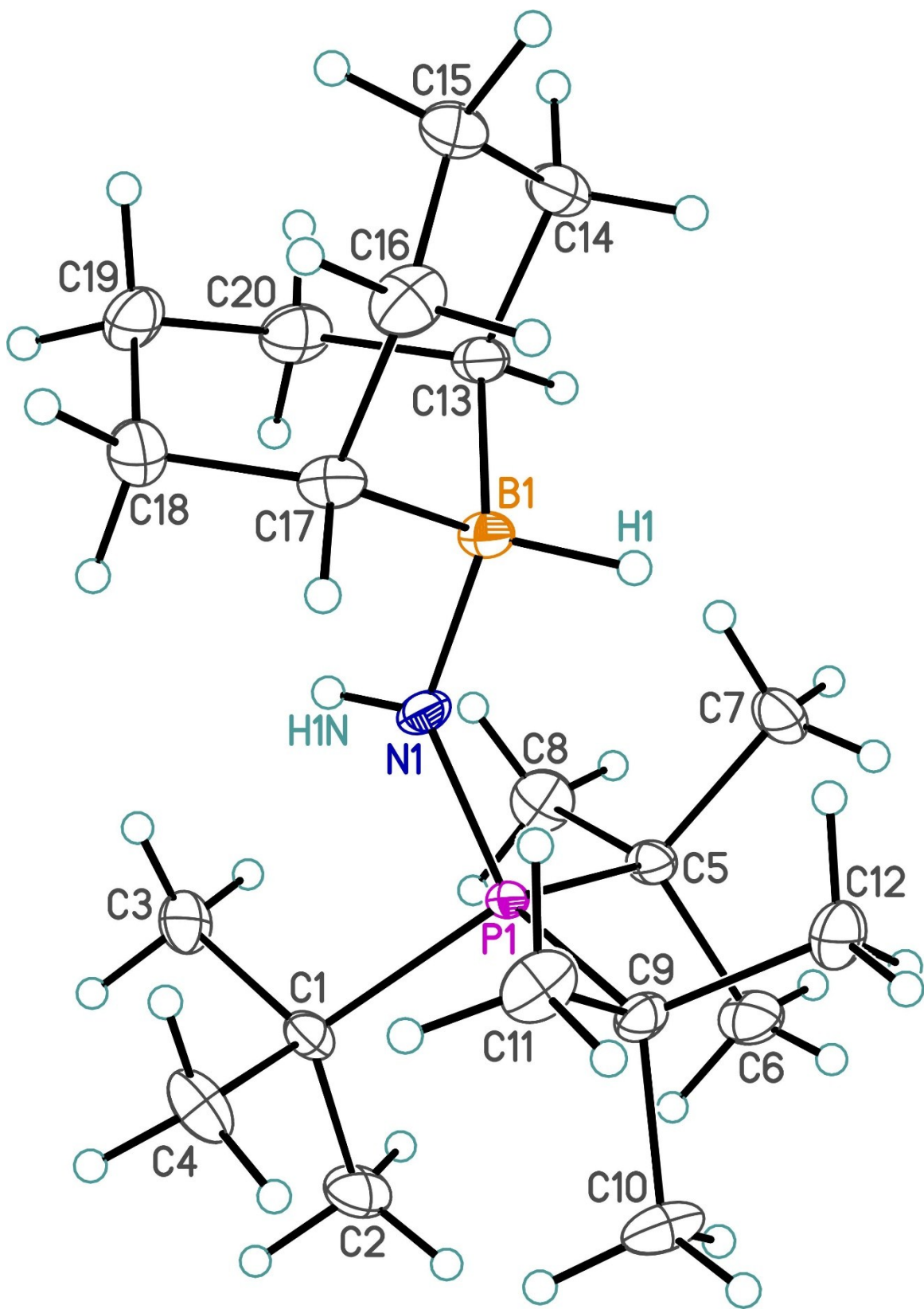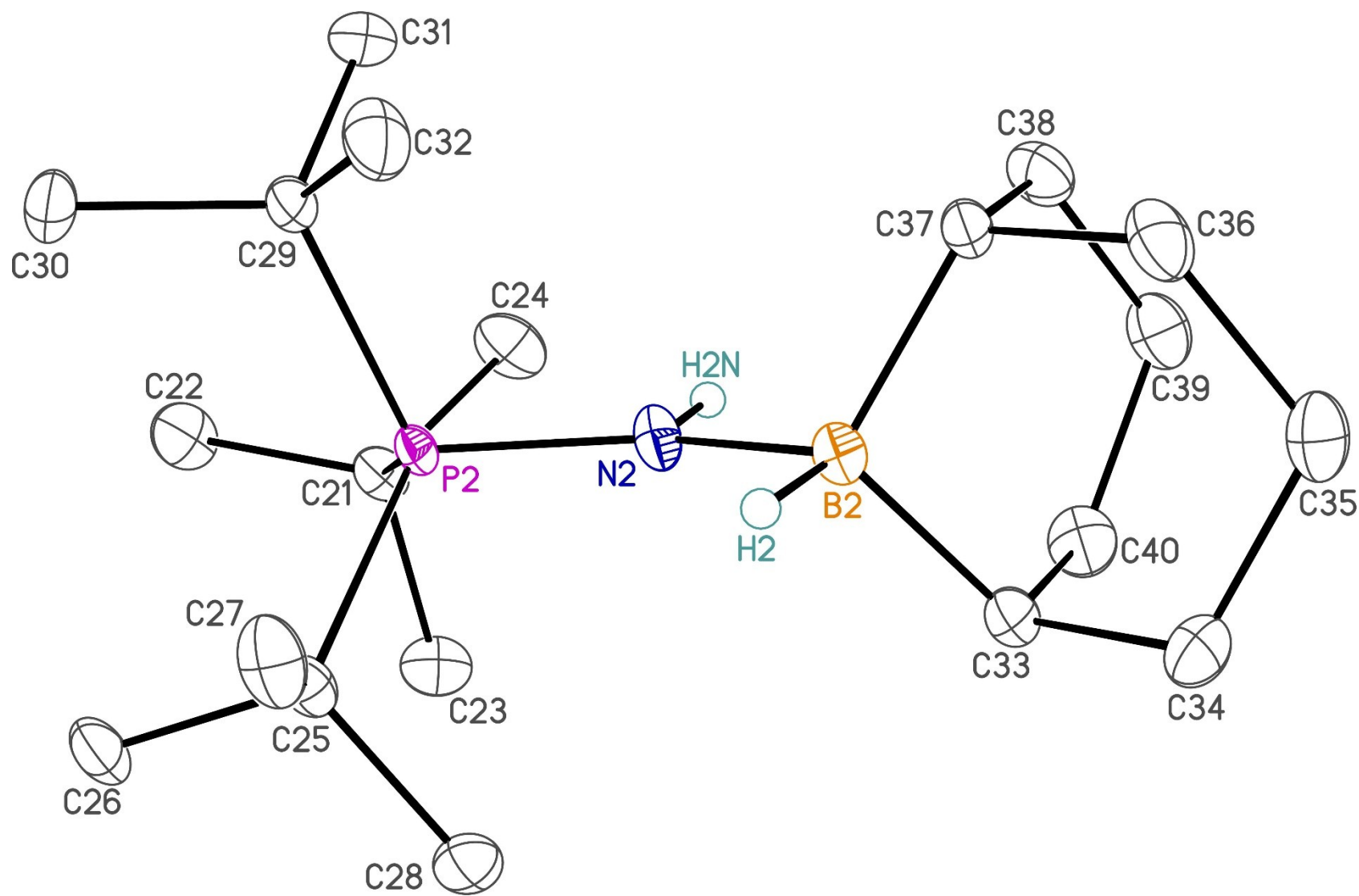
Table 1. Crystallographic Experimental Details

A. Crystal Data

formula	$C_{20}H_{43}BNP$
formula weight	339.33
crystal dimensions (mm)	$0.34 \times 0.18 \times 0.02$
crystal system	monoclinic
space group	$P2_1/n$ (an alternate setting of $P2_1/c$ [No. 14])
unit cell parameters[a]	
a (Å)	11.2003 (3)
b (Å)	12.8397 (3)
c (Å)	29.6057 (7)
β (deg)	99.3644 (14)
V (Å^3)	4200.81 (18)
Z	8
ρ_{calcd} (g cm^{-3})	1.073
μ (mm^{-1})	1.128

B. Data Collection and Refinement Conditions

diffractometer	Bruker D8/APEX II CCD[b]
radiation (λ [Å])	Cu Kα (1.54178) (microfocus source)
temperature (°C)	−100
scan type	ω and ϕ scans (1.0°) (15 s exposures)
data collection 2θ limit (deg)	140.66
total data collected	57344 ($-13 \leq h \leq 13$, $-15 \leq k \leq 15$, $-35 \leq l \leq 36$)
independent reflections	7859 (R_{int} = 0.0966)
number of observed reflections (*NO*)	5837 [$F_o^2 \geq 2\sigma(F_o^2)$]
structure solution method	intrinsic phasing (*SHELXT-2014*[c])
refinement method	full-matrix least-squares on F^2 (*SHELXL–2014*[d])
absorption correction method	Gaussian integration (face-indexed)
range of transmission factors	1.0000–0.6603
data/restraints/parameters	7859 / 0 / 449
goodness-of-fit (*S*)[e] [all data]	1.021
final *R* indices[f]	
R_1 [$F_o^2 \geq 2\sigma(F_o^2)$]	0.0637
wR_2 [all data]	0.1896
largest difference peak and hole	1.076 and −0.335 e Å^{-3}

[a]Obtained from least-squares refinement of 8025 reflections with 9.00° < 2θ < 140.40°.

[b]Programs for diffractometer operation, data collection, data reduction and absorption correction were those supplied by Bruker.

Table 1. Crystallographic Experimental Details (continued)

[c]Sheldrick, G. M. *Acta Crystallogr.* **2015**, *A71*, 3–8. (*SHELXT-2014*)

[d]Sheldrick, G. M. *Acta Crystallogr.* **2015**, *C71*, 3–8. (*SHELXL-2014*)

[e]$S = [\Sigma w(F_o{}^2 - F_c{}^2)^2/(n - p)]^{1/2}$ (n = number of data; p = number of parameters varied; w = $[\sigma^2(F_o{}^2) + (0.1031P)^2 + 1.6316P]^{-1}$ where $P = [\text{Max}(F_o{}^2, 0) + 2F_c{}^2]/3$).

[f]$R_1 = \Sigma||F_o| - |F_c||/\Sigma|F_o|$; $wR_2 = [\Sigma w(F_o{}^2 - F_c{}^2)^2/\Sigma w(F_o{}^4)]^{1/2}$.

Sample chromatogram and mass spectra of GC-MS analysis of the products produced form the hydrodesulfurization of DBT.

```
                        Area Percent Report

Data File : E:\20140428\0201002.D                  Vial: 2
Acq On    : 28 Apr 20114 123:0              Operator: WDM
Sample    : BROWN OB-2-015                 Inst    : GCMS1
Misc      :                                Multiplr: 1.00
                                       Sample Amount: 0.00
MS Integration Params: autoint1.e

Method    : C:\HPCHEM\1\METHODS\DEFAULT.M (Chemstation Integrator)
Title     :

Signal    : TIC

peak  R.T. first  max last  PK   peak      peak     peak    % of
  #    min  scan scan scan  TY  height     area   % max.   total
---  ----- ----- ---- ---- ---  -------   -------  ------  -------
  1  13.109   832  842  889 PV     41377  1350234  59.35%  28.046%
  2  15.002  1004 1008 1023 BV 2    1405    34779   1.53%   0.722%
  3  16.055  1084 1100 1127 PV     36737  1101891  48.43%  22.887%
  4  18.085  1249 1278 1326 BV     50340  2275079 100.00%  47.255%
  5  20.656  1495 1503 1509 BV 2    2413    52447   2.31%   1.089%



                  Sum of corrected areas:     4814431

 0201002.D  DEFAULT.M     Tue Apr 29 07:56:40 2014
```
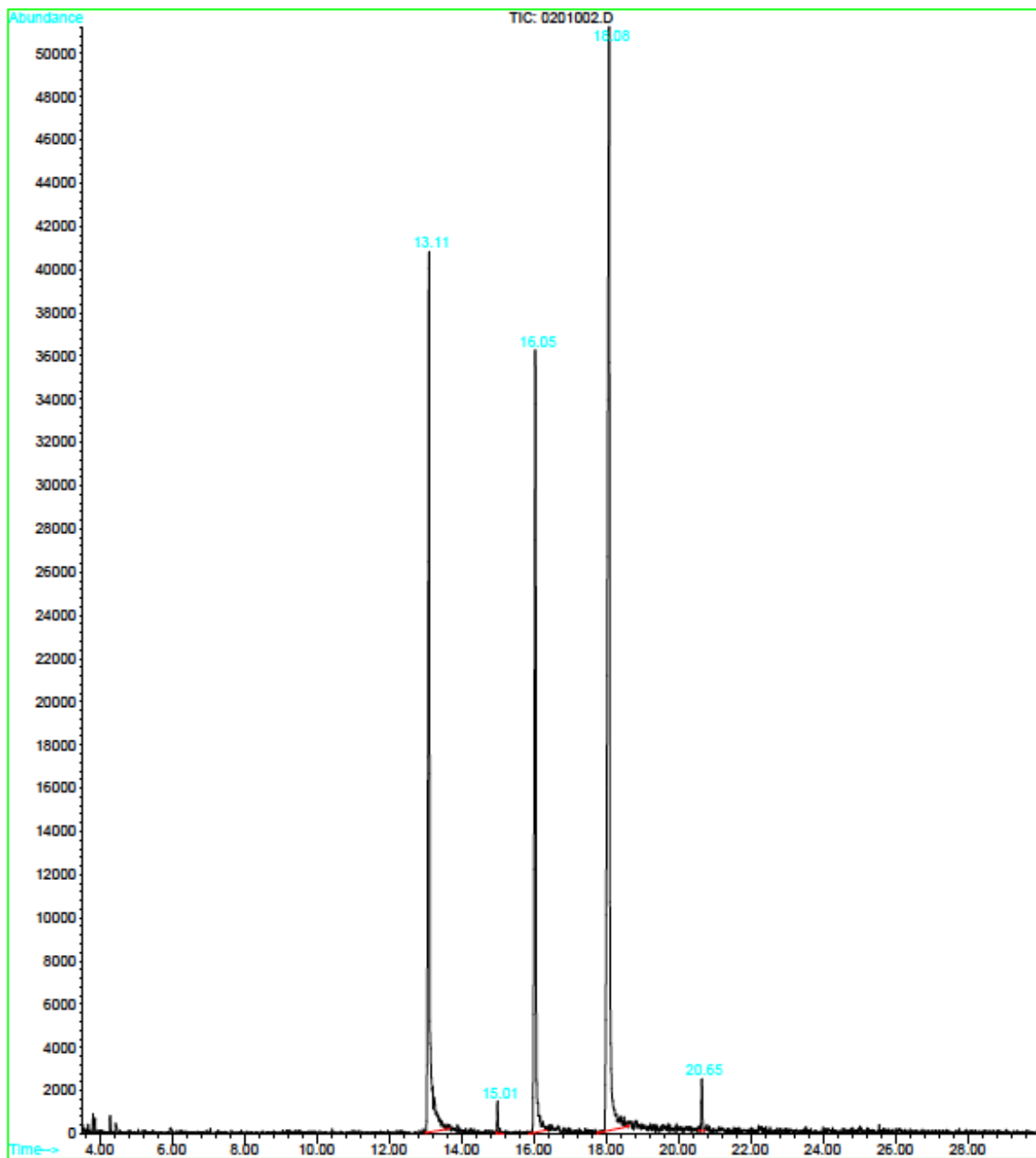
Unknown: Average of 13.074 to 13.177 min.: 0201002.D
Compound in Library Factor = 146
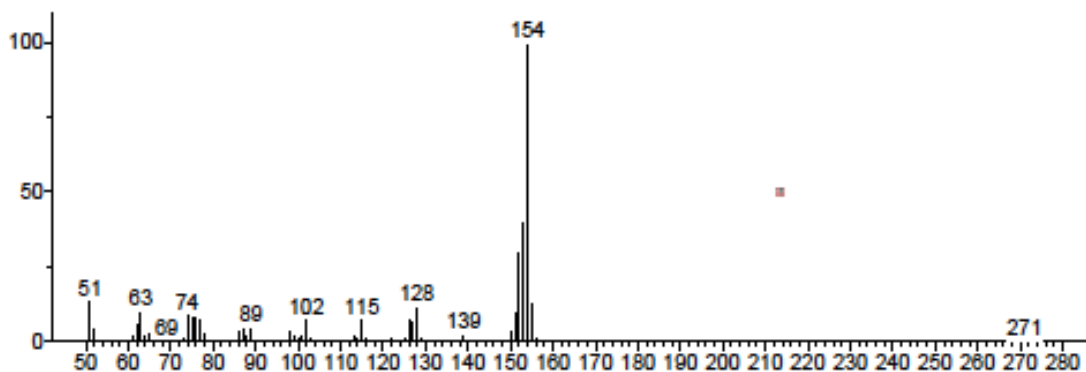
Hit 1 : Biphenyl
C12H10; MF: 919; RMF: 932; Prob 75.8%; CAS: 92-52-4; Lib: mainlib; ID: 127483.
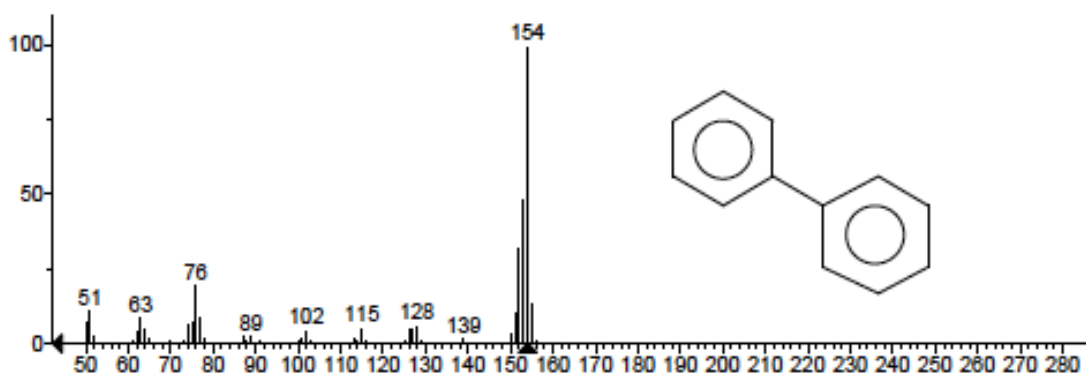
Hit 2 : Biphenyl
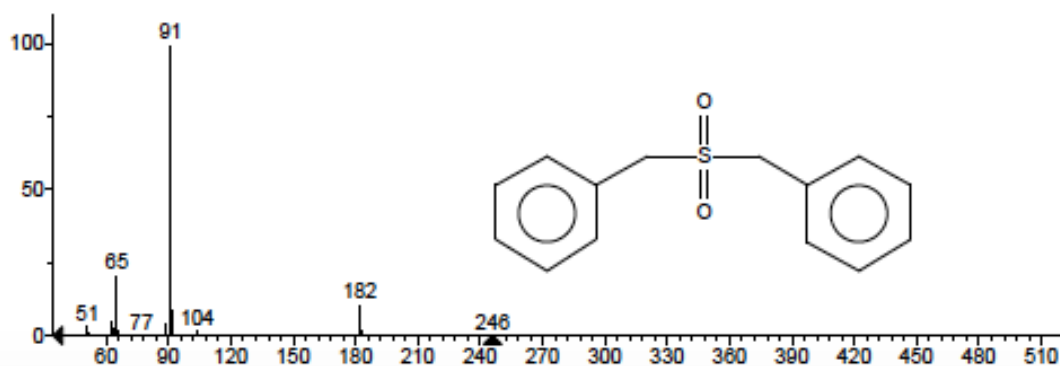C12H10; MF: 916; RMF: 918; Prob 75.8%; CAS: 92-52-4; Lib: replib; ID: 22436.
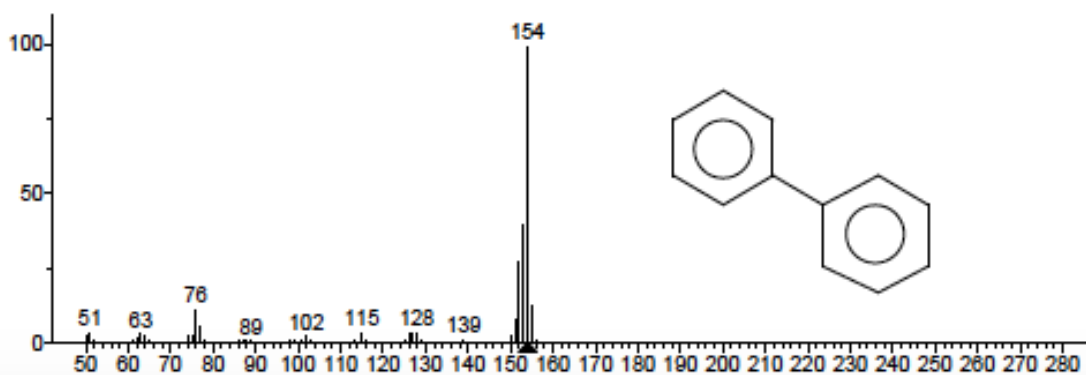
Unknown: Average of 14.979 to 15.013 min.: 0201002.D
Compound in Library Factor = -257
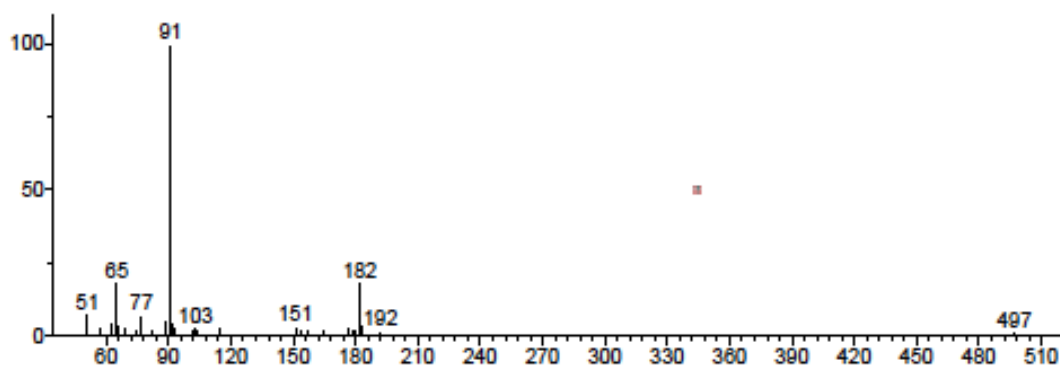
Hit 1 : Bibenzyl
C14H14; MF: 757; RMF: 809; Prob 50.6%; CAS: 103-29-7; Lib: mainlib; ID: 57487.
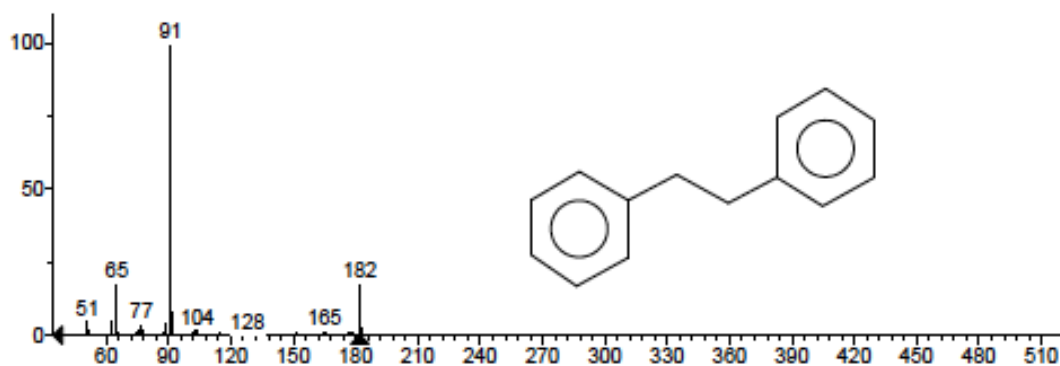
Hit 2 : Benzyl sulfone
C14H14O2S; MF: 749; RMF: 898; Prob 37.8%; CAS: 620-32-6; Lib: mainlib; ID: 54387.

Unknown: Average of 16.008 to 16.055 min.: 0201002.D
Compound in Library Factor = -119
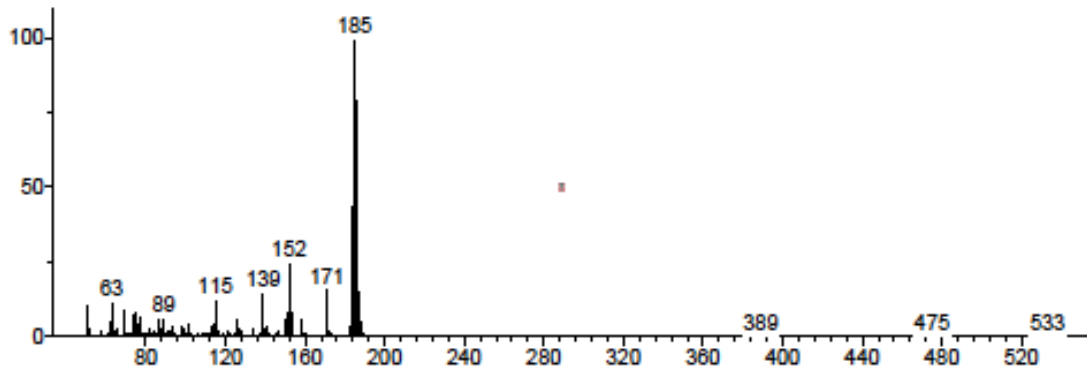
Hit 1 : Naphtho[2,3-c]thiophene, 1,3-dihydro-
C12H10S; MF: 835; RMF: 840; Prob 78.5%; CAS: 58948-53-1; Lib: mainlib; ID: 152379.
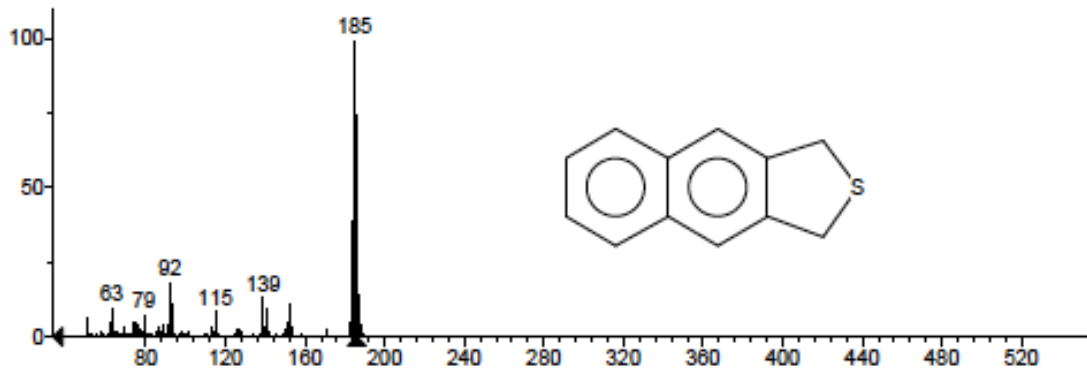
Hit 2 : Diphenyl sulfide
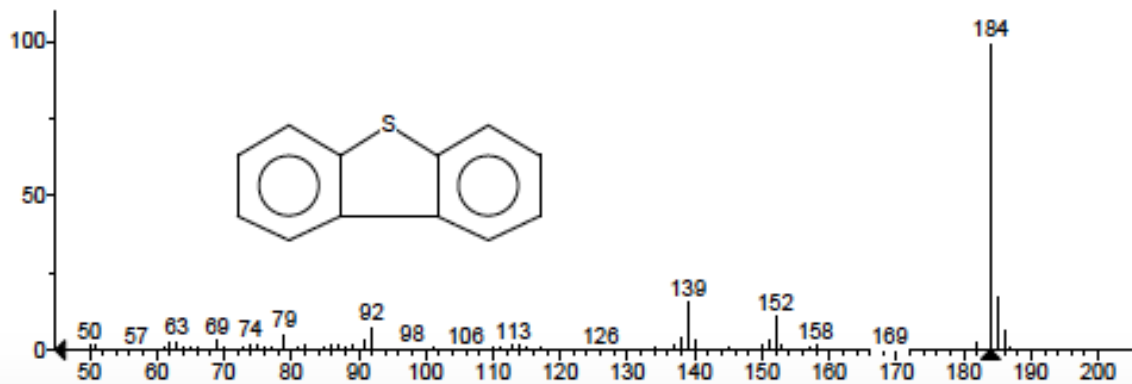C12H10S; MF: 788; RMF: 798; Prob 16.4%; CAS: 139-66-2; Lib: mainlib; ID: 153783.
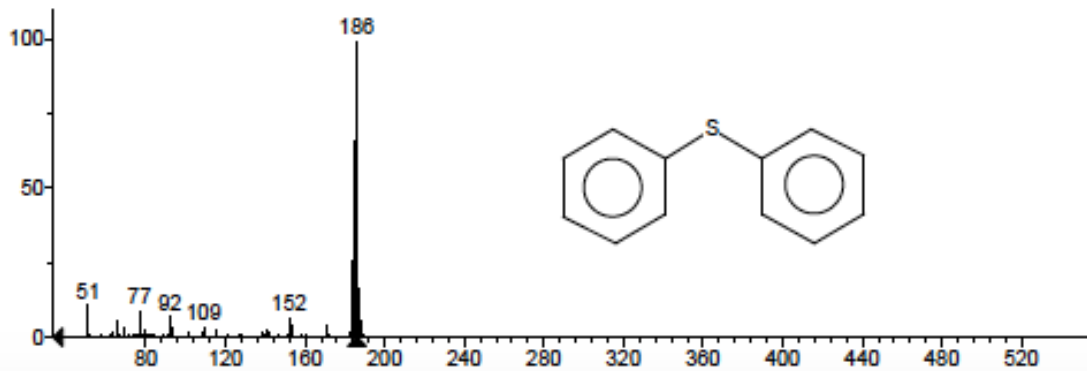
Unknown: Average of 18.018 to 18.131 min.: 0201002.D
Compound in Library Factor = 200
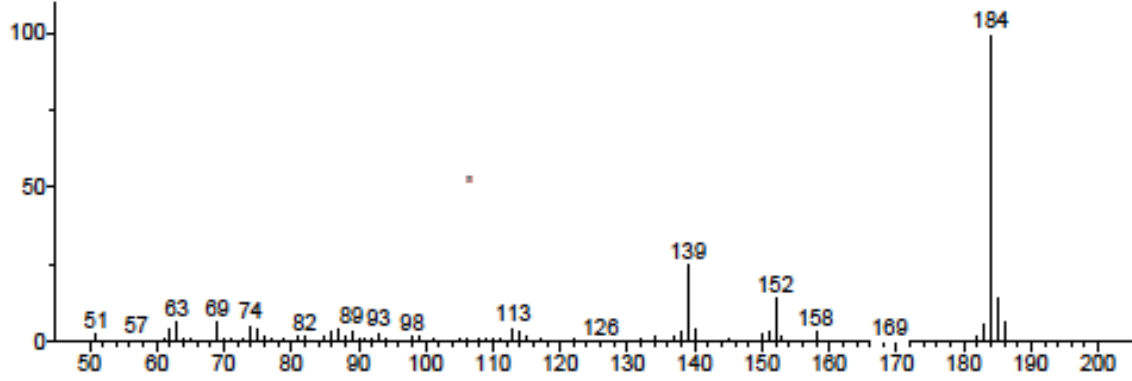
Hit 1 : Naphtho[1,2-b]thiophene
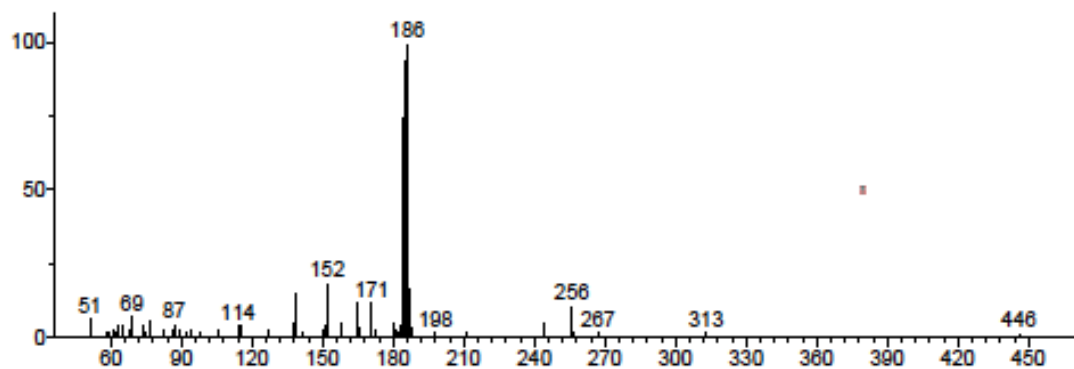C12H8S; MF: 881; RMF: 895; Prob 30.7%; CAS: 234-41-3; Lib: mainlib; ID: 151284.
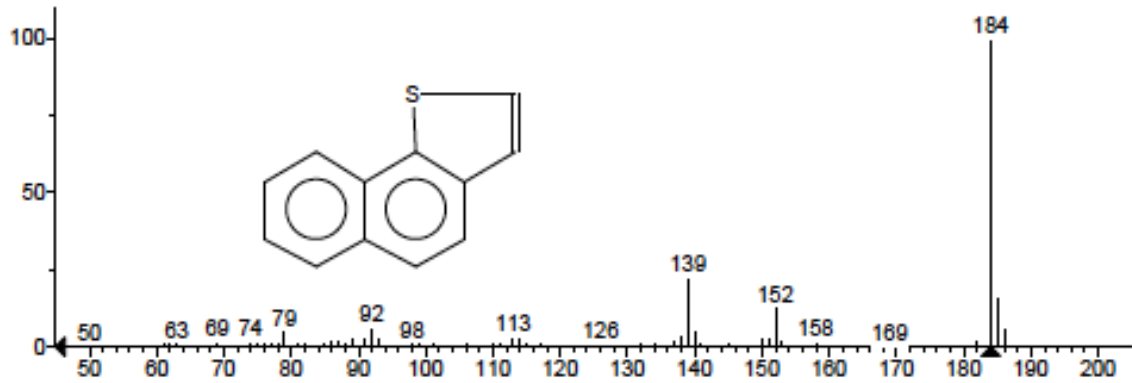
Hit 2 : Dibenzothiophene
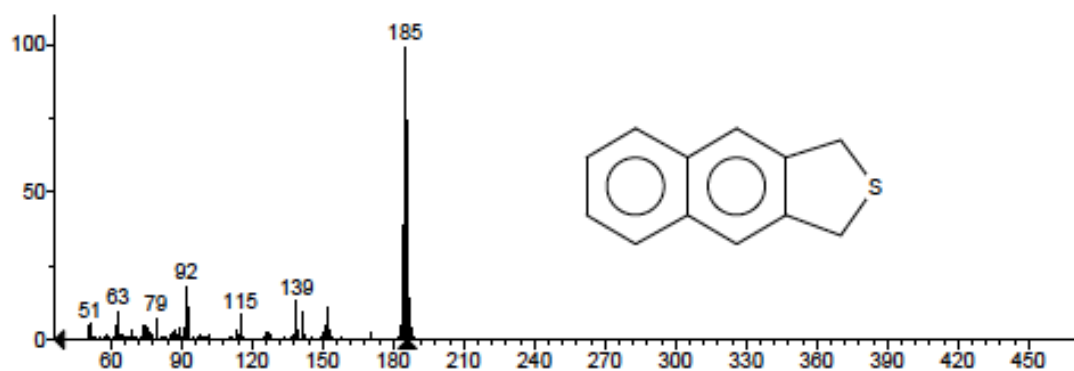C12H8S; MF: 878; RMF: 896; Prob 27.1%; CAS: 132-65-0; Lib: mainlib; ID: 151494.

259

Unknown: Average of 20.634 to 20.667 min.: 0201002.D
Compound in Library Factor = -403

Hit 1 : Naphtho[2,3-c]thiophene, 1,3-dihydro-
C12H10S; MF: 711; RMF: 779; Prob 46.6%; CAS: 58948-53-1; Lib: mainlib; ID: 152379.

Hit 2 : Diphenyl sulfide
C12H10S; MF: 704; RMF: 784; Prob 35.7%; CAS: 139-66-2; Lib: mainlib; ID: 153783.

260